A STUDY OF THE MASS TRANSPORT AND ELECTROCHEMICAL PROPERTIES OF MATERIALS FOR CERAMIC OXYGEN GENERATORS.

John Derrick Sirman

A thesis submitted for the degree of the Doctor of Philosophy
of the University of London
and for the Diploma of Imperial College.



Department of Materials,
Imperial College of Science, Technology and Medicine,
Prince Consort Road,
London. SW7 2BP

January 1998

Abstract.

The work in this thesis is primarily concerned with the oxygen ion diffusion and exchange properties of materials used in ceramic oxygen generation devices. The two principal methods used to determine oxygen ion transport properties in these materials were $^{16}O/^{18}O$ isotope exchange followed by Secondary Ion Mass Spectrometry (SIMS) and AC impedance spectroscopy. From the SIMS data, oxygen tracer diffusion coefficients and oxygen surface exchange coefficients were calculated. Oxygen ion conductivity and electrode polarisation resistances were determined from AC impedance spectroscopy.

The electrode polarisation resistance of $La_{0.6}Sr_{0.4}Co_{0.2}Fe_{0.8}O_{3-\delta}$ was calculated as a function of temperature using AC impedance spectroscopy. A model for the electrode reaction was used to calculate the theoretical electrode resistance using oxygen diffusion and exchange coefficients determined from SIMS. The calculated and experimental values compared very well.

Oxygen tracer diffusion coefficients were determined for a selection of gadolinia doped ceria (CGO) and yttria stabilised zirconia (YSZ) materials. The CGO materials showed a minimum in the activation energy for diffusion at 10mol% Gd_2O_3 dopant concentration. The activation energy for diffusion of YSZ was generally higher than for CGO of a similar composition. The oxygen ion conductivity of CGO and YSZ was determined from AC impedance spectroscopy. Conductivity diffusion coefficients were calculated from the conductivity using the Nernst-Einstein equation. The tracer diffusion coefficients were then compared to the conductivity diffusion coefficients. The two measurement techniques gave similar activation energies for diffusion. However, the conductivity diffusion coefficient was between a factor of 6 and 9 higher than the tracer diffusion coefficient. This was attributed to the presence of charged defect associates, particularly at low temperatures, contributing to the conductivity but not to the long range diffusivity.

Oxygen surface exchange coefficients were calculated for CGO and YSZ. A change in the activation energy of surface exchange occurred between 650 and 750°C. At high temperatures the activation energy was high and at low temperatures the activation energy was low. It was postulated that the rate limiting step in the exchange process was the supply of electrons at high temperatures and the supply of oxygen vacancies at low temperatures.

Acknowledgements.

I would like to thank my supervisor Prof. John Kilner for his help, guidance and sarcastic encouragement over the past three years. I would also like to thank my industrial sponsors Normalair-Garrett Ltd. for their additional funding of this work, and in particular to Mr. Rob Phillips and Mr. Adrian Simmons for their help and entertainment during my study.

There are a many members of the Ceramic Ion Conducting Membranes group at Imperial College to whom I am greatly indebted for their contribution to this work. I would like to express my thanks to Dr. Jon Lane, Dr. Dave Waller and Mr. Philip Manning for their contribution to the science of this project, and also for their tremendous ability to encourage me to make a fool of myself and thus keep me sane during my Ph.D. I would also like to acknowledge Prof. Brian Steele, Dr. Roger De Souza, Mr. Richard Chater, Mr. Bob Rudkin and Dr. David McPhail for their scientific expertise; Miss Cynthia Shaw, Dr. Jon Lane and Dr. Roger De Souza (again) for proof reading my thesis; and Mr. Jonathan Wells for carrying out the SEM and Dr. David Waller for performing the XRD. I also acknowledge my fellow students for their humour and arguments during this long struggle; Mr. James Ralph, Mr. Enrique Ruiz-Trejo, Mr. Simon Hogg, Miss Sarah Benson and Miss Sarah Fearn.

Lastly, I would like to thank my parents for providing me with the opportunity to study at university for six years, without complaint or criticism.

"*...knowledge is something that is acquired - a precious ore hacked from the grey strata of ignorance.*"

Terry Pratchett, 1996.

Table of Contents.

Abstract. Page 2

Acknowledgements. Page 3

Table of Contents. Page 4

List of Figures. Page 12

List of Tables. Page 23

1. Oxygen Generators For Military Aircraft. Page 26

1.1. Introduction. Page 26

1.2. Pressure Swing Adsorption Method. Page 33

1.3. Pressure Driven Ceramic Oxygen Separator. Page 43

1.3.1. Materials Requirements for a Pressure Driven Ceramic Oxygen Generator. Page 48

1.4. Electrically Driven Ceramic Oxygen Generator. Page 49

1.4.1. Materials Requirements for a COG. Page 53

1.4.1.1. Electrolyte. Page 54

1.4.1.2. Cathode. Page 55

1.4.1.3. Anode. Page 57

1.4.1.4. Interconnect. Page 57

1.4.1.5. Balance of Plant. Page 58

1.4.2. Stack Design for a COG. Page 58

1.4.3. Aerospace Considerations. Page 60

1.5. References. Page 64

2. Solid Oxide Fuel Cells. Page 68

2.1. Introduction. Page 68

2.2. Fuel Cell Efficiency and Operating Temperature. Page 70

2.3. Fuel Cell Component Requirements. Page 73

2.3.1. Interconnect. Page 74

2.3.2. Anode. Page 75

2.3.3. Electrolyte. Page 77

2.3.4. Cathode. Page 78

2.4. SOFC Stack Design. Page 79

2.4.1. Tubular SOFC. Page 79

2.4.2. Planar SOFC. Page 80

2.5. References. Page 81

3. Crystal Structure and Defect Chemistry of Perovskite and Fluorite Oxides. Page 86

3.1 Introduction. Page 86

3.2. Perovskite Crystal Structure. Page 86

3.3. Nonstoichiometry and Defect Chemistry of $R_ET_MO_{3\pm\delta}$ Perovskites. Page 88

3.4. Brouwer Diagrams. Page 91

3.5. Fluorite Crystal Structure. Page 98

3.6. Nonstoichiometry and Defect Chemistry of Acceptor Doped Fluorites. Page 99

3.7. Brouwer Diagrams of acceptor Doped Fluorites Page 102

3.8. Defect Association in Fluorites. Page 106

3.9. References. Page 109

4. Oxygen Ion, Electronic and Protonic Transport in Perovskite and Fluorite Oxides. Page 113

4.1 Introduction. Page 113

4.2 Ionic Conduction and Diffusion. Page 113

4.3 Types of Diffusion Coefficient. Page 118

4.4 Experimental Behaviour of the Oxygen Transport in Fluorite Materials. Page 123

4.5 Experimental Behaviour of the Oxygen Transport in Perovskite Materials. Page 127

4.6 Electronic Conduction. Page 131

4.7 Protonic Conduction. Page 132

4.8. References. Page 133

5. Cation Diffusion in Fluorite Oxides. Page 136

5.1. Introduction. Page 136

5.2. Electrode/Electrolyte Reactivity. Page 136

5.3. Solubility of Transition Metal Cations in YSZ and CGO. Page 137

5.4. Cation Diffusion in Fluorites. Page 138

5.5. References. Page 140

6. Oxygen Exchange on Oxide Surfaces. Page 142

6.1. Introduction. Page 142

6.2. The Surface Exchange Coefficient. Page 151

6.3. Experimental Behaviour of k for Perovskite Oxides. Page 156

6.4. Experimental Behaviour of k for Fluorite Oxides. Page 160

6.5. Atomistic Mechanisms of Surface Exchange. Page 164

6.6. References. Page 166

7. Experimental Techniques. Page 169

7.1. Introduction. Page 169

7.2. Sample Preparation. Page 169

7.2.1. Dense Ceramic Samples. Page 169

7.2.2. Electrode Preparation. Page 171

7.3. X-ray Diffraction. Page 172

7.4. Scanning Electron Microscopy. Page 172

7.5. Atomic Force Microscopy. Page 172

7.6. AC Impedance Spectroscopy. Page 173

7.6.1. Response of an Electrolyte Under an AC field. Page 174

7.6.2. Response of an Electrode Under an AC field. Page 179

7.7. Diffusion Measurements. Page 180

7.7.1. $^{16}O/^{18}O$ Isotope Exchange. Page 180

7.7.2. Cation Diffusion Couples. Page 182

7.8. Determination of the Diffusion Profile Using SIMS. Page 185

7.8.1. The Atomika 6500 Ion Microprobe. Page 185

7.8.2. Depth Profiling Mode of Analysis. Page 187

7.8.3. Line-scanning Mode of Analysis. Page 189

7.8.4. Limitations of the SIMS Instrument. Page 190

7.9. References. Page 195

8. Electrode Behaviour of Perovskite Cathodes on $Ce_{0.9}Gd_{0.1}O_{1.95}$. Page 196

8.1. Introduction. Page 196

8.2. Slow Oxygen Ion Conductors. Page 197

8.3. Fast Oxygen Ion Conductors. Page 201

8.4. Morphology of the $La_{0.6}Sr_{0.4}Co_{0.2}Fe_{0.8}O_{3-\delta}$ Electrode. Page 207

8.5. Polarisation Behaviour of the $La_{0.6}Sr_{0.4}Co_{0.2}Fe_{0.8}O_{3-\delta}$ Electrodes. Page 208

8.6. Comparison of the Experimental Polarisation to the Models. Page 210

8.7. References. Page 214

9. Conductivity of $Ce_{1-x}Gd_xO_{2-\delta}$ and $Zr_{1-x}Y_xO_{2-\delta}$ Electrolytes. Page 216

9.1. Introduction. Page 216

9.2. $Ce_{0.69}Gd_{0.31}O_{1.845}$ Single Crystal. Page 217

9.3. $Ce_{0.9}Gd_{0.1}O_{1.95}$ Polycrystal. Page 220

9.4. $Zr_{0.85}Y_{0.15}O_{1.925}$ Polycrystal. Page 224

9.5. $Zr_{0.81}Y_{0.19}O_{1.905}$ Single Crystal. Page 226

9.6. Comparison of the Conductivity Data for the Fluorite Materials. Page 228

9.7. References. Page 230

10. Oxygen Diffusion in Doped Cerium and Zirconium Oxides. Page 232

10.1. Introduction. Page 232

10.2. Oxygen Diffusion in Single Crystal $Ce_{0.69}Gd_{0.31}O_{1.845}$. Page 232

10.3. Oxygen Diffusion in Polycrystalline $Ce_{0.9}Gd_{0.1}O_{1.95}$. Page 237

10.4. Oxygen Diffusion in $Ce_{0.8}Gd_{0.2}O_{1.9}$ and $Ce_{0.8}Gd_{0.18}Pr_{0.02}O_{2-x}$ Polycrystals. Page 240

10.5. Oxygen Diffusion in Polycrystalline $Zr_{0.85}Y_{0.15}O_{1.925}$. Page 246

10.6. Comparison of Tracer Diffusivities Obtained for Different Materials. Page 249

10.7. Comparison of Tracer Diffusivities with Data from the Literature. Page 251

10.8. Comparison of Tracer Diffusion with Ionic Conductivity from AC Impedance Spectroscopy. Page 254

10.9. References. Page 260

11. Oxygen Exchange on the Surface of Fluorites. Page 262

11.1. Introduction. Page 262

11.2. Surface Exchange Coefficients of Polycrystalline $Ce_{0.9}Gd_{0.1}O_{1.95}$. Page 262

11.3. Surface Exchange Coefficients of Single Crystal CGO. Page 265

11.4. Surface Exchange Coefficients of Polycrystalline $Ce_{0.8}Gd_{0.2}O_{1.9}$. Page 267

11.5. Surface Exchange Coefficients of Polycrystalline $Ce_{0.8}Gd_{0.18}Pr_{0.02}O_{2-x}$. Page 268

11.6. Surface Exchange Coefficients of Polycrystalline $Zr_{0.85}Y_{0.15}O_{1.925}$. Page 269

11.7. Comparison of the Surface Exchange Coefficients of CGO and YSZ. Page 270

11.8. Comparison of Surface Exchange Data with Data from the Literature. Page 276

11.9. Atomistic Mechanism of Oxygen Surface Exchange. Page 281

11.9.1. Suggested Mechanism for Surface Exchange on Fluorites at High Temperatures. Page 281

11.9.2. Suggested Mechanism for Surface Exchange on Fluorites at Low Temperatures. Page 283

11.10. References. Page 287

12. Conclusions and Future Work. Page 288

List of Publications. Page 291

Appendix A. Cation Diffusion in YSZ and CGO. Page 293

A.1. Introduction. Page 293

A.2. Manganese Diffusion in Single Crystal YSZ. Page 294

A.3. Manganese Diffusion in Polycrystalline YSZ. Page 296

A.4. Cobalt and Iron Diffusion in Polycrystalline CGO. Page 301

A.5. References. Page 304

List of Figures.

Chapter 1.

Figure 1.1a. Concentration of oxygen physiologically required as a function of altitude.

Figure 1.1b. Partial pressure of oxygen in the lungs as a function of altitude when the oxygen concentration is maintained at 21%.

Figure 1.1c. Partial pressure of oxygen in the lungs as a function of altitude when the concentration follows the function in figure 1.1a.

Figure 1.2. Typical cabin altitude as a function of aircraft altitude.

Figure 1.3. Cabin pressure and ambient pressure as functions of aircraft altitude.

Figure 1.4a. Oxygen concentration supplied to the pilot as a function of aircraft altitude, where the minimum alveolar pO_2 is 30 mmHg.

Figure 1.4b. Alveolar pO_2 in the lungs in the pressurised and depressurised condition as a function of aircraft altitude, where the minimum alveolar pO_2 is 30 mmHg.

Figure 1.5a. Oxygen concentration supplied to the pilot as a function of aircraft altitude, where the minimum alveolar pO_2 is 60 mmHg.

Figure 1.5b. Alveolar pO_2 in the lungs in the pressurised and depressurised condition as a function of aircraft altitude, where the minimum alveolar pO_2 is 60 mmHg.

Figure 1.6. Basic Steps of Pressure Swing Adsorption.

Figure 1.7a. Possible Three Bed Configuration for an MSOC.

Figure 1.7b. Valve Timing Sequence for Figure 1.7a.

Figure 1.8a. Schematic diagram of a possible design for an MSOC.

Figure 1.8b. Valve Timing Sequence for Figure 1.8a.

Figure 1.9. Schematic diagram of an up and over bed design.

Figure 1.10. Oxygen concentration of product gas produced by an MSOC as a function of altitude.

Figure 1.11. Oxygen concentration of product gas produced by an MSOC as a function of the inlet gas pressure.

Figure 1.12. Oxygen concentration of product gas produced by an MSOC as a function of the temperature of the molecular sieve.

Figure 1.13. Oxygen concentration of product gas produced by an MSOC as a function of the volumetric flow rate of the product gas.

Figure 1.14. Schematic representation of a Pressure Driven Ceramic Oxygen Separator.

Figure 1.15. Schematic representation of the dependence of oxygen flux on membrane thickness for a pressure driven ceramic oxygen generator. (Calculated for σ_{ion}=0.1 S/cm, k=10^{-6} cm/s, $pO_2^{'}/pO_2^{''} = 1000$ and T=1000K.)

Figure 1.16. Schematic representation of the dependence of oxygen flux on the oxygen partial pressure ratio across the membrane for a pressure driven ceramic oxygen generator. (Calculated for σ_{ion}=0.1 S/cm, k=10^{-6} cm/s, L=100 microns and T=1000K.)

Figure 1.17. Schematic illustration of a single cell COG.

Figure 1.18. Schematic representation of the dependence of molar flow rate of oxygen on electrolyte thickness for an electrically driven ceramic oxygen generator. (Calculated from resistance data at 750K in air).

Figure 1.19. Schematic representation of the dependence of molar flow rate of oxygen on cell temperature for an electrically driven ceramic oxygen generator. (Calculated from resistance data for an electrolyte thickness of 100 microns.)

Figure 1.20. Exploded schematic illustration of a planar design for an electrically driven ceramic oxygen generator.

Figure 1.21. Schematic illustration of a planar design with an interrupted fin interconnect for an electrically driven ceramic oxygen generator.

Figure 1.22. Input-output, power continuity diagram for a COG on board a military aircraft.

Chapter 2.

Figure 2.1. Schematic illustration of the solid oxide fuel cell.

Figure 2.2. Schematic illustration of the modular nature of a solid oxide fuel cell.

Figure 2.3. Typical Polarisation behaviour of a solid oxide fuel cell.

Figure 2.4. Air electrode supported type tubular solid oxide fuel cell design.

Chapter 3.

Figure 3.1. The unit cell of an ideal cubic perovskite.

Figure 3.2. Brouwer diagram of an acceptor doped perovskite.

Figure 3.3. Theoretical nonstoichiometric behaviour of an acceptor doped transition metal perovskite.

Figure 3.4. Oxygen content of $La_{1-x}Sr_xCoO_{3\pm\delta}$ as a function of pO_2 at 800°C.

Figure 3.5. Oxygen content of $La_{1-x}Sr_xMnO_{3\pm\delta}$ as a function of pO_2 at 1000°C.

Figure 3.6. Oxygen content of $La_{0.9}Sr_{0.1}BO_{3\pm\delta}$ as a function of pO_2 at 1000°C (B=Cr,Fe,Mn,Co).

Figure 3.7. Crystal structure of the fluorite crystal structure.

Figure 3.8. Brouwer diagram of an acceptor doped fluorite.

Figure 3.9. Partial conductivity graph of an acceptor doped fluorite.

Figure 3.10. Graph of the conductivity of gadolinia doped ceria as a function of gadolinia content at 500°C.

Chapter 4.

Figure 4.1. Schematic illustration of atoms diffusing with a concentration gradient.

Figure 4.2. Graph of bulk conductivity as a function of temperature for various zirconia and ceria based fluorite materials.

Figure 4.3. Graph of diffusivity as a function of temperature for various zirconia and ceria based fluorite materials.

Figure 4.4. Arrhenius plot of D_σ (circles) and D_T (triangles), for 9.5mol% YSZ single crystal.

Figure 4.5. Graph of diffusivity as a function of temperature for various $R_E T_M O_{3\pm\delta}$ perovskites.

Figure 4.6. A comparison of the tracer diffusion coefficient of $LaCoO_{3-\delta}$ single crystal using SIMS and gas phase analysis.

Figure 4.7. A comparison of the tracer diffusion coefficient of $Zr_{0.81}Y_{0.19}O_{1.905}$ with $La_{0.8}Sr_{0.2}CoO_{3\pm\delta}$, $La_{0.6}Sr_{0.4}Co_{0.2}Fe_{0.8}O_{3\pm\delta}$ and $Sm_{0.5}Sr_{0.5}CoO_{3-\delta}$.

Chapter 5.

Figure 5.1. Lattice parameter of Mn doped YSZ as a function of Manganese content.

Figure 5.2. Graph of the apparent diffusion coefficient of Mn, Y, and Zr in YSZ, (P) indicates a polycrsystal and (S) a single crystal.

Chapter 6.

Figure 6.1. Schematic illustration of the exchange process described by equation 6.2.

Figure 6.2. Schematic illustration of a defective crystal in the presence of a labelled gas.

Figure 6.3. Schematic illustration of atomic exchange on a defective crystal where a surface oxygen vacancy is the preferred site for adsorption.

Figure 6.4. Schematic illustration of molecular exchange on a defective crystal where a surface oxygen vacancy is the preferred site for adsorption.

Figure 6.5. Schematic illustration of atomic exchange on a defective crystal with no preferred sites for adsorption.

Figure 6.6. Schematic illustration of molecular exchange on a defective crystal with no preferred sites for adsorption.

Figure 6.7. Schematic illustration of an adsorbed surface oxygen being incorporated into the bulk of the material.

Figure 6.8. Schematic illustration of the exchange process (with no subsequent diffusion) for a slow exchanger (a) and a fast exchanger (b).

Figure 6.9. Schematic illustration of the exchange process for a slow diffuser (a) and a fast diffuser(b) where the exchange coefficient is constant.

Figure 6.10. The surface isotopic fraction as a function of the dimensionless parameter h'.

Figure 6.11. The surface exchange coefficient for a selection of $R_ET_MO_3$ perovskites as a function of temperature.

Figure 6.12. Graph showing the relation ship between ΔH_{EX} and strontium content in $(La,Sm)_{1-x}Sr_xCoO_{3-\delta}$.

Figure 6.13. The pO_2 dependence of the surface exchange coefficient for two perovskite materials.

Figure 6.14. Arrhenius plot of the surface exchange coefficient for a variety of fluorite oxides.

Figure 6.15. Arrhenius plot of the surface exchange coefficient for single crystal $Zr_{0.81}Y_{0.19}O_{1.905}$.

Figure 6.16. Gas phase analysis of powdered 9.5 mol% YSZ sample at 900°C.

Figure 6.17. Gas phase analysis of powdered 9.5 mol% YSZ sample at 450°C.

Chapter 7.

Figure 7.1. Generated AC impedance spectra given two responses of 100kΩ and (a) $\tau_1 = 10^{-7}\,\text{sec s}, \tau_2 = 10^{-4}\,\text{sec s}$ and (b) $\tau_1 = 10^{-5}\,\text{sec s},\ \tau_2 = 10^{-4}\,\text{sec s}$.

Figure 7.2. Schematic illustration of the $^{16}O/^{18}O$ isotope exchange apparatus.

Figure 7.3 Schematic illustration of the diffusion systems used for the study of cation diffusion.

Figure 7.4. Schematic illustration of the Atomika 6500 Ion Microprobe.

Figure 7.5. SIMS raw data for a depth profile of manganese into polycrystal YSZ at 1250°C.

Figure 7.6. Schematic diagram summarising the SIMS/line-scan technique.

Figure 7.7. SIMS raw data for a line-scan for ^{18}O diffusion into single crystal CGO at 858°C.

Figure 7.8. AFM images of the surface of (a) Polycrystal $Ce_{0.9}Gd_{0.1}O_{1.95}$ and (b) single crystal YSZ.

Figure 7.9. Effect of changing k on the shape of the diffusion profile at given values of D_T and anneal times.

Figure 7.10. Effect of changing k on the shape of the diffusion profile at $D_T = 3 \times 10^{-6}, t = 600$.

Chapter 8.

Figure 8.1. Schematic illustration of the electrode process in (a) a slow oxygen ion conductor and (b) a fast oxygen ion conductor.

Figure 8.2. Impedance spectra for fast oxygen ion conducting cathodes where surface exchange and bulk diffusion are rate limiting.

Figure 8.3. Scanning electron micrograph of the cross sectional view of a $La_{0.6}Sr_{0.4}Co_{0.2}Fe_{0.8}O_{3-\delta}$ electrode on a $Ce_{0.9}Gd_{0.1}O_{1.95}$ electrolyte.

Figure 8.4. Atomic force micrograph of the top view of a $La_{0.6}Sr_{0.4}Co_{0.2}Fe_{0.8}O_{3-\delta}$ electrode on a $Ce_{0.9}Gd_{0.1}O_{1.95}$ electrolyte.

Figure 8.5. Impedance spectra for symmetrical $La_{0.6}Sr_{0.4}Co_{0.2}Fe_{0.8}O_{3-\delta}$ electrodes at 420°C and 439°C in air.

Figure 8.6. Area specific resistance of $La_{0.6}Sr_{0.4}Co_{0.2}Fe_{0.8}O_{3-\delta}$ electrodes in air as a function of temperature.

Figure 8.7. Impedance spectrum of $La_{0.6}Sr_{0.4}Co_{0.2}Fe_{0.8}O_{3-\delta}$ at 420°C together with a generated profile using equations 8.26, 8.25 and 8.27.

Figure 8.8. Comparison of experimental polarisation resistance for $La_{0.6}Sr_{0.4}Co_{0.2}Fe_{0.8}O_{3-\delta}$ with the resistance obtained from the ALS model.

Figure 8.9. Comparison of experimentally obtained polarisation resistance for $La_{0.6}Sr_{0.4}Co_{0.2}Fe_{0.8}O_{3-\delta}$ with the resistance obtained from the sum of the finite length diffusion resistance and the surface exchange resistance.

Chapter 9.

Figure 9.1. Impedance spectra obtained for single crystal CGO in oxygen.

Figure 9.2. Arrhenius graph of conductivity of single crystal CGO in various atmospheres.

Figure 9.3. Impedance spectra obtained for polycrystal $Ce_{0.9}Gd_{0.1}O_{1.95}$ in wet and dry nitrogen.

Figure 9.4. Arrhenius graph of the bulk and grain boundary conductivity of $Ce_{0.9}Gd_{0.1}O_{1.95}$ in a wet and dry atmosphere.

Figure 9.5. Conductivity of polycrystalline $Ce_{0.9}Gd_{0.1}O_{1.95}$ in air as a function of temperature.

Figure 9.6. Comparison of the total conductivity of $Ce_{0.9}Gd_{0.1}O_{1.95}$ in a wet and dry nitrogen atmosphere and air.

Figure 9.7. Conductivity of polycrystal $Zr_{0.85}Y_{0.15}O_{1.925}$ and single crystal $Zr_{0.81}Y_{0.19}O_{1.905}$ as a function of temperature.

Figure 9.8 Conductivity of single crystal of YSZ as a function of temperature in the wet and dry atmospheres.

Figure 9.9. Comparison of polycrystal and single crystal YSZ in different atmospheres.

Figure 9.10. Comparison of the conductivity of YSZ and CGO materials obtained using AC impedance spectroscopy.

Chapter 10.

Figure 10.1. Raw line-scan data for oxygen diffusion in a $Ce_{0.69}Gd_{0.31}O_{1.845}$ single crystal annealed at 858°C for 571 seconds.

Figure 10.2 Typical high temperature ^{18}O diffusion profiles obtained for single crystal $Ce_{0.69}Gd_{0.31}O_{1.845}$.

Figure 10.3. Typical low temperature (568°C) ^{18}O diffusion profile obtained for single crystal $Ce_{0.69}Gd_{0.31}O_{1.845}$.

Figure 10.4. Tracer diffusivity of single crystal $Ce_{0.69}Gd_{0.31}O_{1.845}$ as a function of reciprocal temperature.

Figure 10.5. Typical high temperature ^{18}O diffusion profiles obtained for polycrystalline $Ce_{0.9}Gd_{0.1}O_{1.95}$.

Figure 10.6. Tracer diffusivity of polycrystalline $Ce_{0.9}Gd_{0.1}O_{1.95}$ as a function of temperature.

Figure 10.7. Typical diffusion profiles for polycrystalline $Ce_{0.8}Gd_{0.18}Pr_{0.02}O_{2-x}$.

Figure 10.8. Optical micrograph of $Ce_{0.8}Gd_{0.18}Pr_{0.02}O_{2-x}$.

Figure 10.9. Typical diffusion profiles $Ce_{0.8}Gd_{0.2}O_{1.9}$ compared with $Ce_{0.8}Gd_{0.18}Pr_{0.02}O_{2-x}$ at the same temperature and anneal times.

Figure 10.10. Tracer diffusion coefficient of $Ce_{0.8}Gd_{0.18}Pr_{0.02}O_{2-x}$ and $Ce_{0.8}Gd_{0.2}O_{1.9}$ as a function of temperature.

Figure 10.11. Typical ^{18}O diffusion profiles obtained for polycrystalline $Zr_{0.85}Y_{0.15}O_{1.925}$.

Figure 10.12. Tracer diffusivity of polycrystalline $Zr_{0.85}Y_{0.15}O_{1.925}$ and single crystal $Zr_{0.81}Y_{0.19}O_{1.905}$ as a function of reciprocal temperature.

Figure 10.13. Oxygen tracer diffusivity in various fluorite materials as a function of reciprocal temperature.

Figure 10.14. Comparison of the oxygen tracer diffusivity of CGO with other ceria based fluorites.

Figure 10.15. Comparison of the oxygen tracer diffusivity of YSZ with other zirconia based fluorites.

Figure 10.16. Comparison of the tracer diffusion coefficient with the AC conductivity diffusion coefficient for single crystal $Ce_{0.69}Gd_{0.31}O_{1.845}$.

Figure 10.17. Comparison of the tracer diffusion coefficient with the AC conductivity diffusion coefficient for polycrystalline $Ce_{0.9}Gd_{0.1}O_{1.95}$.

Figure 10.18. Comparison of the tracer diffusion coefficient with the AC conductivity diffusion coefficient for polycrystalline $Zr_{0.85}Y_{0.15}O_{1.925}$.

Chapter 11.

Figure 11.1. Oxygen surface exchange coefficient of polycrystalline $Ce_{0.9}Gd_{0.1}O_{1.95}$ as a function of reciprocal temperature.

Figure 11.2. "h-plane" plot of k and D_T values obtained for single crystal $Zr_{0.81}Y_{0.19}O_{1.905}$ and polycrystalline $Ce_{0.9}Gd_{0.1}O_{1.95}$.

Figure 11.3. Oxygen surface exchange coefficient of single crystal $Ce_{0.69}Gd_{0.31}O_{1.845}$ as a function of reciprocal temperature.

Figure 11.4. Oxygen surface exchange coefficient of polycrystalline $Ce_{0.8}Gd_{0.2}O_{1.9}$ as a function of reciprocal temperature.

Figure 11.5. Oxygen surface exchange coefficient of polycrystalline $Ce_{0.8}Gd_{0.18}Pr_{0.02}O_{2-x}$ as a function of reciprocal temperature.

Figure 11.6. Oxygen surface exchange coefficient of polycrystalline $Zr_{0.85}Y_{0.15}O_{1.925}$ as a function of reciprocal temperature.

Figure 11.7 "h-plane" plot of k and D_T values obtained for YSZ and CGO materials.

Figure 11.8. Graph of the surface exchange coefficient of various CGO materials as a function of reciprocal temperature.

Figure 11.9. Graph of the surface exchange coefficient of polycrystalline and single crystal YSZ materials as a function of reciprocal temperature.

Figure 11.10. Arrhenius Graph of the surface exchange coeffciient of various fluorites.

Figure 11.11. Effect on the ^{18}O surface concentration by coating CGO with platinum particles. (Bare CGO annealed at 486°C for 2730 seconds, Pt coated CGO annealed at 493°C for 2892 seconds).

Figure 11.12. Comparison of the ^{18}O surface concentration of CGO covered with LSCF particles and platinum particles.

Figure 11.13. Schematic illustration of the proposed mechanism for oxygen exchange on fluorite surfaces at high temperatures.

Figure 11.14. Schematic illustration of the proposed mechanism for oxygen exchange on fluorite surfaces at low temperatures.

Appendix A.

Figure A.1. Diffusion profile of manganese into single crystal YSZ at 1300°C.

Figure A.2. Arrhenius graph of the diffusion coefficient of manganese into single crystal YSZ from a Mn_2O_3 source.

Figure A.3. Diffusion profile of manganese into YSZ at 1100°C from a Mn_2O_3 source.

Figure A.4. Diffusion profile of manganese into YSZ at 1400°C from a Mn_2O_3 source.

Figure A.5. Diffusion profile of manganese into YSZ from a LSM source at 1500°C.

Figure A.6. Diffusion profile of lanthanum into YSZ from a LSM source at 1500°C.

Figure A.7. Comparison of the diffusion coefficient of manganese, lanthanum and strontium in polycrystalline YSZ from a Mn_2O_3 and LSM source.

Figure A.8. Comparison of the diffusion coefficient of manganese in single crystal and polycrystalline YSZ from a Mn_2O_3 source.

Figure A.9. X-ray diffraction patterns of iron/CGO solid solutions.

Figure A.10. Lattice parameter of iron/CGO and cobalt/CGO as a function of dopant concentration.

Figure A.11. Arrhenius graph of the diffusion coefficient of iron and cobalt into polycrystalline CGO.

List of Tables.

Chapter 1.

Table 1.1. Heats of adsorption of various sorbate gases for two zeolite materials..

Table 1.2. Inlet air gas contaminants.

Chapter 3.

Table 3.1. Stability of transition metal perovskites with respect to pO_2 at 1000°C.

Chapter 7.

Table 7.1. Sintering temperatures and times employed in preparation of dense ceramic samples.

Table 7.2. Densities of samples obtained after sintering.

Table 7.3. Atmospheres used for examining electrical behaviour of samples using AC impedance spectroscopy.

Table 7.4. Diffusion conditions and subsequent SIMS analysis method used for cation diffusion at various temperatures.

Table 7.5. Limitations to the oxygen tracer diffusion coefficient measurable using $^{16}O/^{18}O$ exchange/SIMS technique.

Table 7.6. Limitations to the diffusion coefficient measurable using $^{16}O/^{18}O$ exchange/SIMS technique.

Chapter 9.

Table 9.1 Activation energy for the conductivity of selected fluorites.

Chapter 10.

Table 10.1. Anneal temperatures and times in the diffusion experiments on $Ce_{0.69}Gd_{0.31}O_{1.845}$.

Table 10.2. Values of the tracer diffusion coefficient and the surface exchange coefficient for single crystal $Ce_{0.69}Gd_{0.31}O_{1.845}$.

Table 10.3. Anneal temperatures and times in the diffusion experiments on $Ce_{0.9}Gd_{0.1}O_{1.95}$.

Table 10.4. Values of the tracer diffusion coefficient and the surface exchange coefficient for polycrystalline $Ce_{0.9}Gd_{0.1}O_{1.95}$.

Table 10.5. Anneal temperatures and times used in the diffusion experiments on $Ce_{0.8}Gd_{0.2}O_{1.9}$ and $Ce_{0.8}Gd_{0.18}Pr_{0.02}O_{2-x}$.

Table 10.6. Tracer diffusion and surface exchange coefficients obtained for polycrystalline $Ce_{0.8}Gd_{0.18}Pr_{0.02}O_{2-x}$.

Table 10.7. Tracer diffusion and surface exchange coefficients obtained for polycrystalline $Ce_{0.8}Gd_{0.2}O_{1.9}$.

Table 10.8. Anneal temperatures and times used in the diffusion experiments on $Zr_{0.85}Y_{0.15}O_{1.925}$.

Table 10.9. Tracer diffusion and surface exchange coefficients obtained for polycrystalline $Zr_{0.85}Y_{0.15}O_{1.925}$.

Table 10.10. Activation energy for oxygen tracer diffusivity in various fluorite materials.

Table 10.11. Haven ratio for $Ce_{0.69}Gd_{0.31}O_{1.845}$, $Ce_{0.9}Gd_{0.1}O_{1.95}$ and $Zr_{0.85}Y_{0.15}O_{1.925}$.

Chapter 11.

Table 11.1. Activation energy for oxygen surface exchange on various fluorite materials.

Table 11.2. Comparison of the activation energy of k and D_T for various YSZ and CGO materials.

Appendix A.

Table A.1. Values of the diffusion coefficient of Mn in single crystal YSZ from a Mn_2O_3 source.

Table A.2. Values of the diffusion coefficient of Mn into polycrystalline YSZ from a Mn_2O_3 source.

Table A.3. Values of the diffusion coefficient of manganese, lanthanum and strontium in polycrystalline YSZ from a LSM source.

Table A.4. Values of the diffusion coefficient of Co and Fe in polycrystalline CGO.

1. Oxygen Generators For Military Aircraft.

1.1. Introduction.

Aircrew of agile, high performance military fighter aircraft are provided with a supply of oxygen enriched breathing gas via demand regulators and mask assemblies for the physiological protection required at high altitudes and during high "g" manoeuvres. The concentration and the pressure of the oxygen are dependent on the altitude of the aircraft. At sufficiently high altitudes 100% oxygen is required. The flow rate of breathing gas required depends greatly on the work load of the pilot, and the breathing gas supply must therefore be able to cope with sudden changes in demand.

Figure 1.1a shows the concentration of oxygen within the breathing gas that is physiologically required to be inhaled by a human to avoid reducing the partial pressure of oxygen (pO_2) in the blood. This graph is derived from the basic physiological environment within the lungs, such as the partial pressures of water, carbon dioxide and oxygen typically present in the lungs at ground level, and the oxygen exchange efficiency of the lungs. The parameters listed below are found within the lungs are typical of a healthy human [1].

Oxygen exchange efficiency of the alveoli = 0.85
pH_2O = 47 mmHg (6.3kPa)
pCO_2 = 39 mmHg (5.3kPa)
PO_2 = 103 mmHg (13.7kPa)

Figure 1.1b shows the partial pressure of oxygen in the lungs of a typically healthy human as a function of altitude when the concentration of oxygen is maintained at 21%. Figure 1.1c shows the partial pressure of oxygen in the lungs if the concentration of oxygen given to the pilot is that shown in figure 1.1a. It is clear that the ground level equivalent pO_2 in the lungs is maintained up to altitudes of 30,000 feet. The minimum pO_2 in the lungs recommended by the Royal Airforce (and many other European Airforces) is 30 mmHg, while the US Airforce have 60 mmHg requirement. It is clear from figure 1.1b that without providing a supply of breathing gas enriched with oxygen, the maximum recommended altitude for RAF requirements would be restricted to 14000 ft and 9200 ft for USAF pilots. It is also evident from figure 1.1c that above 33000 ft,

the pO_2 in the lungs drops from the ground level equivalent 103 mmHg even with a breathing gas containing 100% oxygen. At 100% O_2, the pO_2 in the lungs drops below 60 mmHg at 39000 ft and below 30 mmHg at 44000 ft.

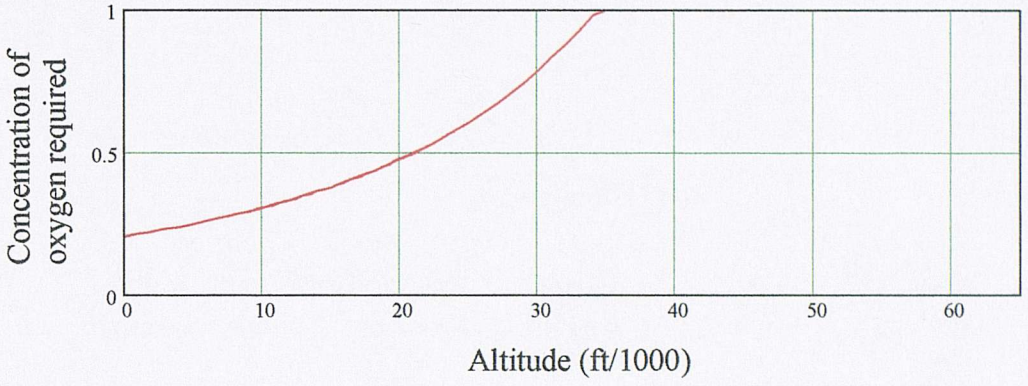


Figure 1.1a. Concentration of oxygen physiologically required as a function of altitude.

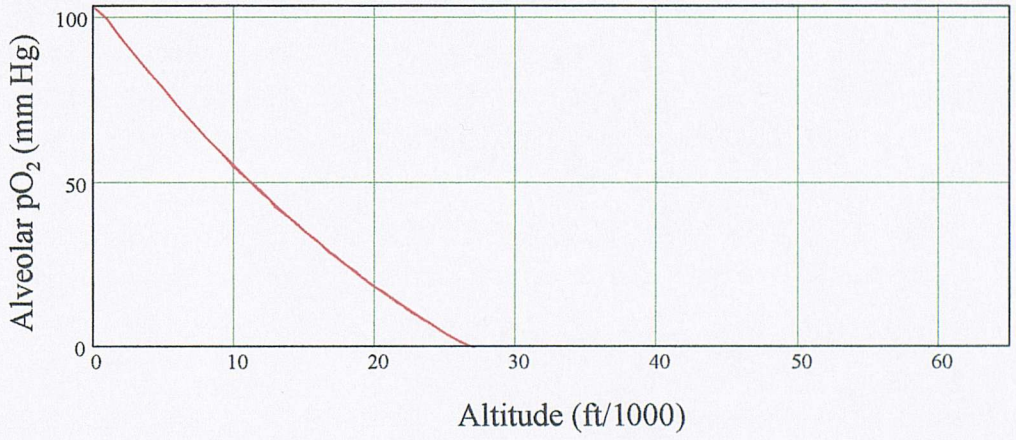


Figure 1.1b. Partial pressure of oxygen in the lungs as a function of altitude when the oxygen concentration is maintained at 21%.

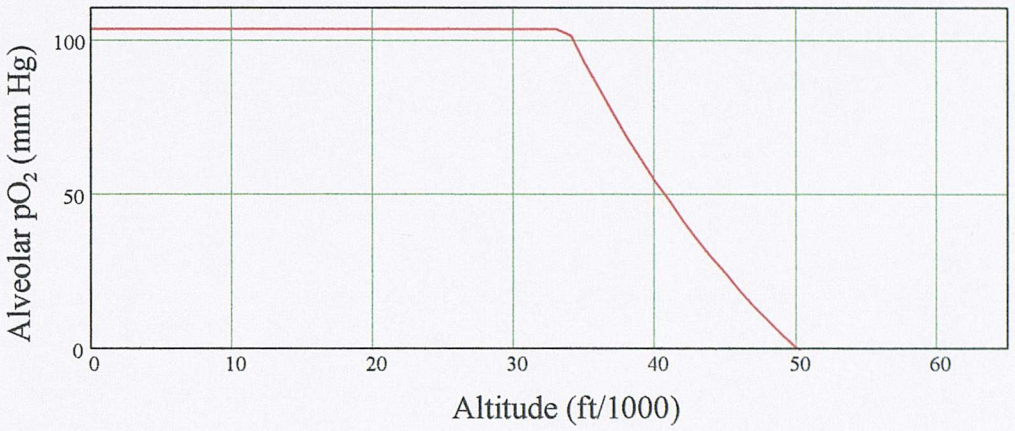


Figure 1.1c. Partial pressure of oxygen in the lungs as a function of altitude when the concentration follows the function in figure 1.1a.

The data presented in figures 1.1 are obtained from a model developed by Phillips [2] using the physiological parameters from [1] given above.

Military requirements dictate that maximum aircraft altitude is considerably higher than 40000 ft. Typical modern fighter aircraft have a ceiling of 65000 ft. As a result of this, the aircraft cockpit is progressively pressurised with increasing aircraft altitude to reduce the equivalent altitude seen by the aircrew. A typical cockpit pressurisation schedule is shown in figures 1.2 and 1.3. The altitude in figure 1.2 is the equivalent aircraft altitude at the cabin pressure.

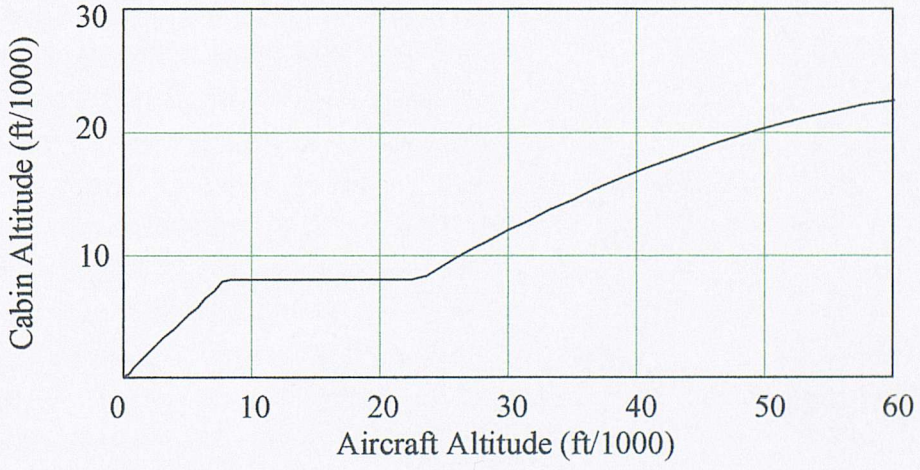


Figure 1.2. Typical cabin altitude as a function of aircraft altitude.

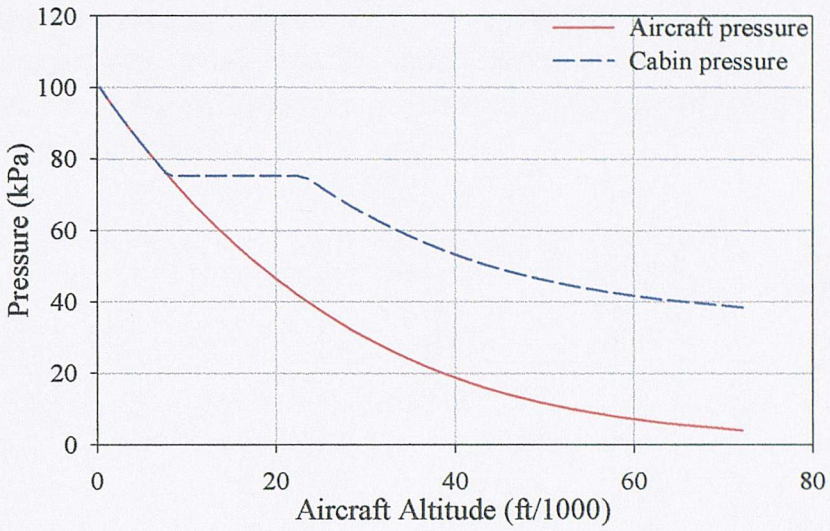


Figure 1.3. Cabin pressure and ambient pressure as functions of aircraft altitude.

From figures 1.2 and 1.3 it is clear that at an aircraft altitude of 65000 ft, the cabin pressure is equivalent to 24000 ft, well within the physiological constraints typically specified by the RAF.

In the event of a sudden depressurisation, the cabin altitude will decompress to the aircraft altitude. This results in a drop in the oxygen partial pressure seen by the pilot and hence a rapid drop in the pO_2 in the lungs. At the higher altitudes, even if the oxygen concentration given to the pilot is increased to 100% within a few a seconds, the alveolar pO_2 can drop below the critical 30 mmHg. If the alveolar pO_2 is below the critical level for a time equivalent to 140 mmHg.s, there is likely to be a loss of consciousness [3]. In order to avoid this catastrophic decrease in the alveolar pO_2, the oxygen concentration before depressurisation must be increased. In the event of depressurisation at very high altitudes, 100% oxygen is not sufficient to prevent a drop below 30 mmHg pO_2 in the lungs. Therefore pressure breathing is used where the pressure of gas in the oxygen mask is greater than in the cabin and hence oxygen is forced into the lungs. There is a physical limit to the degree of pressure breathing and the pressure difference is thus typically restricted to a maximum of 68 mmHg.

The concentration of oxygen required to prevent a drop below 30 mmHg alveolar pO_2 in the event of pressure loss (safety concentration) is shown in figure 1.4a

together with the nominal oxygen concentration required at that altitude in a non-pressurised environment. Figure 1.4b shows the pO_2 in the alveoli when the inhaled oxygen concentration is the safety concentration given in figure 1.4a. The dotted line in figure 1.4b is the pO_2 in the alveoli that will be reached in the event of depressurisation.

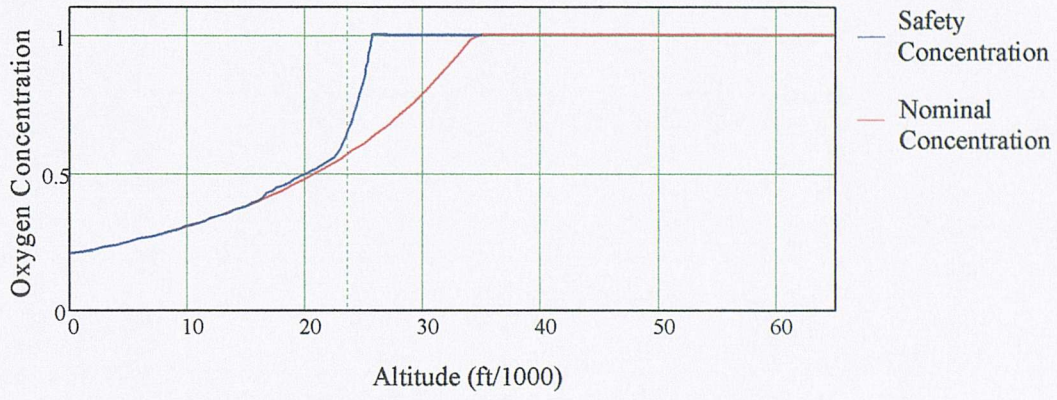


Figure 1.4a. Oxygen concentration supplied to the pilot as a function of aircraft altitude, where the minimum alveolar pO_2 is 30 mmHg.

The vertical, green dotted line in figure 1.4a is the equivalent altitude of the cabin at the maximum altitude of the aircraft (65000 ft), before any depressurisation takes place.

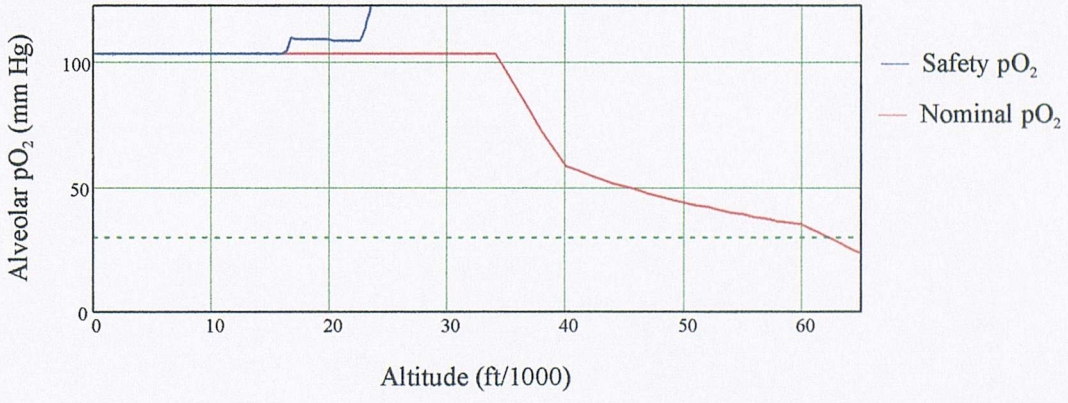


Figure 1.4b. Alveolar pO_2 in the lungs in the pressurised and depressurised condition as a function of aircraft altitude, where the minimum alveolar pO_2 is 30 mmHg [2].

Figures 1.5a and 1.5b show the same function as figures 1.4a and 1.4b but with a critical alveolar pO_2 of 60 mmHg. It is clearly evident from the figures that to avoid the possibility of a drop in pO_2 below 60 mmHg, the maximum aircraft altitude must be below 40000 ft. Furthermore, the pO_2 in the lungs is often required to be greater than 200 mmHg and prolonged periods of this situation can lead to neurological disorder. Therefore the USAF guidelines are rarely adhered to.

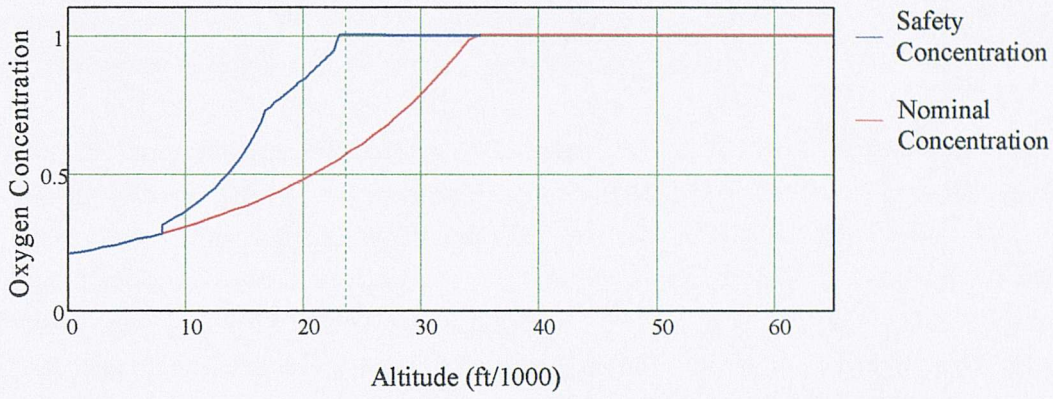


Figure 1.5a. Oxygen concentration supplied to the pilot as a function of aircraft altitude, where the minimum alveolar pO_2 is 60 mmHg.

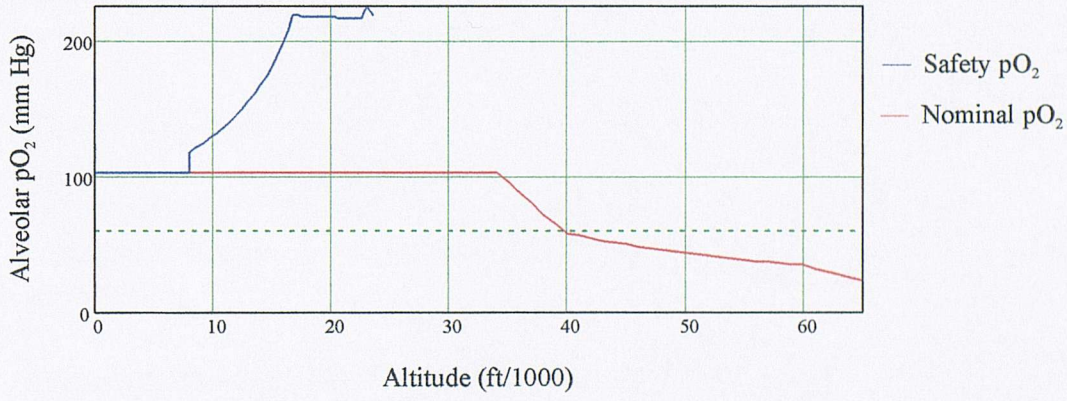


Figure 1.5b. Alveolar pO_2 in the lungs in the pressurised and depressurised condition as a function of aircraft altitude, where the minimum alveolar pO_2 is 60 mmHg [2].

The data in figures 1.4 and 1.5 have been obtained from the model developed by Phillips [2].

Historically, oxygen gas was carried in cylinders within the cockpit area and supplied to the pilot when required. This was not a very satisfactory situation, as the cylinder of oxygen needed to supply a pilot was both large and heavy, and needed removal from the aircraft for recharging. Both space and weight in a military aircraft are tightly constrained. Therefore, liquid oxygen vessels were employed because significantly more oxygen could be provided in a considerably smaller volume. Liquid oxygen vessels are still used in the majority of aircraft breathing systems. A separate small gaseous bottle which supplies emergency oxygen in the event of ejection from the aircraft is also provisioned, and is fitted to the ejector seat to provide sufficient pure oxygen to the pilot until lower altitudes are reached, where air can be safely breathed.

One of the problems with using liquid oxygen (LOX) tanks is that it is only a storage vessel and not an on board oxygen generation system. This means the tanks have to be re-filled at regular intervals because of the inability to stop the liquid oxygen from boiling away despite being contained in a vacuum walled container. The LOX can either be produced locally at an airbase or centrally and then transported to each site. In both cases the cost of supplying the LOX is exceedingly large and a reduction in such expenditure is required by the military. This problem is particularly apparent for naval airforce requirements. Considerable deck space is taken up by the LOX storage vessels, and some 30 tonnes of equipment is required. If large quantities of LOX are stored on an aircraft carrier, then this presents a major fire hazard. There is also a substantial loss in the quantity of LOX over time due to the high rates of evaporation.

Recognising this challenge, the Naval Air Warfare Centre proposed the production of pure oxygen in flight using ceramic membrane technology. Normalair-Garrett Ltd. were one of several companies awarded the contract for a conceptual design of a ceramic oxygen generator (COG) for use in military aircraft.

Current technology for the production of localised oxygen is based on the pressure swing adsorption method using zeolite molecular sieves. This is commonly known by the acronyms OBOGS (On-Board Oxygen Generation System) or MSOC (Molecular Sieve Oxygen Concentrator). However, this technology can only produce a maximum of 95% oxygen; while satisfactory for most environments, it is not ideal for high altitude military aerospace requirements. Furthermore, the product gas concentration will reduce with increasing demand flow and several other factors. Therefore the separation of

oxygen from air using ceramic oxygen ion conducting materials has been investigated and has been proven to be able to produce 100% oxygen, which will not reduce with increasing demands etc.

In the remainder of this chapter, the different possible methods of separating oxygen from air are discussed, together with the requirements and constraints typically employed by Normalair-Garrett Ltd. for military aerospace applications.

1.2. The Pressure Swing Adsorption Method.

The pressure swing adsorption (PSA) method utilises an adsorbent porous material to retain an adsorbed gas phase and produce an enriched gas phase of different composition to the feeder gas. This can be achieved by either molecular sieving or selective adsorption. Molecular sieving is where one gas composition can diffuse through to the adsorbent sites more quickly than another; selective adsorption is where one phase is adsorbed preferentially, allowing passage of the other phase. An ideal adsorbent for PSA is where these two processes work together.

In the case of oxygen separation from air, a zeolite that preferentially adsorbs nitrogen over oxygen is used. Zeolites are microporous, alumino silicate ceramic minerals. The framework of the zeolite is an assembly of SiO_4 and AlO_4 tetrahedra, creating a three-dimensional network of uniform cavities in the crystal, typically between 3 and 13Å. Each oxygen is shared between two tetrahedral Al or Si atoms giving an SiO_2 or AlO_2 stoichiometry for each tetrahedral unit. Each aluminium atom thus introduces one negative charge to the framework that is balanced by an exchangeable cation. Most zeolites have the general unit cell structure of $M_z[(AlO_2)_x(SiO_2)_y]$, where M can be sodium, potassium, calcium, strontium or barium. When exposed to air (or any water containing environment) there is a partial hydration of the zeolite.

The three dimensional network of pores allows the permeation of gas through the zeolite. The exchangeable cations, used to maintain charge neutrality, are located at preferred sites within the framework and affect the size of the cavities. Adsorptive selectivity may depend on a difference in either adsorption kinetics or adsorption equilibrium. The kinetic selectivity is measured by the ratio of the intracrystalline diffusivities of the gases passed through the sieve. Differences in

diffusion rates between molecules of comparable molecular weight, such as nitrogen and oxygen, are determined primarily by the diameter of the cavities. Hence the exchangeable cations can play an important role in the adsorptive properties of the crystal.

The zeolite currently used in PSA devices for aircraft is type 13X. A unit cell of type 13X sieve has the formula $Na_{86}[(AlO_2)_{86}(SiO_2)_{106}]$. The structure is a series of interconnecting silica and alumina tetrahedra creating a large pore size. The X-type structure possesses an effective pore diameter of 8.4Å [4]. This uniform pore size allows the screening of input gas on the basis of size and configuration.

The adsorption process in zeolite materials is physical adsorption. Unlike chemical adsorption, which involves the formation of chemical bonds, physical adsorption involves weak, intermolecular forces and as such, has a low heat of adsorption. Physical adsorption is therefore a rapid, reversible process. The most common forces involved in physical adsorption are Van der Waals forces and electrostatic interactions. Although there is no electron transfer between the adsorbent surface and the sorbate, polarisation may occur, leading to electrostatic interactions. The Van der Waals forces are always present, whereas the electrostatic forces are only significant when the sorbate is easily polarised. In small, dipolar molecules such as H_2O and NH_3, the electrostatic contribution is considerably greater than the Van der Waals forces. In some cases, the electrostatic force is so great as to lead to heats of adsorption more commonly associated with chemisorption. This means that in the case of H_2O and NH_3, the adsorption process can be irreversible under the operating conditions of the molecular sieve. Typical heats of adsorption for types 13X and 5A sieves are given in table 1.1. Type 5A sieve is also used to separate oxygen from air and has the unit cell formula of $Ca_5Na_2[(AlO_2)_{12}(SiO_2)_{12}]$ and an effective pore size of 4.4Å.

It is clearly evident from table 1.1 that non-polar gases such as methane, argon, krypton and xenon have the lowest heats of adsorption for both sieve types. The heats of adsorption change depending on the type of polarity associated with the sorbate gas. Water and ammonia are strongly dipolar and thus have the highest heat of adsorption. The heat of adsorption of the strongly quadrupolar CO_2 is greater than that of CO which has a small dipole, and N_2 which has a small quadrupole.

Type 13X Sieve		Type 5A Sieve	
Sorbate Gas	$-\Delta H_{ad}$ (kJ/mol)	Sorbate Gas	$-\Delta H_{ad}$ (kJ/mol)
Ar	12.7 [5]	Ar	13.7 [4]
Kr	18.4 [5]	CH_4	21.3 [4]
Xe	23.4 [5]	CH_4	19.0 [4]
N_2	27.2 [6]	C_2H_6	27.6 [7]
CO_2	51.0 [6]	C_2H_4	33.5 [7]
NH_3	75.3 [6]	CO_2	42.7 [7]
H_2O	142.3 [6]	N_2	23.8 [7]
		O_2	13.8 [7]
		N_2	24.0 [8]
		CO	30.5 [8]
		CO_2	59.5 [8]
		NH_3	93.0 [8]

Table 1.1. Heats of adsorption of various sorbate gases for two zeolite materials. (Data taken from ref. [4,5,6,7,8]).

It is also evident from table 1.1 that oxygen has a lower heat of adsorption than nitrogen. This, coupled with steric effects, means oxygen diffuses through the sieve faster than nitrogen and produces an equilibrium separation factor of 3.0-3.5 [4,9]. This is sufficient to essentially remove all the nitrogen from the product gas. However, argon also has a lower heat of adsorption than nitrogen and so is present in the product gas.

There are a limited number of sites for adsorption in the molecular sieve and so the zeolite must be purged of nitrogen and other adsorbed species at regular intervals. This means a continuous process is not possible as the number of adsorbent sites decreases as nitrogen is adsorbed. In order to produce an uninterrupted supply of oxygen a two or, more commonly, three stage process is used where the three beds are sequentially cycled through generating and venting cycles [10]. This process is schematically represented in Figure 1.6.

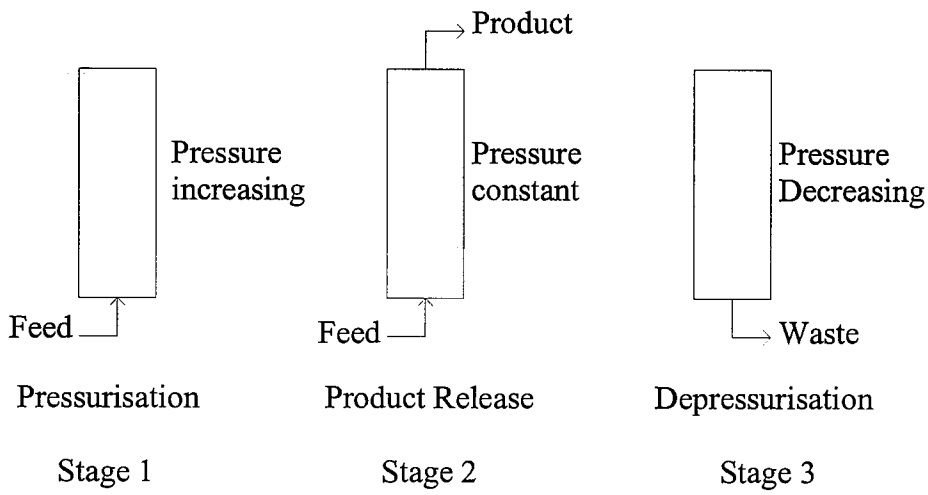


Figure 1.6. Basic Steps of Pressure Swing Adsorption [10].

The first step is to feed the source gas (air) into the zeolite with top end closed to allow pressurisation. The top end is then opened, and the product gas is released while the source gas is being fed to maintain pressure. The final stage is to close the top end of the bed and depressurise or vent the charged bed by allowing the waste gas to discharge from the bottom of the bed [11].

To produce a continuous supply of oxygen, multiple beds are required to be cycled, operating out of phase. For a small fighter aircraft the number of beds is typically three, whereas a large bomber may have six beds, dependent on the required performance and number of aircrew. This increases both the volume and the mass of the system. If three cylindrical beds are arranged concentrically, this can reduce overall dimensions and weight with minimal impact on performance.

As mentioned previously, pressure swing adsorption can only produce a theoretical maximum of 95% oxygen. However, a more realistic yield is 93% due to residual argon and other trace gases in the air. Further treatments to the gas could be utilised to increase the purity of the oxygen but this would produce additional size and weight problems. If the zeolite bed is only vented to ambient pressure, as represented in figure 1.6, the maximum oxygen concentration after a few cycles would be limited to around 30%. This low performance is due to incomplete desorption of the adsorbed nitrogen. To encourage sieve regeneration, some of the product gas from a bed is flowed back through a vented bed to ensure desorption of the nitrogen. This leads to a considerably more complicated set-up than depicted in figure 1.6. Figures 1.7a and 1.8a show two

possible configurations for pressure swing adsorption devices. The basic sequence for any MSOC is: charging, product, venting and purging.

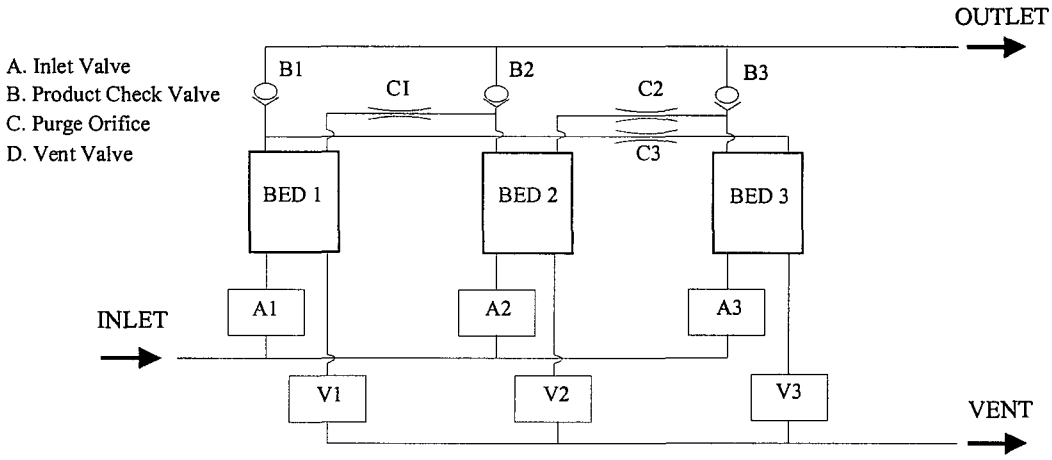


Figure 1.7a. Possible Three Bed Configuration for an MSOC.

In figure 1.7a the sequence used to pressurise and purge each bed is as follows:

1. Inlet valve A1 opens to pressurise bed 1.
2. As soon as the pressure in bed 1 exceeds the product pressure, product valve B1 opens. This allows the breathing gas to flow.
3. After a pre-set time, inlet valve A1 closes. This time is dependent on both the molecular sieve and the product oxygen concentration required.
4. Product valve B1 closes and vent valve V1 opens.
5. Purge gas is induced from bed 2 through orifice C1 due to the pressure difference between the two beds.
6. Vent valve V1 closes.

This sequence applies to each bed and they operate out of phase such that as one bed is venting the other two beds are either charging or producing oxygen. The valve timing sequence is shown in figure 1.7b.

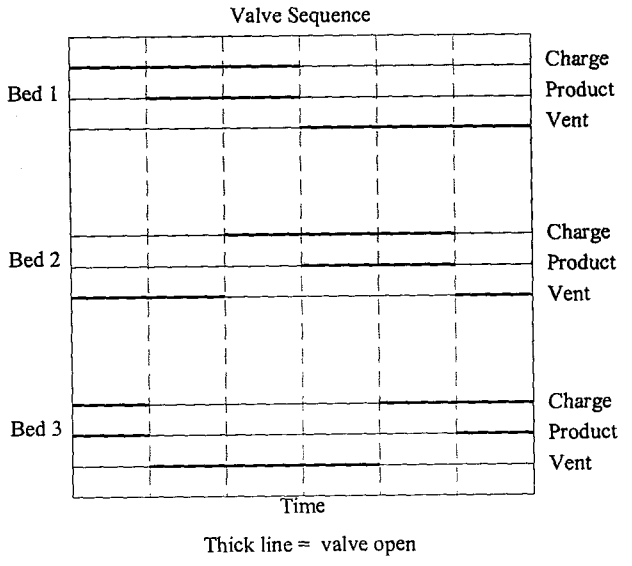


Figure 1.7b. Valve Timing Sequence for Figure 1.7a.

Figure 1.8a is a slightly more complicated situation and includes cross-feeding between beds. This means that instead of venting the gas immediately after the product gas closes, the gas remaining in the sieve (which is still of relatively high oxygen concentration) is used to partially charge the second bed.

The sequence used in figure 1.8a is described below:

1. Inlet valve I1 opens to pressurise bed 1.
2. Purge valve P1 opens for a short time to purge bed 3.
3. As soon as the pressure in bed 1 exceeds the product pressure, the product check valve opens.
4. After a pre-set time, inlet valve I1 closes. Again, this time is dependent on both the molecular sieve and the product oxygen concentration required. The product check valve on bed 1 will then automatically close.
5. Cross-feed valve C2 opens to partially pressurise bed 2.
6. Vent valve V1 opens.
7. Purge valve P2 opens to purge bed 1.
8. Vent valve V1 closes.

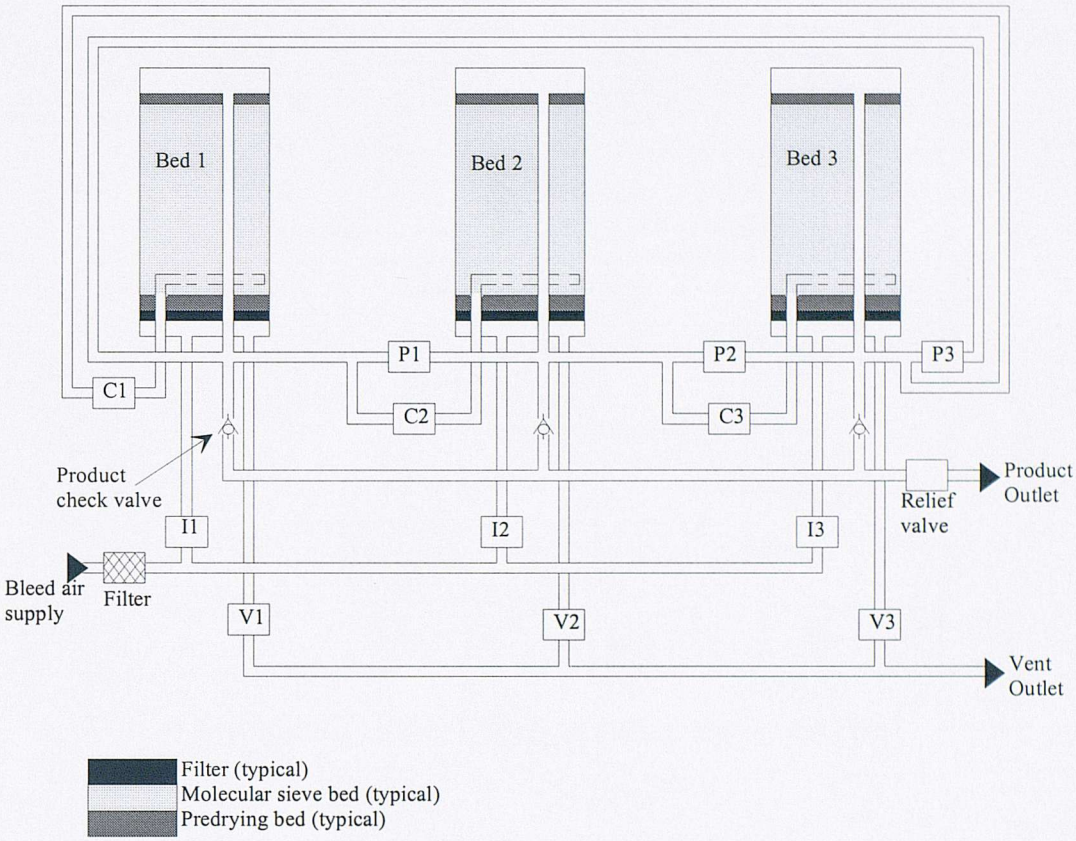


Figure 1.8a. Schematic diagram of a possible design for an MSOC.

Again this sequence applies to each bed, operating out of phase to provide a continuous oxygen product gas. Figure 1.8b shows the valve timing sequence for MSOC depicted in figure 1.8a.

It can be seen in the schematic figure 1.8a that one end of the bed is closed and the inlet, product and vent lines are all at the same end. This type of set-up is called an up and over (U&O) design and a schematic diagram of a bed is shown in figure 1.9.

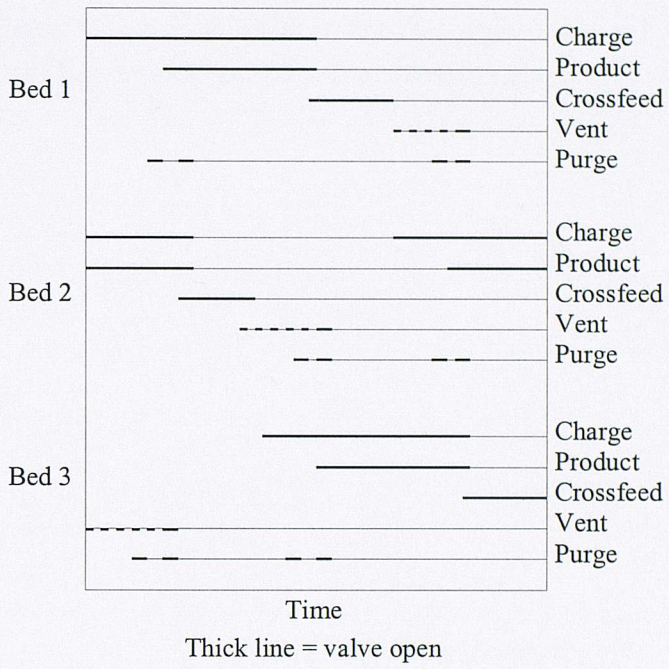


Figure 1.8b. Valve Timing Sequence for Figure 1.8a.

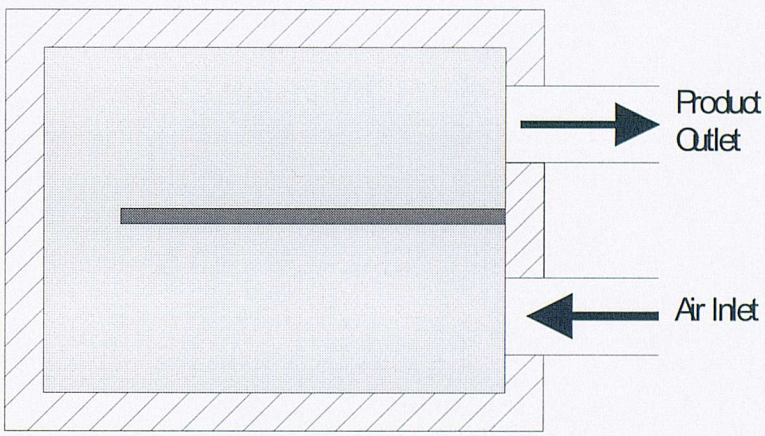


Figure 1.9. Schematic diagram of an up and over bed design.

It is evident from figures 1.7 and 1.8 that the pressure swing adsorption devices rely heavily on the use of valves. This is a problem as the valves have moving parts, and thus increase the probability of mechanical wear as well as electrical malfunction.

Another problem with pressure swing adsorption devices for generating oxygen is that the concentration of oxygen produced is not always constant but depends on

many factors including altitude, inlet pressure, temperature and volumetric flow rate of the product gas, as well as the valve timing sequence. These variations are shown in figures 1.10 - 1.13.

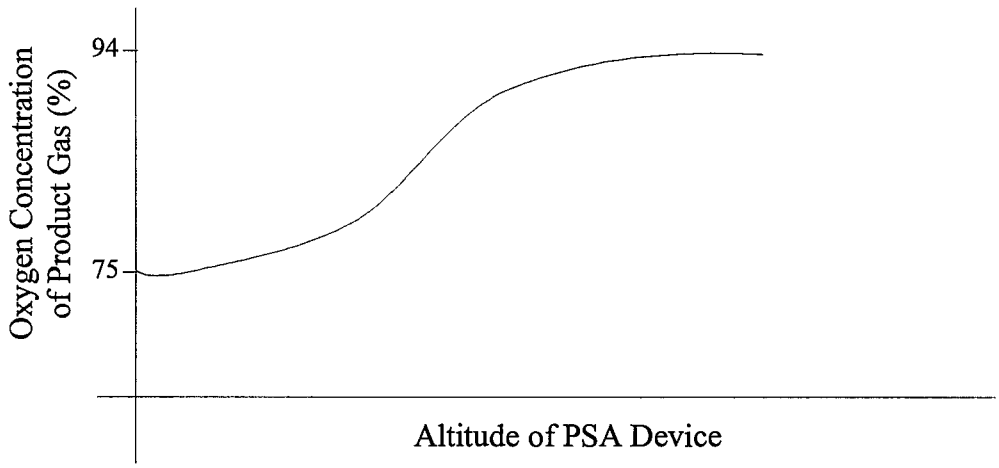


Figure 1.10. Oxygen concentration of product gas produced by an MSOC as a function of altitude.

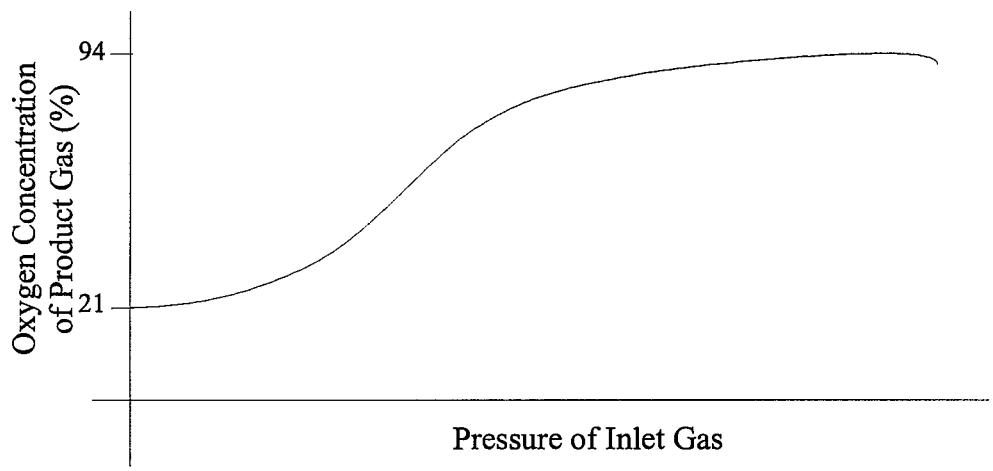


Figure 1.11. Oxygen concentration of product gas produced by an MSOC as a function of the inlet gas pressure.

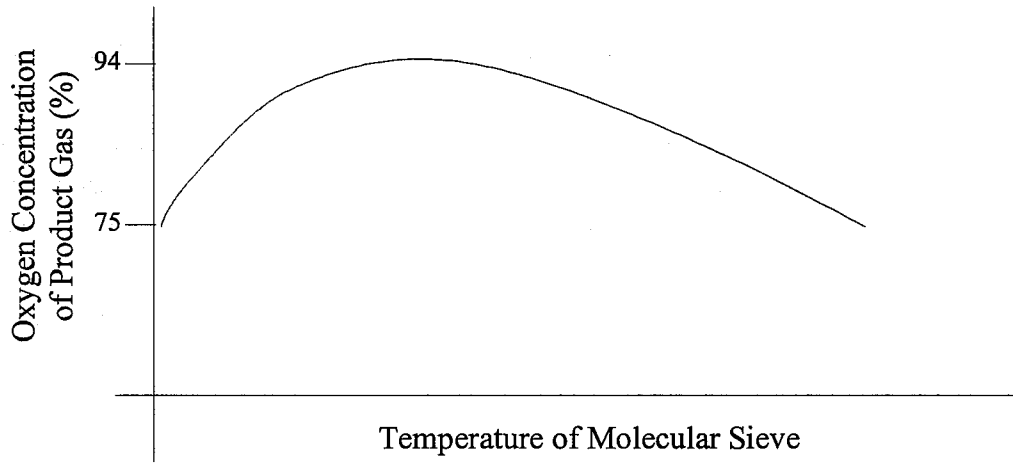


Figure 1.12. Oxygen concentration of product gas produced by an MSOC as a function of the temperature of the molecular sieve.

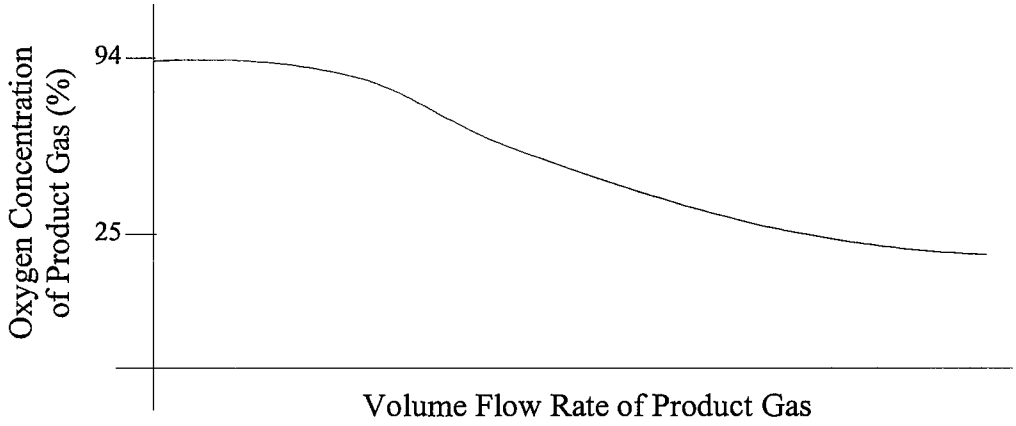


Figure 1.13. Oxygen concentration of product gas produced by an MSOC as a function of the volumetric flow rate of the product gas.

The size of the values presented in figures 1.10 to 1.13 are dependent on the type of oxygen concentrator, and on the particular aircraft in which it is used. Furthermore, the shape and magnitude of the individual curves are dependent on the values in every other graph. Therefore, an on-board oxygen monitor with an integral feed-back loop is required to ensure the correct concentration of oxygen is supplied to the pilot. The oxygen monitor takes up extra space and also involves additional complexities to the system.

1.3. Pressure Driven Ceramic Oxygen Separator.

A ceramic oxide which has a small resistance to oxygen ion diffusion can be used to separate oxygen from air. If a thin plate of the ceramic oxide is subjected to a large oxygen partial pressure gradient, a driving force for the diffusion of oxygen through the material is present. Unlike molecular sieves, where the oxygen is transported through the material as a molecule, in the case of ceramic membranes the oxygen is reduced to its ionic state and is transported through oxygen vacancies in the crystal lattice of ceramic. This means that both mass transport and charge transport occur. In order to prevent charge build up at the surface which would thus impede further ionic movement, the material must also allow rapid diffusion of electrons in the direction opposite to the oxygen flow. This type of material is known as a mixed electronic-ionic conductor (MEIC). Since oxygen transport takes place via hopping of oxygen ions through the crystal lattice, the transport of any other species is excluded. This means the ceramic membrane can produce 100% oxygen.

A typical membrane configuration is shown below in figure 1.14.

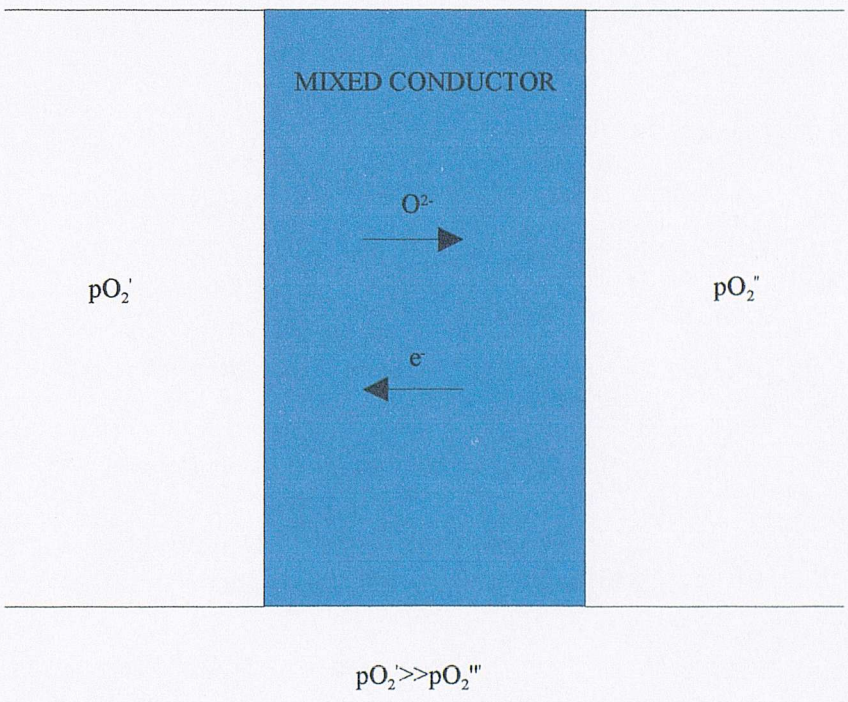


Figure 1.14. Schematic representation of a Pressure Driven Ceramic Oxygen Separator.

The thermodynamic driving force for oxygen permeation through a mixed electronic ionic conducting oxide membrane is the oxygen partial pressure gradient across the membrane. The oxygen flux through the sample is therefore governed by the difference in oxygen activity on either side of the membrane. The oxygen flux is also affected by resistance to oxygen transport in the ceramic, and is often affected by the kinetics of oxygen exchange between the surface of the MEIC and the gases on either side of the membrane [12]. The resistance to oxygen transport is a function of the oxygen ion diffusivity and the geometry of the membrane.

It can be shown, from Wagner's tarnishing equation, that oxygen flux through an MEIC membrane where there are no surface reaction limitations, can be expressed thus:

$$J_O = \frac{RTV_m}{16F^2L}.t_{ion}t_{elec}\sigma_{amb}.\ln\left(\frac{pO_2^{'}}{pO_2^{''}}\right) \qquad \text{eqn. (1.1)}$$

where,

J_O is the oxygen flux density (cm^3 (STP) $cm^{-2}s^{-1}$)

σ_{amb} is the ambipolar conductivity (S/cm) which approximates to $\sigma_{amb} \approx \frac{\sigma_{elec}\sigma_{ion}}{\sigma_{elec}+\sigma_{ion}}$, σ_{ion} and σ_{elec} are the oxygen ion and electronic conductivity, respectively

$pO_2^{'}$ and $pO_2^{''}$ are the oxygen partial pressures on the inlet and outlet sides of the membrane wall, respectively

t_{elec} is the electronic transference number $\left(t_{elec} = \frac{\sigma_{elec}}{\sigma_{total}}\right)$

t_{ion} is the ionic transference number $\left(t_{ion} = \frac{\sigma_{ion}}{\sigma_{total}}\right)$

L is the thickness of the membrane (cm)

V_m is the molar volume of the gas (cm^3/mol)

and the other parameters have there usual meaning.

In the case of the MEIC's of interest for oxygen separation, the total conductivity is considered to be due only to the oxygen ion conductivity and the electronic

conductivity. Furthermore, the electronic conductivity is generally so much greater than the oxygen ion conductivity that it does not limit the transport process. This means that $t_{elec} \approx 1$ and the term $t_{ion}t_{elec}\sigma_{amb}$ reduces to σ_{ion}. Thus equation (1.1) can be expressed as equation (1.2):

$$J_O = \frac{RTV_m}{16F^2L}.\sigma_{ion}.\ln\left(\frac{pO_2^{'}}{pO_2^{''}}\right) \qquad \text{eqn. (1.2)}$$

Equation (1.2) assumes there are no surface limitations. In reality the following reactions have to occur on each side of the membrane.

$$\tfrac{1}{2}O_{2(gas)} + 2e^- \rightarrow O^{2-}{}_{(solid)} \text{ inlet side} \qquad \text{eqn. (1.3)}$$

$$O^{2-}{}_{(solid)} \rightarrow \tfrac{1}{2}O_{2(gas)} + 2e^- \text{ outlet side} \qquad \text{eqn. (1.4)}$$

These reactions can limit the permeation rate depending on the geometry of the sample. In most practical cases, it is a combination of the oxygen diffusion and the exchange reactions which determines the oxygen flux. Liu [12] has added an additional term to equation (1.2) to account for the surface exchange process. A modified version of this (where the current density is converted to oxygen flux density) is given as equation (1.5).

$$J_O = \left[\frac{\sigma_{ion}}{L + \sigma_{ion}\left(RT/2Fi_O\right)}\right]\frac{RTV_m}{16F^2}.\ln\left(\frac{pO_2^{'}}{pO_2^{''}}\right) \qquad \text{eqn. (1.5)}$$

where i_O is the exchange current density. The exchange current density can be converted to a equilibrium constant which is more readily measured using equation (1.6).

$$k = \frac{i_O V_s}{4F} \qquad \text{eqn. (1.6)}$$

k is the surface exchange coefficient (cm/s) and V_s is the molar volume of the solid.

It should be noted that equations (1.1), (1.2) and (1.5) only hold for small changes in pO_2, such that the stoichiometry of the material is not different on the high and low oxygen activity sides of the membrane.

It is evident from the nature of equation (1.5) that apart from the materials dependent parameters (oxygen ion conductivity and surface exchange coefficient), the thickness of the membrane and the oxygen partial pressure gradient across the membrane will affect the oxygen flux. The effects of the thickness and oxygen partial pressure gradient are shown schematically in figures 1.15 and 1.16, respectively, assuming a situation where the oxygen diffusion and surface exchange rates are similar.

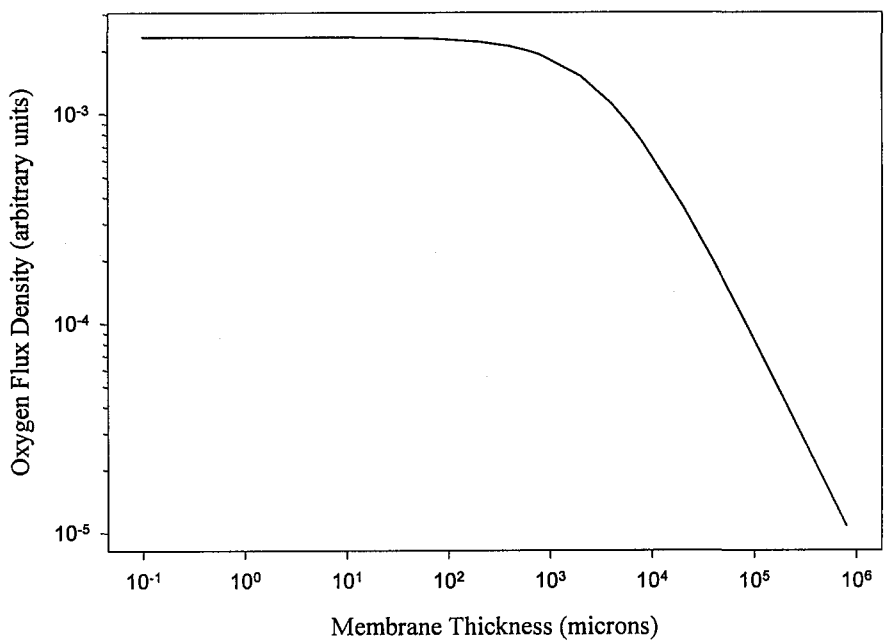


Figure 1.15. Schematic representation of the dependence of oxygen flux on membrane thickness for a pressure driven ceramic oxygen generator. (Calculated for σ_{ion}=0.1 S/cm, k=10^{-6} cm/s, $pO_2^{'}/pO_2^{''}$ =1000 and T=1000K.)

It is immediately apparent from figure 1.15 that there is a minimum thickness of the ceramic membrane beyond which no additional benefit to the oxygen flux is obtained. This critical thickness is dependent on the relative magnitudes of the oxygen diffusivity and surface exchange, but also on the oxygen partial pressure gradient across the membrane and the operational temperature of the device.

Typically, it is anticipated that for a MEIC, the critical thickness will be of the order of 100 microns [13,14,15]. It is also clear that if too thick a membrane is used, for example, to provide increased mechanical support, then the oxygen flux will decrease dramatically.

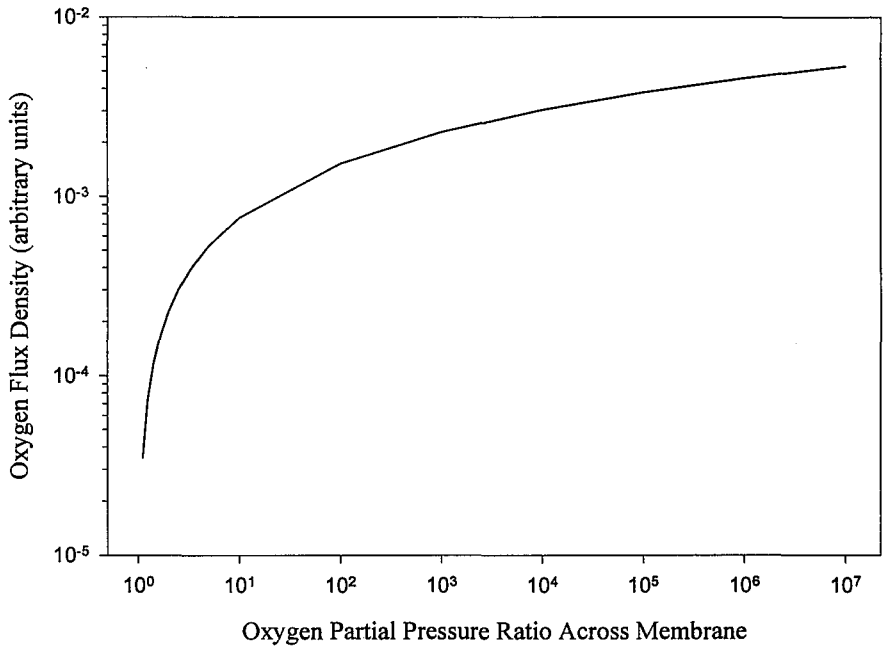


Figure 1.16. Schematic representation of the dependence of oxygen flux on the oxygen partial pressure ratio across the membrane for a pressure driven ceramic oxygen generator. (Calculated for σ_{ion}=0.1 S/cm, k=10^{-6} cm/s, L=100 microns and T=1000K.)

Figure 1.16 illustrates that a reasonably large oxygen partial pressure difference is required before any appreciable oxygen flux is obtained. There is, however, a diminishing return on increasing the pressure gradient as the oxygen flux density tails off towards a maximum. The larger the pressure difference across the membrane, the thicker it will have to be to support the pressure induced stress. Therefore, a compromise between increasing the oxygen flux (by decreasing the membrane thickness or increasing the partial pressure gradient) and the mechanical integrity of the membrane must be made.

The oxygen ion conductivity (or oxygen diffusion) and exchange processes are both thermally activated and hence are strongly dependent on temperature, i.e. the higher the temperature, the faster the diffusion and exchange of oxygen.

However, the electronic conductivity of the material must be sufficiently high so that the charge transport of the oxygen ions is not inhibited. The electronic conductivity of this type of MEIC exhibits a maximum at a given temperature, above which the conductivity decreases. Furthermore, as the temperature is increased more thermo-chemical and thermo-mechanical problems are encountered.

Clearly the rate of oxygen diffusion and surface exchange are important parameters for these materials to be used to produce oxygen, but there are other requirements that these materials must fulfil. These are outlined in the next section.

1.3.1. Materials Requirements for Pressure Driven Ceramic Oxygen Generator.

As mentioned previously, for a material to be suitable for use in a pressure driven ceramic oxygen generator, it must have a high ionic diffusivity or conductivity. The high operating temperature and difference in oxygen partial pressure subjected to these devices adds many more stringent demands to the materials. The physical properties required for the pressure driven ceramic membrane are summarised below.

high electronic conductivity
high oxygen ion conductivity (diffusivity)
chemically stable in high (up to 5 bar) and low (down to 10^{-4} bar) pressure oxygen
low volatility at operating temperature
low differential thermal expansion
no destructive phase transitions within operating or sintering temperatures
high sinterability
easy to form into large area, thin dense tubes
moderate cost of raw materials and formation

Very few of the ceramic oxides exhibiting any significant oxygen ion conductivity show sufficient electronic conductivity to be used in a pressure driven oxygen separation membrane [16,17]. One such group is the perovskite materials. Perovskites have the general formula ABO_3, where A and B are cations whose valence sum to 6+. The perovskite structure and materials properties of this class of material are discussed in detail in chapter 3. In

particular it is doped $ReTmO_{3\pm\delta}$ type perovskites which show a suitable combination of electronic and ionic conductivity. Re is a rare earth, most commonly lanthanum and Tm is a transition metal: iron, manganese, cobalt, nickel, and chromium. Due to the variable valence of the transition metals, the perovskite normally exhibits some form of non-stoichiometry, which is represented by the $\pm\delta$ term in the chemical formula. In order to produce the required ionic or electronic conductivity, the perovskites are often doped on the A-site with an alkaline earth, e.g. strontium or calcium.

Of the five transition metals listed, $ReMnO_{3\pm\delta}$ and $ReCrO_{3\pm\delta}$ have too low an ionic conductivity and $ReNiO_{3\pm\delta}$ is not sufficiently stable in reducing atmospheres to be used as a pumped oxygen separator. $ReFeO_{3\pm\delta}$ is not a particularly good oxygen ion conductor nor a good electronic conductor, but does possess most of the other selection criteria. $ReCoO_{3\pm\delta}$ is a very good oxygen ion and electronic conductor, but has a tendency to lose oxygen from the lattice in non-oxidising atmospheres. This loss of oxygen leads to a large thermal expansion, and hence the creation of chemically induced stresses. It is therefore anticipated that to achieve an appropriate separator material, the B cation site will also have to be doped, for example $(La,Sr)(Co,Fe)O_{3\pm\delta}$.

More recently there has been a suggestion that a composite of a MEIC perovskite and a fluorite material such as yttria stabilised zirconia (YSZ) or gadolinia doped ceria (CGO) could be used as a separator material. YSZ and CGO are very good ionic conductors (although poor electronic conductors) and YSZ in particular is chemically very stable over a large oxygen partial pressure range.

1.4. Electrically Driven Ceramic Oxygen Generator.

The electrically driven ceramic oxygen generator (hereafter called COG) is in many ways more complicated than the pressure driven device. Here, the driving force for oxygen transport is provided by an electrical potential, rather than a chemical gradient. This means that an MEIC could not be used as the separation material, since $\sigma_{elec} >> \sigma_{ion}$ the electronic carriers would provide a short circuit path for the current. Hence a material where t_{ion} approaches unity (i.e. a solid oxide electrolyte) is required. However, materials which are purely ionic conductors show very poor catalytic activity for the reduction of oxygen at the surface and so electrodes must be added to the electrolyte material.

As with the pressure driven device, the oxygen is transported through the COG in the form of oxygen ions. This leads to infinite selectivity of the membrane [18]. A schematic representation of a COG is given below in figure 1.17.

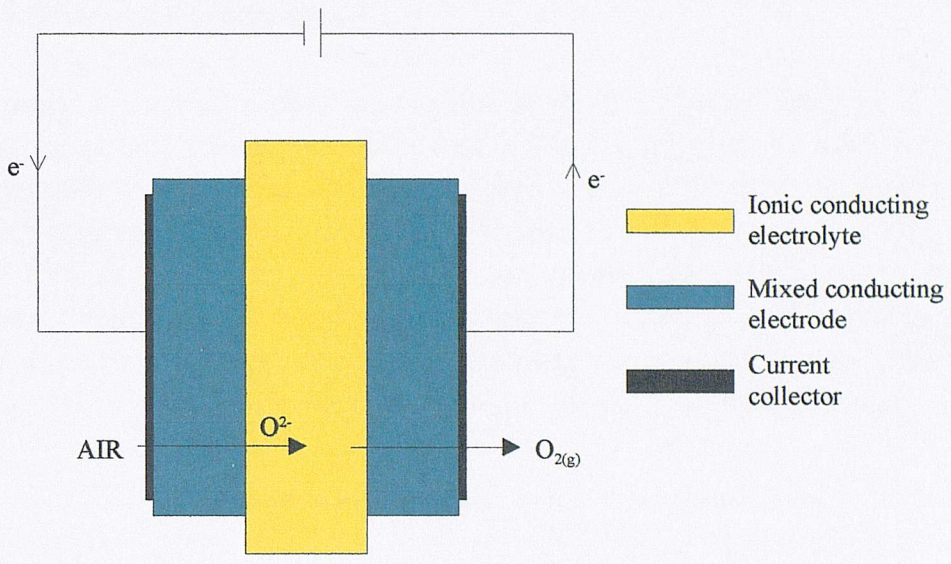


Figure 1.17. Schematic illustration of a single cell COG.

The application of a dc voltage to the cell leads to current flowing through the circuit. The solid electrolyte only conducts oxygen ions so this current can be converted to a molar flow rate of oxygen, using equation (1.7).

$$\dot{N} = \frac{j_0}{2zF} \qquad \text{eqn. (1.7)}$$

where, $\dot{N}$ is the area specific molar flow rate of oxygen (mol/cm^2/s)
j_0 is the current density (A/cm^2)
z is the valence of oxygen (z=2)
F is Faraday's constant (F=96485 C/mol)

The current density through the cell is determined by the applied voltage and the resistance of the cell, through equation (1.8).

$$j_0 = V / r_{cell} \qquad \text{eqn. (1.8)}$$

where V is the applied potential (volts) and r_{cell} is the area specific resistance of the cell (Ω/cm^2). The area specific resistance of the cell is the sum of the resistance of the electrolyte, the two electrodes, the two current collectors and the lead wires. In general, the resistance of the current lead wires and current collectors is considered to be negligible compared to the resistance of the electrolyte and the electrodes.

In order to generate a considerable flux of oxygen, the surface area of the cell must be large. This is achieved by connecting a sequence of cells in electrical series into a multi-layer stack. The cells are connected by an electronically conducting interconnect material. The interconnect can be metallic or a ceramic, but it must have negligible oxygen ion conductivity and a high electronic conductivity. Clearly, the interconnect material possesses an electrical resistance and so this must be included when calculating the area specific resistance of the stack. Thus the area specific resistance of a stack can be expressed thus:

$$r = r_{electrode(air)} + r_{electrolyte} + r_{electrode(oxygen)} + r_{interconnect} \qquad \text{eqn. (1.9)}$$

The air electrode is generally called the cathode and the oxygen electrode the anode. Combining equations (1.7), (1.8) and (1.9) the molar flow rate of oxygen can be determined in terms of the applied voltage and the resistance of the components.

$$N = \frac{V}{2zF(r_{cathode} + r_{electrolyte} + r_{anode} + r_{interconnect})} \qquad \text{eqn. (1.10)}$$

From equation (1.10), it is evident there are two methods of increasing the flux of oxygen through the membrane. The first is to increase the applied potential to the device. The potential is determined however by aircraft and material requirements (see section 1.4.3). The second method is to decrease the resistance of the components. The majority of the resistance of the cell is comprised of the electrolyte and the two electrodes. There are several ways to reduce the cell resistance: (a) by increasing the ionic conductivity of the electrolyte. This relies on the use and development of new materials or by increasing the operating temperature (the electrolyte conductivity is thermally activated); (b) by reducing the thickness of the electrolyte membrane. There have been many advances in processing routes such as tape calendering [19] colloidal deposition [20] and aerosol assisted chemical vapour deposition [21] allowing the production of

electrolyte membranes as thin as 5-10μm; (c) by reducing the resistance of the electrodes. The area specific resistance of the electrodes is strongly dependent on their catalytic activity for the exchange of oxygen. New materials or microstructures could markedly decrease the electrode resistance. The electrode resistance is also thermally activated so an increase in the temperature will reduce the resistance.

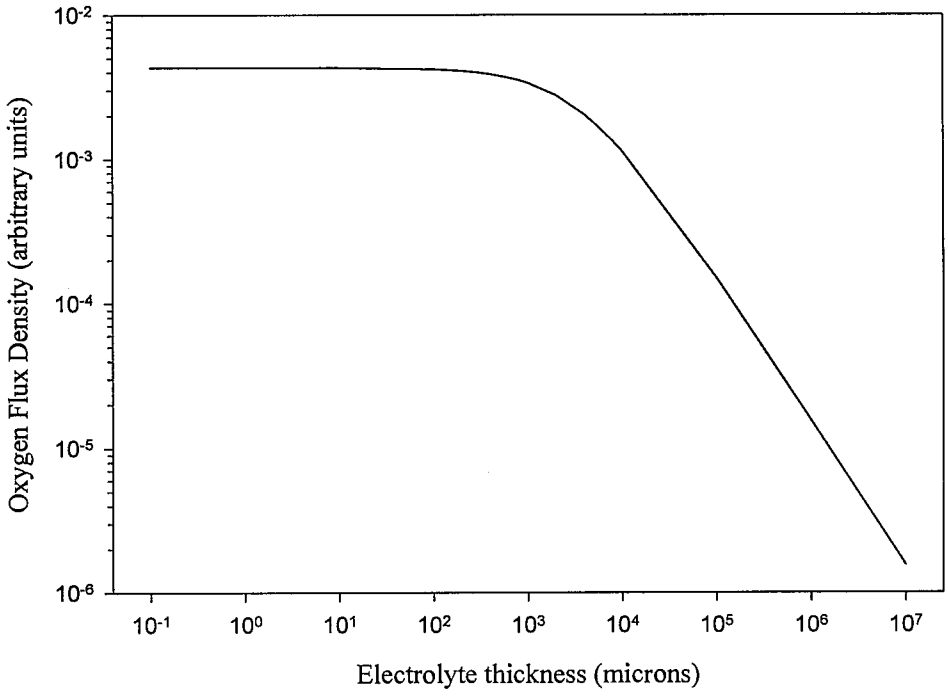


Figure 1.18. Schematic representation of the dependence of molar flow rate of oxygen on electrolyte thickness for an electrically driven ceramic oxygen generator. (Calculated from resistance data at 750K in air).

Figures 1.18 and 1.19 show the effects of electrolyte thickness and temperature, respectively, on the molar flow rate of oxygen through the COG, using data obtained for LSCF electrodes and a CGO electrolyte. If different electrodes or a different electrolyte were chosen, then the shapes of the curves may be different.

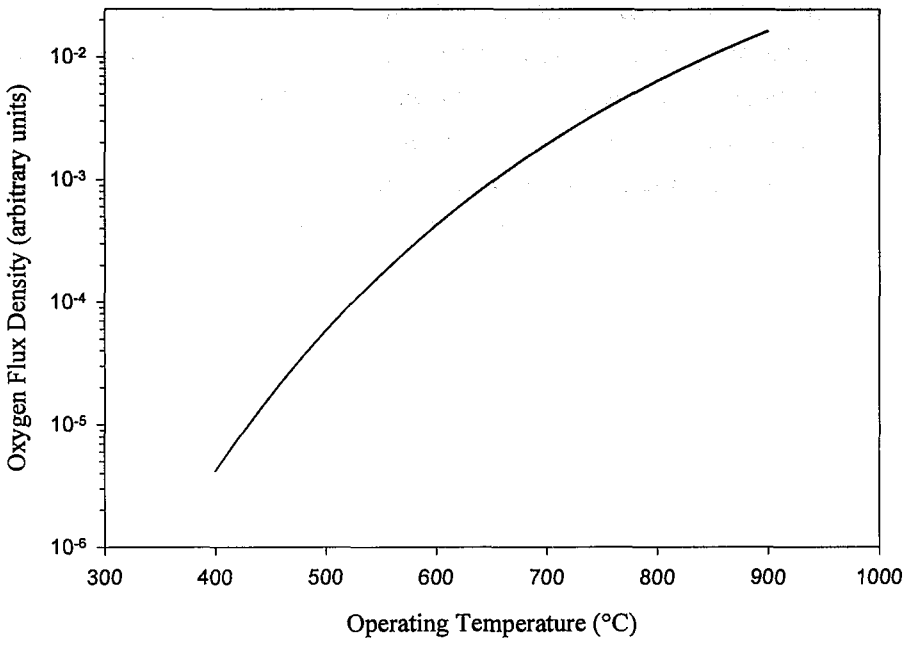


Figure 1.19. Schematic representation of the dependence of molar flow rate of oxygen on cell temperature for an electrically driven ceramic oxygen generator. (Calculated from resistance data for an electrolyte thickness of 100 microns.)

It can be seen from figure 1.18 that with this combination of materials, there is little benefit in reducing the electrolyte thickness below 100 microns. This is because of the very high ionic conductivity of the ceria electrolyte. If zirconia were being used, then a benefit in flux density would be expected down to around 10 microns. Figure 1.19 shows the large increase in oxygen flux obtained by increasing the temperature. It should be noted however, that at higher temperatures, the increase becomes less.

1.4.1. Materials Requirements for a COG.

The COG can be divided into a series of components, each requiring different materials properties. These are the cathode, electrolyte, anode, interconnect and the "balance of plant". The balance of plant is all the materials required to complete an oxygen generating unit which are not included in the previous four components. Aside from the individual materials requirements there are some general properties required for all the materials. The materials must all be

chemically stable in the environments they shall be exposed to, and chemically stable with each other. That is, no detrimental reaction products should form between any of the components. The thermal expansion coefficients of all the materials should be similar to minimise thermally induced stresses and the materials must be easy to form into the desired shape and density. Each of the materials properties required will now be considered individually.

1.4.1.1. Electrolyte.

The electrolyte material must have a high ionic conductivity and negligible electronic conductivity at the operating temperature of the device. The ionic conductivity must be large in order to reduce the electrolyte resistance and thus increase the flow rate of oxygen (equation (1.10)) and the electronic conductivity must be small to avoid short circuiting of the cell. The electrolyte must be sufficiently dense so that there are no interconnected pores, as this will allow gas phase diffusion of air through the device and thus reduce the purity of the oxygen produced. The material must not react with the electrode materials, it must be stable in the oxidising environment it is exposed to and it must not undergo any phase transitions within the operating temperature of the cell as these often lead to volume changes which will generate mechanical stresses in the device.

Two electrolyte materials have been considered for this application: yttria stabilised zirconia (YSZ) [18] and gadolinia doped ceria (CGO) [22]. Both materials have the cubic fluorite structure and possessa good ionic conductivity, although that of CGO is somewhat higher than YSZ [13]. The behaviour of the materials in an oxidising environment are very similar and it thus easier to consider first the case of YSZ.

The conduction process in YSZ is via localised hopping of oxygen ions through vacancies in the crystal lattice. The oxygen vacancies are introduced to the zirconia lattice by doping the material with an aliovalent cation such as yttrium, scandium or calcium. This is shown for the case of yttrium using Kroger-Vink notation in equation (1.11).

$$Y_2O_3 \xrightarrow{ZrO_2} 2Y'_{Zr} + V_O^{\cdot\cdot} + 3O_O^{x} \qquad \text{eqn. (1.11)}$$

The addition of substantial amounts dopant (~10 mol%) also has the effect of stabilising the cubic form over the entire temperature range (pure zirconia is monoclinic at room temperature). Scandia doped zirconia exhibits the highest conductivity but due to cost and availability, yttria is the preferred dopant. Typically the concentration of dopant used is 8-10 mol%. This provides an ionic conductivity of about 0.1 S/cm at 1000°C [23]. In comparison, the ionic conductivity of doped ceria has been reported as 0.1S/cm at temperatures as low as 800°C [23,24].

1.4.1.2. Cathode.

The cathode in a ceramic oxygen generator must provide good electrochemical activity for the reduction of gaseous oxygen to its ionic state and allow the oxygen ions to enter the electrolyte. This means the cathode acts as a source of electrons and as such must be a good electronic conductor. The cathode must also be porous to give a large surface area over which the reduction of oxygen can occur. The porosity also allows gas phase diffusion of oxygen through the cathode to the electrolyte/cathode/gas triple phase boundary. The incorporation of oxygen into the electrolyte is enhanced if the cathode can also conduct oxygen ions so the reaction need not be limited to the triple phase boundary. Other properties that the cathode must possessare chemical stability, low volatility at the operating temperature, moderate cost in terms of raw materials and formation, matching thermal expansion coefficient with other cell components, easy to form into thin, porous films and have no destructive phase transitions within the operating or fabrication temperature of the cell.

The high operating temperatures and the oxidising environment of the cathode limit the choice of materials to noble metals and electronically conducting ceramics. Although many noble metals possesshigh catalytic activity and silver possesses reasonable oxygen ion conductivity, the cost of the materials and doubts over their long term stability due to particle sintering discount these materials for commercial use. These materials are, however, frequently used in small scale, demonstration or experimental devices.

Of the ceramic materials, members of the perovskite group are the most likely materials to be considered, specifically those containing transition metals. This is because the variable valence of the transition metal cation introduces electronic

carriers into the ceramic. Lanthanum manganite ($LaMnO_3$) [25,26], lanthanum ferrite ($LaFeO_3$) [27,28], lanthanum cobaltite ($LaCoO_3$) [29,30] and various combinations of these [15,22,31,32] have all been experimented as cathodes for the solid oxide fuel cell, where the requirements are the same. Lanthanum cobaltite shows the highest catalytic activity, but has poor chemical stability and a large difference in thermal expansion behaviour from the prospective electrolytes, YSZ and CGO [29,33]. Lanthanum cobaltite and lanthanum ferrite both react strongly with YSZ, forming deleterious, insulating phases and thus the material favoured for use with YSZ is $LaMnO_3$ despite it having the lowest catalytic activity of the three. A composition containing both iron and cobalt is favoured for use with the CGO electrolyte.

In all cases, neither the electronic nor ionic conductivity of the materials is sufficient for use at practical temperatures. Therefore the perovskite is commonly doped on the A site with an alkaline earth oxide such as SrO, CaO or MgO. This has the effect of introducing electron holes or oxygen vacancies into the lattice, depending on the oxygen partial pressure to which the material is exposed. Two possible scenarios are given in equations (1.12) and (1.13).

$$\tfrac{1}{2}O_2 + 2SrO \xrightarrow{La_2O_3} 2Sr'_{La} + 3O^{\times}_{O} + 2h^{\cdot} \qquad \text{eqn. (1.12)}$$

$$2SrO \xrightarrow{La_2O_2} 2Sr'_{La} + V^{\cdot\cdot}_{O} + 2O^{\times}_{O} \qquad \text{eqn (1.13)}$$

Under the operating conditions, it is a combination of both types of compensation that exists. Typically the dopant level for lanthanum manganite is around 15 mol% strontium and for lanthanum cobaltite around 40 mol%.

One problem with strontium doped lanthanum manganite, apart from its relatively low electronic conductivity and catalytic activity, is it forms insulating phases when in contact with YSZ at elevated temperatures. The perovskite phase $SrZrO_3$ [34] and the pyrochlore $La_2Zr_2O_7$ [34,35] are known to form, and work on the compatibility of $La_{1-x}Sr_xM_yFe_{1-y}O_{3-\delta}$ (M=Co, Fe, Ni) and YSZ has also shown the formation of these two reaction products [36,37]. The formation of these phases is a diffusion limited process and is also connected to the reactivity and solubility of the transition metal B-site cations [37]. The partial substitution of the B-site with Co causes the highest reactivity with the YSZ electrolyte [37,38]. The diffusion of manganese into YSZ may also be problematic The diffusion rate has been reported [35,39] but there appear to be large inconsistencies in the rates of diffusion.

Strontium doped lanthanum cobaltate has a higher electronic and ionic conductivity than lanthanum manganite, but the thermal expansion coefficient is too large for use as a cathode with either YSZ or CGO. It has therefore been doped on the B site with iron. $La_{0.6}Sr_{0.4}Co_{0.2}Fe_{0.8}O_{3\pm\delta}$ (LSCF) is the most commonly studied composition [22,40,41]. LSCF also reacts with YSZ to form $SrZrO_3$ and $La_2Zr_2O_7$, but does not appear to react with CGO [42].

1.4.1.3. Anode.

The reaction occurring at the anode is given by equation (1.14).

$$O^{2-} \rightarrow \tfrac{1}{2}O_2 + 2e^- \qquad \text{eqn. (1.14)}$$

It is evident from this reaction that aside from allowing rapid oxygen exchange at the surface, the anode must have a high electronic conductivity and allow rapid diffusion of gaseous oxygen away from the reaction site. This means that the anode must be porous, but it is also beneficial for it to have a high oxygen ion conductivity. The anode is exposed to an atmosphere of pure oxygen and so, as with the case of the cathode, the materials considered are limited to electronically conducting ceramics. Since the reaction at the anode is simply the reverse of that at the cathode, and the environmental conditions are similar, it is reasonable to use the same material for the anode as the cathode. Thus a symmetrical cell is created.

1.4.1.4. Interconnect.

The interconnect material provides an electrical connection between each symmetrical cell, while separating the inlet and product gas streams. It must therefore have a very high electronic conductivity as any resistance leads to wasted power. It is also important that no air or oxygen can pass through the interconnect as this will lead to a decrease in the purity of product gas or a reduction in the efficiency of the device. Therefore the interconnect must be gas tight and have negligible oxygen diffusion. The interconnect is in intimate contact with the electrodes and must therefore possess a thermal expansion

coefficient similar to the chosen electrode material. The interconnect is exposed to highly oxidising conditions and thus the choice is limited to noble metals, highly corrosion resistant alloys or electronically conducting ceramics. Noble metals are generally considered to be too expensive as the interconnect material must be thick (>1 mm) to allow necessary gas channels. $La_{1-x}Sr_xCrO_{3\pm\delta}$ possesses good electronic conductivity with limited ionic conductivity at 1000°C, but if the operating temperature of the device is to be lowered to allow the use of LSCF and CGO (<800°C), the electronic conductivity is insufficient. Therefore high nickel and chromium content alloys are being considered.

1.4.1.5. Balance of Plant.

The balance of plant includes the pipes used to supply and remove the two gas streams, heat exchangers and sealant materials. The pipes must be corrosion resistant at high temperatures since the product gas will exit the system at essentially the same temperature as the ceramic membrane itself. Therefore, high nickel content stainless steels are considered for the piping. The sealant material is required to prevent mixing of the product and input gases at the edge of the ceramic plates. Sealants used in solid oxide fuel cells are usually glass ceramics such as alumino silicates. In the COG design similar glasses are being considered. In either case, the sealant must clearly be both corrosion resistant and gas tight.

1.4.2. Stack Design for a COG.

In order to achieve an appreciable flux of oxygen, a large active surface area is required. There are many ways of achieving this such as sealed end tubes (a common SOFC design). However, efforts at Imperial College have concentrated on a planar stack design, similar to that employed by several SOFC producers. This modular design is illustrated in figure 1.20.

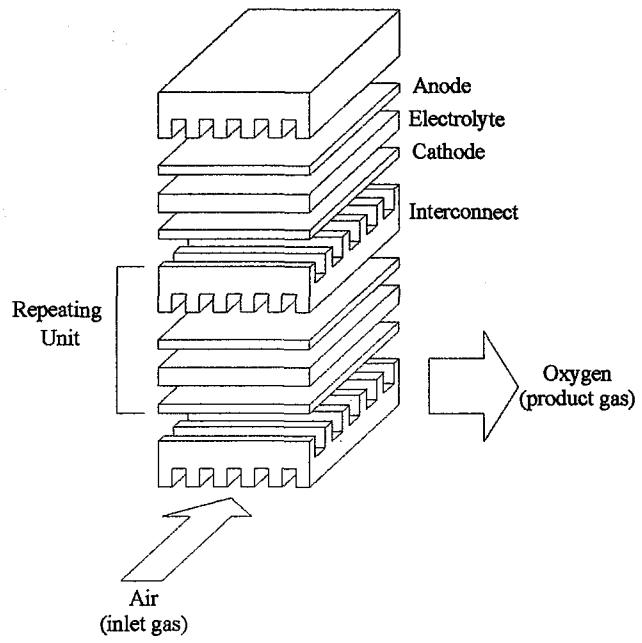


Figure 1.20. Exploded schematic illustration of a planar design for an electrically driven ceramic oxygen generator. (Adapted with permission from R.A. De Souza [43].)

This design allows the electrolyte to be produced by well established methods such as tape casting [44,45]. The electrodes can be either screen printed or tape cast. A metallic interconnect with appropriate gas channels can be formed with intricate gas channels by spark erosion or chemical etching. One possible design for the interconnect is the so-called interrupted fin design, developed by Normalair-Garrett Ltd. and Allied Signal. A schematic illustration of this is given in figure 1.21.

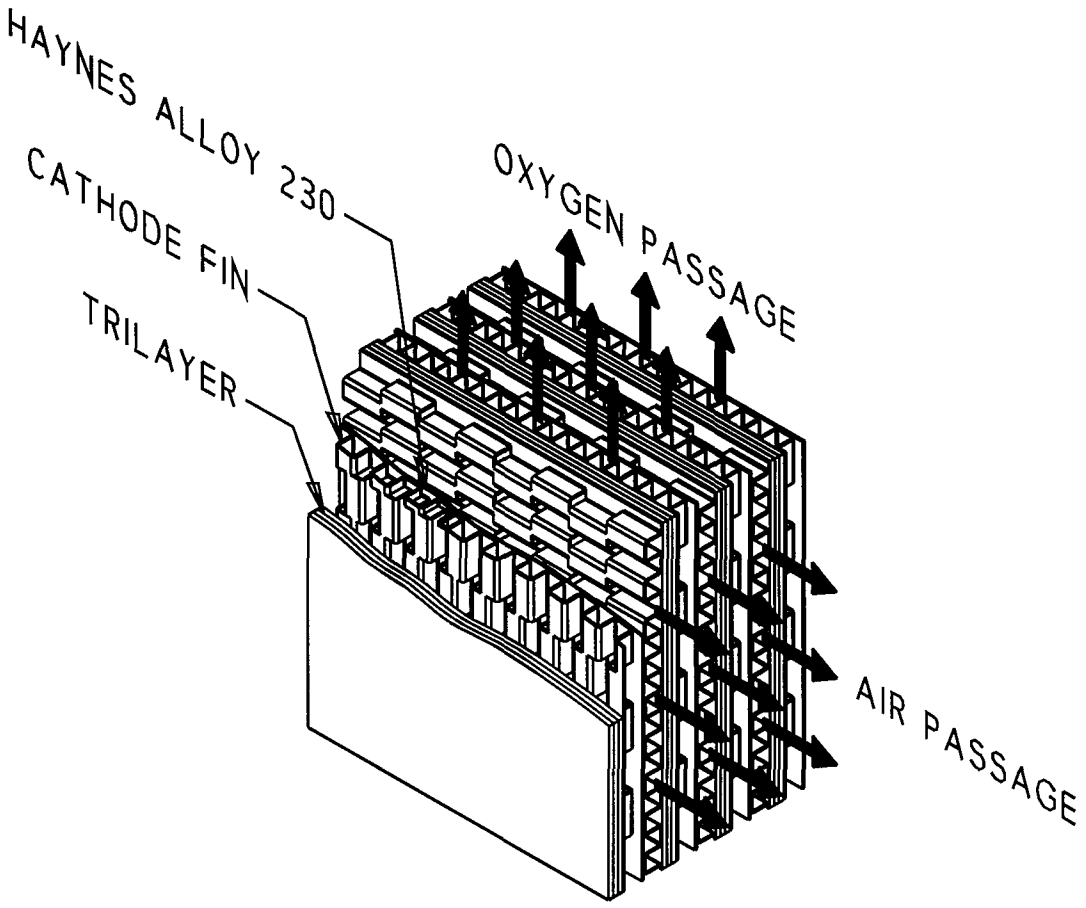


Figure 1.21. Schematic illustration of a planar design with an interrupted fin interconnect for an electrically driven ceramic oxygen generator. (Drawn by D. Peacey, NGL and reproduced with permission from NGL).

The design likely to be employed in future work at Imperial College utilises a self-supporting, tape cast CGO electrolyte of ~120 microns. Porous LSCF electrodes are deposited by screen printing. Primary concerns with the design are oxidation of the interconnect material leading to spalling and increased contact resistance, and gas tight sealing of the device.

1.4.3. Aerospace Considerations.

It is envisaged that the COG will be used in a military aircraft to provide a source of oxygen for the aircrew. This leads to specific design constraints which are not

necessarily required for ground based oxygen separators. Major constraints are mass and volume limitations. In order to compete with existing technology the entire device has to be less than 300 x 300 x 300 mm. This limits the active ceramic component to about half of this volume, the remainder being taken up by gas manifolding and heat exchangers etc.

One limitation of using CGO as the electrolyte is that the applied potential across each plate must be restricted to about 0.8V. If the potential is increased it leads to the partial reduction of the cerium cation, i.e. $Ce^{4+} \rightarrow Ce^{3+} + e^{-}$. This means electronic carriers are introduced into the ceramic and the efficiency of the device is reduced. Fighter aircraft have a specific voltage power supply which cannot be altered. Therefore, there is a minimum number of plates which must be in the stack, all connected in electrical series.

Another major problem with using the COG on-board an aircraft is the high levels of stress the device is exposed to. Components can be exposed to vibrational forces as high as 14 "g" when the aircraft passes through the sonic barrier. This is a major issue in the PSA devices currently used to supply on-board oxygen.

For a COG to be suitable for use in military aircraft it must have a rapid start-up time. It is therefore important that the device be able to withstand large thermal shocks and to be able to be heated to operating temperature within ~10 minutes.

Other considerations are that the oxygen produced must be of a suitable quality for the aircrew to breathe. This means that the oxygen must be cooled down from the temperature it exits the ceramic membrane module (CMM), around 800°C, to less than 40°C by the time it reaches the pilot. This is achieved with the use of heat exchangers. Figure 1.22. shows an input-output, power continuity, block diagram for the system. The electrical power supplied to the pre-heater and the CMM are controlled by the electronic control unit (ECU). The inlet air is drawn from the engine bleed air by a pair of vain axial fans. Once the ceramic is at a given temperature, the pre-heater will switch off and the power is delivered to the ceramic membrane. The heat exchangers will heat the inlet air to a temperature somewhat below the temperature of the ceramic stack and at the same time cool the product gas before it enters the breathing regulator.

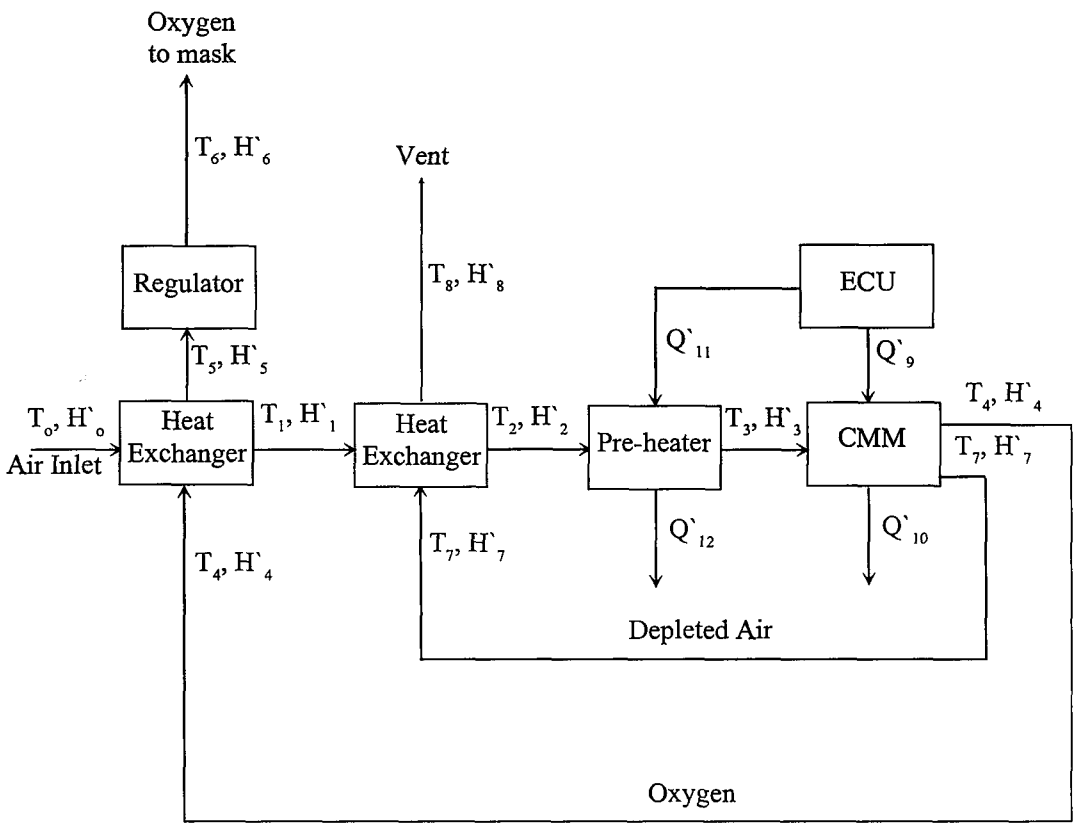


Figure 1.22. Input-output, power continuity diagram for a COG on board a military aircraft.

In the above diagram T represents the temperature of the gas at each stage in the process and H` is the associated power of the gas $(H`= c \cdot m` \cdot T)$, where c is the specific heat of the gas and m` is the mass flow rate. Q` is the power applied to the stack. In this design, the electrical power supplied to the pre-heater is the same as that applied to the ceramic stack, so a simple switching device could be used.

It is apparent from figure 1.22 that the power supplied to the ceramic stack (both electrically and from the inlet air) must be equal to the power exiting the stack. This is to ensure that neither a thermal runaway nor a quenching effect is produced. Thus, the following equations must hold.

$$Q`_9 + H`_3 = H`_4 + H`_7 + Q`_{10} \qquad \text{eqn. (1.15)}$$

$$H`_7 + H`_1 = H`_8 + H`_2 \qquad \text{eqn. (1.16)}$$

$$H`_4 + H`_0 = H`_1 + H`_6 \qquad \text{eqn. (1.17)}$$

$$H`_5 \cong H`_6 \qquad \text{eqn. (1.18)}$$

$Q`_{10} = 0$, $T_7$ is approximately the ceramic operating temperature and $T_o$ is the bleed air temperature. $H`_2 \cong H`_3$ when the stack is operating (i.e. there is no electrical power supplied to the pre-heater). $T_6<40°C$.

One final point that should be considered is that the air inlet supply comes from the engine bleed air. This means that a higher number of contaminants are likely to be present, some of which may be deleterious to the electrode. A list of contaminants from a typical fighter aircraft are given in table 1.2.

Engine bleed contaminants	Inlet contaminant quantity (ppm by volume)
Carbon dioxide	5000
Carbon monoxide	50
Total hydrocarbons	250
Nitrogen oxides	5
Acrolein	0.1
Total aldehydes	1
Engine generated oil particles	0.5 mg/m^3
Nickel	0.5 mg/m^3
Cobalt	0.1 mg/m^3
Ethanol	1000
Hydrogen fluoride	0.1
Hydrogen peroxide	1
Aviation fuels	250
Methyl alcohols	200
Methyl bromide	20
Oil breakdown products	1
Ozone	0.1

Table 1.2. Inlet air gas contaminants.

Because of the infinite selectivity of the ceramic, none of these contaminants should pass through membrane. However, it is possible that some of the inlet contaminants may poison the electrodes, and thus decrease the product flow rate.

1.5. References.

[1] J.Ernsting and P. King, in Aviation Medicine, 2nd Edition, Pub. Butterworths (1988) p45.

[2] R. Phillips, presented at Survival and Flight Equipment Association, Eastbourne, (4-6th March 1997).

[3] J.Ernsting and P. King, in Aviation Medicine, 2nd Edition, Pub. Butterworths (1988) Figure 5.4, p50.

[4] D.M. Ruthven, in Principals of Adsorption and Adsorption Processes, Pub. John Wiley & Sons (1984) p29.

[5] P. Broier, A.V. Kiselev, A.A. Lopatkin and S. Shpigil, Doklady Akad. Nauk. SSSR **Vol 161** (1965) p853.

[6] R.M. Barrer, J. Coll. Interface Sci. **Vol 21** (1966) p415.

[7] D.M. Ruthven, K.F. Loughlin and R.I. Derrah, Adv. Chem. **Vol 102** (1973) p330.

[8] T. Masuda, K. Tsutsuni and H. Takahashi, in Proc. of the Fifth International Conference on Zeolites, Naples. Ed. L.V.C. Rees, Heyden, London (1980) p476.

[9] G.A. Soriel, W.H. Granville and W.O. Daly, Chem. Eng. Sci. **Vol 38** (1983) p1517.

[10] N.F. Kirkby, in Proc. 4th BOC Preistley Conference, Leeds, The Royal Society of Chemistry (1986) p218.

[11] Captain G.W. Miller, K.G. Ikels and P.A. Lozano, SAFE Journal **Vol 16**, No.4 (1992) p28.

[12] M. Liu, in Proc. of the 1st Int. Symp. On Ionic and Mixed Conducting Ceramics, Eds. T.A. Ramanarayanan and H.L. Tuller, The Electrochemical Society, Inc., Pennington, NJ, **PV 91-12**, (1991) p95.

[13] B.C.H. Steele, Solid State Ionics, **Vol 75**, (1995) p157.

[14] J.A. Kilner, in Proc. of the 2nd Int. Symp. On Ionic and Mixed Conducting Ceramics, Eds. T.A. Ramanarayanan, W.L. Worrel and H.L. Tuller, The Electrochemical Society, Inc., Pennington, NJ, **PV 94-12**, (1994) p174.

[15] S.J. Benson, R.J. Chater and J.A. Kilner, in Proc. of the 3rd Int. Symp. On Ionic and Mixed Conducting Ceramics, Eds. T.A. Ramanarayanan, W.L. Worrel, H.L. Tuller, M. Mogensen and A.C. Khandkar, The Electrochemical Society, Inc., Pennington, NJ, **PV 97-24**, Paris (1997).

[16] L. Qiu, T.H. Lee, L.-M. Liu, Y.L Yang and A.J. Jacobson, Solid State Ionics, **Vol 76** (1995) p321.

[17] J.E. ten Elshof, H.J.M. Bouwmeester and H. Verweij, in Proc. 1st Int. Symp. On Ceramic Membranes, Eds. H.U. Anderson, A.C. Khandkar and M. Liu, Electrochemical Society, Inc., **PV 95-24**, Chicago, (1995) 37.

[18] D.J. Clark, R.W. Losey and J.W. Suitor, Gas Separation and Purification **Vol 6** (1992) p201.

[19] N.Q. Minh and K. Montgomery, in Proc. of the 5th International Symposium on SOFC, Eds. U. Stimming, S. Singhal, H. Tagawa and W. Lehnert, The Electrochemical Society, Inc., **PV 97-40**, Aachen, (1997) p153.

[20] S.J. Visco, C Jacobseon and L.C. de Jonghe, in Proc. of the 5th International Symposium on SOFC, Eds. U. Stimming, S. Singhal, H. Tagawa and W. Lehnert, The Electrochemical Society, Inc., **PV 97-40**, Aachen, (1997) p710.

[21] K-L Choy, W.Bai and B.C.H. Steele, in Proc. of the 5th International Symposium on SOFC, Eds. U. Stimming, S. Singhal, H. Tagawa and W. Lehnert, The Electrochemical Society, Inc., **PV 97-40**, Aachen, (1997) p1177.

[22] D. Waller, J.A. Kilner and B.C.H. Steele, in Proc. 1st Int. Symp. On Ceramic Membranes, Eds. H.U. Anderson, A.C. Khandkar and M. Liu, Electrochemical Society, Inc., **PV 95-24**, Chicago, (1995) p48.

[23] B.C.H. Steele, in Ceramic Oxygen Ion Conductors and Their Technological Applications, Ed. B.C.H. Steele, British Ceramic Proceedings Volume 56, Cumbria (1996) p151.

[24] G.B. Balazs and R.S. Glass, in Proc. of the 2nd Int. Symp. On Ionic and Mixed Conducting Ceramics, Eds. T.A. Ramanarayanan, W.L. Worrel and H.L. Tuller, The Electrochemical Society, Inc., Pennington, NJ, **PV 94-12**, (1994) p478.

[25] A. Hammouche, E. Siebert and A. Hammou, Mat Res. Bull., **Vol 24** (1989) p367.

[26] J.H. Kuo, H.U. Anderson and D.M. Sparlin, J. Solid State Chem., **Vol 87** (1990) p55.

[27] L.W. Tau, M.M. Nasrallah, H.U. Anderson, in Proc. 3rd Int. Symp. On Solid Oxide Fuel Cells, The Electrochemical Society Inc. Eds. S.C. Singhal and H. Iwahara, Honolulu (1993) p241.

[28] D. Kuscer, J. Holc, M. Hrovat, S. Bernik and D. Kolar, in Proc. of the 5th International Symposium on SOFC, Eds. U. Stimming, S. Singhal, H. Tagawa and W. Lehnert, The Electrochemical Society, Inc., **PV 97-40**, Aachen, (1997) p947.

[29] J. Mizusaki, Y. Mima, S. Yamauchi, K. Fueki and H. Tagawa, J. Sol. St. Chem. **Vol 80** (1989) p102.

[30] S.B. Adler, in Proc. of the 3rd Int. Symp. On Ionic and Mixed Conducting Ceramics, Eds. T.A. Ramanarayanan, W.L. Worrel, H.L. Tuller, M. Mogensen and A.C. Khandkar, The Electrochemical Society, Inc., Pennington, NJ, **PV 97-24**, Paris (1997).

[31] D. Waller, J.A. Lane, J.A. Kilner and B.C.H. Steele, Solid State Ionics, **Vol 86-88** (1996) p767.

[32] E. Ivers-Tiffée, M. Schießl, H.J. Oel, W. Wersing, in: Proc. 3rd Int. Symp. on SOFC, Eds. S. Singhal, H. Iwahara, Electrochemical Soc., Pennington, NJ, (1993), p631.

[33] T. Nakamura, G. Petzow and L.J. Gauckler, Mat. Res. Bull., **Vol 14**, (1979) p649.

[34] K. Wiik, C.R. Schmidt, S. Shamsili, M.-A. Einarsrud and T. Grande, in Proc. of the 17th Risø International Symposium on Materials Science, Eds. F.W. Poulsen, N. Bonanos, S. Linderoth, M. Mogensen and B. Zachau-Christiansen, Denmark (1996) p491.

[35] A. Weber, R. Männer, B. Jobst, M. Schiele, H. Cerva, R.Waser and E. Ivers-Tiffée, in Proc. of the 17th Risø International Symposium on Materials Science, Eds. F.W. Poulsen, N. Bonanos, S. Linderoth, M. Mogensen and B. Zachau-Christiansen, Denmark (1996) p473.

[36] O. Yamamoto, Y. Takeda, R. Kanno and M. Noda, Solid State Ionics, **Vol 22** (1987) p241.

[37] L. Kindermann, D.Das, H. Nickel, K. Hilpert, Solid State Ionics, **Vol 89** (1996) p215.

[38] C.C. Chen, M.M. Nasrallah, H.U. Anderson, in Proc. Of 3rd Solid Oxide Fuel Cells,. Eds. S.C. Singhal and H. Iwahara, The Electrochemical Society Inc., Pennington, NJ, (1993) p598.

[39] S.K. Lau and S.C. Singhal, in Proc. of the International Corrosion Forum, Paper number 345 Boston, Massachusettes (1985).

[40] J.A. Lane, P.H. Middleton, H. Fox, B.C.H. Steele, J.A. Kilner, in Proc. of the 2nd Int. Symp. On Ionic and Mixed Conducting Ceramics, Eds. T.A. Ramanarayanan, W.L. Worrel and H.L. Tuller, The Electrochemical Society, Inc., Pennington, NJ, **PV 94-12**, (1994) p489.

[41] H.U. Anderson, L-W. Tai, C.C. Chen, and M.N. Nasrallah, in Proc. of the 2nd Int. Symp. On Ionic and Mixed Conducting Ceramics, Eds. T.A. Ramanarayanan, W.L. Worrel and H.L. Tuller, The Electrochemical Society, Inc., Pennington, NJ, **PV 94-12**, (1994) p376.

[42] J.A. Lane, Ph.D. thesis, University of London (1995).
[43] R.A. de Souza, Ph.D. thesis, University of London (1996).
[44] A. Khandkar and S. Elangovan, Denki Kagaku, **Vol 58**, (1990) p551.
[45] J.P.P. Huijsmans, E.J. Siewers, F.H. van Heuveln and J.P. de Jong, in Proc. of the 2nd Int. Symp. On Solid Oxide Fuel Cells, Eds. F. Gross, P. Zegers, S.C. Singhal and O. Yamamoto, Commission of the European Communities, Athens, Greece (1991) p113.

2. Solid Oxide Fuel Cells.

2.1. Introduction.

A fuel cell is an electrochemical device for converting chemical energy into electrical energy. The device does not involve combustion of a fuel, but instead electrochemically oxidises the fuel, similar to the operation of a battery [1]. Like a battery, direct current (DC) electricity is produced, but unlike a battery, the reactants are not stored in a container, but the fuel and the oxidant are both supplied externally. This enables the fuel cell to be used continuously, without having to be recharged, as is the case with a battery. There are several different types of fuel cell, however in this chapter only the solid oxide fuel cell (SOFC) will be discussed.

The solid oxide fuel cell is modular, consisting of three functional components separated by an interconnect material to enable the production of a stack of these components in series. The three components are the cathode, the electrolyte and the anode. The electrochemical cell can be schematically illustrated as shown in figure 2.1, while figure 2.2. shows an example of the modular nature of the SOFC, including the interconnect material.

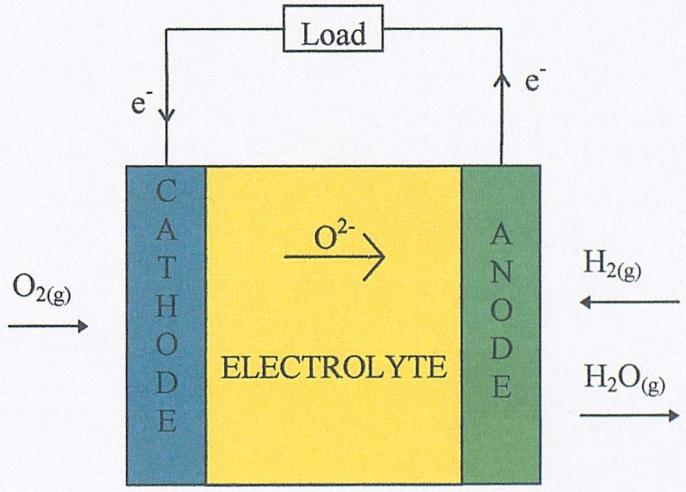


Figure 2.1. Schematic illustration of the solid oxide fuel cell.

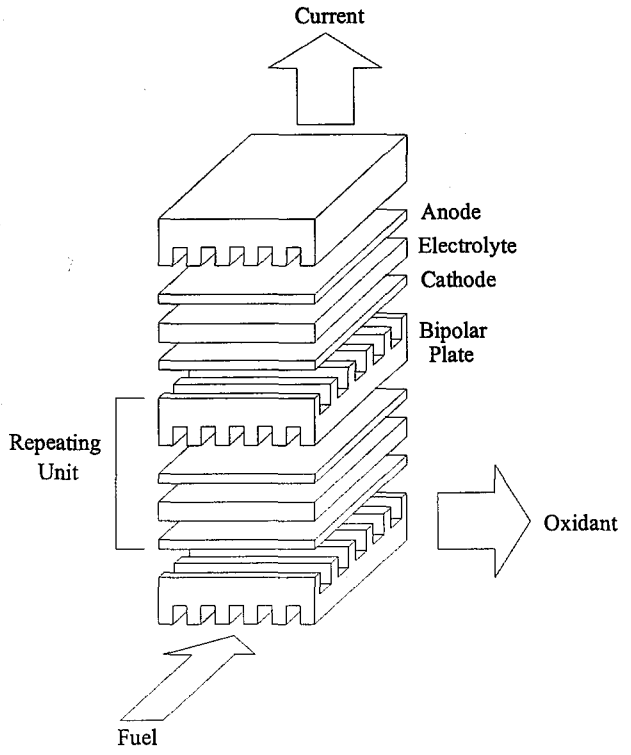


Figure 2.2. Schematic illustration of the modular nature of a solid oxide fuel cell (reproduced with permission from R.A. de Souza [2].

At the anode the fuel is oxidised while at the cathode the oxidant (usually oxygen) is reduced and oxygen ions are incorporated into the system. The electrons produced by the oxidation of the fuel are able to flow in an external circuit to the cathode to allow the reduction of oxygen. The charge flow through the external circuit is compensated by the flow of negatively charged oxygen ions through the electrolyte in the opposite direction of the electron flow. Power is drawn from the system due to the flow of electrons in the external circuit.

In figure 2.1, where hydrogen is the fuel and oxygen is the oxidant, the reactions at the two electrodes are as follows:

Cathode Reaction: $\frac{1}{2}O_2 + V_O^{\bullet\bullet} + 2e^- \rightarrow O^{2-}$ (Reduction process) eqn. (2.1)

Anode Reaction: $H_2 + O^{2-} \rightarrow H_2O + V_O^{\bullet\bullet} + 2e^-$ (Oxidation process) eqn (2.2)

These two equations can be combined to give an overall reaction for the fuel cell.

$$\text{Total Reaction:} \qquad H_2 + \tfrac{1}{2}O \rightarrow H_2O \qquad \text{eqn (2.3)}$$

As can be seen, the only product of the reaction with hydrogen is water vapour. One of the major advantages of the solid oxide fuel cell is that because the efficiency is high, there are very few harmful emissions. This is because the energy is taken from the fuel in an electrochemical process and not through combustion, which produces nitrogen oxides and sulphur oxides. Furthermore, in combustion, a multistage process of producing electrical energy from chemical energy through heat energy is required. This process is restrained by the Carnot cycle. Since the SOFC is an electrochemical device and does not involve combustion, it is not subject to the Carnot Cycle. Thus the theoretical energy conversion efficiencies for an SOFC are considerably higher. In addition, the waste heat produced can be used for combined heat and power systems. In practice, the efficiencies achieved are below the theoretical values due to losses in the system. The efficiency will be discussed in the next section.

2.2. Fuel Cell Efficiency and Operating Temperature.

The conventional materials used in an SOFC are yttria stabilised zirconia (YSZ) as the electrolyte, lanthanum strontium manganate (LSM) as the cathode and a composite cermet of nickel and yttria stabilised zirconia (Ni-YSZ) as the anode. This allows the operating temperature of the SOFC to be in the range of 800-1000°C. However, by operating at this temperature, there is a large constraint in terms of mechanical and chemical stability on the materials available for the balance of plant, for example, the pipes used to supply the fuel and oxygen gases to the system must be corrosion resistant.

If the operating temperature of the fuel cell can be reduced, then more conventional materials can be used for the balance of plant, and stainless steel may be used for the interconnect material, instead of the ceramic lanthanum strontium chromite, which is expensive to fabricate and leaks oxygen.

The driving force for the fuel cell is the oxygen partial pressure difference between the anode side and the cathode side of the cell. The partial pressure of oxygen at the oxidant side is approximately one and at the fuel side around 10^{-19}

atmospheres. The open circuit potential of the fuel cell is governed by the Nernst equation [3]:

$$E_{rev} = \frac{RT}{2F} \ln \left\{ \frac{(pO_2)^{\frac{1}{2}}_{CATHODE}}{(pO_2)^{\frac{1}{2}}_{ANODE}} \right\} \qquad \text{eqn (2.4)}$$

The efficiency (ε) of the cell is given by the ratio of the energy output to the total energy change in the system (ΔH).

$$\varepsilon = \frac{\text{energy output}}{\Delta H} \qquad \text{eqn (2.5)}$$

Since the fuel cell is a direct energy conversion device, the maximum theoretical energy produced is the change in free energy of the system, (ΔG). This allows theoretical efficiencies of 95%, the only losses due to reversible entropy changes in the system. In practice, other irreversible losses occur. These are termed polarisation losses, and are separated into three different elements: activation polarisation, ohmic polarisation and concentration polarisation.

The large difference in the partial pressure of oxygen across the cell leads to a flux of oxygen ions through the cell. The resistance to the flow of ions in the electrolyte, and ions and electrons in the electrode, causes an irreversible loss of energy, dissipated as heat, from the system. As the current flowing through the cell is increased, so the energy lost increases. This energy loss is known as ohmic resistance or ohmic polarisation, as it follows Ohm's Law, given in equation 2.6.

$$\eta_{ohm} = i.R_{cell} \qquad \text{eqn (2.6)}$$

where η_{ohm} is the ohmic polarisation, i is the current through the cell and R_{cell} is the electrical resistance of the cell.

As the ionic resistance of the electrolyte and electrode follow a typical Arrhenius function, if the temperature is decreased, then the ohmic polarisation losses will increase. Therefore, if the operating temperature is to be reduced, suitable materials with sufficiently low resistance are required.

Electrochemical reactions are required at the electrodes in the fuel cell as shown in equations 2.1 and 2.2. Under equilibrium conditions, the forward and backward reaction rates are the same, but if current is to be drawn through the cell, one rate will be faster than the other, requiring a potential to drive the reaction. The voltage required is lost from the overall cell voltage. The voltage loss is related to the current by equation 2.7.

$$i \propto \exp(\eta_{act}) \qquad \text{eqn (2.7)}$$

η_{act} is the potential required to drive the reactions at the electrodes and is known as the activation polarisation. η_{act} is also affected by temperature, and the specific activity of the electrode. An increase in temperature, active electrode area or the electrocatalytic activity of the electrode will result in a decrease in the activation polarisation.

In order to draw a constant current from the cell, a constant supply of both fuel and oxidant is needed. The electrochemical activity of the electrodes are decreased if the supply of reactants to the electrodes is restricted. The energy required to drive the reactants to the reactive sites reduces the cell potential. This drop in cell potential is termed concentration polarisation (η_{conc}). The same effect is seen if the products of the electrochemical reaction are not removed at a sufficiently high rate. The presence of product gases effectively reduces the concentration of the reactant. This situation limits the amount of current which can be drawn from the cell, i.e. any further increase in the applied potential results in no increase in the current.

Concentration polarisation losses may be reduced by providing a large reactant surface area. This is achieved by using porous electrodes with a very fine particle size.

The combined effects of these three types of polarisation losses are shown schematically in figure 2.3. It is evident from this that the open circuit voltage is reduced by the polarisation losses, and the terminal cell voltage (i.e. the point at which no more current is drawn) can be expressed by equation 2.8.

$$V = E_{rev} - \eta_{act} - \eta_{ohm} - \eta_{conc} \qquad \text{eqn (2.8)}$$

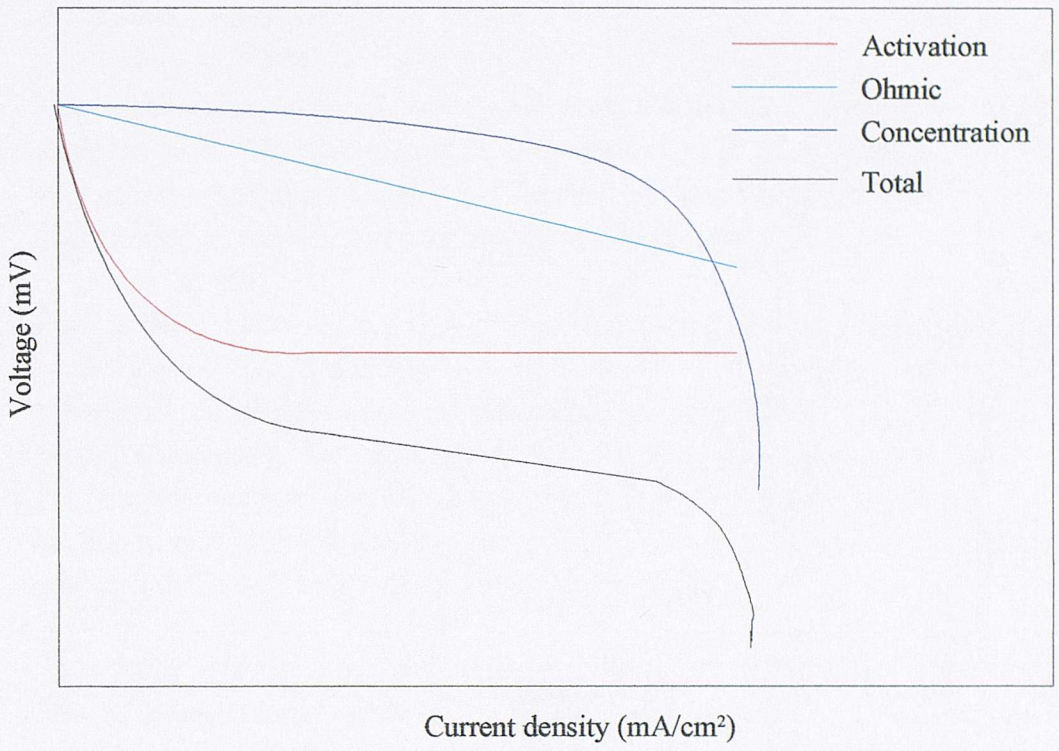


Figure 2.3. Typical Polarisation behaviour of a solid oxide fuel cell

The nature of the curves in figure 2.3 depends on many factors including materials properties, geometry factors and operating temperature. The ohmic and activation polarisation are both decreased with increasing temperature due to faster ionic transport and exchange. The concentration polarisation can also be decreased with increasing temperature due to more rapid gas phase diffusion.

2.3. Fuel Cell Component Requirements.

Figure 2.2 shows that each repeating unit in the SOFC contains four components: the interconnect, anode, electrolyte and cathode. Many of the requirements of the fuel cell components are similar to those for an electrically driven ceramic oxygen generator, as given in section 1.4.1. The main difference is the large gradient in the partial pressure of oxygen seen by the fuel cell. This section thus concentrates on the constraints imposed by the pO_2 range across the cell.

2.3.1. Interconnect.

The interconnect material, or bipolar plate has perhaps the largest constraints imposed on it. The basic function of the interconnect is the same as in the COG, in that it must separate the two gas streams (in this case the fuel and the oxidant) and provide an electrical connection between the ceramic tri-layers in the stack.

Unlike the situation in the COG, where the partial pressure difference between each side of the interconnect is unlikely to be more than a few orders of magnitude, a partial pressure difference of more than eighteen orders of magnitude is seen. Therefore, aside from the constraints given in section 1.4.1.4. the material chosen for the interconnect must be chemically stable in both oxidising and highly reducing atmospheres. It is also important that there is a minimal difference in thermal expansion on the two sides.

The highly reducing environment on the fuel side of the interconnect limits the use of many oxides. Of the ceramic oxides available which are suitably refractory in nature, it is generally only the rare earth/transition metal perovskites which have sufficient electronic conductivity for use as an interconnect. Doped lanthanum chromite shows the most promise in terms of its chemical stability, refractory properties, thermal expansion coefficient, electronic conductivity and low oxygen ion diffusivity [4,5].

$LaCrO_3$ is intrinsically a p-type conductor due to holes in the 3d band of the chromium ions. However, the conductivity is not adequate for the fuel cell and so the material is usually doped on the A-site with a lower valance cation (Sr, Ca or Mg) to increase the number of electron-holes available for conduction [5,6,7]. The addition of strontium to $LaCrO_3$ also stabilises the rhombohedral structure at room temperature [8]. (Undoped $LaCrO_3$ undergoes a phase change at around 240-280°C [8,9].) It is important that the number of phase changes is minimised as they generally lead to volume changes.

In very reducing atmospheres, oxygen can be lost from the doped lanthanum chromite which reduces the concentration of holes and increases the number of oxygen vacancies. This reduces the overall conductivity of the chromite and also increases the oxygen ion diffusivity [10]. The defect chemistry of doped lanthanum chromites is explained in chapter 3.

Due to the high volatility of chromium in air, a major problem with lanthanum chromite is obtaining high density on sintering. There has been substantial work on reducing the sintering temperature required to produce dense lanthanum chromite, and several different techniques have been employed. These include the use of highly reactive powders [11], the use of dopants [11] and improved processing techniques [12]. A brief synopsis of the various developments in the sintering characteristics of lanthanum chromite is given in the review of ceramic fuel cells by Minh [1].

The oxidising environment of the interconnect prohibits the use of most metallic alloys at the high temperatures required for the use of zirconia based fuel cells. If an intermediate or low temperature fuel cell is employed, then metallic alloys such as ferritic stainless steels. These materials are stable in reducing environments, allow minimal oxygen permeation and have more than sufficient electronic conductivity. There is however, a concern about corrosion of the metal on the oxidising side. The formation of an oxide scale affects both the mechanical integrity of the stack and adds a significant contact resistance to the cell. It has been suggested that a metallic interconnect can be protected by coating with a thin film of $LaCrO_3$ [13].

2.3.2. Anode

The anode is exposed to an atmosphere containing the fuel for the SOFC. It is therefore essential that the anode material is stable in atmospheres with a pO_2 around 10^{-19} bar. This allows the use of many metals, but precludes the use of most oxides.

Assuming the fuel used is hydrogen, the reaction at the anode is given in equation 2.2. It is clear from this that the anode has two functions: first, it must allow hydrogen to combine with the oxygen ions provided by the electrolyte, and secondly, it must act as a sink for the electrons produced by the electrochemical reaction.

It is possible to use nickel metal as the anode as it is stable in the highly reducing environment of the fuel, and the electronic conductivity is more than sufficient. Furthermore, nickel readily adsorbs hydrogen and so may catalyse the

electrochemical reaction [14]. The adsorbed hydrogen can then readily migrate along the surface of the nickel particles.

It is possible to divide the reaction given in equation 2.2 into two steps:

(a) $$H_2 + 2Ni \Leftrightarrow 2NiH \qquad \text{eqn. (2.9)}$$

(b) $$2NiH + O_0^x \Leftrightarrow H_2O + 2Ni + V_0^{\cdot\cdot} + 2e^- \qquad \text{eqn. (2.10)}$$

However, there is also evidence to suggest that the electrolyte provides some catalytic activity for the oxidation of hydrogen. Oxygen vacancies in the electrolyte are thought to be electrochemically reactive sites (V_{ERS}) which can incorporate hydrogen, while the electrons can migrate in the plane of the electrolyte-electrode interface. In this case the reaction steps would be [1]:

$$H_2 + 2V_{ERS} \Leftrightarrow 2H_{ERS} \qquad \text{eqn. (2.11)}$$

$$2H_{ERS} + O_0^x \Leftrightarrow H_2O + 2V_{ERS} + V_0^{\cdot\cdot} + 2e^- \qquad \text{eqn. (2.12)}$$

If this is the case, then the main requirement of the anode is simply to provide a sink for the electrons.

Norby and Kofstad [15] suggest that at low temperatures processes involving a hydrogen species are rate limiting (for example, the adsorption of hydrogen onto the nickel surface). However, at high temperatures, the rate limiting step appears to involve oxygen or hydroxide species. This implies that the process is at the YSZ surface. It is apparent that the reaction mechanisms at the anode are not well understood. This is probably due to the fact that the anode polarisation resistance is significantly less than the resistance associated with the cathode.

Whether the nickel or the electrolyte acts as the catalyst, the anode must be porous to allow the hydrogen gas to reach to reach the electrolyte. A major problem with using pure nickel as the anode (apart from its high thermal expansion coefficient) is that nickel particles coarsen over time, thus reducing the catalytic area of the electrode. Therefore a ceramic-metal composite (cermet) is employed to prohibit grain growth. The ceramic used is generally zirconia because of its stability in highly reducing gases and also to reduce the thermal expansion mismatch between the anode and the electrolyte.

The ratio of ceramic to metal is usually 1:1 by volume. Below 30 vol% Ni, there is no complete electrical contact (called the percolation threshold) [16] and as a result the conductivity is around three orders of magnitude lower than that above the percolation threshold. As the nickel content is increased, the thermal expansion coefficient rises approximately linearly. At high nickel concentrations, the difference in thermal expansion coefficient is such that large stresses are induced, and cracking of the membrane can result.

Other materials that have been considered for use in anodes are platinum-YSZ and cobalt-YSZ cermets. However, neither have been employed commercially due to the high costs of the metals with respect to nickel. Furthermore, the oxidation potential of cobalt is higher than YSZ and this may be a problem at the fuel depleted end of the cell.

Recently, interest has been expressed in the use of mixed protonically-electronically conducting ceramics as anodes [17]. Doped $A^{II}B^{IV}O_3$ perovskites such as $SrCeO_3$ [18,19], $BaCeO_3$ [20,21], $CaZrO_3$ [22] and $SrZrO_3$ [23] and some $A^{III}B^{III}O_3$ perovskites ($LaYO_3$ doped on the A site with calcium [24] or strontium [25,26]) are known to be proton conductors. The ionic conductivity can be enhanced by doping on either the A- or B-sites. By introducing a variable valance transition metal cation such as iron, sufficient electronic conduction can be achieved. A major problem with these ceramics is the large thermal expansion coefficient in comparison to the electrolyte. Work completed in the Department of Materials at Imperial College has shown that cracking of the electrolyte occurs when attaching the anode [27]. Another problem, particularly with the cerates, is concern over the stability of the materials in the highly reducing fuel atmosphere [28].

2.3.3. Electrolyte.

The constraints on the electrolyte are essentially those described in section 1.4.1.1. for the COG, and as such the most commonly used materials are acceptor doped fluorites such as zirconia or ceria. The only difference in the case of the SOFC is the pO_2 gradient that occurs across the electrolyte membrane. At the anode side, the pO_2 is expected to be some 15 orders of magnitude lower than at the oxidant side. This means that the electrolyte material for a fuel cell must be more resistant to reduction than in the case of the COG. If the electrolyte is

reduced at the anode side, it is likely to be a reduction of the zirconium or cerium atom, that is

$$2A_A^x + 4O_O^x \rightarrow 2A_A^{'} + 3O_O^x + V_O^{\bullet\bullet} + \tfrac{1}{2}O_2 \qquad \text{eqn. (2.13)}$$

where A can be either cerium or zirconium.

This introduces electronic carriers into the electrolyte which will significantly reduce the operating efficiency of the cell. Furthermore, the larger ionic radii of the A^{3+} cation gives rise to lattice expansion and can lead to cracks at the electrode/electrolyte interface or detachment of the anode from the electrolyte.

The reduction of the cerium cation occurs more readily than for the zirconium cation, and significant levels of non-stoichiometry have been seen to occur in pure ceria when exposed to a reducing atmosphere [29,30]. Electronic conductivity leads to a reduction in the open circuit voltage of the cell, and thus reduces the efficiency of the device. Therefore, gadolinia doped ceria, despite its large ionic conductivity [31] may not be as useful as the electrolyte for a fuel cell due to doubts over its chemical stability in reducing atmospheres [32,33]. It is thus likely that unless the so called p^- point (which will be discussed in Chapter 3) can be reduced, YSZ will be used in preference to CGO.

New electrolytes are being developed based on the perovskite crystal structure. $LaGaO_3$ doped on both the A- and B-sites shows promise as a low temperature replacement for zirconia due to its high ionic conductivity and low electronic transference number [34,35,36]. However, this material is still very much in the development stage, and considerable testing is required before a $LaGaO_3$ based fuel cell is likely to be employed commercially.

2.3.4. Cathode.

The requirements for the cathode of the solid oxide fuel cell are the same as the cathode in the electrically driven ceramic oxygen generator. The incorporation of gaseous oxygen into the ceramic follows the same pathways in both cases, and hence the electrode has the same catalytic requirements.

2.4. SOFC Stack Design.

As illustrated in section 2.1, the SOFC is modular in nature. Each cathode/electrolyte/anode tri-layer is electrically connected to another to allow a practicable voltage to be produced. There are two designs which are commonly used, the tubular design (favoured in the USA) and the planar design (favoured in Europe). The main difference is their geometry and the gas manifolding. The planar design is similar to the design used for the COG, outlined in section 1.4.2.

2.4.1. Tubular SOFC.

The tubular designed SOFC is primarily being developed by Westinghouse Electric Corporation in the USA, and is the most technologically advanced. Westinghouse have produced a 120kW assembly using the YSZ based system.

Early designs utilised a closed end, porous support tube (often calcia stabilised zirconia) around which the active cell components are deposited. The tube is then covered with a porous cathode material (e.g. LSM). However, this design lead to large concentration polarisation losses and more recent designs use the cathode material itself as the support tube. This is illustrated in figure 2.4 [37].

The LSM tube is extruded and then sintered to about 35% porosity. A thin (40μm), gas tight electrolyte (YSZ) is then deposited on the electrode by chemical vapour deposition (CVD). A strip of around 9mm is left with the cathode exposed. This strip of exposed cathode is coated with a gas tight, 40μm covering of the interconnect material (Mg doped $LaCrO_3$), originally by CVD but now using plasma spraying. The electrolyte surface is then covered with the anode material (Ni-YSZ cermet). There must be no contact between the anode and the interconnect to avoid a short circuit effect in the cell. As devices are scaled up the active length and diameter of the tube have increased. Commercial prototype cells have an active length of 150cm and a diameter of 2.2cm.

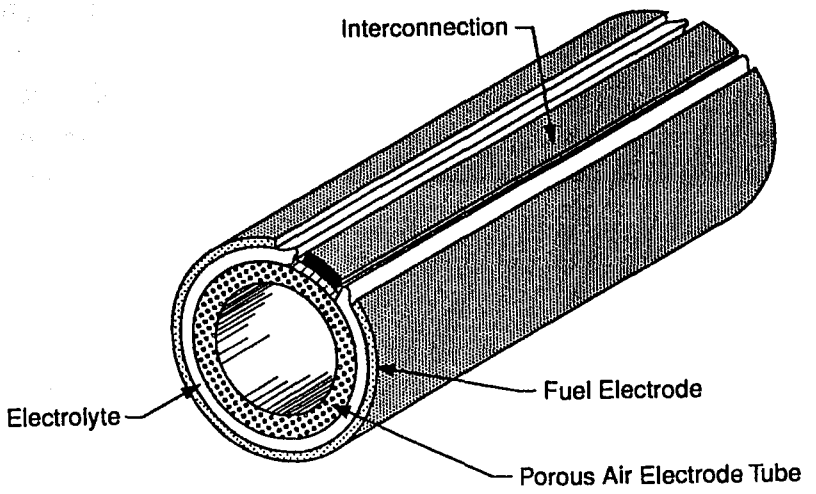


Figure 2.4. Air electrode supported type tubular solid oxide fuel cell design [37].

The tubular cells are stacked together using a nickel felt at the interconnect to connect the cells electrically in parallel and series. Air is injected inside the closed end tube and the fuel flows outside the tubes. This removes the need for any extra sealing materials that are required with the planar design. By using very thin electrolyte materials it may be possible to reduce the operating temperature of the fuel cell and thus permit the use of cheaper balance of plant materials.

2.4.3. Planar SOFC.

The planar SOFC design is essentially the same as that used for the COG. It therefore suffers from the same problems associated with the COG, i.e. gas manifolding, sealing and thermal shock. An example of a planar stack design is given in figure 2.2. A major advantage of the planar design over the tubular design is that the ceramic processing routes to produce the cells are far better established, less time-consuming and most importantly less costly. Electrolytes can be produced by tape casting [38,39,40] or tape calendering [41] and the electrodes can be applied by screen printing [41,42], tape casting [39], slurry

coating [43] or plasma spraying [44]. Various components can also be co-fired, thus reducing the number of processing steps in the system [40,45]. Another advantage of the flat planar design over the sealess tubular design is that the electrolyte and the interconnect can be manufactured independently. This reduces the problem associated with the high vapour pressure of chromium since it allows a lower sintering temperature for the interconnect material. The main drawback with the planar design is the necessity for a gas tight seal. Current SOFC design incorporate a glass, glass-ceramic or cement seal. At the elevated temperatures required for manufacture and to some extent operation, these seals have a tendency to react with the ceramic stack. Furthermore, the tolerances required for the seals are very high to avoid non-uniform stress distributions throughout the stack.

In general, flat plate designs of SOFC use a thick electrolyte (100-200μm) sandwiched between two porous electrode materials [46]. The dense interconnect material also adds support to the stack structure. More recently, considerable study has gone into thin film electrolytes supported by either the cathode or the anode [47,48,49].

While the technological status of the planar SOFC is behind that of the tubular design, some long term degradation experiments have been carried out with success [47,50].

2.5. References.

[1] N.Q. Minh, J. Am. Ceram. Soc., **Vol 76**, (1993) p563.

[2] R.A. de Souza, Ph.D. Thesis, University of London (1996).

[3] J. O'M. Bockris, N. Bonciocat and F. Gutmann, in An Introduction to Electrochemical Science, Wykeham Publications Ltd., London (1974).

[4] Srilomsak, D.P. Schilling and H.U Anderson, in Proceedings of the 1st International Symposium on SOFC, Eds. S. Singhal, The Electrochem. Soc., Pennington, NJ, (1989) p242.

[5] I. Yasuda, K. Ogasawra, N. Hishinuma, in Proc. of the 2nd Int. Symp. On Ionic and Mixed Conducting Ceramics, Eds. T.A. Ramanarayanan, W.L. Worrel and H.L. Tuller, The Electrochemical Society, Inc., Pennington, NJ, **PV 94-12**, (1994) p164.

[6] R. Berjon, C. Romand and J.P. Coutures, High Temp. Sci., **Vol 13**, (1980) p173.
[7] G.H. Jonker, Physica, **Vol 20**, (1954) p1118.
[8] C.P. Khattak and D.E. Cox, Mat. Res. Bull., **Vol 12**, (1977) p463.
[9] S. Geller and P.M. Raccah, Phys. Rev. B, **Vol 2**, (1970) p1167.
[10] D.B. Meadowcroft, Br. J. Appl. Phys., **Vol 2**, (1969) p1225.
[11] L.A. Chick, J.L. Bates and L.R. Peterson, in Proceedings of the 1st International Symposium on SOFC, Eds. S. Singhal, The Electrochem. Soc., Pennington, NJ, (1989) p170.
[12] L.W. Tai and P.A. Lessing, J. Am. Ceram. Soc., **Vol 74**, (1991) p155-160.
[13] H. Tenmei, H. Michibata, T. Namikawa and Y. Yamazaki, Denki Kagaku, Vol 58 (1981) p1072.
[14] E.J.L. Schouler and M. Kleitz, J. Electrochem. Soc., **Vol 134**, (1987) p1045.
[15] T. Norby and P. Kofstad, in Proc. of the 17th Risø International Symposium on Materials Science, Eds. F.W. Poulsen, N. Bonanos, S. Linderoth, M. Mogensen and B. Zachau-Christiansen, Denmark (1996) p381.
[16] D.W. Dees, T.D. Claar, T.E. Easler, D.C. Fee and F.C. Mrazek, J. Electrochem. Soc., **Vol 134**, (1987) p2141.
[17] B.C.H. Steele, in Proceedings of the 1st European Solid Oxide Fuel Cell Forum (1994) p375.
[18] T. Takahashi and H. Iwahara, Rev. Chim. Miner., **Vol 17,** (1980) p243.
[19] H. Iwahara, T. Esaka, H. Uchida and N. Maeda, Solid State Ionics, **Vol 3/4,** (1981) p359.
[20] N. Bonanos, B. Ellis, K.S. Knight and M.N. Mahmood, Solid State Ionics, **Vol 35,** (1989) p179.
[21] K.D. Kreuer, E. Schönherr and J. Maier, Solid State Ionics, **Vol 70/71,** (1994) p278.
[22] N. Kurita, N. Fukatsu, K. Ito and T. Ohashi, J. Electrochem. Soc. **Vol 142,** (1995) p1552.
[23] T. Yajima, H. Suzuki, T. Yogo and H. Iwahara, Solid State Ionics, **Vol 51,** (1992) p101.
[24] T.Takahashi and H. Iwahara, Rev. Chim. Min. **Vol 17** (1980) p243.
[25] E. Ruiz-Trejo and J.A. Kilner, in Proceedings of the 17th Risø International Symposium on Materials Science, Eds. F.W. Poulsen, N. Bonanos, S. Linderoth, M. Mogensen and B. Zachau-Christiansen, Denmark (1996) p411.

[26] E. Ruiz-Trejo and J.A. Kilner, Solid State Ionics **Vol 97** (1997) p529.
[27] J.A. Lane, *Private Communication.*
[28] M.J. Scholten, J. Schoonman, J.C. van Miltenburg and H.A.J. Oonk, Solid State Ionics, **Vol 61,** (1993) p83.
[29] R.J. Panlener, R.N. Blumenthal and J.E. Garnier, J. Phys. Chem. Solids, **Vol 36,** (1975) p1213.
[30] K. Eguchi, T. Setoguchi, T. Inoue and H. Arai, Solid State Ionics, **Vol 52,** (1992) p165.
[31] H.L. Tuller and A.S. Nowick, J. Electrochem. Soc., **Vol 122**, (1975) p255.
[32] J.M. Ralph and J.A. Kilner, in Proc. of the 5th International Symposium on SOFC, Eds. U. Stimming, S. Singhal, H. Tagawa and W. Lehnert, The Electrochemical Society, Inc., **PV 97-40**, Aachen, (1997) p1021.
[33] N. Sammes, Z. Cai and G.A. Tompsett, in Proc. of the 5th International Symposium on SOFC, Eds. U. Stimming, S. Singhal, H. Tagawa and W. Lehnert, The Electrochemical Society, Inc., **PV 97-40**, Aachen, (1997) p1021.
[34] H. Matsuda, T. Ishihara, Y. Mizuhara and Y. Takita, in Proceedings of the 3rd International Symposium on SOFC, Eds. S. Singhal and H. Iwahara, The Electrochem. Soc., Pennington, NJ, (1993) p129.
[35] T. Ishihara, H. Matsuda, and Y. Takita, Solid State Ionics, **Vol 79,** (1995) p147.
[36] T, Ishihara, M. Honda, H. Nishiguchi and Y. Takita, in Proc. of the 5th International Symposium on SOFC, Eds. U. Stimming, S. Singhal, H. Tagawa and W. Lehnert, The Electrochemical Society, Inc., **PV 97-40**, Aachen, (1997) p301.
[37] S.C. Singhal, in Proc. of the 5th International Symposium on SOFC, Eds. U. Stimming, S. Singhal, H. Tagawa and W. Lehnert, The Electrochemical Society, Inc., **PV 97-40**, Aachen, (1997) p37.
[38] M. Dokiya, N. Sakai, T. Kawada, H. Yokokawa and I. Anzai, in Proc. of the 5th International Symposium on SOFC, Eds. U. Stimming, S. Singhal, H. Tagawa and W. Lehnert, The Electrochemical Society, Inc., **PV 97-40**, Aachen, (1997) p127.
[39] J.P.P. Huijsmans, E.J. Siewers, F.H. van Heuveln and J.P. de Jong, in Proc. of the 2nd Int. Symp. On Solid Oxide Fuel Cells, Eds. F. Grosz, P. Zegers, S.C. Singhal and O. Yamamoto, Commision of the European Communities, Athens, Greece (1991) p113.

[40] F.P.F. van Berkel, F.H. van Heuveln and J.P.P. Huijsmans, in Proceedings of the 3rd International Symposium on SOFC, Eds. S. Singhal and H. Iwahara, The Electrochem. Soc., Pennington, NJ, (1993) p774.

[41] H. Christnsen, T.P. Anderson, J. Dudek and J. Kjaer, in Proc. of the 2nd Int. Symp. On Solid Oxide Fuel Cells, Eds. F. Grosz, P. Zegers, S.C. Singhal and O. Yamamoto, Commision of the European Communities, Athens, Greece (1991) p839.

[42] T. Hikita, T. Hishinuma, T. Kawashima, I. Yasuda, T. Koyama and Y. Matsuzaki, , in Proceedings of the 3rd International Symposium on SOFC, Eds. S. Singhal and H. Iwahara, The Electrochem. Soc., Pennington, NJ, (1993) p714.

[43] S. Murakami, Y. Akiyama, N. Ishida, T. Yasuo, T.Saito and N. Furukawa, in Proc. of the 2nd Int. Symp. On Solid Oxide Fuel Cells, Eds. F. Grosz, P. Zegers, S.C. Singhal and O. Yamamoto, Commision of the European Communities, Athens, Greece (1991) p839.

[44] L.W. Tai and P.A. Lessing, J. Am. Ceram. Soc., **Vol 74** (1991) p501.

[45] H. Takagi, H. Taira, A. Shiratori, K. Nishida and Y. Sakabe, , in Proc. of the 2nd Int. Symp. On Solid Oxide Fuel Cells, Eds. F. Grosz, P. Zegers, S.C. Singhal and O. Yamamoto, Commision of the European Communities, Athens, Greece (1991) p99.

[46] G.M. Christie and J.P.P. Huijsmans, in Proc. of the 5th International Symposium on SOFC, Eds. U. Stimming, S. Singhal, H. Tagawa and W. Lehnert, The Electrochemical Society, Inc., **PV 97-40**, Aachen, (1997) p718.

[47] H.P. Buchremer, U. Diekmann, L.G.J. de Haart, H. Kabs, U. Stimming and D. Stöver, in Proc. of the 5th International Symposium on SOFC, Eds. U. Stimming, S. Singhal, H. Tagawa and W. Lehnert, The Electrochemical Society, Inc., **PV 97-40**, Aachen, (1997) p160.

[48] N.Q. Minh and K. Montgomery, H.P. Buchremer, U. Diekmann, L.G.J. de Haart, H. Kabs, U. Stimming and D. Stöver, in Proc. of the 5th International Symposium on SOFC, Eds. U. Stimming, S. Singhal, H. Tagawa and W. Lehnert, The Electrochemical Society, Inc., **PV 97-40**, Aachen, (1997) p153.

[49] S.J. Visco, C. Jacobson and L.C. De Jonghe, H.P. Buchremer, U. Diekmann, L.G.J. de Haart, H. Kabs, U. Stimming and D. Stöver, in Proceedings of the 2nd International Symposium on SOFC, Eds. F. Grosz, P. Zegers, S.C. Singhal and O. Yamamoto, Commision of the European Communities, Athens, Greece (1991) p710.

[50] K. Ogasawara, I. Yasuda, Y. Matsuzaki, T. Ogiwara and M. Hishinuma, in Proceedings of the 2nd International Symposium on SOFC, Eds. F. Grosz, P. Zegers, S.C. Singhal and O. Yamamoto, Commision of the European Communities, Athens, Greece (1991) p143.

3. Crystal Structure and Defect Chemistry of Perovskite and Fluorite Oxides.

3.1. Introduction.

Perovskite and fluorite materials form a technologically interesting group of materials. In both cases the regular array of oxygen ions often permit rapid transport of oxygen through the bulk of the crystal lattice. Perovskites with the general formula ABO_3 and fluorites with the formula MO_2 can both be doped in a similar manner to significantly change their electrical and physical properties. It is due to these phenomena that both classes of materials are used widely in solid oxide fuel cells and ceramic oxygen generators.

3.2. Perovskite Crystal Structure.

A perovskite is a ternary compound of the general formula ABO_3 where the A cation is considerably larger than the B cation. A true perovskite displays a cubic structure where the A-site cation and the oxygen ion form a face centred cubic sublattice (FCC) and the B-site cations occupy the octahedral sites in the array. The A ion has co-ordination number 12 and the B ion co-ordination number 6 [1]. The unit cell of a cubic perovskite is shown in figure 3.1. However, perovskites are often distorted from cubic symmetry. In a cubic cell where the ions are in contact with each other, the geometry states that:

$$(r_A + r_O) = \sqrt{2}(r_B + r_O) \qquad \text{eqn (3.1)}$$

where r_A, r_B, r_O are the ionic radii of the A cation, B cation and oxygen ion, respectively. Lists of ionic radii can be found in Shannon [2] and a specific list of the rare earth elements in Jia [3]. Distortion from cubic symmetry arises when the cation radii do not permit equation 3.1 to equate. A tolerance factor has been hypothesised such that;

$$t = {}^{r_A + r_o}\!\Big/\!_{\sqrt{2}(r_B + r_o)} \qquad \text{eqn (3.2)}$$

where t is the Goldshmidt tolerance factor. [4].

For a cubic system t = 1. A perovskite structure can exist until $t \approx 0.75$ at which point the ilmenite structure becomes stable. For values of $0.9<t<1$, the rhombohedral structure exists and for $0.75<t<0.9$, the symmetry is orthorhombic [5]. The values are only guidelines as they apply to theoretical systems assuming the ions are spherical. The cubic system can exist in situations where $t \neq 1$, particularly at high temperatures. Changes in crystal symmetry are often seen with changes in temperature, for example, rhombohedral perovskites are often seen to transform to cubic as the temperature is increased.

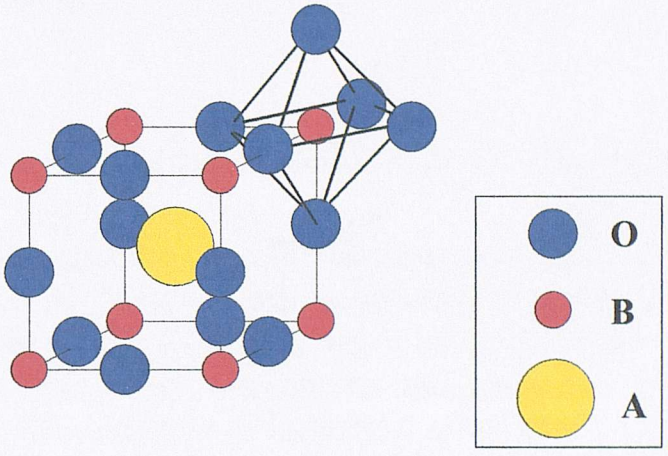


Figure 3.1. The unit cell of an ideal cubic perovskite.

The perovskite can exist in many different stoichiometries depending on the valence of the A and B cations. The most common of these are the $A^{2+}B^{4+}O_3$ such as $BaTiO_3$ and $SrZrO_3$; and the $A^{3+}B^{3+}O_3$ such as $SmAlO_3$ and $LaGaO_3$. Perovskites which are of the type $R_ET_MO_3$ are more complex as the T_M cation can have a mixed valence (i.e. T_M^{2+}, T_M^{3+}, and T_M^{4+}). R_E represents a rare earth element and T_M a transition metal. This type of perovskite is often non-stoichiometric and is given the general formula $R_ET_MO_{3\pm\delta}$. Depending on the nature of the transition metal, the perovskite can either be oxygen deficient or in oxygen excess. Oxygen deficiency (often termed hypostoichiometry or substoichiometry) is more common than oxygen excess (termed hyperstoichiometry or superstoichiometry) in air. By changing the partial pressure of oxygen to high values ($pO_2>1$), oxygen superstoichiometry can prevail. The close packing nature of the perovskite structure makes the presence of oxygen interstitial sites very unlikely and therefore when the material is

superstoichiometric, metal vacancies are considered to be the dominant defect. Perovskites which are suitable for use as cathodes in SOFC or COG, or for membrane materials in a pressure driven oxygen separator are generally of the form $R_ET_MO_{3\pm\delta}$. In order to provide the perovskite lattice with a sufficient number of mobile oxygen vacancies to produce a large oxygen ion conductivity, the perovskite is doped on the A-site with an alkaline earth cation. Such doping can dramatically alter the electronic, crystallographic and mechanical properties of the perovskite. Lanthanum cobaltate exists in rhombohedral symmetry at room temperature. However, by acceptor doping the A site with strontium, a cubic symmetry can be obtained. This occurs when the strontium occupies 55% of the A sites, at room temperature.

3.3. Nonstoichiometry and Defect Chemistry of $R_ET_MO_{3\pm\delta}$ Perovskites.

Defects in a crystal lattice occur at all temperatures above absolute zero. Different types of imperfections may be present in a crystalline material. The most common defects in a ceramic are voids or pores (three dimensional defects), grain boundaries (two dimensional defects), dislocations (one dimensional defects) and point defects (zero dimensions). Point defects are arguably the most important with regard to the impact on the electrical properties of a ceramic. The types of point defects that may exist in a ceramic are vacancies (i.e. the absence of an ion where one should sit), an interstitial (the presence of an ion where one should not be) and an impurity or dopant (the presence of a foreign ion on a site normally occupied by a host ion). Other point defects can exist but are much less common.

The concentration of point defects can be derived by treating the defects as a chemical species within the bulk of the crystal. This is called the Wagner-Schottky model [6]. The main assumptions of the model are that the defects obey the Law of Mass Action, the activities of all point defects are equal to their concentration and any normal positions in the lattice have unit activity.

In order to adequately describe defect relations, it is important for a comprehensive notation system to be used. The system used in this work is that employed by Kröger and Vink [7], where the symbol represents the ionic species (a vacancy is represented by V), the superscript represents the effective charge the defect has on the lattice (i.e. a vacant oxygen site has an effective 2^+ charge).

A positive charge is represented with a dot, a negative charge a prime and a neutral species a cross. The subscript represents the lattice site on which the defect is sitting. In the case of an interstitial site, the subscript "i" is used.

In a pure perovskite several intrinsic defect equilibria are possible. These are the spontaneous formation of A, B and O vacancies (Schottky disorder) and the spontaneous formation of an electron and a hole (electronic disorder). Frenkel and Anti-Frenkel disorder can also occur, but these are less energetically favourable. The defect equations for Schottky and electronic disorder are, respectively:

$$"\text{null}" \rightarrow V_A''' + V_B''' + 3V_O^{\bullet\bullet}$$

$$"\text{null}" \rightarrow e' + h^{\bullet}$$

The $R_ET_MO_{3\pm\delta}$ of technological interest generally have lanthanum or praseodymium on the A-site and chromium, manganese, iron, cobalt or nickel on the B-site. The stability of the perovskites in a range of oxygen activities is dependent primarily upon the B-site cation. Chromium has the widest range of stability, then manganese, iron, cobalt and lastly nickel. However, all these perovskites are subject to oxygen loss from the lattice in certain temperature and pO_2 regimes.

These nonstoichiometric perovskites are in chemical equilibrium with their surroundings, thus a change in the pO_2 or temperature may introduce cation or anion vacancies. Equation 3.3 shows the formation of oxygen vacancies as the pO_2 is decreased and equation 3.4. shows the formation of cation vacancies (i.e. going to oxygen superstoichiometry) as the pO_2 is increased. In both equations, Kröger-Vink [7] notation is used.

$$2La_{La}^{\times} + 2Co_{Co}^{\times} + 6O_O^{\times} \Leftrightarrow 2La_{La}^{\times} + 2Co_{Co}' + 5O_O^{\times} + V_O^{\bullet\bullet} + \tfrac{1}{2}O_2 \quad \text{eqn. (3.3)}$$

$$\tfrac{3}{2}O_2 + 6La_{La}^{\times} + 6Co_{Co}^{\times} + 18O_O^{\times} \Leftrightarrow 6La_{La}^{\times} + 6Co_{Co}^{\bullet} + 21O_O^{\times} + V_{La}''' + V_{Co}''' \text{ eqn. (3.4)}$$

These redox reactions occur readily due to the ease with which the transition metal cation can change its valence from 3^+ to 2^+ or 4^+.

As stated previously, the electronic and crystallographic properties of the material can be changed radically by the introduction of a dopant cation. When the A-site ion of a perovskite is substituted with a lower valence cation, two compensation regimes are possible: one where oxygen vacancies balance the effective negative charge introduced by the dopant (vacancy compensation); and the other where the balance is by holes (electronic compensation). Alternatively, both can occur simultaneously (mixed compensation).

$$2(SrCoO_3) \xrightarrow{2(LaCoO_3)} 2Sr'_{La} + 2Co^{x}_{Co} + V^{\bullet\bullet}_{O} + 5O^{x}_{O} + \tfrac{1}{2}O_2 \quad \text{eqn. (3.5)}$$

$$(SrCoO_3) \xrightarrow{(LaCoO_3)} Sr'_{La} + Co^{\bullet}_{Co} + 3O^{x}_{O} \quad \text{eqn. (3.6)}$$

$$4(SrCoO_3) \xrightarrow{2(LaCoO_3)} 4Sr'_{La} + 2Co^{x}_{Co} + 2Co^{\bullet}_{Co} + V^{\bullet\bullet}_{O} + 11O^{x}_{O} + \tfrac{1}{2}O_2 \quad \text{eqn. (3.7)}$$

In all cases charge neutrality and mass and site balance must be observed.

As well as the introduction of charged defects into the crystal lattice, which will lead to changes in the electrical behaviour of the material, the replacement of a given cation by another of different size will alter the crystallographic structure of the compound resulting in distortion of the structure (e.g. cubic to rhombohedral).

Many interesting $R_ET_MO_{3\pm\delta}$ perovskites exist in the mixed compensation regime at atmospheric oxygen activity where the A ion is a lanthanide and the B site is occupied by a transition element such as manganese [8,9,10,11], iron [12,13,14,15] or cobalt [16,17,18,19,20,21].

As previously mentioned, even though the presence of defects introduces localised charges, charge neutrality of the crystal must be preserved. Charge neutrality for an acceptor doped perovskite can be expressed by equation 3.8. Due to their high formation energy, interstitial sites are not included.

$$n + 3[V'''_A] + 3[V'''_B] + [AL'_A] = p + 2[V^{\bullet\bullet}_O] \quad \text{eqn. (3.8)}$$

AL represents an alkaline earth such as strontium or calcium, n and p are the concentrations of electrons and holes respectively.

The concentration of defects present in a perovskite is dependent on many factors such as temperature and oxygen activity as well as the concentration of artificial impurity added. In order to work out the concentration of any given defects present in the crystal, some assumptions must be made. The system derived by Brouwer assumes that under any equilibrium condition only one particular defect species dominates on each side of the charge neutrality equation, (3.8) [22].

3.4. Brouwer Diagrams.

The Brouwer diagram is a plot of the logarithm of concentration of point defects as a function of the logarithm of partial pressure of oxygen. It is split into different regions depending on the dominant defect present in the crystal at any given pO_2.

The Brouwer diagram shown below in figure 3.2 is taken from the work of Anderson [16] for an acceptor doped perovskite such as $LaCoO_{3\pm\delta}$ where p-type disorder prevails. The other assumptions made are that the A to B-site ratio is constant and unity such that $\left[V_A'''\right]=\left[V_B'''\right]$, the acceptor dopant, M, on the A-site has a 2^+ charge and that the predominant intrinsic disorder is of Schottky and electronic type (i.e. no interstitial sites are present).

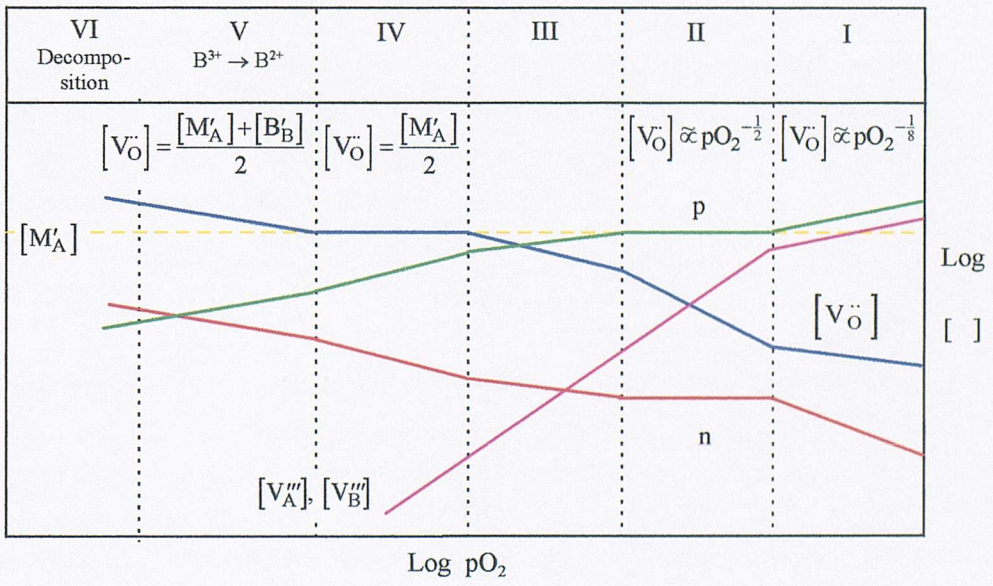


Figure 3.2. Brouwer diagram of an acceptor doped perovskite [16].

The concentrations of defects can be multiplied by their respective mobilities to give a partial conductivity diagram as a function of pO_2. In general the mobilities of the conducting species follow $\mu_n, \mu_p > \mu_{V_O^{\bullet\bullet}} > \mu_{V_A^{'''}}, \mu_{V_B^{'''}}$, where μ_i is the mobility of species i. This means if figure 3.2. were converted to a partial conductivity plot the p and n curves would be shifted up, the $V_A^{'''}, V_B^{'''}$ curve shifted down and the $V_O^{\bullet\bullet}$ remain at the same relative level.

It is clear that irrespective of the pO_2 the dopant concentration remains constant. However, only in region IV does the dopant concentration solely control the concentration of oxygen vacancies. If the concentration and mobility of vacancies in this regime is sufficient that the transport of vacancies dominates the conduction process then this is called the ionic or electrolytic domain of the material. In electrolyte materials, the range of pO_2 over which the ionic domain spans is critical to their use as candidate materials for SOFC. However, for mixed conducting perovskites to be used for cathodes or dense oxygen separation membranes the material should not be in this domain.

In region I of figure 3.2., where the oxygen partial pressure is high, the material becomes oxygen superstoichiometric, such that the dominant defect is cation vacancies. These are compensated by the presence of electron holes so the electroneutrality condition becomes,

$$p = 3\left[V_A^{'''}\right] + 3\left[V_B^{'''}\right] \qquad \text{eqn. (3.9)}$$

In this region the conductivity will be predominately p-type and controlled by the pO_2 of the gas. In region II, the concentration of cation vacancies decreases such that the dominant defect becomes the dopant cation. Therefore the electroneutrality condition becomes,

$$p = \left[M_A^{'}\right] \qquad \text{eqn. (3.10)}$$

In this region the conductivity is still predominately p-type but is now independent of pO_2. Further reduction of the pO_2 leads to a region where the concentration of oxygen vacancies increases to a level where they are no longer trivial and it is therefore not appropriate to assume only one defect is predominant. The electroneutrality condition in region III thus becomes,

$$p + 2\left[V_O^{\bullet\bullet}\right] = \left[M_A^{'}\right] \qquad \text{eqn. (3.11)}$$

In region III both the concentration of holes and vacancies show a dependence on pO_2. The concentration of holes increases with increasing pO_2 and the concentration of oxygen vacancies decreases with increasing pO_2. Although the concentrations are plotted as straight lines in figure 3.2, it is more likely that they will curve in this region. At the lower pO_2 end of region III, the change in concentration of vacancies will tend towards zero, until region IV is reached where the concentration of vacancies reaches the dopant concentration. In region IV the electroneutrality condition is thus represented by equation 3.12.

$$2\left[V_O^{\bullet\bullet}\right] = \left[M_A^{'}\right] \qquad \text{eqn. (3.12)}$$

When the partial pressure of oxygen is reduced further, the perovskite will lose oxygen from the lattice and the transition metal cation (the B-site species) will undergo partial reduction, i.e.

$$2B_B^{\times} + 3O_O^{\times} \rightarrow 2B_B^{'} + V_O^{\bullet\bullet} + 2O_O^{\times} + \tfrac{1}{2}O_2 \qquad \text{eqn. (3.13)}$$

This is illustrated by region V in figure 3.2. The concentration of vacancies can be expressed as equation 3.14.

$$2\left[V_O^{\bullet\bullet}\right] = \left[M_A^{'}\right] + \left[B_B^{'}\right] \qquad \text{eqn. (3.14)}$$

However at the lower pO_2 end of region V, $\left[B_B^{'}\right] >> \left[M_A^{'}\right]$ such that equation 3.14 becomes,

$$2\left[V_O^{\bullet\bullet}\right] \cong \left[B_B^{'}\right]$$

As the concentration of B^{2+} cations increases the perovskite structure becomes unstable until region VI is reached where the perovskite decomposes into its different constituent components. The partial pressure of oxygen where breakdown occurs is strongly dependent upon the B-site cation. Table 3.1. shows the pO_2 at which various $LaT_MO_{3\pm\delta}$ perovskites undergo decomposition. Acceptor doping on the A-site introduces further oxygen vacancies and thus will increase the pO_2 at which decomposition occurs [16,23]. (The increase in

oxygen substoichiometry due to acceptor doping is illustrated in figures 3.4 and 3.5.)

Perovskite Species	$-\log_{10}(pO_2^{decomposition}/atm)$ @ 1000°C
$LaNiO_{3\pm\delta}$	0.6
$LaCoO_{3\pm\delta}$	7.0
$LaMnO_{3\pm\delta}$	15.05
$LaFeO_{3\pm\delta}$	16.95
$LaCrO_{3\pm\delta}$	>20

Table 3.1. Stability of transition metal perovskites with respect to pO_2 at 1000°C (from [23,24]).

As can be seen from table 3.1, the nickel based perovskite is the least stable at 1000°C. Decomposition starts at a pO_2 sufficiently high to render $LaNiO_3$ redundant for use as a cathode material in a SOFC. $LaCoO_3$ is the next least stable. However, decomposition does not start until around 10^{-7} atmospheres of oxygen, and so the material is suitable for use as a cathode [24,25,26,]. Lanthanum manganite [24,27,28] and lanthanum ferrite [24] are stable over a significantly larger pO_2 range. Lanthanum chromite shows no signs of decomposition down to $pO_2<10^{-20}$ atm [23].

From the Brouwer diagram it is possible to estimate the degree of oxygen nonstoichiometry in these acceptor doped perovskites [16,29]. The concentration of vacancies can be transferred to the term δ in the chemical formula $LaBO_{3\pm\delta}$. Figure 3.3 is a graph of the oxygen nonstoichiometry as a function of pO_2 for a typical transition metal perovskite [16].

At high oxygen partial pressures the concentration of oxygen vacancies is small. However, cation vacancies can be present to an extent such that the material is superstoichiometric, as illustrated in region I of figure 3.3. As the pO_2 is decreased the concentration of cation vacancies decreases until stoichiometry is reached (i.e. $\delta=0$). In this region the atomic defects are in the minority and the concentration of electronic defects is independent of pO_2, i.e. region II. If the material is further reduced, oxygen vacancies will be formed to a significant level and so the material will appear substoichiometric, i.e. region III. In this region, there is a transfer from electronic compensation to ionic compensation, until region IV is reached. In region IV the compensation for the dopant cation is

provided solely by the formation of oxygen vacancies, such that $2[V_O^{\bullet\bullet}]=[M'_A]$. Hence δ is again independent of pO_2. In region V, the partial reduction of the B-site cation leads to the formation of further oxygen vacancies as represented previously by equation 3.13.

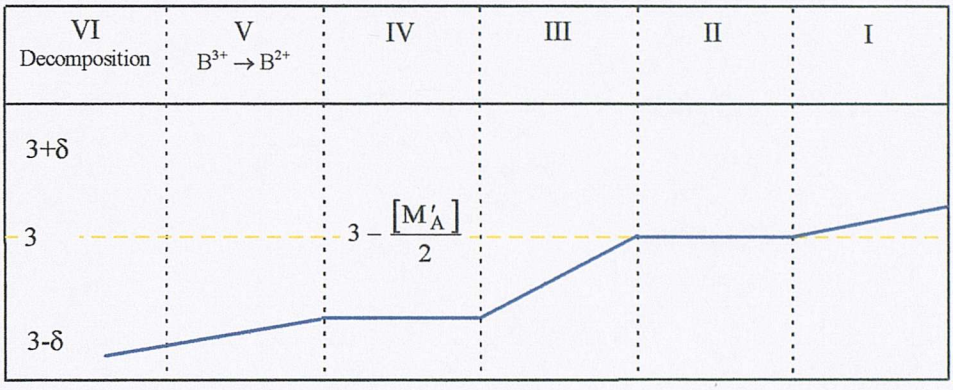


Figure 3.3. Theoretical nonstoichiometric behaviour of an acceptor doped transition metal perovskite [16].

Most perovskites do not undergo all regions given in figure 3.3 in a normal operating range of oxygen partial pressure. Figures 3.4, 3.5, and 3.6 show examples of the nonstoichiometric behaviour of several perovskites. Figure 3.4 illustrates $La_{1-x}Sr_xCoO_{3\pm\delta}$ as a function of x [25], figure 3.5 shows $La_{1-x}Sr_xMnO_{3\pm\delta}$ as a function of x [23] and figure 3.6. shows $La_{0.9}Sr_{0.1}B_{3\pm\delta}$ (B=Cr, Fe, Mn, Co) [23,25,30,31].

Several interesting features can be seen from figure 3.6. The most notable is that none of the four perovskites shown exhibit all the regions depicted in figure 3.3. Lanthanum manganite shows the oxygen superstoichiometry associated with region I, then as the pO_2 is decreased cation vacancies are consumed until the material is in the stoichiometric regime (region II). The material then enters region III as a transference from electronic to ionic compensation occurs. However, the material does not appear to enter region IV where purely ionic compensation for the dopant cation occurs. This is because the Mn^{3+} cation has already started to reduce to its 2^+ state and hence a direct transfer from region III to region V occurs. Decomposition then occurs shortly afterwards. The cobaltite material behaves in the same way as the manganite except that in the pO_2 range examined in this work the material does not become superstoichiometric.

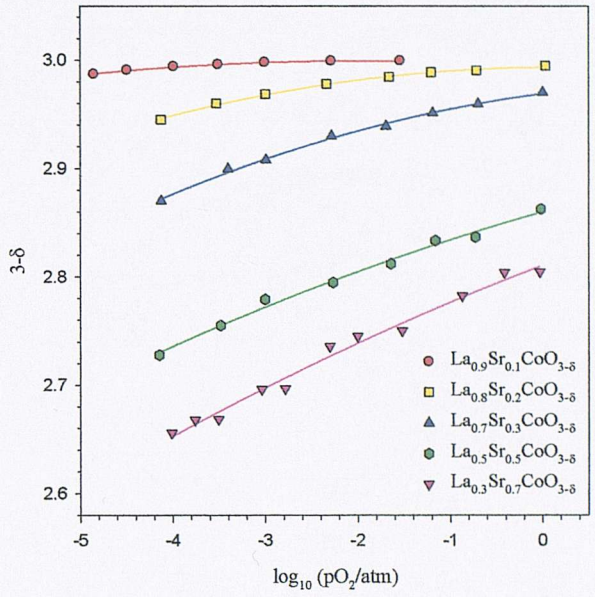


Figure 3.4. Oxygen content of $La_{1-x}Sr_xCoO_{3\pm\delta}$ as a function of pO_2 at 800°C [25].

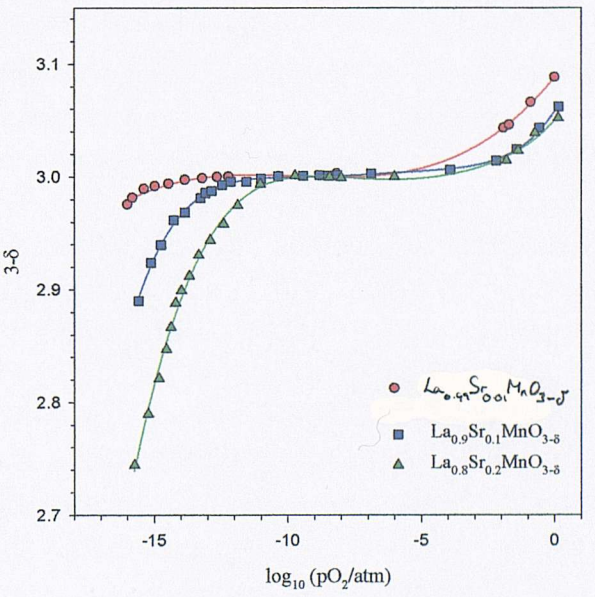


Figure 3.5. Oxygen content of $La_{1-x}Sr_xMnO_{3\pm\delta}$ as a function of pO_2 at 1000°C [23].

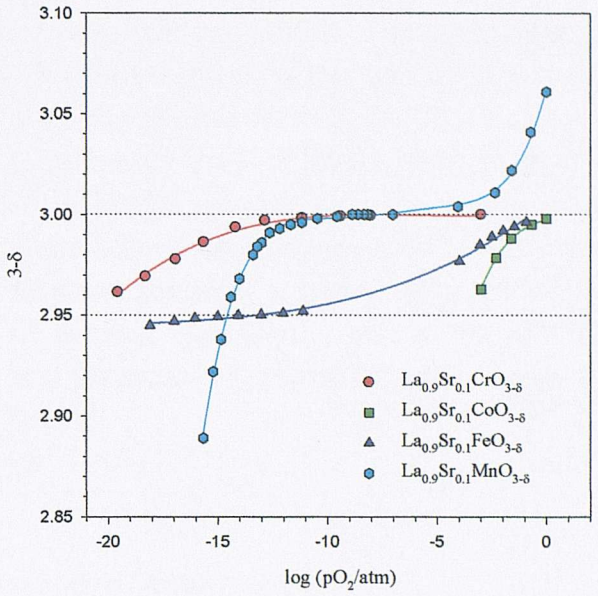


Figure 3.6. Oxygen content of $La_{0.9}Sr_{0.1}BO_{3\pm\delta}$ as a function of pO_2 at 1000°C [23,25,30,31] (B = Cr,Fe,Mn,Co).

Lanthanum ferrite also does not exhibit superstoichiometry within the range of pO_2 examined. It does however show the second plateau where $2\left[V_O^{\bullet\bullet}\right]=\left[M_A^{'}\right]$ before the Fe^{3+} reduces to Fe^{2+}. Lanthanum chromite shows the broadest range of oxygen stoichiometry, from pO_2 = 1 to ~10^{-12} atmospheres. It also appears to approach the ionic plateau, however this is not reached in figure 3.6.

The other important difference seen between the theoretical behaviour shown in figure 3.2 and experimental data in figure 3.6 is the experimental data shows a gradual change between regimes whereas the Brouwer diagram shows a dramatic change at each region. This is because of the assumption made in using the Brouwer diagram that only one defect is dominant in each regime. However, this is not the case as a gradual change in concentration of cation vacancies, oxygen vacancies and electronic defects occurs leading to regions where, for example $p=\left[V_O^{\bullet\bullet}\right]$ as may occur in region III. However, despite this fact, the four transition metal perovskites discussed here are well described by Brouwer behaviour.

As well as doping on the A-site, doping on the B-site can also be used. The mass transport and electronic properties can be radically affected as well as the crystallographic structure and the chemical stability of the resultant perovskite.

Most of the transition metal cations are fully interchangeable, with no limitation on their solubility. The most common of this type of perovskite is a cobalt doped lanthanum ferrite, with the general formula $La_{1-x}Sr_xCo_{1-y}Fe_yO_{3\pm\delta}$. This class of material has come to be known as LSCF [29,32,33,34,35,36,37]. Another system that has been studied is $La_{1-x}Sr_xCo_{1-y}Mn_yO_{3\pm\delta}$ [38,39,40]. Both these materials show the high catalytic activity and oxygen mobility associated with acceptor doped lanthanum cobaltate but show a greater degree of chemical stability and lower coefficient of thermal expansion. Further alterations to the chemical structure and electrical properties of perovskites can be made by altering the A to B-site cation ratio [34,35].

3.5. Fluorite Crystal Structure.

A fluorite material has the general formula MO_2 where M is a 4^+ cation such as zirconium, cerium or uranium. The fluorite crystal structure, represented in figure 3.7, has a simple cubic packing of the oxygen ions with the cation in eightfold co-ordination. In order to form the fluorite structure the minimum ratio of the cation radius to oxygen ion radius is 0.732. Because of this, very few single element oxides exist with cubic symmetry, most being distorted to some extent. For example ZrO_2 is monoclinic at room temperature, although it does form a cubic structure above 2370°C [41]. The cubic symmetry can be obtained by acceptor doping with an aliovalent cation. In the case of zirconia, the addition of Y_2O_3, Sm_2O_3, Sc_2O_3 or CaO to the solution reduces the degree of distortion from cubic symmetry. With yttria stabilised zirconia (YSZ, $Zr_{1-x}Y_xO_{2-\delta}$), cubic symmetry is reached at $x \approx 0.16$ [41,42]. Pure CeO_2 is cubic at room temperature [43] and is able to accommodate significant levels of acceptor doping with a variety of rare earth elements without apparent distortion from cubic symmetry.

Of all the fluorite materials, acceptor doped zirconias are the most widely studied. This is due to many factors including excellent chemical stability over a large range of pO_2 [43,44], high ionic conductivity [45,46] and negligible electronic conductivity [47,48] over this range of pO_2 and good mechanical strength [49,50]. The reason for the large range of stability and low electronic conductivity is the high energy associated with reducing the zirconium cation, i.e.

$$2Zr_{Zr}^{\times} + 4O_O^{\times} \rightarrow 2Zr_{Zr}^{'} + 3O_O^{\times} + V_O^{\bullet\bullet} + \tfrac{1}{2}O_2 \qquad \text{eqn. (3.15)}$$

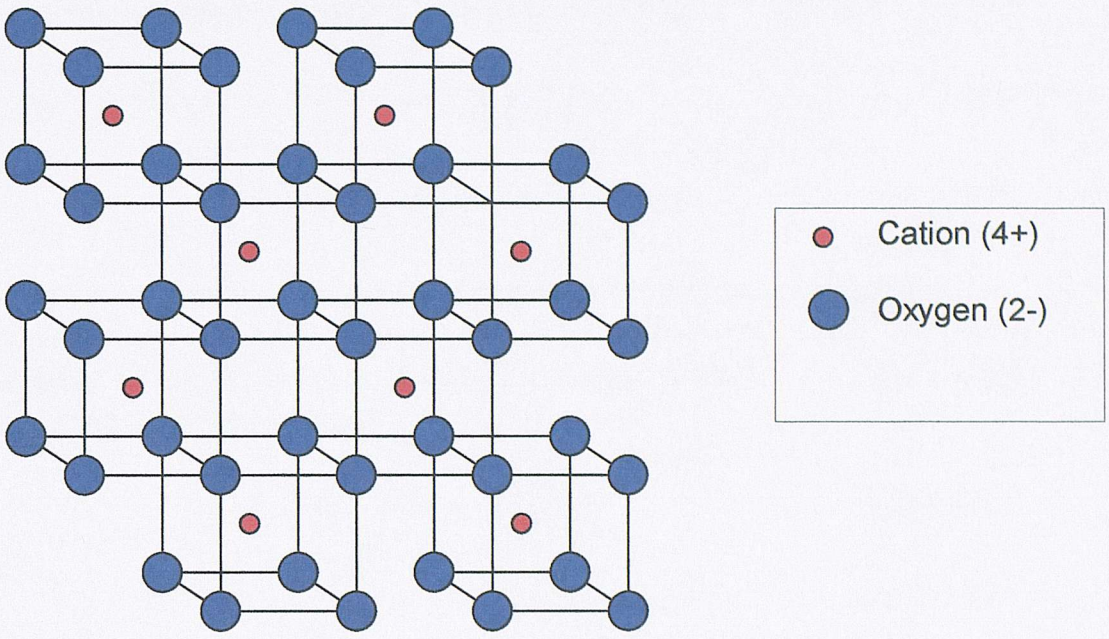


Figure 3.7. Crystal structure of the fluorite crystal structure.

In the case of ceria, the reduction of the Ce^{4+} to Ce^{3+} occurs much more readily and so the defect chemistry of these materials can be more complex. The defect structure and nonstoichiometry of acceptor doped fluorite materials is discussed in the next section.

3.6. Nonstoichiometry and Defect Chemistry of Acceptor Doped Fluorites.

In a fluorite material several types of intrinsic disorder can occur to a greater or lesser extent. These are Schottky, electronic and anti-Frenkel disorder. These processes can be represented by equations 3.16, 3.17 and 3.18, respectively.

$$\text{"null"} \rightarrow V_M^{''''} + 2V_O^{\bullet\bullet} \qquad \text{eqn. (3.16)}$$

$$\text{"null"} \rightarrow e' + h^{\bullet} \qquad \text{eqn. (3.17)}$$

$$O_O^{\times} \rightarrow O_i^{''} + V_O^{\bullet\bullet} \qquad \text{eqn. (3.18)}$$

In this examination of the defect structure of acceptor doped fluorites, Frenkel disorder is considered insignificant.

The respective equilibrium constants for equations 3.16 and 3.17 (K_S and K_e) are:

$$K_S = \left[V_M^{''''}\right] \cdot \left[V_O^{\bullet\bullet}\right]^2 \qquad \text{eqn. (3.19)}$$

$$K_e = np \qquad \text{eqn. (3.20)}$$

The charge compensation regime can be altered under different pO_2 regimes. In an oxidising environment, electron holes are introduced which can be compensated by either metal vacancies or oxygen interstitials. These are represented by equations 3.19 and 3.20.

$$O_2 \rightarrow 2O_O^{\times} + V_M^{''''} + 4h^{\bullet} \qquad \text{eqn. (3.21)}$$

$$\tfrac{1}{2}O_2 \rightarrow O_i^{''} + 2h^{\bullet} \qquad \text{eqn. (3.22)}$$

The respective equilibrium constants are,

$$K_{OX1} = \frac{\left[V_M^{''''}\right]p^4}{pO_2} \qquad \text{eqn. (3.23)}$$

$$K_{OX2} = \frac{\left[O_i^{''}\right]p^2}{pO_2^{\frac{1}{2}}} \qquad \text{eqn. (3.24)}$$

However, the formation of oxygen interstitials is considered more likely given anti-Frenkel disorder. In a reducing atmosphere electrons are generated which are compensated by oxygen vacancies or metal interstitials. These are shown in equations 3.25 and 3.26.

$$O_O^{\times} \rightarrow V_O^{\bullet\bullet} + 2e' + \tfrac{1}{2}O_2 \qquad \text{eqn. (3.25)}$$

$$M_M^{\times} + 2O_O^{\times} \rightarrow M_i^{\bullet\bullet\bullet\bullet} + 4e' + O_2 \qquad \text{eqn. (3.26)}$$

The production of oxygen vacancies is energetically more favourable than the generation of metal interstitials and so equation 3.25 dominates. The equilibrium constant for equation 3.25 is,

$$K_{RE} = \left[V_O^{\bullet\bullet}\right] n^2 pO_2^{1/2} \qquad \text{eqn. (3.27)}$$

When the fluorite is reduced oxygen loss from the lattice is accompanied by a change in valence of the host cation. It should be noted that aside from introducing electronic conduction into the material the loss of oxygen also causes expansion of the lattice leading to significant chemically induced stresses [51,52].

When a fluorite material such as zirconia or ceria is doped with an acceptor cation of a 3^+ (or 2^+) charge, the effectively negative species must be charge compensated by an effectively positive species. There are three possible defect models whereby this can occur. The first is a cation interstitial compensation, the second is oxygen vacancy compensation and third is a mixed compensation. Interstitial compensation is shown in equation 3.28 and vacancy compensation represented by equation 3.29.

$$A_2O_3 \xrightarrow{MO_2} A_M^{'} + 2O_O^{x} + A_i^{\bullet} + \tfrac{1}{2}O_2 \qquad \text{eqn. (3.28)}$$

$$A_2O_3 \xrightarrow{MO_2} 2A_M^{'} + 3O_O^{x} + V_O^{\bullet\bullet} \qquad \text{eqn. (3.29)}$$

It is generally acknowledged that oxygen vacancies are the primary form of charge compensation in both acceptor doped zirconia and ceria as the presence of large concentrations of vacancies has been established [53,54,55].

As is the case with the perovskites a general electroneutrality equation involving the above defects can be produced, given by equation 3.30.

$$\left[A_M^{'}\right] + 2\left[O_i^{''}\right] + n = 2\left[V_O^{\bullet\bullet}\right] + p \qquad \text{eqn. (3.30)}$$

The formation energy associated with $M_i^{\bullet\bullet\bullet\bullet}$ and $V_M^{''''}$ is large enough that their concentration is not expected to be significant. They have thus been excluded from the electroneutrality equation.

The concentration of defects is dependent upon temperature, oxygen activity and the concentration of dopant added. Again, as with the perovskite system, to calculate the concentration of any given defects present in the crystal, Brouwer assumptions must be made such that under any equilibrium condition only one

particular defect is dominant on each side of equation 3.30. The system is again divided into a series of pO_2 regimes where one defect may dominate and an appropriate Brouwer diagram can be derived.

3.7. Brouwer Diagrams of Acceptor Doped Fluorites.

The acceptor doped fluorites generally exist in four different regimes depending on the partial pressure of oxygen. In very high oxygen partial pressures (region I) the dominant defects are oxygen interstitials and electron holes such that,

$$2[O_i''] = p \qquad \text{eqn. (3.31)}$$

Equations 3.24 and 3.31 can be rearranged to give the concentration of holes and oxygen interstitials, such that,

$$p = (2K_{OX2})^{1/3} . pO_2^{1/6} \qquad \text{eqn. (3.32)}$$

$$[O_i''] = (1/4 K_{OX2})^{1/3} . pO_2^{1/6} \qquad \text{eqn. (3.33)}$$

It is thus clear that both defects will follow a $pO_2^{1/6}$ dependence.

The concentration of minor defects can be calculated from the equilibrium constants to give,

$$n = \frac{K_e}{(2K_{ox})^{1/3}} \cdot pO_2^{-1/6} \qquad \text{eqn. (3.34)}$$

$$[V_O^{\bullet\bullet}] = \frac{K_{RE} \cdot (2K_{ox})^{2/3}}{K_e^{\,2}} \cdot pO_2^{-1/6} \qquad \text{eqn. (3.35)}$$

As the oxygen partial pressure is reduced, a controlled valence regime (region II) will exist. The concentration of holes will reduce to an extent that they are now controlled by the concentration of the dopant cation, such that,

$$\left[A'_M\right] = p \qquad \text{eqn. (3.36)}$$

Again the concentration of the minor defects can be expressed in terms of the various equilibrium constants.

$$n = \frac{K_e}{\left[A'_M\right]} \qquad \text{eqn. (3.37)}$$

$$\left[O''_i\right] = \frac{K_{OX}}{\left[A'_M\right]^2} \cdot pO_2^{1/2} \qquad \text{eqn. (3.38)}$$

$$\left[V_O^{\bullet\bullet}\right] = \frac{K_{RE}\left[A'_M\right]^2}{K_e^{\,2}} \cdot pO_2^{-1/2} \qquad \text{eqn. (3.39)}$$

In this regime the concentration of oxygen vacancies will increase with decreasing partial pressure until region III is reached where the concentration of oxygen vacancies is controlled by the dopant. In this region equation 3.40 holds.

$$\left[A'_M\right] = 2\left[V_O^{\bullet\bullet}\right] \qquad \text{eqn. (3.40)}$$

In this region the concentration of oxygen vacancies and hence the ionic conductivity is independent of pO_2. Since the dominant defects in this region are oxygen vacancies, the material is essentially a pure ionic conductor with the ionic transference number tending to unity.

The concentration of electrons and holes in this region can be expressed as,

$$n = \left(\frac{2K_{RE}}{\left[A'_M\right]}\right)^{1/2} pO_2^{-1/4} \qquad \text{eqn. (3.41)}$$

$$p = K_e\left(\frac{2K_{RE}}{\left[A'_M\right]}\right)^{-1/2} pO_2^{1/4} \qquad \text{eqn. (3.42)}$$

The concentration of oxygen interstitials is,

$$\left[O_i''\right] = \frac{2K_{RE}K_{OX}}{K_e^{\,2}\left[A_M'\right]} \qquad \text{eqn. (3.43)}$$

As the oxygen partial pressure is decreased still further and the lattice reduces, the concentration of oxygen vacancies will increase beyond that provided by the dopant and electrons will become the dominant defect. This is represented by equation 3.39.

$$n = 2\left[V_O^{\bullet\bullet}\right] \qquad \text{eqn. (3.44)}$$

The concentration of electrons and oxygen vacancies are given in equations 3.45 and 3.46.

$$n = \left(2K_{RE}\right)^{1/3} \cdot pO_2^{\,-1/6} \qquad \text{eqn. (3.45)}$$

$$\left[V_O^{\bullet\bullet}\right] = \left(\tfrac{1}{4}K_{RE}\right)^{1/3} \cdot pO_2^{\,-1/6} \qquad \text{eqn. (3.45)}$$

The electron hole and oxygen interstitial concentration can be expressed thus,

$$p = K_e\left(2K_{RE}\right)^{-1/3} \cdot pO_2^{\,1/6} \qquad \text{eqn. (3.46)}$$

$$\left[O_i''\right] = \frac{K_{OX}\left(2K_{RE}\right)^{2/3}}{K_e^{\,2}} \cdot pO_2^{\,1/6} \qquad \text{eqn. (3.47)}$$

From equations 3.32 to 3.47 a Brouwer diagram for a typical acceptor doped fluorite can be constructed. This is illustrated in figure 3.8.

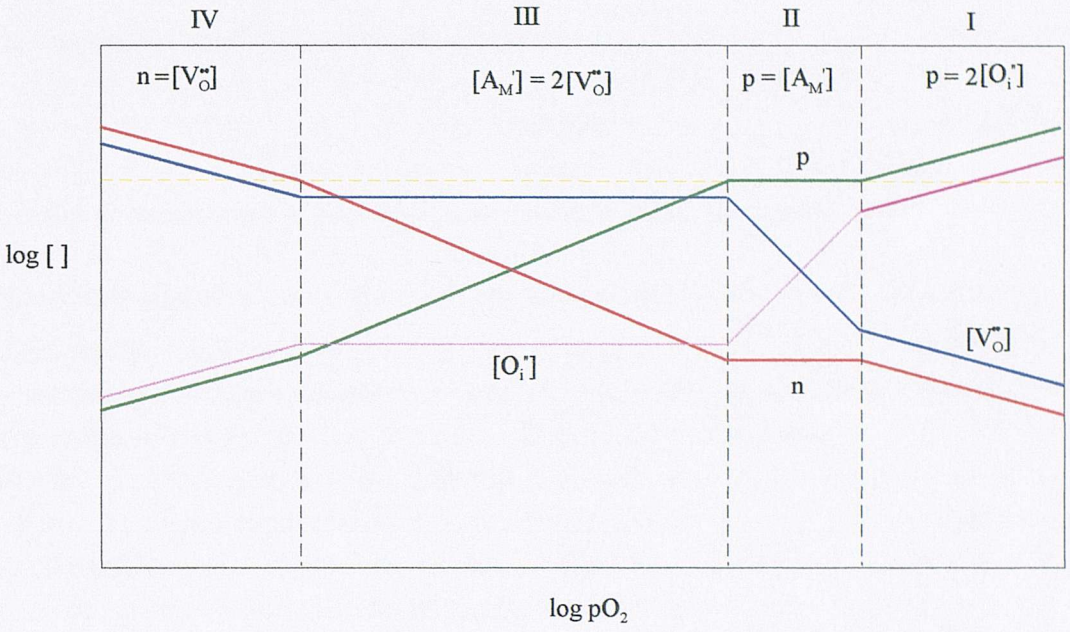


Figure 3.8. Brouwer diagram of an acceptor doped fluorite.

From the Brouwer diagram an a knowledge of the mobilities of the respective defects, a partial conductivity diagram can be drawn.

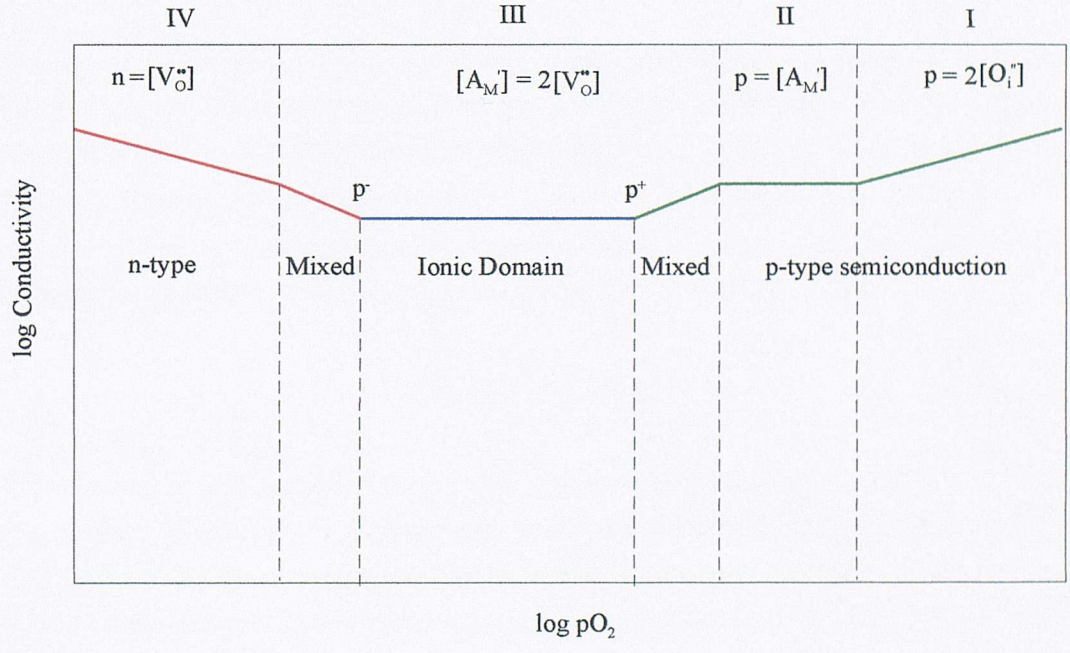


Figure 3.9. Partial conductivity graph of an acceptor doped fluorite.

The conductivity of each species is given by,

$$\sigma_i = n_i z_i e \mu_i \qquad \text{eqn. (3.48)}$$

n_i is the concentration of species i, z_i is its valence and μ_i its mobility.

The points p^- and p^+ on figure 3.9 are the points where $\sigma_i = \sigma_n$ and $\sigma_i = \sigma_p$, respectively. The pO_2 at which the p^- and p^+ points occur is critical in determining a suitable material for a SOFC where the electrolyte is subjected to vast range of oxygen partial pressure. One of the main problems with CGO is that the p^- point occurs at a relatively high pO_2 and so the material starts to become an n-type semiconductor at the anode side of the fuel cell. It should be noted that the useful electrolytic domain is smaller than the range between p^- and p^+ since at these points the ionic transference number is 0.5. To minimise the energy loss due to electronic conduction the ionic transference number should approach unity.

3.8. Defect Association in Fluorites.

The above discussion of the nonstoichiometry of fluorites assumes a random distribution of non-interacting defects. However, the magnitude of dopant material added to the fluorites makes this unlikely. The equation for acceptor doping a fluorite given as equation 3.29, shows the formation of A'_M and $V_O^{\bullet\bullet}$ defects. Due to Coulombic and elastic attractive forces between these two defects, the presence of two associates can be postulated, i.e.

$$\left(A'_M V_O^{\bullet\bullet}\right)^{\cdot} \text{ or } \left(A'_M V_O^{\bullet\bullet} A'_M\right)^{\times}$$

The charged defect is more likely to occur due to the random distribution of the A'_M defect. However, at high dopant concentrations both defects are probable. The presence of these defect associates can significantly affect the concentration of free vacancies and hence reduce the ionic conduction within the material [56]. At higher defect concentrations more complex defect clusters can form and ordered microdomains of second phases can form a homogeneous, essentially vacancy free matrix. For example in YSZ a long range ordered domain of $Zr_3Y_4O_{12}$ is known to form [57,58].

There is an observed decrease in the ionic conductivity as the defect concentration is increased in both doped zirconias and cerias [56,59,60] and this has been attributed to the trapping of oxygen vacancies in these clusters. The vacancies are not immobile but have an association energy which they must overcome to take part in conduction. The data of Ralph and Kilner [59] showing the conductivity of gadolinia doped ceria as a function of gadolinia content is shown in figure 3.10. This shows first an increase in the conductivity with dopant concentration as the concentration of vacancies is increased, followed by a subsequent decrease in the conductivity as the vacancies are trapped in defect associates.

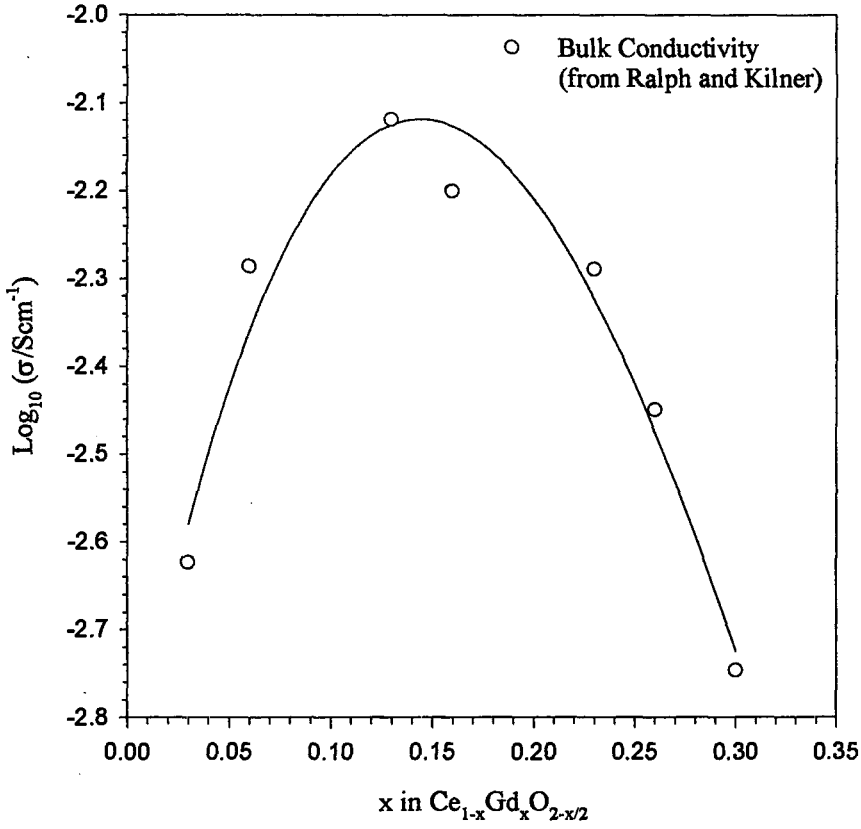


Figure 3.10. Graph of the conductivity of gadolinia doped ceria as a function of gadolinia content at 500°C.

Kilner *et al* [61] have shown that the binding enthalpy of an associate can significantly affect the population of free vacancies. The concentration of free vacancies can be calculated following the methods given by Kilner *et al* [61] and Manning *et al* [62].

The free vacancy population is controlled by the dissociation of the charged associate i.e.

$$(A'_M V_O^{\cdot\cdot})^{\cdot} \leftrightarrow A'_M + V_O^{\cdot\cdot} \qquad \text{eqn. (3.49)}$$

which gives the mass action equation

$$[A'_M][V_O^{\cdot\cdot}] / [(A'_M V_O^{\cdot\cdot})^{\cdot}] = W^{-1} \exp(-\Delta H_A / kT) = E / W \qquad \text{eqn. (3.50)}$$

Where ΔH_A is the associate binding enthalpy, E represents the exponential term, and W represents the number of possible defect orientations. The terms in the square brackets represent site fractions. It is easier to use site fractions at this point as they can be directly used in calculations of diffusivity.

The electroneutrality condition is

$$2[V_O^{\cdot\cdot}]\tfrac{1}{2}m + [(A'_M V_O^{\cdot\cdot})^{\cdot}] = [A'_M] \qquad \text{eqn. (3.51)}$$

where the term m represents the oxygen to metal ratio to maintain site balance.

The total concentration of dopant C_M, is constant, thus

$$[A'_M] + [(A'_M V_O^{\cdot\cdot})^{\cdot}] = C_M \qquad \text{eqn. (3.52)}$$

At low temperatures where association is almost complete eqn. 3.51 is approximated so that

$$[V_O^{\cdot\cdot}] << [(A'_M V_O^{\cdot\cdot})^{\cdot}]$$

which leads to

$$[V_O^{\cdot\cdot}] = E / W \qquad \text{eqn. (3.53)}$$

and so the oxygen vacancy concentration is independent of dopant concentration. At higher temperatures, this approximation is no longer valid and so eqns 3.52, 3.51 and 3.50 are combined to eliminate $[(A'_M V_O^{\cdot\cdot})^{\cdot}]$ and $[A'_M]$ to give,

$$[V_O^{\cdot\cdot}]^2 + [V_O^{\cdot\cdot}]\left(\frac{C_M}{m} + \frac{E}{W}\right) - \left(\frac{C_M E}{mW}\right) = 0 \qquad \text{eqn. (3.54)}$$

The solution to which is

$$[V_O^{\cdot\cdot}] = -\frac{1}{2}\left(\frac{C_M}{m} + \frac{E}{W}\right) + \frac{1}{2}\sqrt{\left(\frac{C_M}{m} + \frac{E}{W}\right)^2 - \frac{4C_M E}{mW}} \qquad \text{eqn. (3.55)}$$

Thus if the binding enthalpy for association is known, the concentration of free vacancies can be calculated as a function of temperature. The presence of defect associates is very important in determining the ionic conductivity of fluorite materials (as illustrated by figure 3.10) and thus it is important to know their concentration as a function of temperature. Equation 3.55 can be coupled with the equation for ionic conductivity (given in the following chapter) to determine the migration and association enthalpy of fluorite materials. A more complete understanding of the relative importance of the migration and association enthalpy are required in order to further advance the ionic conductivities of these materials.

3.9. References.

[1] N. Ramadass, Mat. Sci. Eng. **Vol 36** (1978) p231.

[2] R.D. Shannon, Acta Crystallogr. **Vol A32** (1976) p751.

[3] Y.Q. Jia, J. Solid State Chem. **Vol 95** (1991) p184.

[4] V.M. Goldshmidt, Skr. Nor. Vidensk. Akad. Oslo, **Vol 2** (1926).

[5] L. Tejuca, J.L.G. Fierro, Advances in Catalysts, **Vol 36** p237.

[6] C. Wagner and W. Schottky, Z. Phys. Chem., B11, (1931) p163.

[7] F.A Kröger, H.J. Vink, in Solid State Physics, eds. F. Seitz and D. Turnbill, **Vol 3** (Academic Press, New York, 1965) p307.

[8] H.U. Anderson, Solid State Ionics **Vol 52** (1992) p33.

[9] J. Mizusaki, H. Tagawa, K. Naraya, T. Sasamoto, Solid State Ionics **Vol 49** (1991) p111.

[10] R.A. De Souza, J.A. Kilner, B.C.H. Steele, in Supplement & Corrections to the Proc. of the 4th SOFC Conference, Yokohama, (1995).

[11] I. Yasuda, M. Hishinuma, in Proc. of the 2nd Int. Symp. On Ionic and Mixed Conducting Ceramics, Eds. T.A. Ramanarayanan, W.L. Worrel and H.L. Tuller, The Electrochemical Society, Inc., Pennington, NJ, **PV 94-12**, (1994) p209.

[12] B.A. van Hassel, T. Kawada, N. Sakai, H. Yokokawa, M. Dokiya, H.J.M. Bouwmeester, Solid State Ionics **Vol 66** (1993) p295.

[13] T. Ishigaki, S Yamauchi, K. Kishio, J. Mizusaki, K. Fueki, J. Solid State Chem. **Vol 73** (1988) p179.

[14] M.C. Kim, S.J. Park, H. Haneda, J. Tanaka, T. Mitsuhasi, S. Shirasaki, J. Mat. Sci. Letters. **Vol 9** (1990) p102.

[15] J. Mizusaki, Solid State Ionics **Vol 52** (1992) p79.

[16] H.U. Anderson, in Proc. of the 14th Risø International Symposium on Materials Science, edited by F.W. Poulsen, J.J. Bentzen, T. Jacobsen, E. Skou and M.J.L. Østergård, Risø National Laboratory, Denmark, (1993) p.1.

[17] Ch. Ftikos, S. Carter, B.C.H. Steele, J. Europ. Ceram. Soc. **Vol 12** (1993) p79.

[18] K. Gaur, S.C. Verma, H.B. Lal, J. Mat. Sci. **Vol 23** (1988) p1725.

[19] V.V. Kharton, E.N. Naumovich, P.P. Zhuk, A.K. Demin, A.V. Nikolaev, Soviet Electrochemistry **Vol 28** (1992) p1376.

[20] J.A. Lane, P.H. Middleton, H. Fox, B.C.H. Steele, J.A. Kilner, in Proc. of the 2nd Int. Symp. On Ionic and Mixed Conducting Ceramics, Eds. T.A. Ramanarayanan, W.L. Worrel and H.L. Tuller, The Electrochemical Society, Inc., Pennington, NJ, **PV 94-12**, (1994) p489.

[21] A.N. Petrov, O.F. Kononchuk, A.V. Andreev, V.A. Cherepanov, P. Kofstad. Solid State Ionics **Vol 80** (1995) p189.

[22] F.A. Kröger, in The Chemistry of Imperfect Crystals, Interscience, New York (1964).

[23] J.H. Kuo, H.U. Anderson and D.M. Sparlin, J. Solid State Chem., **Vol 83**, (1989) p52.

[24] T. Nakamura, G. Petzow and L.J. Gauckler, Mat. Res. Bull., **Vol 14**, (1979) p649.

[25] J. Mizusaki, Y. Mima, S. Yamauchi, K. Fueki and H. Tagawa, J. Sol. St. Chem. **Vol 80** (1989) p102.

[26] T. Arakawa, N. Ohara and J. Shiokawa, J. Mat. Sci., **Vol 21**, (1986) p1824.

[27] A. Hammouche, E. Siebert, A. Hammou, M. Kleitz and A. Caneiro, J. Electrochem. Soc., **Vol 138** (1991) p1212.

[28] P. Kofstad and A. Petrov, in Proc. of the 14th Risø International Symposium on Materials Science, edited by F.W. Poulsen, J.J. Bentzen, T. Jacobsen, E. Skou and M.J.L. Østergård, Risø National Laboratory, Denmark, (1993) p287.

[29] J.A. Lane, Ph.D. Thesis, University of London (1996).

[30] J. Mizusaki, M. Yoshihiro, S. Yamauchi and K. Fueki, J. Solid State Chem., **Vol 58** (1985) p.257.

[31] J. Mizusaki, S. Yamauchi, K. Fueki and A. Ishikawa, Solid State Ionics, **Vol 12** (1984) p.19.

[32] C.C. Chen, M.M. Nasrallah and H.U. Anderson, in Proc. 3rd Int. Symp. On SOFC, Eds. S.C. Singhal and H. Iwahara, Electrochemical Soc., Pennington, NJ, (1993) p252.

[33] L.W. Tai, M.M. Nasrallah and H.U. Anderson, in Proc. 3rd Int. Symp. On SOFC, Eds. S.C. Singhal and H. Iwahara, Electrochemical Soc., Pennington, NJ, (1993) p241.

[34 D. Waller, J.A. Lane, J.A. Kilner and B.C.H. Steele, Materials Letters, **Vol 27** (1996) p225.

[35] D. Waller, J.A. Lane, J.A. Kilner and B.C.H. Steele, Solid State Ionics, **Vol 86-88** (1996) p767.

[36] S.J. Benson, R.J. Chater and J.A. Kilner, in Proc. of the 3rd Int. Symp. On Ionic and Mixed Conducting Ceramics, Eds. T.A. Ramanarayanan, W.L. Worrel, H.L. Tuller, M. Mogensen and A.C. Khandkar, The Electrochemical Society, Inc., Pennington, NJ, **PV 97-24**, Paris (1997).

[37] J.A. Lane, D. Waller and J.A. Kilner, to be published in the Proc. of the XIth Conference on Solid State Ionics, Honolulu (1997).

[38] E. Ivers-Tiffée, M. Schießl, H.J. Oel, W. Wersing, in: Proc. 3rd Int. Symp. on SOFC, Eds. S. Singhal, H. Iwahara, The Electrochemical Soc., Inc., Pennington, NJ, (1993) p631.

[39] E. Ivers-Tiffée, M. Schießl, H.J. Oel, W. Wersing, in Proc. of the 14th Risø International Symposium on Materials Science, edited by F.W. Poulsen, J.J. Bentzen, T. Jacobsen, E. Skou and M.J.L. Østergård, Risø National Laboratory, Denmark, (1993) p69.

[40] R.A. De Souza, Ph.D. Thesis, University of London (1996).

[41] H.G. Scott, J. Mater. Sci., **Vol 10** (1975) p1527.

[42] Y. Suzuki and T. Takahashi, J. Chem. Soc. Japan (1977) p1610.

[43] N.Q. Minh and T. Takahashi, in Science and technology of Ceramic of Fuel Cells, Elsevier Science B.V., Oxford (1995).

[44] R.E.W. Casselton, J. Appl. Electrochem. **Vol 4** (1974) p25.

[45] V.S. Stubican, R.C. Hink and S.P. Ray, J. Am. Ceram. Soc. **Vol 61** (1978) p17.
[46] A.E. Hughes and S.P.S. Badwal, Solid State Ionics **Vol 46** (1991) p265.
[47] W. Weppner, J. Solid State Chem. **Vol 20** (1977) p305.
[48] J.H. Park and R.N. Blumenthal, J. Electrochem. Soc., **Vol 136** (1989) p2867.
[49] B.C.H. Steele, in Science and Technology of Zirconia V, Eds. S.P.S. Badwal, M.J. Bannister and R.H.J. Hannink, Technomic Publishing Company, Lancaster PA, (1993) p713.
[50] O. Yamamoto, Y. Takeda, N. Imanishi, T. Kawahara, G.Q. Shen, M. Mori and T. Abe, in Proc. of the 2nd Int. Symp. On Solid Oxide Fuel Cells, Eds. F. Grosz, P. Zegers, S.C. Singhal and O. Yamamoto, Commission of The European Communities, Luxembourg, (1991) p437.
[51] A. Atkinson, in Proc. Of the 2nd European SOFC Forum, Eds. B. Thorstensen, Oslo, Norway (1996) p707.
[52] A. Atkinson, Solid State Ionics, **Vol 95** (1997) p249.
[53] T.Y. Tien and E.C. Subbatao, J. Chem. Phys., **Vol 39** (1962) p572.
[54] J. Faber, Jr., M.A. Seitz and M.H. Muller, J. Phys. Chem. Soc., **Vol 37** (1976) p903.
[55] J. Faber, Jr., M.A. Seitz and M.H. Muller, J. Phys. Chem. Soc., **Vol 37** (1976) p909.
[56] J.A. Kilner and B.C.H. Steele, in Nonstoichiometric Oxides, Ed. O.T. Sorensen, Academic Press, New York (1981) p233.
[57] M.R. Thornber, D.J.M. Bevan and J. Graham, Acta Cryst. B, **Vol 24** (1968) p1183.
[58] S.B. Ray and D.E. Cox, J. Solid State. Chem., **Vol 15** (1975) p333.
[59] J.M. Ralph and J.A. Kilner, in Proc. Of the 2nd European SOFC Forum, Eds. B. Thorstensen, Oslo, Norway (1996) p773.
[60] J.F. Baumard and P. Aberlard, in Science and Technology of Zirconia II, Eds. N. Claussen, M. Ruhle and A.H. Heuer, American Ceramic Society, Columbus, OH (1984) p744.
[61] J.A. Kilner and C.D. Waters, Solid State Ionics, **Vol 6** (1982) p253.
[62] P.S. Manning, J.D. Sirman, R.A. de Souza and J.A. Kilner, Solid State Ionics, **Vol 100** (1997) p1.

4. Oxygen Ion, Electronic and Protonic Transport in Perovskite and Fluorite Oxides.

4.1. Introduction.

In the previous chapter, it was shown that significant concentrations of defects can exist in perovskite and fluorite oxides, depending on the conditions to which the material is exposed. It was also shown that the concentration of defects determines the nature and magnitude of conductivity within a material. In this chapter, the transport of oxygen ions and electrons in both fluorite and perovskite materials will be discussed. It is assumed that the conduction of oxygen ions takes place via a vacancy mechanism. A brief discussion of protonic transport in these materials is also included.

4.2. Ionic Conduction and Diffusion.

The atomistic interpretation of the diffusion of ions in a solid solution is that the movement takes place by a localised hopping process from one site to a neighbouring site. In the case of many acceptor doped fluorites and perovskites, oxygen ion transport occurs by hopping from one vacant site to the next. The transport of an ion from one site to the next, through a saddle point requires energy. This energy is provided by variations in thermal vibrations of neighbouring ions. It is clear therefore that conduction by a hopping method is thermally activated and this has been verified experimentally.

The ions reach the energy state required to move through the saddle point with a particular jump frequency which is dependent on the nature of the lattice. This frequency can be expressed thus,

$$\Gamma = \nu_i \exp\left(-\Delta G_m / kT\right) \qquad \text{eqn. (4.1)}$$

where ν_i is the characteristic lattice frequency.

Using random walk theory (the process in which an atom is able to jump from its current site to any neighbouring site with equal opportunity) it can be shown that [1],

$$J = \tfrac{1}{2}(n_1 - n_2)\Gamma \qquad \text{eqn. (4.2)}$$

where J is the net flux between planes n_1 and n_2. The concentration of the two planes are,

$$C_1 = n_1 / a_i \qquad \text{eqn. (4.3)}$$

and

$$C_2 = n_2 / a_i \qquad \text{eqn. (4.4)}$$

a_i is the distance between equivalent sites (i.e. the jump distance). The concentration gradient, dC/dx, is given by,

$$dC/dx = \frac{C_1 - C_2}{a_i} = \frac{n_1 - n_2}{a_i^2} \qquad \text{eqn. (4.5)}$$

This process is more clearly illustrated in figure 1 (from Chiang *et al* [2]). The flux can then be expressed in the form of Fick's first law.

$$J = -\left(\tfrac{1}{2} a_i^2 \Gamma\right)\frac{dC}{dx} \qquad \text{eqn. (4.6)}$$

Thus the one dimensional diffusion coefficient can be given by equation 4.7.

$$D = \tfrac{1}{2} a_i^2 \Gamma \qquad \text{eqn. (4.7)}$$

Equation 4.7 can be combined with equation 4.1, to yield,

$$D = \tfrac{1}{2} a_i^2 \nu_i \exp\left(-\Delta G_m / kT\right) \qquad \text{eqn. (4.8)}$$

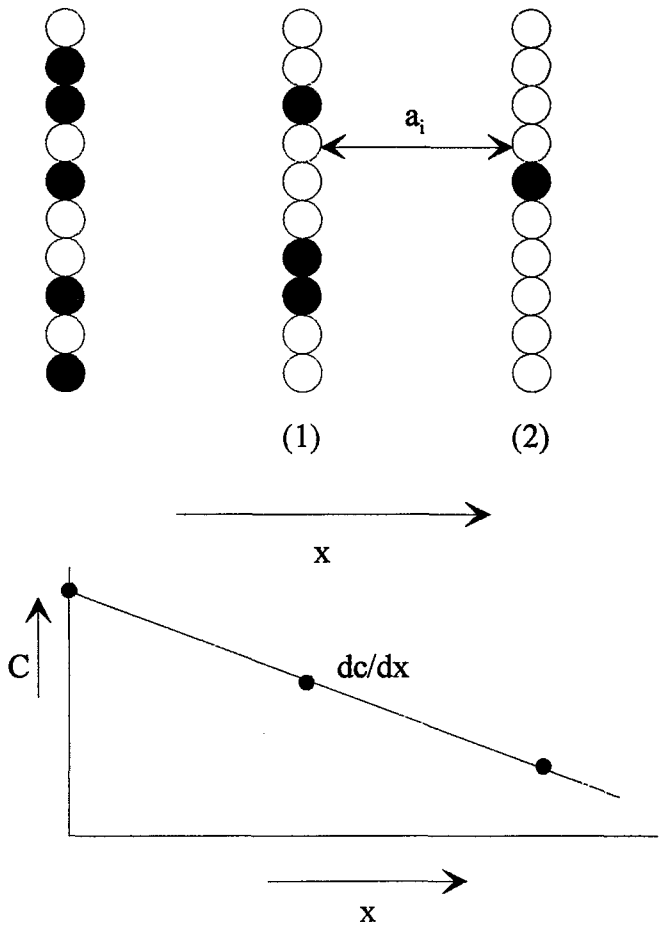


Figure 4.1. Schematic illustration of atoms diffusing with a concentration gradient [2].

In the case of a simple cubic lattice of atoms, where diffusion takes place by a vacancy mechanism, the diffusion coefficient can be described as

$$D = \frac{z}{6}(1-C)a_i^2 \nu_i \exp\left(\frac{-\Delta G_m}{kT}\right) \qquad \text{eqn. (4.9)}$$

where z is the number of nearest neighbour positions, and (1-C) is the fraction of unoccupied lattice sites. In the case of oxygen ions diffusing through a three dimensional crystal lattice, this equation then becomes,

$$D_i = \frac{z_i}{6}\left[V_O^{\bullet\bullet}\right]a_i^2 \nu_i \exp\left(\frac{-\Delta G_m}{kT}\right) \qquad \text{eqn. (4.10)}$$

D_i is the self-diffusion coefficient of oxygen, z_i is the anion co-ordination number and $\left[V_O^{\bullet\bullet}\right]$ is the concentration of free oxygen vacancies expressed as a site fraction. The free energy associated with the activated hopping process can be resolved into its enthalpic and entropic terms to give,

$$D_i = {}^{z_i}/_{6}\left[V_O^{\bullet\bullet}\right]a_i^{\,2}\nu_i \exp\left(-{}^{\Delta H_m}/_{kT}\right)\exp\left({}^{\Delta S_m}/_{k}\right) \qquad \text{eqn. (4.11)}$$

If we define γ as,

$$\gamma = {}^{z_i}/_{6}\exp\left(-{}^{\Delta S_m}/_{k}\right) \qquad \text{eqn. (4.12)}$$

then equation 4.11 can be simplified to,

$$D_i = \gamma\left[V_O^{\bullet\bullet}\right]a_i^{\,2}\nu_i \exp\left(-{}^{\Delta H_m}/_{kT}\right) \qquad \text{eqn. (4.13)}$$

This is then further simplified to equation 4.14.

$$D_i = D_{iO}\exp\left(-{}^{\Delta H_m}/_{kT}\right) \qquad \text{eqn. (4.14)}$$

which is of the form of the general Arrhenius equation for thermally activated processes.

This equation is only appropriate for dilute solutions where the concentration of defects is small enough such that there is no interaction between them. However, as was illustrated in Chapter 3, this is unlikely to be the case in the heavily doped materials used in SOFC or COG. Therefore, an association enthalpy term must be added to equation 4.14, to give,

$$D_i = D_{iO}\exp\left(\frac{-(\Delta H_m + \Delta H_a)}{kT}\right) \qquad \text{eqn. (4.15)}$$

This equation can be derived from an alternative method where the ionic conductivity due to species k, is given by,

$$\sigma_k = n_k q_k \mu_k \qquad \text{eqn. (4.16)}$$

Where q_k and μ_k are the respective charge and mobility of the carrier. In this case the carrier is an oxygen ion, and so the carrier density n_k, may be expressed as:

$$n_k = \left[V_O^{\bullet\bullet}\right]\left\{1-\left[V_O^{\bullet\bullet}\right]\right\}N \approx \left[V_O^{\bullet\bullet}\right]N \qquad \text{eqn. (4.17)}$$

Where N is the number of anion sites per unit volume. The mobility of the carrier can be expanded to give:

$$\mu_k = \frac{\gamma q}{kT} a_i^{\,2} \nu_i \exp\left(-\frac{\Delta H_m}{kT}\right) \qquad \text{eqn. (4.18)}$$

Combining equations 4.16 to 4.18 gives,

$$\sigma_k = N[V_O^{\cdot\cdot}]\frac{\gamma q^2}{kT} a_i^{\,2} \nu_i \exp\left(-\frac{\Delta H_m}{kT}\right) \qquad \text{eqn. (4.19)}$$

The ionic conductivity can be converted to an oxygen diffusion coefficient using the Nernst-Einstein equation,

$$D_\sigma = \frac{kT\sigma}{Nq^2} \qquad \text{eqn. (4.20)}$$

D_σ is the diffusion coefficient obtained from ionic conductivity data. D_σ is equivalent to the self-diffusion coefficient if the charge carriers are unaffected by the presence of an electric field [3]. That is, the availability of mobile defects is equal with or without the influence of an electric field.

We can obtain the ionic oxygen diffusion coefficient in terms of atomistic parameters, by substituting eqn. 4.19 into 4.20 to give:

$$D_\sigma = \gamma[V_O^{\cdot\cdot}]a_i^{\,2}\nu_i \exp\left\{-\frac{\Delta H_m}{kT}\right\} \qquad \text{eqn. (4.21)}$$

Again, using the simplification applied to equation 4.13 and including an association enthalpy, we obtain,

$$D_\sigma = D_{\sigma O} \exp\left(\frac{-(\Delta H_m + \Delta H_a)}{kT}\right) \qquad \text{eqn. (4.22)}$$

which is mathematically equivalent to equation 4.15.

As stated previously, D_σ is equivalent to the self-diffusion coefficient under the condition that the charge carriers move in such a way that the availability of mobile defects is unaffected by the presence of an electric field. However, this may not be the case when charged defect associates are present. In the case of DC conductivity measurements, the voltage applied to the sample is unlikely to affect the strong Coulombic attraction between the defect associate pairs. Under an AC field, however, it is more likely that the defect will behave as a dipole and reorientate under the electric field, thus contributing to the conductivity [4]. Therefore, a conductivity (or ionic) correlation factor can be introduced such that $D_\sigma = D_i f_c$, where f_c is the conductivity correlation factor and D_i is the self-diffusion coefficient, thus

$$D_\sigma = f_c \gamma [V_O^{\cdot\cdot}] \lambda^2 \nu_i \exp\left\{-\frac{(\Delta H_m + \Delta H_a)}{kT}\right\} \qquad \text{eqn. (4.23)}$$

Hence, when measuring the self-diffusion coefficient of an oxygen ion using an electrical method, a conductivity correlation factor should be applied. It should be noted that in most experimental cases in the literature where the concentration of defects is relatively low, the conductivity correlation factor is considered to be unity.

4.3. Types of Diffusion Coefficient.

Two types of diffusion coefficient have already been mentioned above, the self-diffusion coefficient (D_i) and the conductivity diffusion coefficient (D_σ). Both self-diffusion and conductivity diffusion apply to a host lattice ion. A very similar diffusion coefficient applies when a tracer ion, which is chemically alike to the host ion, but of a different isotope is introduced. This then introduces a tracer correlation factor, f_D to equation 4.13, to give,

$$D_T = f_D \gamma [V_O^{\cdot\cdot}] \lambda^2 \nu_i \exp\left\{-\frac{(\Delta H_m + \Delta H_a)}{kT}\right\} \qquad \text{eqn. (4.24)}$$

such that,

$$D_T = f_D D_i \qquad \text{eqn. (4.25)}$$

The tracer correlation factor reflects the fact that successive diffusive jumps of a tracer ion are correlated. Atomistically, the difference between self-diffusion and tracer diffusion is that the motion of a tracer ion is biased by the probability that once a lattice jump has been made, the next jump simply returns it to its former position. Successive jumps are said to be correlated [2,3,5,6]. The value of the correlation factor depends on the atomic co-ordination number and the relative frequencies with which the vacancy exchanges with tracer and lattice ion. Stochastic computer simulations predict that for diffusion by a vacancy mechanism, in simple, dilute solution, cubic structures (i.e. anion diffusion in fluorite structures, $f_D = 0.65$ [6]. However, if the solution is more concentrated, and defect associates are formed, then f_D will be smaller. If the case is reached where microdomains of second phases are formed due to the high concentration of defects, then the tracer diffusion coefficient may be significantly altered. The ratio of the tracer correlation factor to the conductivity correlation factor (and hence the ratio of the tracer diffusivity to the diffusivity obtained from the ionic conductivity) is known as the Haven ratio [3].

Another type of diffusion coefficient is that involving the diffusion of a specific defect, such as an oxygen vacancy. This can be a useful coefficient to compare different materials with, as it effectively removes the concentration of defects from the calculation. The vacancy diffusion coefficient can be expressed in terms of the self-diffusion coefficient by equation 4.26.

$$D_V = \frac{D_i C_i}{C_v} \qquad \text{eqn. (4.26)}$$

where C_i and C_v are the concentration of oxygen sites and vacancies, respectively. If C_i and C_v are expressed as site fractions, equation 4.26 becomes,

$$D_V = \frac{D_i}{[V_O^{\bullet\bullet}]} \qquad \text{eqn. (4.27)}$$

In low defect concentrations, D_V is independent of defect concentration. This is because the vacancy must move to an occupied site. (It cannot move to another vacant site.) Thus the probability of the adjacent site being available is approaching unity. As a result, each vacancy movement occurs without affecting another. As the defect concentration is increased however, the probability of the neighbouring site being a vacancy, and thus unavailable, increases. Therefore, one vacancy motion may affect another.

Chemical diffusion is the diffusion of a species due to a chemical gradient within the sample. An example of chemical diffusion is the reaction between two solids. The chemical, or interdiffusion coefficient can be expressed in terms of the individual self-diffusion coefficients by the Darken equation [7].

$$D_{chem} = \left(C_1 D_2 + C_2 D_1\right)\left(1 + \frac{\partial \ln a_1}{\partial \ln C_1}\right) \qquad \text{eqn. (4.28)}$$

C_1 and C_2 are the site fractions of species 1 and 2, respectively, D_1 and D_2 are their self-diffusivities and a_1 is the activity coefficient of species 1. In an ideal or dilute solution, $\left(\frac{\partial \ln a_1}{\partial \ln C_1}\right) \rightarrow 0$, to give,

$$D_{chem} = \left(C_1 D_2 + C_2 D_1\right) \qquad \text{eqn. (4.29)}$$

If the case of a ceramic membrane is considered where one side is exposed to given a partial pressure of oxygen, pO_2^I, it will have a given stoichiometry and hence, vacancy concentration, $\left[V_O^{\bullet\bullet}\right]^I$. If the other side is exposed to a different oxygen partial pressure, pO_2^{II}, then the material will have a different oxygen stoichiometry at this side, $\left[V_O^{\bullet\bullet}\right]^{II}$. Thus an oxygen chemical gradient will exist in the material, and oxygen diffusion will occur. The rate of oxygen chemical diffusion through the material is proportional to the rate of change in concentration of vacancies with the rate of change in pO_2 and also the magnitude of the vacancy diffusion coefficient. The Darken equation will then become,

$$D_{chem} = \left(C_i D_e + n D_i\right)\left(1 + \frac{\partial \ln pO_2}{\partial \ln C_i}\right) \qquad \text{eqn. (4.30)}$$

D_e and n are the diffusion and concentration of electrons, respectively.

In order for chemical diffusion of an ionic species to occur (i.e. where there is charge transport, as well as mass transport), a different charged entity must diffuse in the opposite direction to avoid long range charge separation. The second charged species must diffuse in the opposite direction at a rate to give a net charge transport of zero such that overall charge neutrality is maintained. This has the affect of coupling the two charged species, slowing down the faster and accelerating the slower. The effective diffusion coefficient is called the ambipolar diffusion. The value of the ambipolar diffusivity is bound at the two extremes by the diffusivities of the two species involved. In the case of mixed conducting perovskites such as the strontium doped lanthanum manganites and cobaltites, electrons provide the counter flow of charge to the oxygen ions. For electroneutrality to be maintained, the flux condition must be,

$$2J_{V_O^{\bullet\bullet}} = J_{e'} \qquad \text{eqn. (4.31)}$$

where J_k is the flux of species k.

The two species are coupled such that they have a common chemical diffusion coefficient or ambipolar diffusion coefficient. The individual fluxes of the two species can then be expressed in terms of Fick's first law as,

$$J_{V_O^{\bullet\bullet}} = -D_{amb}\left(\frac{d[V_O^{\bullet\bullet}]}{dx}\right) \qquad \text{eqn. (4.32)}$$

and

$$J_{e'} = -D_{amb}\left(\frac{dn}{dx}\right) \qquad \text{eqn. (4.33)}$$

If the electroneutrality condition is given by $n = 2[V_O^{\bullet\bullet}]$ then it can be shown that [2],

$$D_{amb} = \frac{3D_V D_e}{2D_V + D_e} \qquad \text{eqn. (4.34)}$$

This is equivalent to [8],

$$D_{amb} = D_V t_e + D_e t_i \qquad \text{eqn. (4.35)}$$

Equation 4.34 is often expressed in terms of conductivity, such that,

$$\sigma_{amb} = \frac{\sigma_i \sigma_e}{\sigma_i + \sigma_e} \qquad \text{eqn. (4.36)}$$

In the case of strontium doped lanthanum manganite and cobaltite, the flow of electrons is much more rapid than the transport of ions. Thus equation 4.34 can be approximated to,

$$D_{amb} \approx 3D_V \qquad \text{eqn. (4.37)}$$

For the acceptor doped fluorite materials the ionic conductivity is much greater than the electronic conductivity so in this case,

$$D_{amb} \approx \tfrac{3}{2} D_e \qquad \text{eqn. (4.38)}$$

In a more rigorous examination, it can be shown that in a system where the ambipolar diffusion is limited by the transport of vacancies, the ambipolar or chemical diffusion coefficient can be expressed as [8,9,10,11],

$$D_{amb} = -2D_V \frac{\partial \ln[V_O^{\bullet\bullet}]}{\partial \ln pO_2} \qquad \text{eqn. (4.39)}$$

which is mathematically similar to the Darken equation given by equation 4.30. Equation 4.39 is often reduced to,

$$D_{amb} = \frac{D_V}{A} \qquad \text{eqn. (4.40)}$$

where A, the thermodynamic factor is,

$$A = -\tfrac{1}{2} \frac{\partial \ln pO_2}{\partial \ln[V_O^{\bullet\bullet}]} \qquad \text{eqn. (4.41)}$$

Another type of diffusion is impurity or solute diffusion. It is possible for the impurity ion to diffuse interstitially or via a vacancy mechanism utilising the host

ion sites. If the solute diffusion occurs via a vacancy mechanism, then it will still differ from the self-diffusivity of host ions. This is because the impurity ion will be of a different size (and possibly valence) to the host ions. This leads to a difference in the jump attempt frequency. Furthermore, there may be an association between the impurity ion and a vacancy. This will alter the probability of a vacancy appearing on a neighbouring site.

A further consideration which must applied to all the above mentioned types of diffusion is transport down a one or two dimensional path such as a dislocation or grain boundary. The disruption to the crystal lattice at these linear or planar defects can substantially alter the transport properties of anions, cations or impurities. The effects of this complex form of diffusion are not discussed in detail in this work, but the reader is referred to other texts which provide good descriptions of grain boundary and dislocation diffusion [12,13,14,15].

4.4. Experimental Behaviour of the Oxygen Transport in Fluorite Materials.

In the literature there are predominantly two methods used to measure the oxygen transport in fluorite oxides. These are electrical testing methods and tracer diffusion methods. Electrical measurements are split into two groups; AC impedance spectroscopy [16] and DC conductivity experiments. Tracer measurements have predominately been carried using secondary ion mass spectrometry (SIMS) [12,17]. These analysis techniques will be described in chapter 7 of this thesis. Other methods that have been used to characterise the tracer diffusion coefficient of oxygen are Raman spectroscopy [18], gas phase analysis [19,20], and a sectional technique using a solid source mass spectrometer [21].

Some typical values of conductivity for a variety of zirconia and ceria based fluorites are given in figure 4.2 [22,23,24,25,26]. All these data have used an AC impedance spectroscopy method to determine the conductivity. The data shown is for the grain interior (bulk) conductivity, except the data of Aberlard *et al* [23] and Manning *et al* [26], where single crystals were used. It should be noted that most of the data has a degree of non-linearity produced by the formation of defect associates [26,27,]. Using the method described in section 3.8, Manning *et al* [26] has used this curvature to deconvolute the apparent activation energy into the association enthalpy and migration enthalpy.

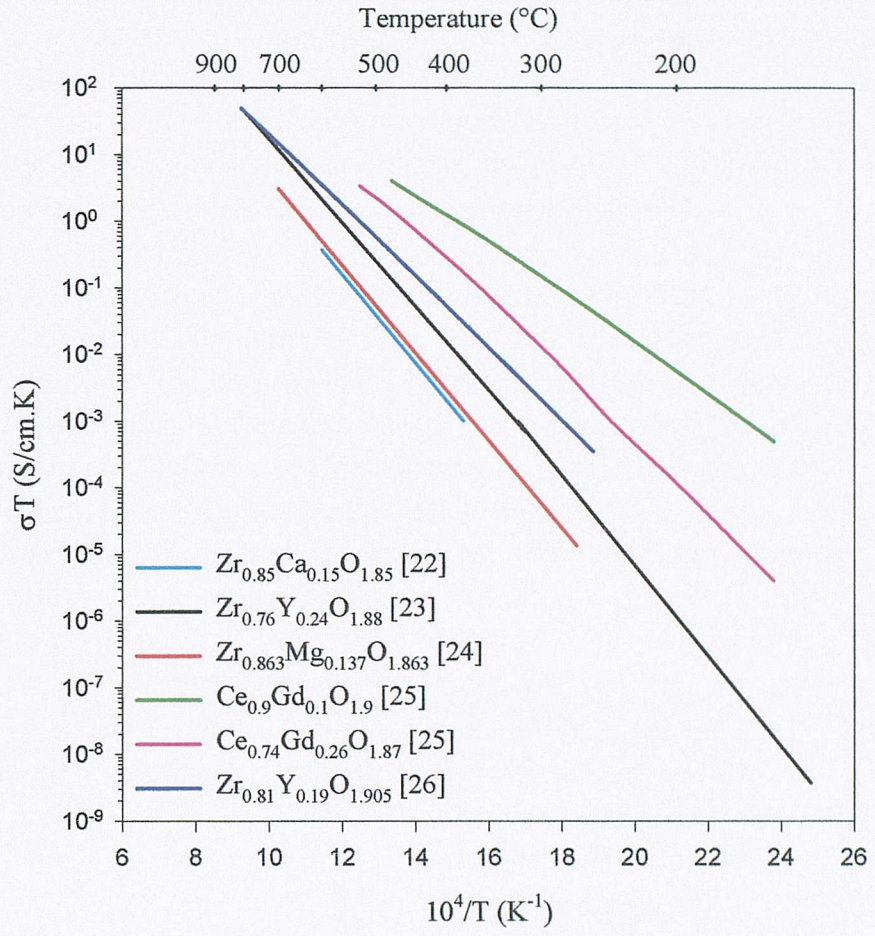


Figure 4.2. Graph of bulk conductivity as a function of temperature for various zirconia and ceria based fluorite materials [22,23,24,25,26].

There are several interesting features that can seen in figure 4.2. First the absolute values of the conductivity of ceria based materials are higher than the zirconia based materials. Secondly the conductivity of the 5mol% Gd_2O_3 doped ceria is higher than the 13mol% doped material. This is also the case in the YSZ system, where the 9.5mol% Y_2O_3 doped material exhibits a higher conductivity than the 12mol% material. This is in agreement with the suggestion that defect associates formed at higher concentrations effectively trap out the free oxygen vacancies (see section 3.8). The activation energy of $Zr_{0.85}Ca_{0.15}O_{1.85}$ (127kJ/mol), $Zr_{0.76}Y_{0.24}O_{1.88}$ (128kJ/mol at T<315°C) and $Zr_{0.863}Ca_{0.137}O_{1.863}$ (126kJ/mol) in which the concentration of oxygen vacancies are very similar, all have essentially the same activation energy. In the case of the $Ce_{0.9}Gd_{0.1}O_{1.95}$ and $Ce_{0.74}Gd_{0.26}O_{1.95}$ the activation energies are noticeably different. This leads to the

suggestion that the activation energy for conduction is to some extent controlled by the concentration of vacancies. The increase in activation energy seen in $Ce_{0.74}Gd_{0.26}O_{1.95}$ over $Ce_{0.9}Gd_{0.1}O_{1.95}$ (and also $Zr_{0.76}Y_{0.24}O_{1.88}$ over $Zr_{0.81}Y_{0.19}O_{1.905}$ (E_a=106kJ/mol)) is probably due to a change in the migration enthalpy and the association enthalpy of the material due to defect associates or the formation of ordered microdomains of second phases.

There is significantly less work on the oxygen tracer diffusion coefficent published in the literature. This reflects the difficulties in performing tracer experiments on the electronically insulating fluorites, compared to the relative simplicity of electrical measurements. It is also only more recently with the development of SIMS and Raman techniques for measuring oxygen diffusion, that accurate and reproducible data has been obtainable. Figure 4.3 shows a plot of the oxygen diffusivity of various zirconia and ceria based materials.

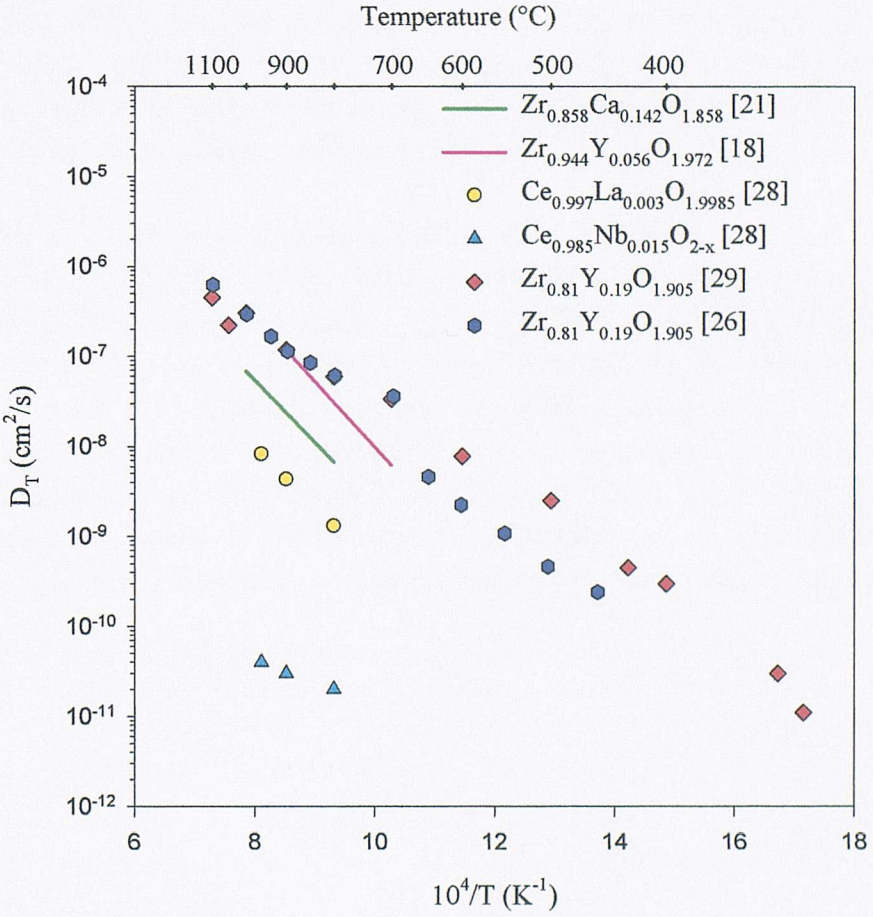


Figure 4.3. Graph of diffusivity as a function of temperature for various zirconia and ceria based fluorite materials [18,21,26,28,29].

The work of Simpson and Carter [21] on $Zr_{0.858}Ca_{0.142}O_{1.858}$ utilises a sectional technique using a solid source mass spectrometer. Kim *et al* [18] uses Raman spectroscopy. They also corroborate there data by performing a gas phase Raman analysis which gives similar results. The other data by Carter *et al* [28], Solmon [29] and Manning *et al* [26] all use SIMS. The high temperature data of Solmon matches well with that of Manning, however there is some deviation at lower temperatures. This was attributed to the presence of impurities in the samples of Solmon, which also gave rise to a "fast" diffusion path at higher temperatures [26]. The data of Kim also shows good agreement with that of Manning *et al* and Solmon, verifying the suitability of both Raman spectroscopy and SIMS as methods with which to measure oxygen diffusion. However, the older data of Simpson and Carter is noticeably lower than the measurements made with more modern analysis tools.

The data on ceria based materials by Carter *et al* [28], substantiates the fact that oxygen diffusion in fluorites occurs primarily by a vacancy mechanism. The low diffusion coefficient of the $Ce_{0.997}La_{0.003}O_{1.9985}$ ties in well with the low concentration of oxygen vacancies, and the ceria which is donor doped with Nb_2O_5 has an even lower diffusion coefficient.

There has been very little work published on comparing the ionic conductivity with the tracer diffusivity for the same material. The work of Manning *et al* [26] on high quality single crystals of 9.5mol% Y_2O_3 doped ZrO_2 being a notable exception. Figure 4.4 is taken from this work and shows, firstly that the Haven ratio is not 0.65 as predicted from computer simulations [6] but also that it changes at a temperature around 650°C. There are several possible explanations for this deviation from the predicted ratio of 0.65. These will be detailed in Chapter 10, however at this stage the possibility of a systematic error in the results obtained from either of the two techniques should not be discounted.

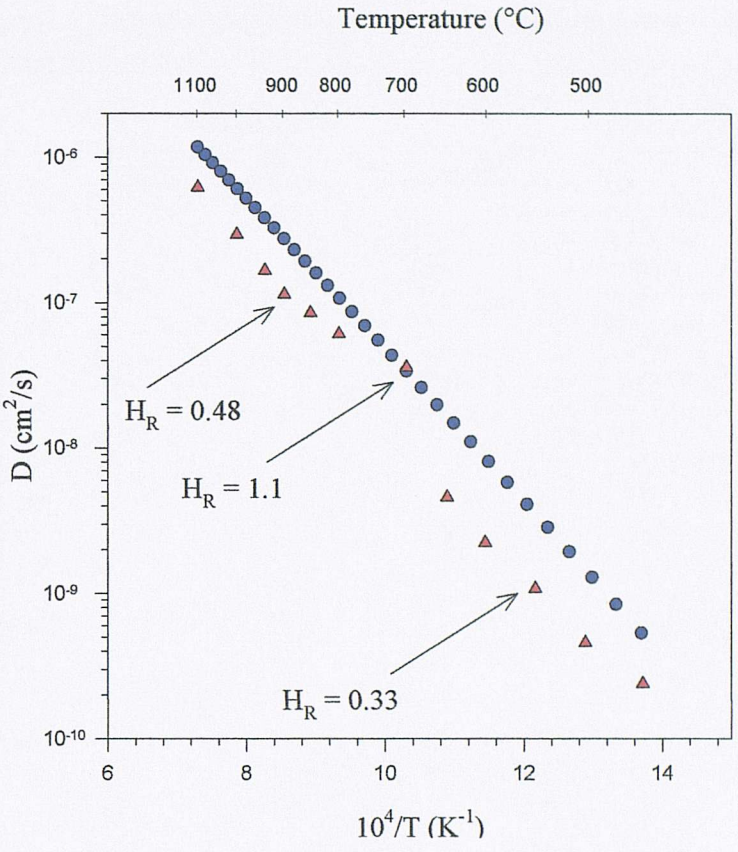


Figure 4.4. Arrhenius plot of D_σ (circles) and D_T (triangles), for 9.5mol% YSZ single crystal [26].

4.5. Experimental Behaviour of the Oxygen Transport in Perovskite Materials.

Measurement of the transport of oxygen ions in perovskites is complicated by the fact, with only a few notable exceptions such as doped lanthanide gallates, the ionic transference number is significantly less than unity. In many cases, in fact, the electronic transference number approaches unity. This means that electrical measurements are made very difficult, the application of electronically blocking electrodes being required. Therefore the majority of oxygen diffusion studies carried out on mixed conducting perovskites have been made by SIMS, and to some extent gas phase analysis. There have been a wide range of studies on various chromites, manganites, ferrites, cobaltites and diverse combinations of

these. Figure 4.5, shows examples of the range of diffusion coefficients obtained in the literature from SIMS.

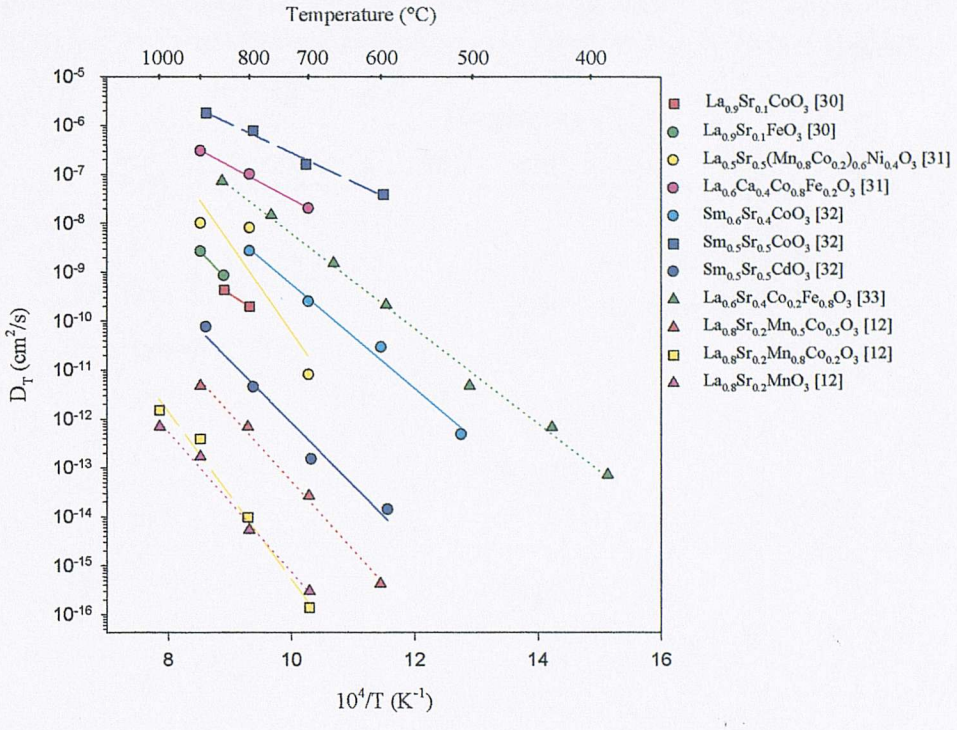


Figure 4.5. Graph of diffusivity as a function of temperature for various $R_ET_MO_{3\pm\delta}$ perovskites [12,30,31,32,33].

It is clear from figure 4.5 that an enormous range of oxygen diffusivities occurs in the transition metal perovskites. For example, at 900°C the tracer diffusivity of $Sm_{0.5}Sr_{0.5}CoO_{3-\delta}$ is about seven orders of magnitude larger than $La_{0.8}Sr_{0.2}MnO_{3\pm\delta}$. This is almost certainly a reflection on the concentration of vacancies in the perovskite, rather than a change in the mobility of the vacancies (i.e. the vacancy diffusion coefficient). The cobaltites have a significantly higher oxygen vacancy concentration than the manganites (see chapter 3) and the higher level of A-site dopant in the $Sm_{0.5}Sr_{0.5}CoO_{3-\delta}$ will introduce further vacancies. Ishigaki *et al* [30] suggest that the vacancy diffusion coefficient is essentially unaffected by the A-site dopant concentration or the nature of the B-site cation. The work of Fullarton *et al* [32] shows the increase in tracer diffusion coefficient with increasing strontium content (and hence increasing $\left[V_O^{\bullet\bullet}\right]$ in $Sm_{1-x}Sr_xCoO_{3-\delta}$ and the work of De Souza [12] shows a similar effect by partial substitution of manganese with cobalt in $La_{0.8}Sr_{0.2}Mn_{1-y}Co_yO_{3-\delta}$.

The work of Ishigaki *et al* [34] on single crystal $LaCoO_{3-\delta}$ gives a comparison of diffusion data obtained from SIMS with data obtained from gas phase analysis. Figure 4.6 shows that the data is in very good agreement, and hence increases the validity of the measurement techniques (at least for single crystal measurements).

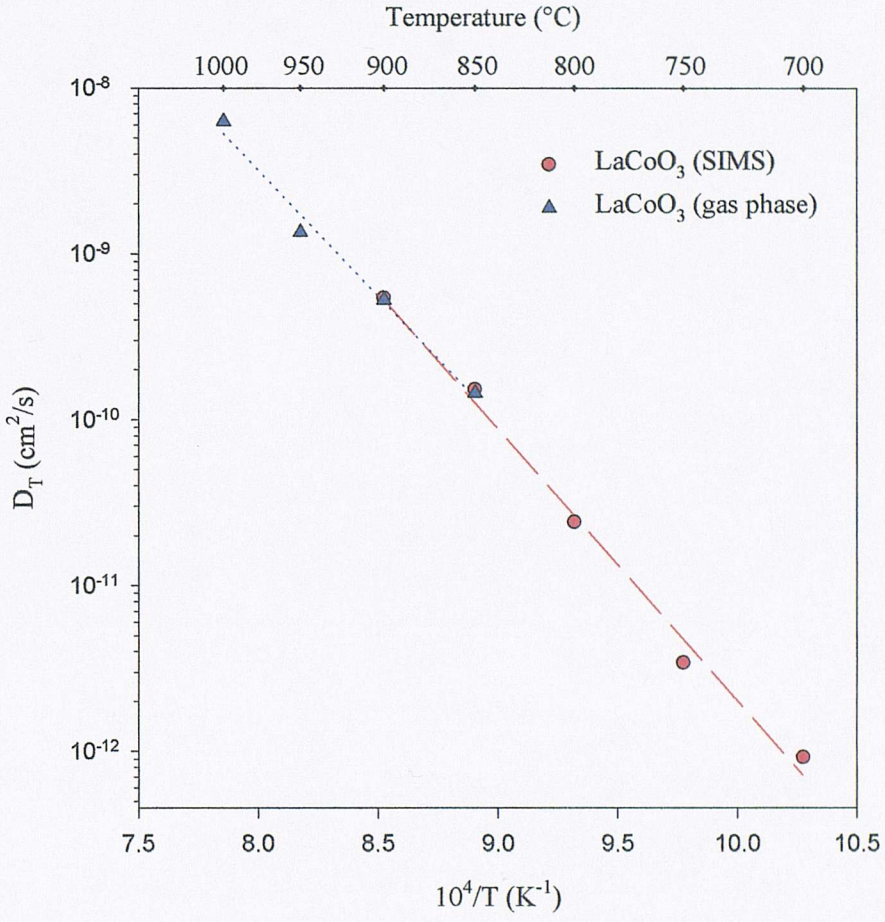


Figure 4.6. A comparison of the tracer diffusion coefficient of $LaCoO_{3-\delta}$ single crystal using SIMS and gas phase analysis (from Ishigaki *et al* [34]).

It is interesting to make a comparison between the fast ion conducting fluorites and the fast ion conducting perosvkites. This is made somewhat difficult due to the lack of high quality data for these materials. Figure 4.7 shows a comparison of the tracer diffusion coefficient of $Zr_{0.81}Y_{0.19}O_{1.905}$ [26] with $La_{0.8}Sr_{0.2}CoO_{3\pm\delta}$ [12], $La_{0.6}Sr_{0.4}Co_{0.2}Fe_{0.8}O_{3\pm\delta}$ [33] and $Sm_{0.5}Sr_{0.5}CoO_{3-\delta}$ [32].

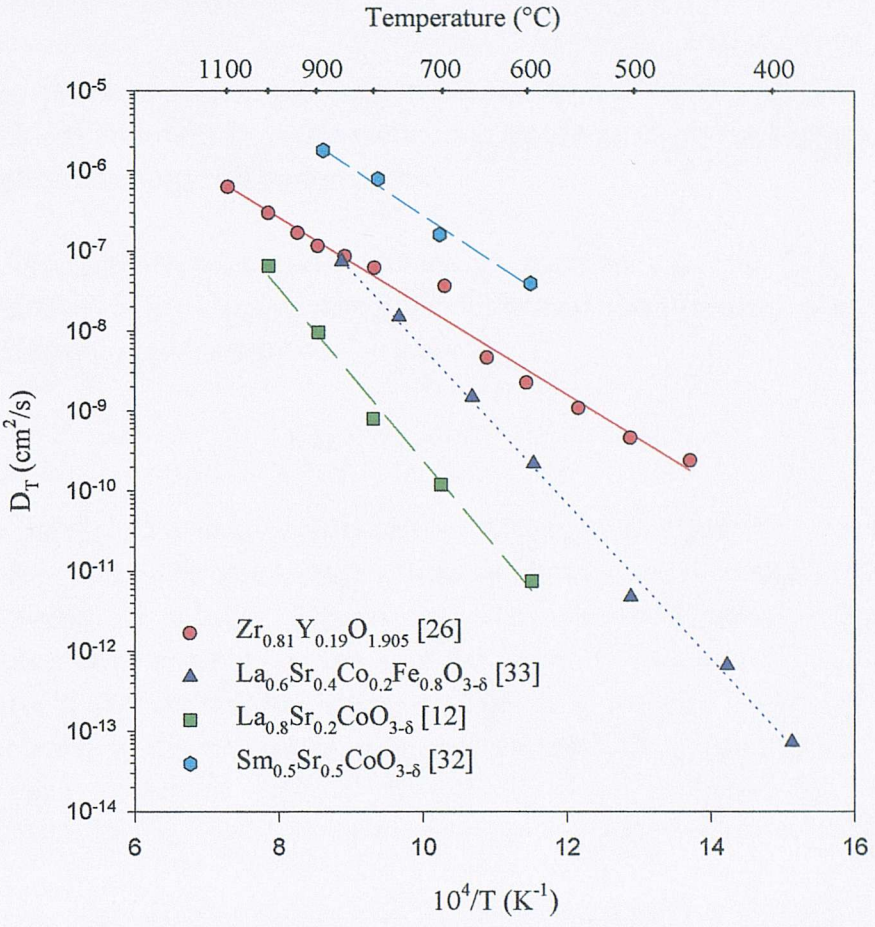


Figure 4.7. A comparison of the tracer diffusion coefficient of $Zr_{0.81}Y_{0.19}O_{1.905}$ [26] with $La_{0.8}Sr_{0.2}CoO_{3\pm\delta}$ [12], $La_{0.6}Sr_{0.4}Co_{0.2}Fe_{0.8}O_{3\pm\delta}$ [33] and $Sm_{0.5}Sr_{0.5}CoO_{3-\delta}$ [32].

The difference in diffusion coefficient can again be explained to some extent by the difference in concentration of oxygen vacancies. The large strontium dopant concentration in the samarium cobaltite produces a very high oxygen diffusivity. In the YSZ, there is a lower dopant concentration, however, the dopant material is compensated solely by oxygen vacancies, and so large diffusivities are also seen. The additional strontium content in the LSCF over the LSC produces more oxygen vacancies and hence LSCF has a higher oxygen tracer diffusion coefficient than the LSC material.

4.6. Electronic Conductivity.

In the previous section the motion of oxygen ions in fluorite and perovskite oxides was considered. In this section the motion of electronic carriers (electrons and electron holes) will be considered.

The conductivity of a given species is given in equation 4.16. The total conductivity being simply a sum of the individual conducting species. Therefore, the electronic conductivity can be given by,

$$\sigma_{e,h} = \sigma_e + \sigma_h = ne\mu_e + pe\mu_h \qquad \text{eqn. (4.42)}$$

Thus the electronic conductivity can be changed by changing the concentration of electrons and holes able to take part in conduction and/or changing the mobility of the electrons or holes. The mobility of the electronic defects is dependent on the electronic structure of the material being investigated. The mobility of electronic carriers and electronic structure is a complex subject and it is not appropriate to the content of this work to detail the fundamentals here. The interested reader is referred to several texts available on the subject [1,9,35,36,37,38]. However, some important features are discussed below.

Electrons can create a deformation in the crystal lattice of an ionic solid which may trap the electron in a potential well. A self-trapped electron an its surrounding polarisation region is termed a polaron [35]. The level of coupling between the electrons and optical phonons governs the nature of the polaron [39]. The polaron is described as large if the coupling is weak to intermediate. When the interaction is strong the polaron is said to be small. In the case of large polarons the electrons move in conduction bands and metallic type conductivity occurs. Small polarons move in a localised hopping process and so the material acts as a semi-conductor. Most of the perovskites and fluorites used in SOFC or COG conduct with small polarons.

The concentration of electronic defects can be changed by the environment in which the oxide material is exposed. This was illustrated by the Brouwer diagrams given in chapter 3. In the working pO_2 range of a COG, the electronic carrier concentration in a fluorite material such as YSZ or CGO is very small. As a result the electronic conductivity is considered to be negligible. In the case of an SOFC, at the low pO_2 anode side, significant electronic conductivity can be

introduced to CGO, although there is no apparent increase in the electronic conductivity of zirconia. In the case of the $R_ET_MO_3$ metal perovskites, the dominant conduction process under cathode conditions is p-type semi-conductivity.

4.7. Protonic Conductivity.

The motion of protons in an ionic crystal lattice is a less well studied process than the motion of either oxygen ions or electrons. However, there is interest in using a protonically conducting electrolyte membrane and/or a mixed electronically/protonically conducting anode in a fuel cell. Several doped $A^{II}B^{IV}O_3$ perovskites such as $SrCeO_3$ [40,41], $BaCeO_3$ [42,43], $CaZrO_3$ [44] and $SrZrO_3$ [45] and some $A^{III}B^{III}O_3$ perovskites ($LaYO_3$ doped on the A site with calcium [46] or strontium [47,48]) are known to be proton conductors. There is very little evidence of significant protonic conduction in the fluorite oxides CGO or YSZ, although Sahibzada [49] has suggested that in CGO there may be proton incorporation under anodic conditions. Wagner [50] quoted the protonic diffusion coefficient in YSZ to be of the order of 10^{-7}-10^{-6} cm^2/s at 900-1000°C. However, he also showed that the solubility of protons in YSZ to be around 10^{-4}, expressed as a site fraction. In contrast to Wagner, Aaberg *et al* [51] has suggested that the diffusion of protons is substantial but also that a larger number of protons may be injected into zirconia to give rise to appreciable conductivity.

Two types of diffusion mechanisms for protonic transport are considered possible. The first is known as a vehicle mechanism where the protons are moving as hydroxyl groups with the oxygen ions. The second, known as the free or Grötthuss mechanism, is where the interstitial protons hop between local stationary oxygen ions, and then rotate around the oxygen to get into position for the next jump [52]. It generally considered that in the fast protonically conducting perovskites the second method occurs [52,53]. The evidence for this is that protonic conductivity has a different activation energy than oxygen ion diffusion and that there is a significant difference in the conductivity if deuterons are incorporated rather than protons [48]. It is interesting to note that the diffusivity of protons in YSZ measured by Wagner [50] in the temperature range of 850°C is very similar to that measured for oxygen diffusion [26]. This result may suggest that that in YSZ, protons may be moving as hydroxyl groups via the

vehicle mechanism. However, no isotope studies have been reported to confirm this.

4.8. References.

[1] W.D. Kingery, H.K. Bowen and D.R. Uhlmann, in Introduction to Ceramics, 2nd Edition, John Wiley and Sons, Inc., New York, (1976).

[2] Y.-M. Chiang, D. Birnie III and W.D. Kingery, in Physical Ceramics, John Wiley & Sons, Inc., New York (1997).

[3] G.E. Murch, Solid State Ionics, **Vol 7** (1982) p177.

[4] M. Weller and H. Schubert, J. Am. Ceram. Soc. **Vol 78** (1986) p573.

[5] R.J.D. Tilley, in "Defect Crystal Chemistry and its Applications", Blackie and Son Ltd., (1987) chapter 3, 60-68.

[6] P. Shewmon, in "Diffusion in Solids", 2nd Edition, The Minerals, Metals, and Materials Society (1989).

[7] L. Darken, Trans. A.I.M.E., **Vol 174** (1948) p184.

[8] J.A. Lane, Ph.D. Thesis, University of London, (1996).

[9] H.L. Tuller, in Nonstoichiometric Oxides, Ed. O.T. Sorensen, Academic Press, New York (1981) p271.

[10] S.B. Adler, J.A. Lane and B.C.H. Steele, J. Electrochem. Soc., **Vol 143** (1996) p3554.

[11] H.J.M. Bouwmeester and A.J. Burgraaf, in Fundamentals of Inorganic Membrane Science and Technology, Eds. A.J. Burgraaf and L. Cot, Elsevier Science, B.V. (1996).

[12] R.A. De Souza, Ph.D. Thesis, University of London, (1996).

[13] A.D. Le Claire, A. Rabinovitch. J. Phys. C: Solid State Phys. **Vol 14** (1981) p3862.

[14] G.R. Purdy, in Diffusion in Materials. Ed. A.L. Lasker, Kluwer Academic Publishers, Netherlands (1990) p309.

[15] N.L. Peterson. International Metals Reviews **Vol 28** (1983) p65.

[16] J.E. Bauerle. J. Phys. Chem. Solids **Vol 30** (1969) p2657.

[17] J.A. Kilner, in Proc. of the 2nd Int. Symp. On Ionic and Mixed Conducting Ceramics, Eds. T.A. Ramanarayanan, W.L. Worrel and H.L. Tuller, The Electrochemical Society, Inc., Pennington, NJ, **PV 94-12**, (1994) p174.

[18] B.-K. Kim, S.J. Park, H. Hamaguchi, J. Am. Ceram. Soc. **Vol 77** (1994) p2648.

[19] K. Ando and Y. Oshi, Solid State Ionics, **Vol 3/4** (1981) p473.

[20] W.D. Kingery, J. Pappis, M.E. Doty and D.C. Hill, J. Am. Ceram. Soc., **Vol 42** (1959) p393.
[21] L.A. Simpson and R.E. Carter, , J. Am. Ceram. Soc. **Vol 49** (1966) p139.
[22] M. Aoki, Y.-M. Chiang, I. Kosacki, J.-R. Lee, H. Tuller and Y. Liu, J.Am. Ceram. Soc. **Vol 79** (1996) p1169.
[23] P. Aberlard and J.F. Baumard, Phys. Rev. B, **Vol 26** (1982) p1005.
[24] E.N.S. Muccillo and M. Kleitz, J. Europ. Ceram. Soc. **Vol 15** (1995) p51.
[25] J.M. Ralph and J.A. Kilner, in Proc. Of the 2nd European SOFC Forum, Eds. B. Thorstensen, Oslo, Norway (1996) p773.
[26] P.S. Manning, J.D. Sirman, R.A. De Souza and J.A. Kilner, Solid State Ionics, **Vol 100** (1997) p1.
[27] J.A. Kilner and R.J. Brook, Solid State Ionics, **Vol 6** (1982) p237.
[28] S. Carter, R.J. Chater, J. Kajda, K.M. Liddicott, J.A. Kilner and B.C.H. Steele, in Proc. of the 1st Int. Symp. On Ionic and Mixed Conductors, Eds. T.A. Ramanarayanan and H. Tuller, The Electrochem. Soc. Inc., Phoenix, Arizona (1991) p84.
[29] H. Solmon, Ph.D. Thesis, Université Paris, (1992).
[30] T. Ishigaki, S. Yamauchi, K. Kishio, J. Mizusaki and K. Fueki, J. Solid State Chem., **Vol 73** (1988) p179.
[31] S. Carter, A. Selcuk, R.J. Chater, J. Kajda, J.A. Kilner and B.C.H. Steele, Solid State Ionics, **Vol 53-56** (1992) p597.
[32] I.C. Fullarton, J.A. Kilner, B.C.H. Steele and P.H. Middleton, in Proc. of the 2nd Int. Symp. On Ionic and Mixed Conducting Ceramics, Eds. T.A. Ramanarayanan, W.L. Worrel and H.L. Tuller, The Electrochemical Society, Inc., Pennington, NJ, **PV 94-12**, (1994) p9.
[33] S.J. Benson, R.J. Chater and J.A. Kilner, in Proc. of the 3rd Int. Symp. On Ionic and Mixed Conducting Ceramics, Eds. T.A. Ramanarayanan, W.L. Worrel, H.L. Tuller, M. Mogensen and A.C. Khandkar, The Electrochemical Society, Inc., Pennington, NJ, **PV 97-24**, Paris (1997).
[34] T. Ishigaki, S. Yamauchi, J. Mizusaki and K. Fueki, J. Solid State Chem., **Vol 54** (1984) p100.
[35] I. Bransky and N.M. Tallan, in Physics of Electronic Ceramics-Part A, Eds. L.L. Hench and D.B. Dove, Marcell Dekker, (1971) p67.
[36] P.M. Raccah and J.B. Goddenough, J. Appl. Phys., **Vol 39** (1967) p932.
[37] H.L. Tuller and A.S. Nowick, J. Phys. Che. Solids, **Vol 38** (1977) p859.
[38] M.H.R. Lankhorst, H.J.M. Bouwmeester and H. Verweij, Solid State Ionics, **Vol 96** (1997) p21.
[39] A.J. Bosman and J.H. van Daal, Adv. Phys., **Vol 19** (1968) p1.

[40] T. Takahashi and H. Iwahara, Rev. Chim. Miner., **Vol 17,** (1980) p243.
[41] H. Iwahara, T. Esaka, H. Uchida and N. Maeda, Solid State Ionics, **Vol 3/4,** (1981) p359.
[42] N. Bonanos, B. Ellis, K.S. Knight and M.N. Mahmood, Solid State Ionics, **Vol 35,** (1989) p179.
[43] K.D. Kreuer, E. Schönherr and J. Maier, Solid State Ionics, **Vol 70/71,** (1994) p278.
[44] N. Kurita, N. Fukatsu, K. Ito and T. Ohashi, J. Electrochem. Soc. **Vol 142,** (1995) p1552.
[45] T. Yajima, H. Suzuki, T. Yogo and H. Iwahara, Solid State Ionics, **Vol 51,** (1992) p101.
[46] T. Takahashi and H. Iwahara, Rev. Chim. Min. **Vol 17** (1980) p243.
[47] E. Ruiz-Trejo and J.A. Kilner, in Proceedings of the 17th Risø International Symposium on Materials Science, Eds. F.W. Poulsen, N. Bonanos, S. Linderoth, M. Mogensen and B. Zachau-Christiansen, Denmark (1996) p411.
[48] E. Ruiz-Trejo and J.A. Kilner, Solid State Ionics **Vol 97** (1997) p529.
[49] M. Sahibzada, R.A. Rudkin, B.C.H. Steele, I.S. Metcalfe and J.A. Kilner, in Proc. of the 5th International Symposium on SOFC, Eds. U. Stimming, S. Singhal, H. Tagawa and W. Lehnert, The Electrochemical Society, Inc., **PV 97-40**, Aachen, (1997) p244.
[50] C. Wagner, Ber. Bunsenges. Physik. Che. **Vol 72** (1968) p778.
[51] R.J. Aaberg, R. Tunold, S. Tjelle and R. Ødegård, in Proceedings of the 17th Risø International Symposium on Materials Science, Eds. F.W. Poulsen, N. Bonanos, S. Linderoth, M. Mogensen and B. Zachau-Christiansen, Denmark (1996) p511.
[52] T. Norby and Y. Larring, in British Ceramic Proceedings, Vol 56, Ed. B.C.H. Steele, University Press, Cambridge, (1996) p83.
[53] K.D. Kreuer, T. Dippel, Y. Baikov and J. Maier, Solid State Ionics, **Vol 86-88** (1996) p613.

5. Cation Diffusion in Fluorite Oxides.

5.1. Introduction.

In comparison to the study of anion transport in fluorite oxides, the amount of investigation into cation diffusion in fluorites has been remarkably small, especially considering the ultimate long term stability of a COG or SOFC is determined by the diffusion of cations. Furthermore, much of the work that has been published is contradictory. Also of interest is the reactivity between the electrodes and the electrolyte, and the solubility of electrode components in the electrolyte. In this chapter, the published literature concerning electrode/electrolyte reactivity, solubility of transition metal cations (Mn, Co and Fe) in fluorites and diffusion of cations in YSZ and CGO are discussed.

5.2. Electrode/Electrolyte Reactivity.

The stability of perovskite oxide cathode materials with YSZ have been extensively studied, due to its importance on the long term performance of a high temperature SOFC [1,2,3,4,5,6,7,8]. Most of the work has concentrated on strontium or calcium doped lanthanum manganite, as it is the favoured high temperature cathode material to be used with YSZ. However, strontium and calcium doped lanthanum manganite both react with YSZ to form the pyrochlore $La_2Zr_2O_7$ [1,6] and at higher strontium dopant levels $SrZrO_3$ [4,9].

The formation of these two high impedance phases is due to the manganese diffusing from the doped lanthanum manganite into the YSZ. Taimatsu *et al* [5] showed by electron probe micro-analysis (EPMA) that manganese diffuses more rapidly into YSZ than lanthanum, thus leaving a lanthanum rich phase to react with the YSZ. Takeda *et al* [6] stated that for long term reactions, calcium doped lanthanum manganites tend to react more strongly with YSZ than strontium doped lanthanum manganites (LSM). Takeda *et al* also showed that the formation of $La_2Zr_2O_7$ decreases with increasing strontium content. The formation of $La_2Zr_2O_7$ may be impeded by using an A-site deficient LSM as an electrode [3,10]. However, this may be accompanied by an increase in the rate of diffusion of manganese into YSZ.

Strontium doped lanthanum ferrite (LSF) has been shown to react with YSZ at 1100°C to form $SrZrO_3$ [2]. Kindermann *et al* has done a systematic study of the chemical compatibility of $La_{0.6}Sr_{0.4}Fe_{0.8}M_{0.2}O_{3-\delta}$ [7], (M=Cr,Mn,Co,Ni). In this work, they show that the cobalt doped sample has the most reactivity, followed by the nickel doped, then the chromite and the least reactive is the sample doped with manganese. They state that this is due to the relative stability of the $SrMO_3$ phase. In their work, Kindermann *et al* also study the A-site deficient materials. In this case there is reduced reactivity for the chromium and manganese doped samples, but no appreciable change for the nickel or cobalt doped samples.

There is very little work on the reactivity of perovskite electrodes with CGO. Lane [11] completed an initial study on the reaction of $La_{0.6}Sr_{0.4}Fe_{0.8}Co_{0.2}O_{3-\delta}$ with CGO. The study was carried out at 1200°C for 12 hours, but no reaction products were detected using XRD.

5.3. Solubility of Transition Metal Cations in YSZ and CGO.

The solubility of manganese in YSZ has been studied by several workers [12,13,14]. Kawada [12] showed that the solubility of manganese in YSZ varies significantly from 1000°C to 1500°C. At 1000°C, the solubility is around 5 mol% and at 1500°C it is as high as 15 mol%. Appel [13] has shown that the solubility of manganese in YSZ is at least 10 mol%, while Waller *et al* [14] gave the solubility limit as around 7 mol%. The data of Waller *et al* is illustrated in figure 5.1. It shows clearly a decrease in the lattice parameter with increasing manganese content, as expected from Vegard's Law, followed by a deviation from linearity as the solid solution reaches its solubility limit [15]. The fact that the lattice parameter decreases with the introduction of manganese suggests that the smaller manganese ion sits on a host cation site, rather than existing as an interstitial.

There is less data available on the solubility of other transition metal cations in YSZ, presumably due to the unsuitability of other $R_ET_MO_3$ as cathode materials due to their reactivity with YSZ. There is also very sparse data concerning the solubility limit of transition metals in CGO. Naumovic *et al* [16] quote the solubility limit of both manganese and cobalt in CGO to be around 10 mol%, stating that a second phase is formed above these compositions. However, they

show no X-ray patterns, nor do they calculate the lattice parameters associated with the varying compositions examined.

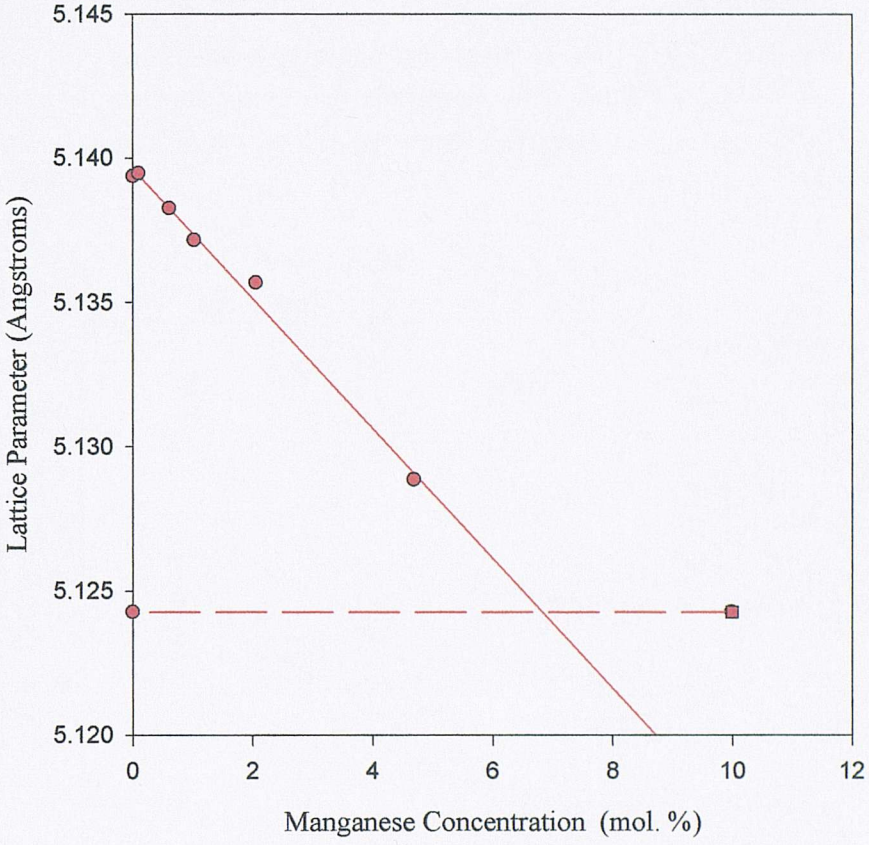


Figure 5.1. Lattice parameter of Mn doped YSZ as a function of Manganese content [14].

5.4. Cation Diffusion in Fluorites.

There is very little work published on transition metal cation diffusion in YSZ and essentially none on CGO. Lau and Singhal [1] have done a preliminary study on manganese diffusion in polycrystal and single crystal YSZ using EPMA. However, their study was limited to one temperature for each type of sample. More recently, Waller *et al* have undertaken a study of manganese diffusion in polycrystal YSZ using Raman spectroscopy [14].

There is more work completed on the tracer diffusion of zirconium and yttrium ions in YSZ. Kilo *et al* [17] have investigated zirconium diffusion in 10 mol% and 24 mol% YSZ using SIMS. Solmon [18] studied both zirconium and yttrium diffusion, also using SIMS in 9.5 mol% and 17.7 mol% YSZ. Dimos and Kohlstedt [19] used a study of creep behaviour to calculate the effective diffusion coefficient of cations assuming zirconium and yttrium had the same rate of diffusion. Figure 5.2 shows the apparent diffusion coefficient obtained for the various materials.

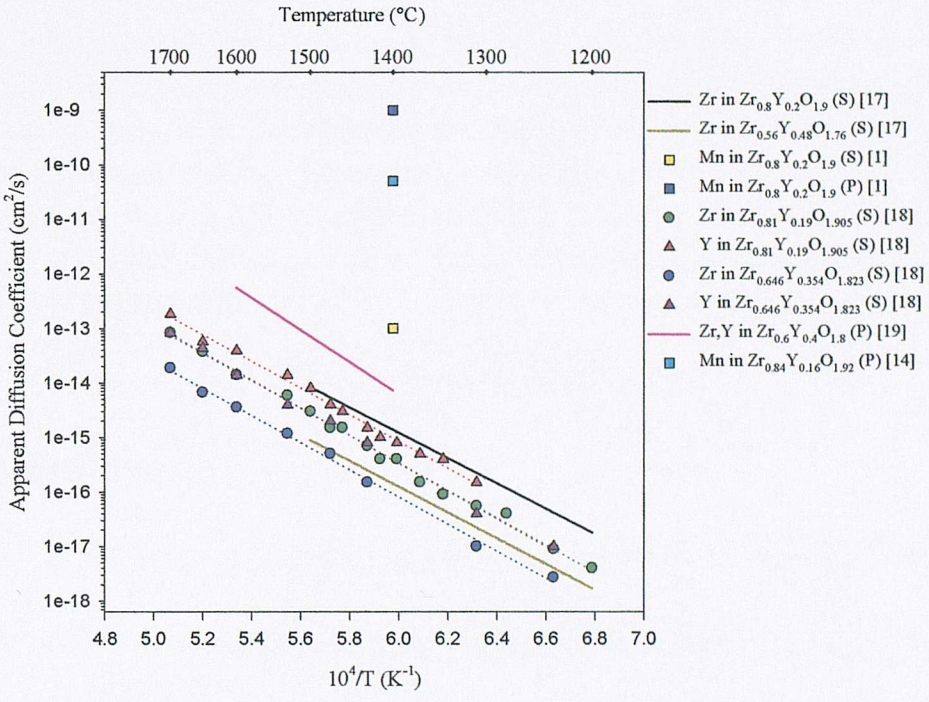


Figure 5.2. Graph of the apparent diffusion coefficient of Mn, Y, and Zr in YSZ [1,14,17,18,19], (P) indicates a polycrystal and (S) a single crystal.

The term "apparent diffusion coefficient" has been used as a variety of diffusion coefficients have been measured, i.e. tracer, solute and self-diffusion. It is immediately clear from figure 5.2 that the diffusion of manganese is substantially more rapid than the diffusion of zirconium or yttrium. This is particularly the case for polycrystalline materials, suggesting that the predominant diffusion path is the grain boundaries. Enhanced grain boundary diffusion of manganese has also been found by Miliken *et al* [20]. It is also evident from Dimos and Kohlstedt that diffusion of zirconium and yttrium is more rapid in a polycrystalline material, although it is noted from the data of Solmon that their

assumption that the diffusion of zirconium and yttrium are the same, is not entirely accurate. The data of Solmon shows that the diffusion of yttrium is about a factor of four faster than the diffusion of zirconium over the entire temperature range given here. It should be noted that the tracer diffusion coefficients measured by Solmon [18] and Kilo [17] all fall within a similar range and have very similar activation energies (~ 450-480 kJ/mol), despite the variety of compositions examined. The activation energy for diffusion of zirconium and yttrium in the polycrystalline sample (560 kJ/mol) is noticeably larger than for the single crystals.

An initial study of cation diffusion has been completed, in conjunction with Dr. D. Waller, as part of this study for completeness of the mass transport properties of electrolytes, and to determine the electrode/electrolyte compatibility of the materials being studied. Some of this work was published in the proceedings of the 5th International Symposium on SOFC [21,22]. The results of this initial study on cation diffusion and on the solubility of cobalt and iron in CGO are given in appendix A.

5.5. References.

[1] S. K. Lau and S.C. Singhal, in Proc. Corrosion 85, Boston, (1985) paper 345.

[2] O. Yamamoto, Y. Takeda, R. Kanno and M. Noda, Solid State Ionics, **Vol 22** (1987) p241.

[3] O. Yamamoto, Y. Takeda, R. Kanno and T. Kojima, in Proc. of the 1st Int. Symp. On SOFC, Ed. S.C. Singhal, The Electrochemical Society, Inc., Pennington, NJ, (1989) p242.

[4] J.A.M. van Roosmalen and E.H.P. Cordfunke, Solid State Ionics, **Vol 52** (1992) p303.

[5] H. Taimatsu, K. Wada, H. Kaneko and H. Yamamura, J. Am. Ceram. Soc., **Vol 75** (1992) p401.

[6] Y. Takeda, Y. Sasaki, T. Ichikawa, N. Imanishi, O. Yamamoto, M. Mori, N. Mori and T. Abe, , Solid State Ionics, **Vol 72** (1994) p303.

[7] L. Kindermann, D. Das, H. Nickel and K. Hilpert, , Solid State Ionics, **Vol 89** (1996) p215.

[8] M. Hrovat, N. Katsarakis, K. Reichmann, S. Bernik, D. Kuscer and J. Holc, Solid State Ionics, **Vol 83** (1996) p99.

[9] K. Wiik, C.R. Schmidt, S. Shamsili, M.-A. Einarsrud and T. Grande, in Proc. of the 17th Risø Int. Symp. on Materials Science, Eds. F.W. Poulsen, N. Bonanos, S. Linderoth, M. Mogensen and B. Zachau-Christiansen, Denmark (1996) p491.

[10] C. Clausen, C. Bagger, J.B. Bilde-Sørensen and A. Horsewell, Solid State Ionics **Vol 70/71** (1994) p59.

[11] J.A. Lane, Ph.D. Thesis, University of London (1996).

[12] T. Kawada, N. Sakai, H. Yokokawa and M. Dokiya, Solid State Ionics **Vol 53-56** (1992) p418.

[13] C.C. Appel, Ionics **Vol 1** (1995) p406.

[14] D. Waller, S. Webb, J.D. Sirman and J.A. Kilner, presented at the 11th Int. Conf. On Solid State Ionics, Honolulu (1997).

[15] A.R. West, in Solid State Chemistry and its Applications, John Wiley and Sons Ltd., Chichester, (1984).

[16] E.N. Naumovich, V.V. Kharton, A.V. Kovalevsky and V.V. Samokhval, in Proc. of the 17th Risø Int. Symp. on Materials Science, Eds. F.W. Poulsen, N. Bonanos, S. Linderoth, M. Mogensen and B. Zachau-Christiansen, Denmark (1996) p375.

[17] M. Kilo, G. Borchardt, S. Weber, S. Scherrer and K. Tinschert, in Solute Point-Defect Interactions, Loccum (1997) p1.

[18] H. Solmon, Ph.D. Thesis, L'Université Paris. (1992).

[19] D. Dimos and D.L. Kohlstedt, J. Am. Ceram. Soc., **Vol 70** (1987) p531.

[20] C. Miliken, D. Tucker, S. Elangovan and A. Khandar, in Ext. Abstracts of 1990 Fuel Cell Seminar Phoenix, Arizona (1990) p218.

[21] J.D. Sirman, D. Waller and J.A. Kilner, in Proc. of the 5th International Symposium on SOFC, Eds. U. Stimming, S. Singhal, H. Tagawa and W. Lehnert, The Electrochemical Society, Inc., **PV 97-40**, Aachen, (1997) p1159.

[22] D. Waller, J.D. Sirman and J.A. Kilner, in Proc. of the 5th International Symposium on SOFC, Eds. U. Stimming, S. Singhal, H. Tagawa and W. Lehnert, The Electrochemical Society, Inc., **PV 97-40**, Aachen, (1997) p1140.

6. Oxygen Exchange on Oxide Surfaces.

6.1. Introduction.

The mechanism of oxygen exchange on perovskite and fluorite oxide surfaces is not a well understood process. Unlike the diffusion of oxygen, where the process can be described in terms of atomistic parameters (see chapter 4), there is no model which explicitly describes the wide range of experimental data on the exchange process. This is in part due to the fact that until recently, the importance of the rate of oxygen exchange on flux densities in oxygen separation membranes and polarisation losses at cathodes, was not realised. It is also due to the fact that the measurement of the oxygen exchange rate in general requires the use of tracer isotopes and specialised UHV equipment which is not widely available.

The oxygen exchange process between a gaseous oxygen species O^1 and lattice oxygen O^2 can simply be described as,

$$O_{2\,gas}^{1} + 2O_{solid}^{2} \leftrightarrow O_{2\,gas}^{2} + 2O_{solid}^{1} \qquad \text{eqn. (6.1)}$$

The result of this process cannot be seen unless one of the two oxygen species above, O^1 or O^2, is labelled. The most common method of labelling an oxygen species is to use an oxygen gas isotopically enriched with an ^{18}O species. Thus equation 6.1, becomes,

$$O_{2\,gas}^{18} + 2O_{solid}^{16} \leftrightarrow O_{2\,gas}^{16} + 2O_{solid}^{18} \qquad \text{eqn. (6.2)}$$

The oxygen in the gas phase is in the form of a molecule and in the solid phase it exists as an ion. The gaseous oxygen can either exchange with two oxygen ions as a molecule, in which case the formation ^{16}O-^{16}O molecules will be seen in the gas phase; or one oxygen atom of the molecule can exchange with one oxygen ion in the solid, producing an ^{16}O-^{18}O molecule. These two processes are shown in figure 6.1.

In figure 6.1, the blue circle represents an ^{18}O species, the red circle an ^{16}O species and the small black circle a M^{2+} cation. Figure 6.1 (a) shows a MO

sample before exchange has taken place. Figure 6.1 (b) shows the situation where atoms of oxygen exchange with oxygen ions on the surface of the solid (atomic exchange) and figure 6.1 (c) shows the situation where oxygen molecules exchange with the surface of the solid (molecular exchange).

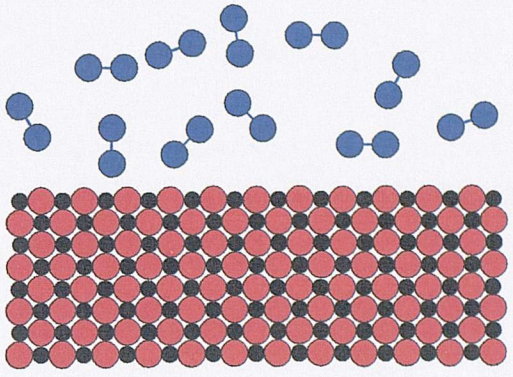


Figure 6.1 (a)

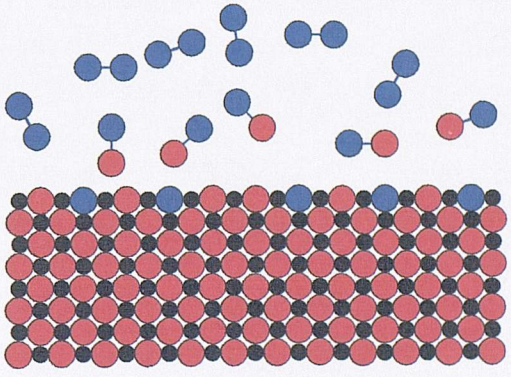


Figure 6.1 (b)

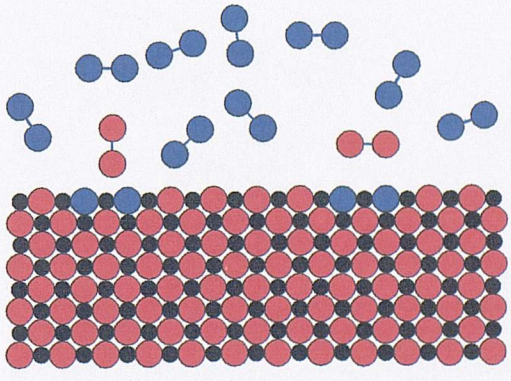


Figure 6.1 (c)

Figure 6.1. Schematic illustration of the exchange process described by equation 6.2.

The process illustrated in figure 6.1 (b) can be represented by equation 6.3 while equation 6.4. represents that seen in figure 6.1 (c).

$$O^{18}_{2,(gas)} + 2O^{16}_{solid} \leftrightarrow \{O^{18} - O^{16}\}_{(gas)} + O^{18}_{solid} + O^{16}_{solid} \qquad \text{eqn. (6.3)}$$

$$O^{18}_{2,(gas)} + 2O^{16}_{solid} \leftrightarrow O^{16}_{2,(gas)} + 2O^{18}_{solid} \qquad \text{eqn. (6.4)}$$

Thus with atomic exchange, the formation of $^{34}O_2$ molecules would be expected whereas with molecular exchange only $^{32}O_2$ molecules would be anticipated to form.

In figure 6.1, it has been assumed there are no preferred sites for adsorption and that there are no defects present in either the bulk or on the surface of the crystal. It also does not include any intermediate stages which may occur in the process of exchange. In the materials of technological importance there are defects present, and in many cases at high concentrations. In the following discussion it is assumed that the only mobile anion defect is an oxygen vacancy.

Figure 6.2 shows a schematic illustration of a heavily acceptor doped oxide (similar to the defects expected in fluorite electrolytes and perovskite cathodes). In this figure it has been assumed that there are no surface structure or segregation effects (i.e. the surface represents a simple termination of the bulk of the crystal) and that there are no interactions between the defects in the crystal (i.e. there is a random distribution of oxygen vacancies). In the following figures the host cations are black and the dopant cations are green.

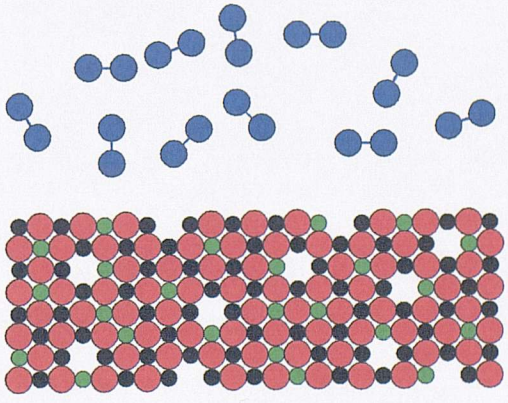


Figure 6.2. Schematic illustration of a defective crystal in the presence of a labelled gas.

Figure 6.3. shows a possible exchange process for a defective crystal. In this case atomic exchange occurs and the site for oxygen adsorption is an oxygen vacancy. Figure 6.4 also illustrates a situation where an oxygen vacancy is the preferred site for adsorption, but on this occasion molecular exchange is represented. It is evident that for this to occur, a second surface oxygen vacancy must migrate to a position adjacent to where the first part of the exchange took place or (as is shown in figure 6.4 (c)) a surface oxygen ion must rotate around a surface cation. The mobility of surface oxygen vacancies will affect which process occurs.

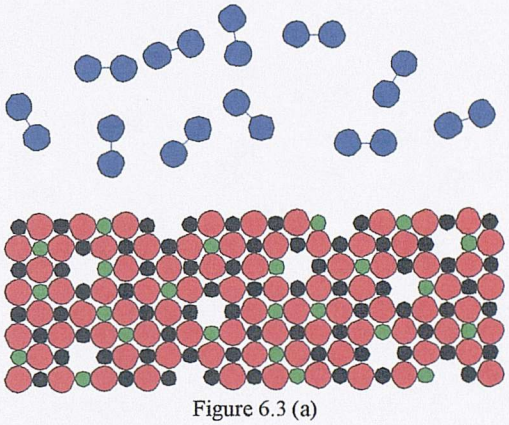


Figure 6.3 (a)

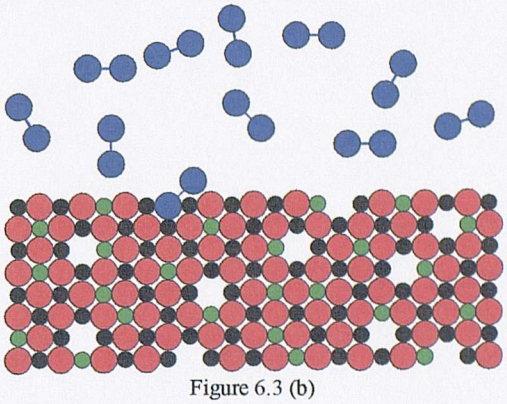


Figure 6.3 (b)

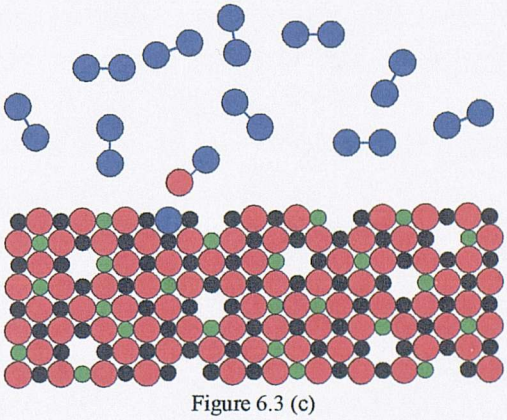


Figure 6.3 (c)

Figure 6.3. Schematic illustration of atomic exchange on a defective crystal where a surface oxygen vacancy is the preferred site for adsorption.

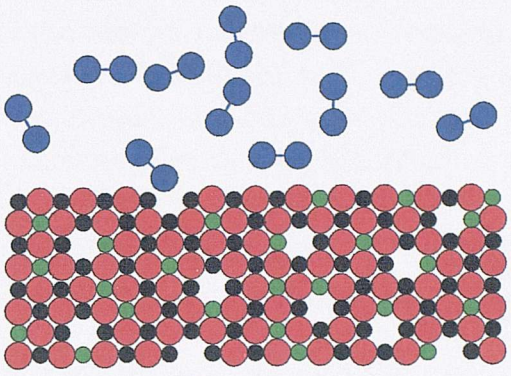


Figure 6.4 (a)

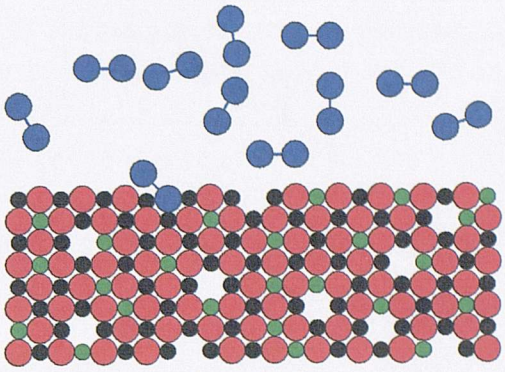


Figure 6.4 (b)

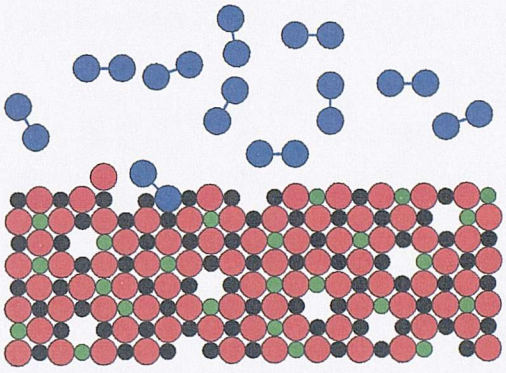


Figure 6.4 (c)

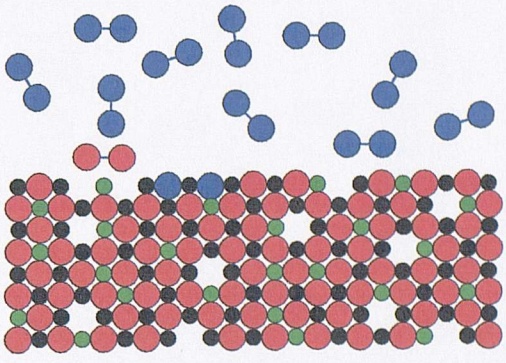


Figure 6.4 (d)

Figure 6.4. Schematic illustration of molecular exchange on a defective crystal where a surface oxygen vacancy is the preferred site for adsorption.

The rates of the various steps in the reaction will determine if molecular or atomic exchange takes place. If the adsorbed O_2 molecule has a long residence time in the vacancy and if surface oxygen vacancies are mobile, a second oxygen vacancy is likely to become available for exchange, thus making molecular exchange possible. If surface oxygen vacancies are not mobile or the oxygen molecular bond is easily broken so there is a short residence time for the adsorbed species then atomic exchange is more likely.

If the exchange process involves a surface oxygen vacancy then it can be represented by equations 6.5 or 6.6.

$$\tfrac{1}{2}O_{2,(gas)} + V^{\times}_{O,surf} \leftrightarrow O^{\times}_{O,surf} \qquad \text{eqn. (6.5)}$$

or

$$\tfrac{1}{2}O_{2,(gas)} + V^{\bullet\bullet}_{O,surf} + 2e^{'} \leftrightarrow O^{\times}_{O,surf} \qquad \text{eqn. (6.6)}$$

Equation 6.5 represents the scenario where the oxygen vacancy is neutral and electrons are trapped at the vacancy while equation 6.6 represents the case were the oxygen vacancy has an effective 2^+ charge, as is the case in the bulk of the material. Electrons are thus required to charge balance equation 6.6. It is readily seen from equations 6.5 and 6.6 that if a surface oxygen vacancy is the site for oxygen adsorption, then the concentration of oxygen vacancies will affect the rate of exchange of oxygen.

An alternative to the mechanism where a surface oxygen vacancy is involved can also be given. In this case there is no preferred adsorption site, the oxygen adatom can sit on what is effectively a new surface site. One possible process for atomic adsorption is illustrated in figure 6.5.

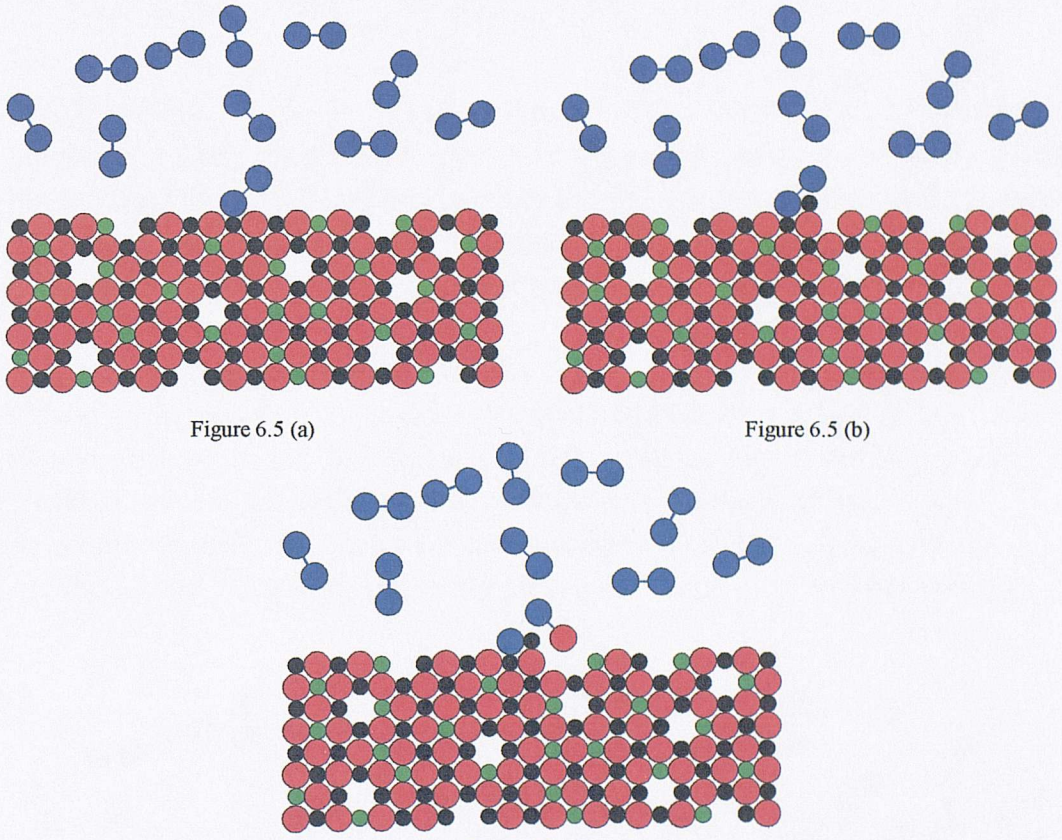


Figure 6.5 (a)

Figure 6.5 (b)

Figure 6.5 (c)

Figure 6.5. Schematic illustration of atomic exchange on a defective crystal with no preferred sites for adsorption.

The process illustrated in figure 6.5 can be represented by equations 6.7 and 6.8.

$$O_{2,(gas)} \leftrightarrow 2O_{ad} \qquad \text{eqn. (6.7)}$$

$$2O_{ad} + O^{\times}_{O,surf} \leftrightarrow O_{2,(gas)} + O^{\times}_{O,new\ surf} + V_O^{\bullet\bullet} + V_M^{''} \qquad \text{eqn. (6.8)}$$

From figure 6.5 it is clear that a cation must rotate around an anion thus effectively forming a surface cation vacancy. It is also clear that a surface oxygen vacancy is created, thus the surface is modified but its charge neutrality is not affected. This can be envisaged as a form of Schottky disorder occurring at the surface of the crystal rather than in the bulk.

For a fluorite material, equation 6.8 is represented by,

$$4O_{ad} + 2O^{\times}_{O,surf} \leftrightarrow 2O_{2,(gas)} + 2O^{\times}_{O,new\ surf} + 2V_O^{\bullet\bullet} + V_M^{''''} \qquad \text{eqn. (6.9)}$$

The formation of $V_M^{''''}$ is a high energy process, thus making this exchange process less likely for a fluorite material. Figure 6.6. shows the same procedure but this time the molecular bond between the ^{18}O-^{18}O is considered to be stronger than the attraction between the adsorbed oxygen and a surface oxygen atom. Thus a new ^{16}O-^{16}O molecule is formed and two ^{18}O ions enter the crystal.

The procedure is very similar but this time two cations are required to rotate around an oxygen ion. Figure 6.6 (b) simply shows the rotation of two cations around an oxygen ion to equivalent surface sites. Figure 6.6 (c) shows the breaking of the molecular bond to form two surface oxygen ions. Two neighbouring surface oxygen ions can then combine to form an oxygen molecule and the second ^{18}O species can rotate around the cation to sit on a vacated site.

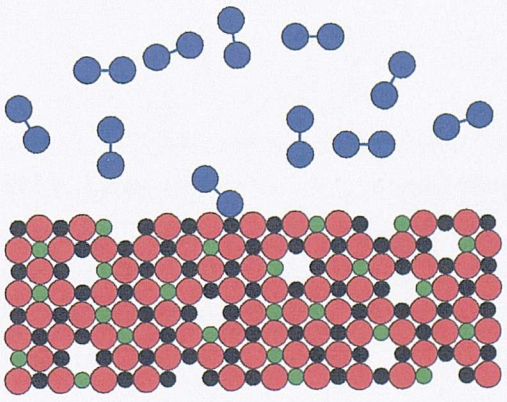


Figure 6.6 (a)

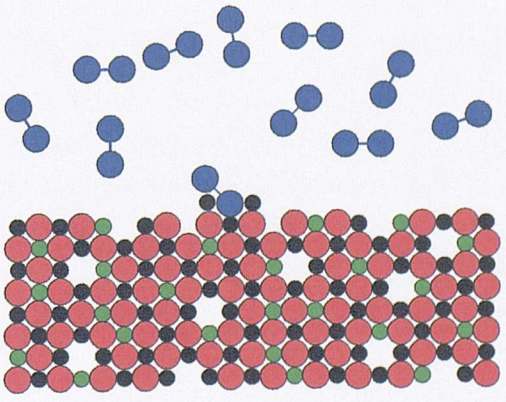


Figure 6.6 (b)

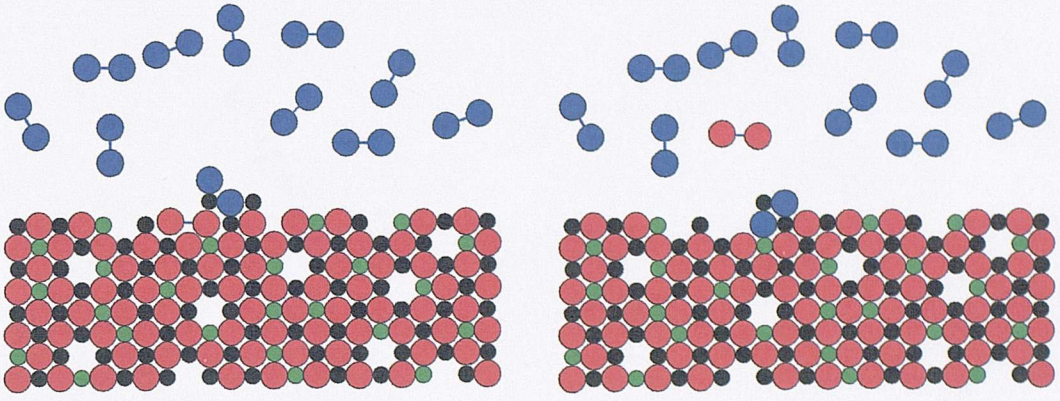


Figure 6.6 (c) Figure 6.6 (d)

Figure 6.6. Schematic illustration of molecular exchange on a defective crystal with no preferred sites for adsorption.

It is essentially the relative strength of the ^{18}O-^{18}O molecular bond to the adatom – $O_O^{\times}$ bond which will determine whether atomic adsorption or molecular adsorption occurs.

The movement of cations (even at the surface of a crystal) requires more energy than anion motion. Therefore the processes depicted by figures 6.5 and 6.6 are less energetically favourable than those given by figures 6.3 and 6.4 which does not require cation motion.

In the above scenarios depicted in figures 6.3-6.6, the ^{18}O must subsequently be incorporated into the bulk of the solid. This can occur by the simple exchange of a bulk oxygen vacancy to the surface and the accompanying movement of the oxygen ion. This is given by equation 6.10 and illustrated schematically in figure 6.7.

$$O_{O,surf}^{\times} + V_{O,bulk}^{\bullet\bullet} \leftrightarrow O_{O,bulk}^{\times} + V_{O,surf}^{\bullet\bullet} \qquad \text{eqn. (6.10)}$$

Figure 6.7 (a) shows the exchanged oxygen sitting on a surface site. Figure 6.7 (b) shows simply the random migration of an oxygen vacancy to a site which now neighbours the labelled oxygen ion. Figure 6.7 (c) then shows the labelled oxygen ion jumping into the newly vacated site and hence is incorporated into the bulk of the material Figure 6.7 (d) shows the result of this process at some given time after the exchange reaction has taken place.

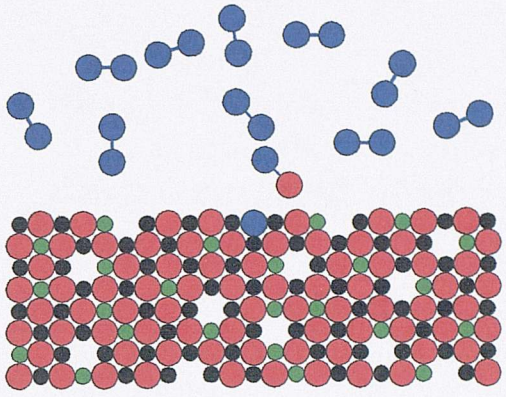


Figure 6.7 (a)

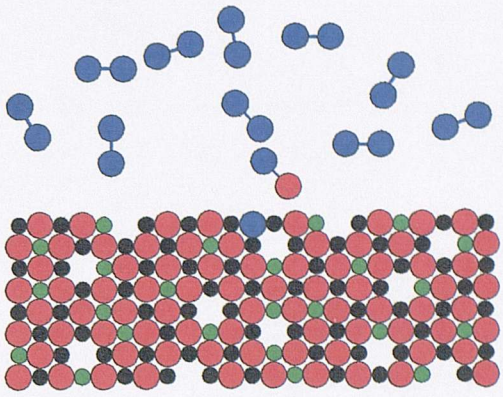


Figure 6.7 (b)

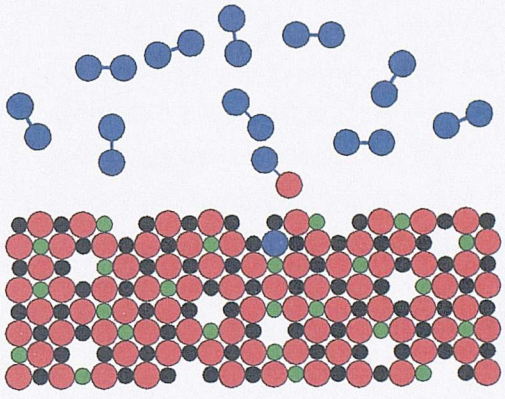


Figure 6.7 (c)

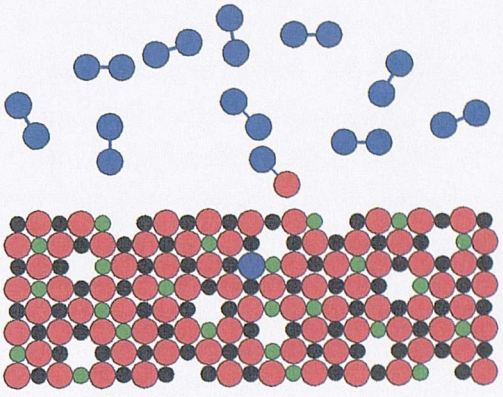


Figure 6.7 (d)

Figure 6.7. Schematic illustration of an adsorbed surface oxygen being incorporated into the bulk of the material.

It is apparent from the above argument that irrespective of whether a surface oxygen vacancy is the active site for adsorption, the overall rate of exchange will depend to some extent on the concentration and mobility of oxygen vacancies in the bulk (and hence by implication at the surface).

The above models represent a very simplistic approach to the behaviour of the oxygen exchange process given by equation 6.2. Returning to equation 6.2 and using the information from figure 6.7 and equation 6.10, the forward reaction of this process can be given by equation 6.11.

$$\tfrac{1}{2}O_{2,(gas)} + V^{\bullet\bullet}_{O,bulk} + 2e' \rightarrow O^{\times}_{O,bulk} \qquad \text{eqn. (6.11)}$$

and the reverse of what is essentially a redox reaction may be regarded as,

$$O^{\times}_{O,bulk} \rightarrow \tfrac{1}{2}O_{2,(gas)} + V^{\bullet\bullet}_{O,bulk} + 2e^{'} \qquad \text{eqn. (6.12)}$$

It is very important to note that there is no net charge transfer in this process, it is merely an equilibrium chemical reaction resulting from the random collisions of gaseous molecules with an oxide surface.

6.2. The Surface Exchange Coefficient.

In order to compare the rate at which reaction 6.2. occurs for a variety of materials it is necessary to have one single continuum parameter which is a function of the process as a whole. It must therefore not depend on which atomistic step is rate limiting in the process, but instead represent a continuum approach to the reaction. Thus a constant of proportionality between the flux across the exchange surface and the difference between the concentration of ^{18}O in the gas phase and the surface of the sample can be used to represent the rate at which reaction 6.2 occurs. Thus, the flux across the surface of the sample can be represented by,

$$J_{exchange} = k\left(C_{gas} - C_{surface}\right) \qquad \text{eqn. (6.13)}$$

where k is the constant of proportionality, C_{gas} and $C_{surface}$ are the concentration of ^{18}O in the gas and at the surface of the solid, respectively, expressed as site fractions. Note that k is a continuum parameter and is not dependent on the atomistic mechanism by which the flux occurs.

It should also be noted that in the experiments in which the exchange (and diffusion) fluxes are measured the solid sample is in equilibrium with the gas, such that the total oxygen chemical potentials are equal. Thus there is no net flux of oxygen [1].

The flux across the exchange surface of the sample must be equal to the flux from the surface of the sample into the bulk. This flux is given by Fick's first law (see equations 4.6 and 4.7) such that,

$$J_{exchange} = J_{bulk} = -D_T \frac{\partial C(x)}{\partial x}\Big|_{x=0} \qquad \text{eqn. (6.14)}$$

where D_T is the tracer diffusion coefficient of the ^{18}O species and C(x) is the concentration of the ^{18}O species at some distance, x into the sample. Note that C(x) at $x = 0$ is equivalent to $C_{surface}$ in equation 6.13. Therefore we can obtain equation 6.15, where,

$$k\left(C_{gas} - C_{surface}\right) = -D_T \frac{\partial C(x)}{\partial x}\Big|_{x=0} \qquad \text{eqn. (6.15)}$$

which can be regarded as a boundary condition.

The time dependent, one dimensional diffusion equation as given by Fick's 2nd law, is,

$$D_T \frac{\partial^2 C(x,t)}{\partial x^2} = \frac{\partial C(x,t)}{\partial t} \qquad \text{eqn. (6.16)}$$

such that after a time, t, the concentration of ^{18}O at the surface of the solid is not equal to the concentration some distance, x, into the solid. Thus equation 6.15 should more correctly be written to include a time dependency on concentration,

$$k\left(C_{gas} - C_{surface}(t)\right) = -D_T \frac{\partial C(x,t)}{\partial x}\Big|_{x=0} \qquad \text{eqn. (6.17)}$$

It can be seen that the constant of proportionality has the units cm/s and is known as the surface exchange coefficient. Under the experimental conditions which are generally used in the literature, and those used to obtained the diffusion results presented later in this work, the diffusion of ^{18}O is accurately described by Fick's second law. (The details of the experimental set-up will be described in chapter 7.) The basic assumption in the experiment are that there is a large volume of gas such that C_{gas} is independent of time. In order to solve Fick's 2nd law an initial condition must be stipulated. This is that before the experiment begins, the solid contains the background level of ^{18}O, represented by equation 6.18.

$$C(x,0) = C_{bg} \qquad \text{eqn. (6.18)}$$

where C_{bg} is the natural isotopic abundance of ^{18}O (0.204%). It is also assumed the solid is thick enough to behave as a semi-infinite medium (i.e. the exchange

surface is at $x = 0$ and at some distance into the sample the concentration of ^{18}O does not increase above the background level). This can be given by equation 6.19.

$$C(\infty, t) = C_{bg} \qquad \text{eqn. (6.19)}$$

Using the initial condition and the boundary condition given in equations 6.18 and 6.17, respectively, then equation 6.16 can be solved. The solution has been given by Crank [2] as,

$$\frac{C(x) - C_{bg}}{C_g - C_{bg}} = \text{erfc}\left\{\frac{x}{2\sqrt{D_T t}}\right\} - \exp\left(hx + h^2 D_T t\right)\text{erfc}\left\{\frac{x}{2\sqrt{D_T t}} + h\sqrt{D_T t}\right\} \qquad \text{eqn. (6.20)}$$

where $h = {}^{k}\!/_{D_T}$.

Almost all of the data published on the tracer diffusion and surface exchange coefficients have been solved using the above solution to Fick's 2nd law of diffusion. Some of the early data did not include a surface limiting step, and there is a significant amount of data where short circuit paths are evident from analysis of the data. Rapid diffusion along a one dimensional line defect or through a planar defect such as a grain boundary combined with slow diffusion in the bulk lead to additional terms in the solution of the diffusion equation (see for example [3,4,5]). In fast anion conductors significant contributions from dislocation or grain boundary diffusion is seldom evident.

It is an interesting aside to note that at any given time, t, the concentration of ^{18}O at the surface is not only dependent upon the surface exchange coefficient but also on the tracer diffusion coefficient. This is illustrated simplistically, but effectively in figures 6.8 and 6.9.

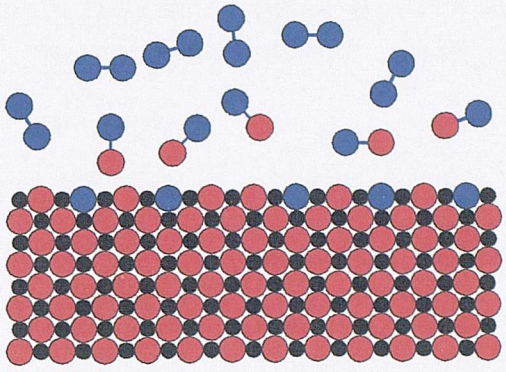


Figure 6.8 (a)

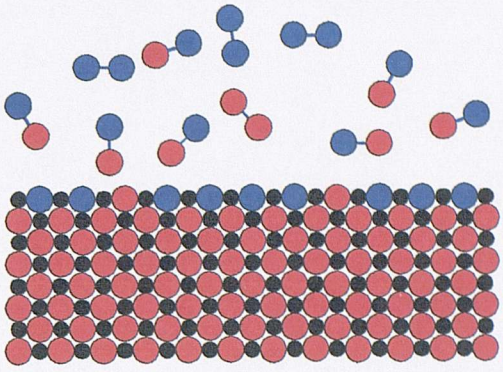


Figure 6.8 (b)

Figure 6.8. Schematic illustration of the exchange process (with no subsequent diffusion) for a slow exchanger (a) and a fast exchanger (b)

In figure 6.8 (a) the rate of exchange is slow (only five atoms have exchanged) and as a result the concentration of ^{18}O on the surface is small. However, in figure 6.8 (b) the exchange rate is fast such that the surface concentration of ^{18}O is high. The diffusion coefficient has been kept constant and very small such that no ions have yet diffused into the bulk. In figure 6.9 the exchange rate has been kept constant. However, in figure 6.9 (a), the surface concentration is high because very few ^{18}O ions have diffused into the solid (i.e. a small tracer diffusion coefficient) whereas in figure 6.9 (b), the concentration of ^{18}O at the surface is significantly lower, due to the rapid transport of ^{18}O away from the surface. Note that even though the exchange rate is kept constant, more ^{18}O has exchanged in figure 6.9 (b). This is because the ^{18}O exchange flux is proportional to $\left(C_{gas} - C_{surface}\right)$ so that as the surface concentration increases, so the exchange flux will decrease.

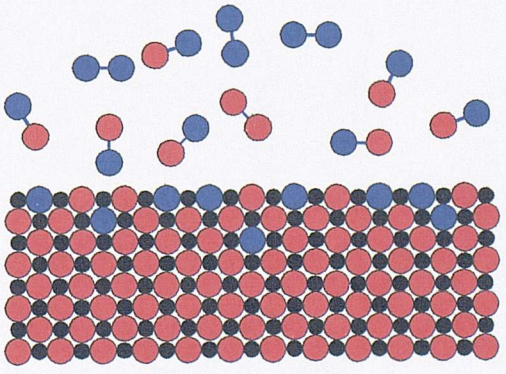


Figure 6.9 (a)

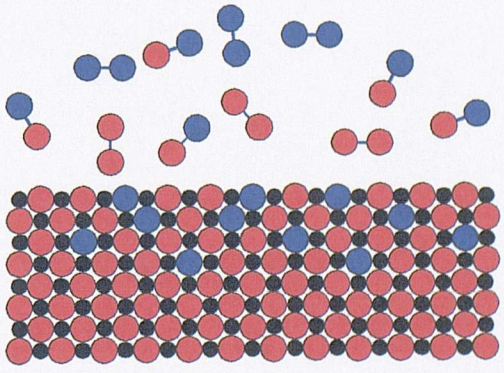


Figure 6.9 (b)

Figure 6.9. Schematic illustration of the exchange process for a slow diffuser (a) and a fast diffuser(b) where the exchange coefficient is constant.

A more mathematical approach has been given by Kilner [1] who expresses the solution to the diffusion equation at $x = 0$, such that,

$$\frac{C(0) - C_{bg}}{C_g - C_{bg}} = 1 - \exp\left(h^2 D_T t\right)\mathrm{erfc}\left\{h\sqrt{D_T t}\right\} \qquad \text{eqn. (6.21)}$$

from which it can be seen that the surface concentration has a positive dependence on k and an inverse dependence on D_T. Kilner has subsequently gone on to plot the surface concentration in terms of a dimensionless parameter dependent upon D_T and k which he calls h', where

$$h' = h\sqrt{D_T t} \qquad \text{eqn. (6.22)}$$

From figure 6.10 it can be seen that the surface concentration asymptotically approaches the concentration of the gas. It is also evident that the there is a range of D_T and t, where any increase in k will have very little effect on the concentration of ^{18}O at the surface of the sample. From equation 6.21, some of the limitations of the SIMS instrument for oxygen exchange work can be determined. These will be discussed in more detail in Chapter 7.

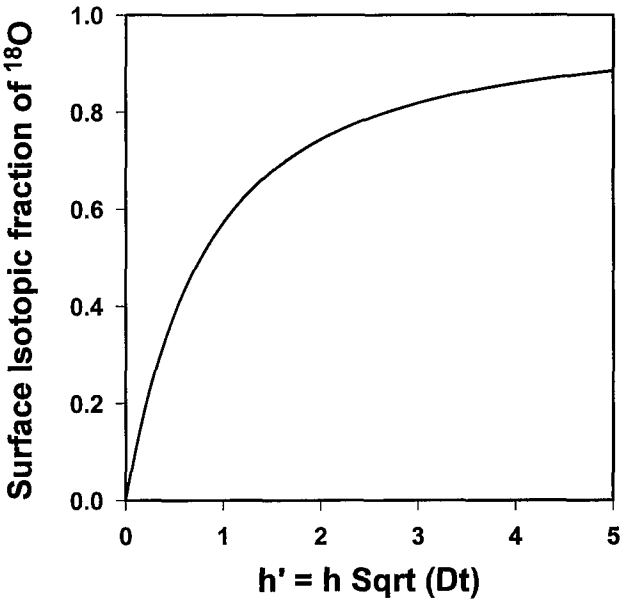


Figure 6.10. The surface isotopic fraction as a function of the dimensionless parameter h' [1].

6.3. Experimental Behaviour of k for Perovskite Oxides.

The experimental behaviour of the surface exchange coefficient as a function of temperature for several $R_ET_MO_3$ perovskites has been reasonably well documented. This is because of the importance of this parameter in determining the oxygen fluxes through thin dense ceramic membranes [6,7,8] and MEIC cathode polarisation resistances [9,10]. However, there are not many methods available for measuring this parameter, the two primary techniques being gas phase analysis and SIMS. Figure 6.11 shows the behaviour of the surface exchange coefficient as a function of temperature for a selected variety of $R_ET_MO_3$ perovskites. In this figure all the data has been obtained using SIMS. This is because the surface exchange coefficient calculated from gas phase analysis has been obtained, by necessity at a low pO_2. The importance of this will become clear shortly.

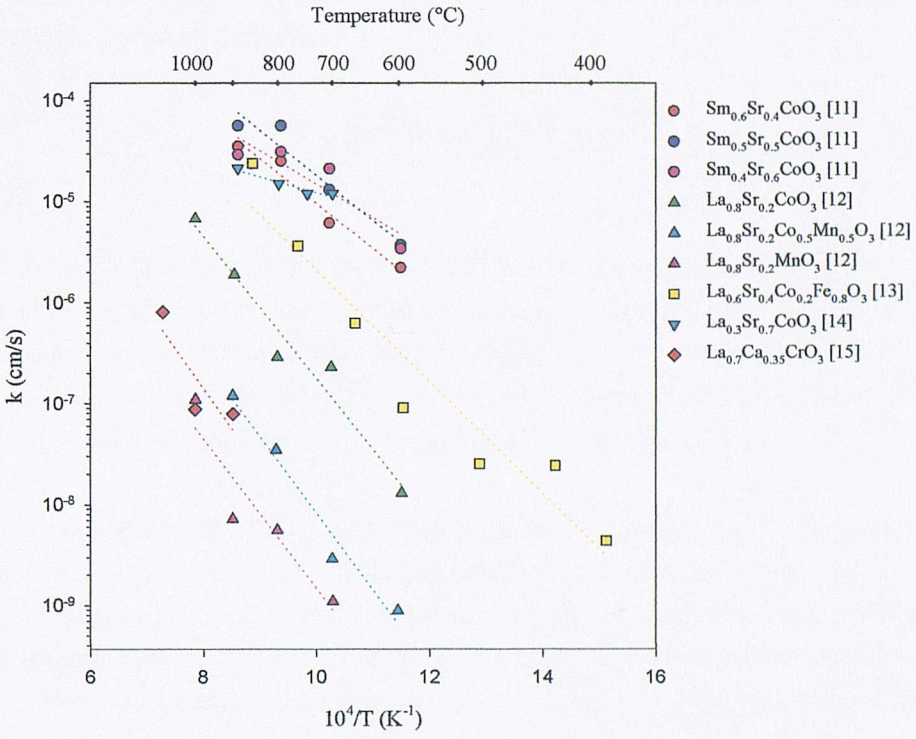


Figure 6.11. The surface exchange coefficient for a selection of $R_ET_MO_3$ perovskites as a function of temperature [11,12,13,14,15].

The measurements of Fullarton *et al* [11] on $Sm_{1-x}Sr_xCoO_{3-\delta}$, De Souza [12] on $La_{0.8}Sr_{0.2}Co_{1-y}Mn_yO_{3-\delta}$, and by Benson *et al* [13] on $La_{0.6}Sr_{0.4}Co_{0.2}Fe_{0.8}O_{3-\delta}$ were all made at pO_2 = 1 atmosphere. The measurements of van Doorn *et al* [14] were

made at pO_2 = 0.21 atmospheres and those of Yasuda *et al* [15] at 0.13 atmospheres of oxygen.

It is immediately clear from figure 6.11 that the surface exchange coefficient behaves in an Arrhenius type manner, such that the following equation will generally hold,

$$k = k_O \exp\left(-\Delta H_{EX} / kT\right) \qquad \text{eqn. (6.23)}$$

The similarity of this behaviour to that of diffusion indicates that there is an effective exchange attempt frequency, in analogy to the jump attempt frequency (given by equation 4.1) for the diffusion process. However, the atomistic parameters in the term k_O are not clear. Kilner *at al* [16] has suggested an atomistic expression based on the theory of an exchange attempt frequency and assuming that oxygen vacancies are the active sites for adsorption. This is given for a simple cubic system by,

$$k_O = a_i m^{-1/3} \left[{}^{s}V_O^{\bullet\bullet}\right] \nu_{EX} \exp\left\{\frac{\Delta S_{EX}}{R}\right\} \qquad \text{eqn. (6.24)}$$

where a_i is the lattice parameter, m is the number of oxygen sites per cell $\left[{}^{s}V_O^{\bullet\bullet}\right]$ is the site fraction of surface oxygen vacancies, ν_{EX} is a characteristic frequency, in analogy to the characteristic lattice frequency, ν_i from equation 4.1. The physical meaning of the term ν_{EX} is not clear. What is evident however, is the similarity between the expression for k_O and D_{iO} (equations 4.11-4.14).

As with the tracer diffusion coefficient, there is a large range of values of the surface exchange coefficient obtained depending on the nature of the T_M cation. The manganites and the chromites have the lowest surface exchange coefficients, while the cobaltites have the highest values of k. By doping the cobaltites on the B-site with either iron or manganese, the exchange coefficient can be reduced. It is also interesting to note that by increasing the level of A-site dopant on the cobaltite materials, the surface exchange coefficient increases. This evidence suggests that the surface exchange coefficient is dependent upon the number of oxygen vacancies in the material, as expected from the argument in section 6.1 and also from the equation given by Kilner *et al* [16] (equation 6.24). It is also interesting to note that the activation energy for the surface exchange coefficient,

ΔH_{EX}, appears to decrease with increasing acceptor dopant concentration. This is shown in figure 6.12, for the cobaltite systems. It has been assumed that the nature of the A-site cation (either lanthanum or samarium) will have little effect on the activation energy for the surface exchange coefficient.

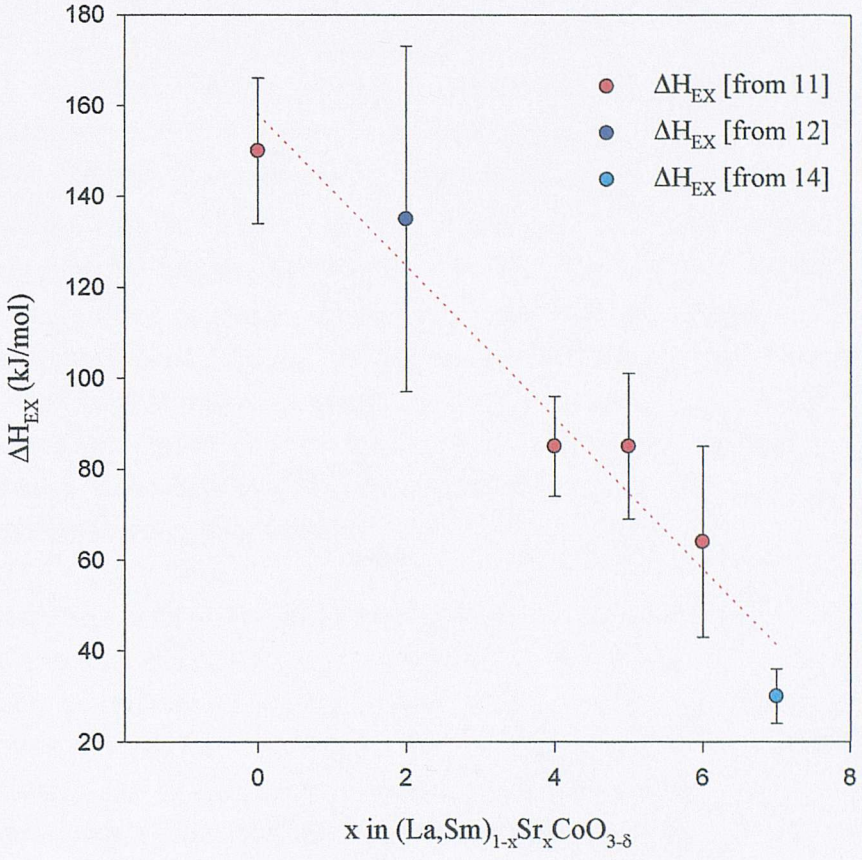


Figure 6.12. Graph showing the relation ship between ΔH_{EX} and strontium content in $(La,Sm)_{1-x}Sr_xCoO_{3-\delta}$ [11,12,14].

The error bars given in figure 6.12 are the standard uncertainties calculated from the linear regression of the data points taken from figure 6.11. The decrease in ΔH_{EX} with strontium content (and hence oxygen vacancy concentration) is clearly shown by figure 6.12. It appears to be an approximately linear decrease, although with the errors associated, this apparent phenomenon may be a coincidence. It should be noted that data of van Doorn *et al* [14] for the highest strontium content may well be at the limits of the experiment indicated by figure 6.10. This will be elaborated on in chapter 7. Furthermore, the diffusion profile shown by van Doorn *et al*, does not appear to correspond to the assumptions made in calculating the solution to the diffusion equation. Therefore, this data point may be somewhat inaccurate.

There has also been a reasonable amount of work undertaken on determining the rate of surface exchange as a function of the partial pressure of oxygen of the exchange gas. This dependence is important since in practical operation, a dense ceramic oxygen separation membrane will be exposed to a range partial pressures of oxygen. Recently there have been pO_2 studies completed on $La_{0.3}Sr_{0.7}CoO_{3-\delta}$ at 800°C by van Doorn *et al* [14] and on $La_{0.6}Sr_{0.4}Co_{0.2}Fe_{0.8}O_{3-\delta}$ by Benson *et al* at 400°C [13] and 800°C [17] using SIMS. Until these studies, the previous data of pO_2 dependence on the oxygen exchange rate was carried out primarily by gas phase analysis. The work of van Doorn *et al* and Benson *et al* is given in figure 6.13. The pO_2 dependence of the surface exchange coefficient for $La_{0.3}Sr_{0.7}CoO_{3-\delta}$ and $La_{0.6}Sr_{0.4}Co_{0.2}Fe_{0.8}O_{3-\delta}$ are very similar at 800°C, both showing $k \alpha pO_2^{0.4}$. The data on $La_{0.6}Sr_{0.4}Co_{0.2}Fe_{0.8}O_{3-\delta}$ at 400°C shows a $k \alpha pO_2^{0.74}$ dependence, although there is a larger uncertainty in this data set. Both van Doorn *et al* [14] and Benson *et al* [17] have proposed a mechanism by which the surface exchange process occurs based on their respective data sets. It is interesting to note that despite the almost exactly equal dependence on pO_2 at 800°C, the two works propose substantially different mechanisms. The respective validity of each hypothesis is not discussed here.

Other workers have studied the pO_2 dependence of the rate of surface exchange for a variety of materials. For example Boukamp *et al* has studied various doped Bi_2O_3 compounds and also $La_{0.4}Sr_{0.6}CoO_{3-\delta}$ using gas phase analysis [18,19]. However there is some difficulty in performing gas phase analysis on rapid diffusers due to gas phase diffusion limitations. In all cases however, a positive dependence of the pO_2 is seen in the exchange rate. For $La_{0.4}Sr_{0.6}CoO_{3-\delta}$, the dependence was given as $pO_2^{0.5}$ at 400°C [19].

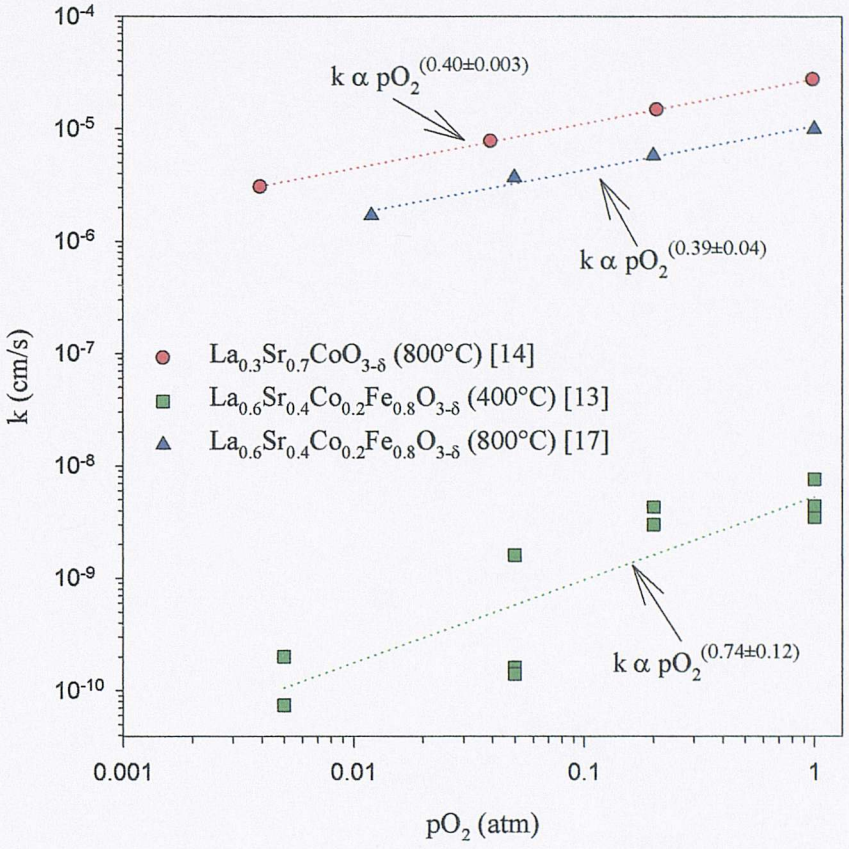


Figure 6.13. The pO_2 dependence of the surface exchange coefficient for two perovskite materials [13,14,17].

6.4. Experimental Behaviour of k for Fluorite Oxides.

There has been much less work undertaken on the oxygen surface exchange rate on fluorite electrolyte materials. This is probably because the technological importance of this rate is less clear since electrolytes are not required to exchange oxygen without the presence of an electrode. However, extension of the triple phase boundary of the gas/electrode/electrolyte may occur if the electrolyte surface is active. It is also a scientifically important parameter and data on these systems may well help in understanding the rate determining processes involved in surface exchange kinetics. Figure 6.14 shows a compilation of some of the data on the oxygen surface exchange coefficient on some fluorite oxides obtained from the literature.

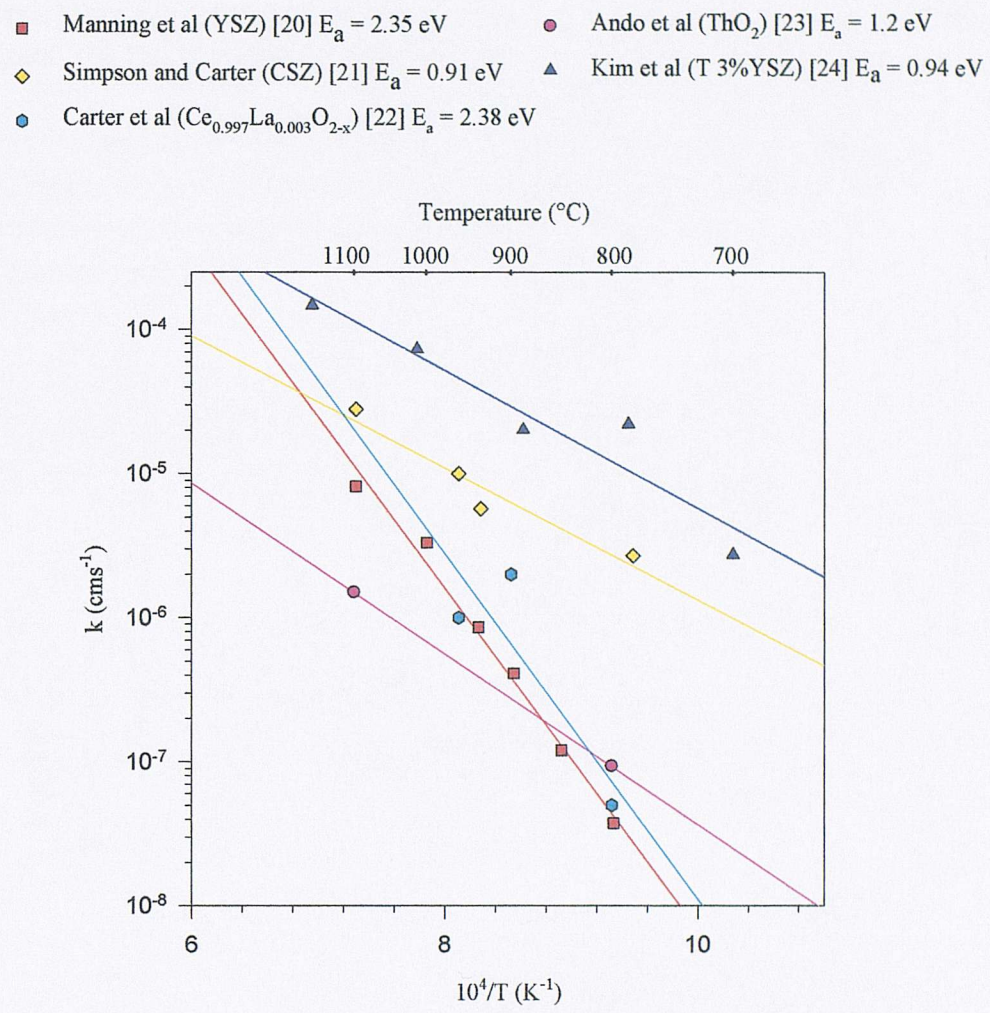


Figure 6.14. Arrhenius plot of the surface exchange coefficient for a variety of fluorite oxides [20,21,22,23,24].

There is clearly a wide range of activation energies reported. The activation energies for ThO_2 [23], $Zr_{0.944}Y_{0.056}O_{1.972}$, (3YTZ) [24], and $Zr_{0.858}Ca_{0.142}O_{1.858}$ (CSZ) [21] all give values of ≈1eV. The activation enthalpies for surface exchange of $Zr_{0.81}Y_{0.19}O_{1.905}$ (YSZ) by Manning *et al* [20] (at T>973K) are significantly higher than those for the other fluorites (ΔH_{EX} = 2.35eV). The work of Carter *et al* [22] on $Ce_{0.997}La_{0.003}O_{1.9985}$ also shows a high activation energy, although the data set is very limited and has a large uncertainty associated with it. It should be noted that in the works of Ando *et al* [23], Kim *et al* [24] and Simpson and Carter [21], the samples were suspended by either a Pt wire or mesh during exchange which, given the catalytic activity of platinum, will affect the rate of exchange. The effect of Pt loading has been shown to significantly reduce the activation enthalpy for surface oxygen exchange in YSZ [25]. It would thus

appear that the measurements of Manning *et al* represent the true behaviour of natural fluorite surfaces most accurately.

Another very interesting feature of the data of Manning *et al* is that the surface exchange coefficient appears to undergo a transition from a low activation energy to a high activation energy at around 700°C. This change in activation energy is illustrated in figure 6.15.

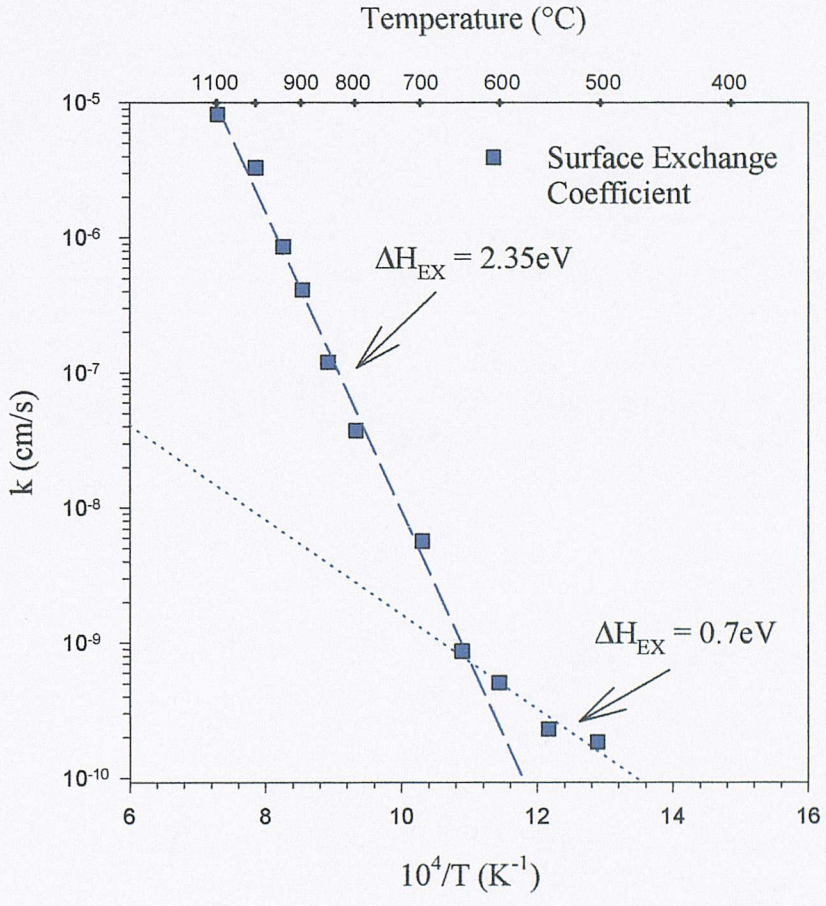


Figure 6.15. Arrhenius plot of the surface exchange coefficient for single crystal $Zr_{0.81}Y_{0.19}O_{1.905}$ (from [20]).

In conjunction with Mr P. Manning, the author also conducted gas phase analysis on powdered YSZ at temperatures above and below the apparent transition in the activation energy for surface exchange. The results were reported in the paper of Manning *et al* [20] and are illustrated below as figures 6.16 and 6.17.

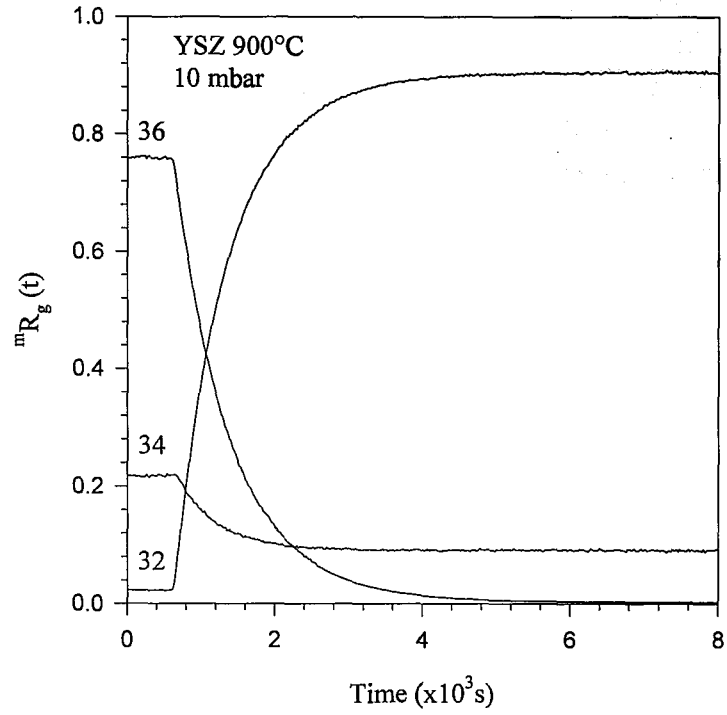


Figure 6.16. Gas phase analysis of powdered 9.5 mol% YSZ sample at 900°C.

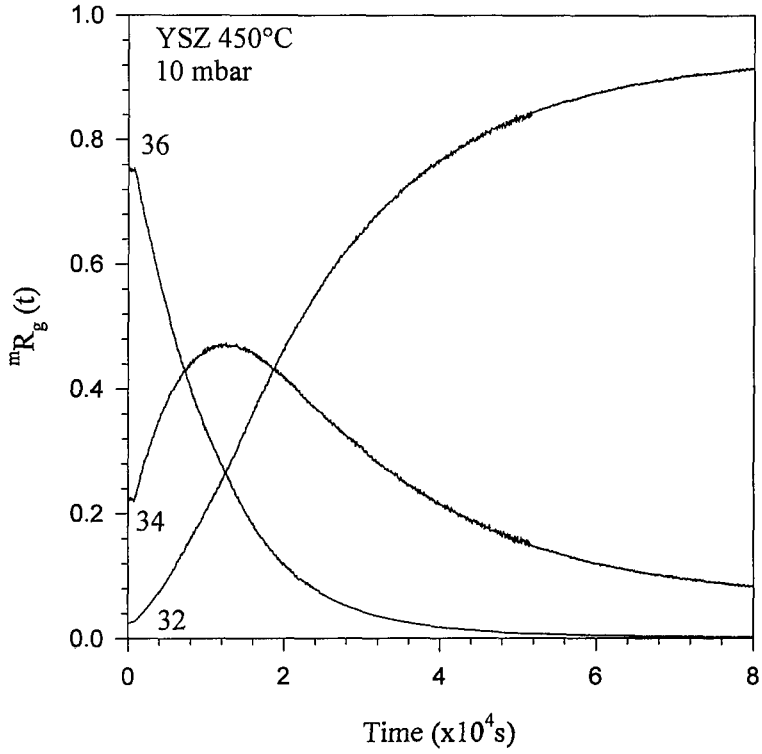


Figure 6.17. Gas phase analysis of powdered 9.5 mol% YSZ sample at 450°C.

At 450°C, there is substantial formation of the cross molecule $\{O^{18} - O^{16}\}$ i.e. $^{34}O_2$ whereas at 900°C there is no evidence of its formation, only an increase in $^{32}O_2$. This implies that at low temperatures atomic exchange takes place and at high temperatures molecular exchange takes place. It was also noted that the activation energy for surface exchange (2.35eV) was approximately half the electronic band gap (4.99eV [26]). This was interpreted as the rate limiting step for the exchange process being the availability of free electrons. These two features will be returned to in chapter 11.

6.5. Atomistic Mechanisms of Surface Exchange.

In this section, some of the many mechanistic steps that have been suggested for the exchange of oxygen on the surface of an oxide material will be given. At this stage the relative merits of each hypothesis will not be discussed. It is important to note that apart from the various steps suggested, there may also be a variation in the rate limiting step of the given process.

One possible pathway has been given by Boukamp *et al* [27], described below,

$O_{2(g)} + S_{ad} \leftrightarrow O_{2(ad)}$	adsorption	(i)
$O_{2(ad)} + e' \leftrightarrow O'_{2(ad)}$	charge transfer	(ii)
$O'_{2(ad)} + e' + S_{ad} \leftrightarrow 2O'_{(ad)}$	dissociation	(iii)
$O'_{(ad)} + e' \leftrightarrow 2O''_{(ad)}$	charge transfer	(iv)
$O''_{(ad)} + V_o^{\cdot\cdot} \leftrightarrow O_o^x + S_{ad}$	incorporation	(v)

S_{ad} is a surface site for adsorption. This model assumes that oxygen is adsorbed as a molecule before being dissociated. Van Doorn *et al* [14] have suggested a mechanism where dissociation of the oxygen molecule occurs simultaneously with adsorption, viz.

$O_{2(g)} + 2S_{ad} \leftrightarrow 2O_{(ad)}$	dissociative adsorption
$O_{ad} + V_o^{\cdot\cdot} \rightarrow O_o^x + S_{ad} + 2h^{\cdot}$	charge transfer and incorporation

Both of these models assume that a surface oxygen vacancy with an effective positive charge is involved in the exchange process. From this type of analysis,

the nature of the adsorption site S_{ad} is not apparent, i.e. if it is a defect site such as a surface vacancy. Neither is it possible to distinguish a mechanism whereby the oxygen is adsorbed elsewhere on the surface and can then diffuse along the interfacial plane to a vacant site. Mogensen [28], has suggested the following mechanism for the oxygen reduction reaction.

$$O_{2,ads} + 2e^- \rightarrow O_2^{2-}$$
$$O_2^{2-} \rightarrow 2O^-$$
$$O^- + e^- \rightarrow O^{2-}$$

In this model, the adsorption sites have been excluded. It has been assumed that the adsorption process is sufficiently rapid so as not to contribute to the energy required to drive the process.

None of the above suggested pathways provide information concerning the rate limiting step within the mechanism, although van Doorn *et al* [14] suggests that the charge transfer and incorporation process is the rate determining step which is in agreement with Takeda *et al* [29].

De Souza [12] has also offered a mechanism for the surface exchange reaction which involves surface vacancies. This mechanism is slightly different in that it suggests that the surface vacancy is a neutral moiety. This is described as,

$O_2(g) + {}^{s}V_O^{\times} \rightarrow \left({}^{s}V_O^{\times} - O_2\right)$	adsorption	(i)
$\left({}^{s}V_O^{\delta+} - O_2{}^{\delta-}\right)$	charge transfer	(ii)
$\left({}^{s}V_O^{\delta+} - O_2{}^{\delta-}\right) + V_O^{\times} \rightarrow 2O_O^{\times}$	dissociation and incorporation	(iii)

This implies that dissociation of the oxygen molecule does not occur until a second oxygen vacancy migrates to the adsorbed oxygen. Thus, this would represent a form of molecular exchange.

Yet another mechanism involving surface vacancies, but also including electronic charge carriers has been suggested by Benson *et al* [17] to explain their data. It is therefore very evident that a wide range of mechanisms are possible, and given the current availability of accurate data, it is not reasonable to suggest that one hypothesis is better than another.

6.6. References.

[1] J.A. Kilner, in Proc. of the 2nd Int. Symp. On Ionic and Mixed Conducting Ceramics, Eds. T.A. Ramanarayanan, W.L. Worrel and H.L. Tuller, The Electrochemical Society, Inc., Pennington, NJ, **PV 94-12**, (1994) p174.

[2] J. Crank, in "The Mathematics of Diffusion", 2nd Edition, Oxford University Press, Oxford (1975).

[3] A.D. Le Claire, A. Rabinovitch. J. Phys. C: Solid State Phys. **Vol 14** (1981) p3862.

[4] G.R. Purdy, in Diffusion in Materials. Ed. A.L. Lasker, Kluwer Academic Publishers, Netherlands (1990) p309.

[5] N.L. Peterson. International Metals Reviews **Vol 28** (1983) p65.

[6] M. Liu, in Proc. of the 1st Int. Symp. On Ionic and Mixed Conducting Ceramics, Eds. T.A. Ramanarayanan and H.L. Tuller, The Electrochemical Society, Inc., Pennington, NJ, **PV 91-12**, (1991) p95.

[7] J.E. ten Elshof, H.J.M. Bouwmeester and H. Verweij, in Proc. 1st Int. Symp. On Ceramic Membranes, Eds. H.U. Anderson, A.C. Khandkar and M. Liu, Electrochemical Society, Inc., **PV 95-24**, Chicago, (1995) p37.

[8] J.A. Lane, D. Waller, S.J. Benson and J.A. Kilner, presented at the 11th Int. Conf. On Solid State Ionics, Honolulu (1997).

[9] S.B. Adler, J.A. Lane and B.C.H. Steele, J. Electrochem. Soc. **Vol 143** (1996) p3554.

[10] S.B. Adler, in Proc. of the 3rd Int. Symp. On Ionic and Mixed Conducting Ceramics, Eds. T.A. Ramanarayanan, W.L. Worrel, H.L. Tuller, M. Mogensen and A.C. Khandkar, The Electrochemical Society, Inc., Pennington, NJ, **PV 97-24**, Paris (1997).

[11] I.C. Fullarton, J.A. Kilner, B.C.H. Steele and P.H. Middleton, in Proc. of the 2nd Int. Symp. On Ionic and Mixed Conducting Ceramics, Eds. T.A. Ramanarayanan, W.L. Worrel and H.L. Tuller, The Electrochemical Society, Inc., Pennington, NJ, **PV 94-12**, (1994) p9.

[12] R.A. de Souza, Ph.D. Thesis, University of London, (1996).

[13] S.J. Benson, R.J. Chater and J.A. Kilner, in Proc. of the 3rd Int. Symp. On Ionic and Mixed Conducting Ceramics, Eds. T.A. Ramanarayanan, W.L. Worrel, H.L. Tuller, M. Mogensen and A.C. Khandkar, The Electrochemical Society, Inc., Pennington, NJ, **PV 97-24**, Paris (1997).

[14] R.H.E. van Doorn, I.C. Fullarton, R. A. de Souza, J.A. Kilner, H.J.M. Bouwmeester and A.J. Burggraaf, Solid State Ionics, **Vol 96** (1997) p1.

[15] I. Yasuda, K. Ogasawara and M. Hishinuma, in Proc. of the 2nd Int. Symp. On Ionic and Mixed Conducting Ceramics, Eds. T.A. Ramanarayanan, W.L. Worrel and H.L. Tuller, The Electrochemical Society, Inc., Pennington, NJ, **PV 94-12**, (1994) p164.

[16] J.A. Kilner, R. A. de Souza and I.C. Fullarton, Solid State Ionics, **Vol 86-88** (1996) p703.

[17] S.J. Benson, D. Waller, J.A. Lane and J.A. Kilner, presented at the 11th Int. Conf. On Solid State Ionics, Honolulu (1997).

[18] B.A. Boukamp, I.C. Vinke, K.J. de Vries and A.J. Burggraaf, Solid State Ionics, **Vol 32/33** (1989) p918.

[19] B.A. Boukamp, H.J.M. Bouwmeester and A.J. Burggraaf, , in Proc. of the 2nd Int. Symp. On Ionic and Mixed Conducting Ceramics, Eds. T.A. Ramanarayanan, W.L. Worrel and H.L. Tuller, The Electrochemical Society, Inc., Pennington, NJ, **PV 94-12**, (1994) p141.

[20] P.S. Manning, J.D. Sirman and J.A. Kilner, Solid State Ionics **Vol 93** (1997) p125.

[21] L. A. Simpson, and R. E. Carter., J. Am. Ceram. Soc., **Vol 49** (1966) p139.

[22] S. Carter, R.J. Chater, J. Kajda, K.M. Liddecott, J.A. Kilner and B.C.H. Steele, in Proc. of the 1st Int. Symp. On Ionic and Mixed Conducting Ceramics, Eds. T.A. Ramanarayanan and H.L. Tuller, The Electrochemical Society, Inc., Pennington, NJ, **PV 91-12**, (1991) p84.

[23] K. Ando, Y. Oishi, and Y. Hidaka, J. Chem. Phys., **Vol 65** (1976) p2751.

[24] B. K. Kim, S. J. Park, and H. Hamaguchi., J. Am. Ceram. Soc., **Vol 76** (1993) p2119.

[25] E. Kh. Kurumchin and Perfiliev, Solid State Ionics, **Vol 42** (1990) p129.

[26] W.H. Strehlow and E.L. Cook, J. Phys. Chem. Ref. Data 2 (1973) p163.

[27] B.A. Boukamp, B.A. van Hassel, I.C. Vinke, K.J. de Vries and A.J. Burggraaf, Electrochim. Acta, **Vol 38** (1993) p1817.

[28] M. Mogensen, in Proc. of the 14th Risø International Symposium on Materials Science, eds. F.W. Poulsen, J.J. Bentzen, T. Jacobsen, E. Skou and M.J. Østergård, 117 (1993).

[29] Y. Takeda, R. Kanno, M. Noda, Y. Tomida and O. Yamamoto, J. Electrochem. Soc., **Vol 134** 1987) p2656.

7. Experimental Techniques.

7.1. Introduction.

The objective of the work presented in this thesis is to investigate the mass transport and electrochemical behaviour of a series of electroceramic materials. In order to achieve this goal a variety of experimental techniques were employed. These are listed in the following sections. Both dense samples for conductivity and diffusion experiments, and porous electrodes were prepared. The morphology of these samples was investigated using optical microscopy, scanning electron microscopy (SEM) and atomic force microscopy (AFM). The conductivity of the materials was investigated using ac impedance spectroscopy and the oxygen diffusion and oxygen surface exchange properties examined using $^{16}O/^{18}O$ isotope exchange and secondary ion mass spectroscopy (SIMS). The diffusion of cations was also investigated using SIMS.

7.2. Sample Preparation.

With only a few exceptions (which will be noted in the following sections), almost all the ceramic powders used in sample preparation were obtained from commercial suppliers: Praxair Speciality Chemicals (PSC, formerly Seattle Speciality Chemicals, SSC), Tosoh (T) or Rhone-Poulenc (RP). Depending on the nature of experiment employed, there were three types of sample preparation techniques used.

7.2.1. Dense Ceramic Samples.

Powders of the required composition were uniaxially pressed at a pressure of ~75Mpa to form pellets of 13mm diameter and a thickness ranging from 0.5mm-3mm. The pellets were then placed in air-tight, rubber bags and isostatically pressed at room temperature with a pressure of 300Mpa. The samples were then sintered in air at a variety of temperatures, depending on the composition used. A

heating and cooling rate of 300°C per minute was employed. The sintering temperatures and times utilised are outlined in table 7.1.

Sample	Temperature (°C)	Time (Hours)
$Ce_{0.9}Gd_{0.1}O_{1.95}$ (SSC)	1550	5
$Ce_{0.8}Gd_{0.2}O_{1.9}$ (SSC)	1550	5
$Ce_{0.8}Gd_{0.18}Pr_{0.02}O_{2-x}$ (SSC)	1550	5
$Zr_{0.85}Y_{0.15}O_{1.925}$ (T)	1500	5
$Ce_{0.9}Gd_{0.1}O_{1.95}$ (RP)	1550	5

Table 7.1. Sintering temperatures and times employed in preparation of dense ceramic samples.

The other dense samples used were a single crystal of $Ce_{0.69}Gd_{0.31}O_{1.845}$ provided by Prof. Y. Baikov of A.F. Ioffe Physico-Technical Institute , Russian Academy of Sciences, and single crystals of $Zr_{0.81}Y_{0.19}O_{1.905}$ obtained commercially from Pi-Kem. The single crystal of $Ce_{0.69}Gd_{0.31}O_{1.845}$ was prepared by inductive melting in a cold crucible as outline by Melekh [1]. The composition was determined from Inductively Coupled Plasma (ICP) analysis.

The density of the samples was obtained using the Archimedes' method. A dried pellet was weighed, giving a mass M_1. The pellet was then weighed submerged in water, suspended from a wire of mass M_w to give a mass M_2. The pellet was then removed from the water and reweighed to give mass M_3. The density of the pellet, ρ_{exp}, can then be calculated according to equation 7.1.

$$\rho_{exp} = \frac{\rho_{water} \times M_1}{(M_3 - M_2) + M_W} \qquad \text{eqn (7.1)}$$

where ρ_{water} is the density of water at the temperature at which the experiment was carried out. The experimentally obtained densities can then be compared with the theoretical densities of the materials. The theoretical density can be obtained from knowledge of the lattice parameter and the molecular weight of the sample.

$$\rho_{Theoretcal} = \frac{MW \times Z}{N_A \times Vol_{unit\ cell}} \qquad \text{eqn (7.2)}$$

where MW is the molecular weight of the sample, Z is the number of these formula in a unit cell and $Vol_{unit\ cell}$ is the volume of the unit cell. The volume of the unit cell is simply calculated from the lattice parameters obtained from X-ray diffraction.

The percentage of theoretical densities obtained for the ceramic samples are given below in table 7.2.

Sample	ρ_{exp} (% $\rho_{Theoretical}$)
$Ce_{0.9}Gd_{0.1}O_{1.95}$ (SSC)	94-99
$Ce_{0.8}Gd_{0.2}O_{1.9}$ (SSC)	95-98
$Ce_{0.8}Gd_{0.18}Pr_{0.02}O_{2-x}$ (SSC)	95-98
$Zr_{0.85}Y_{0.15}O_{1.925}$ (T)	97-100
$Ce_{0.9}Gd_{0.1}O_{1.95}$ (RP)	97-99

Table 7.2. Densities of samples obtained after sintering.

7.2.2. Electrode Preparation.

Symmetrical electrodes of composition $La_{0.6}Sr_{0.4}Co_{0.2}Fe_{0.8}O_{3-\delta}$ (from SSC) were examined using ac impedance spectroscopy. The powder was ball-milled and then made into a slurry by mixing with ethanol. The slurry was then painted on to dense samples of the ceria based materials and allowed to dry overnight. The electrode/electrolyte/electrode samples were then heated at a rate of 1°C per minute to a temperature of 400°C to allow slow removal of the ethanol from the slurry. The electrodes were then heated to 900°C at 300°C per hour and left for two hours, before cooling at 300°C per hour. For examination of the $Zr_{0.85}Y_{0.15}O_{1.925}$, $Ce_{0.69}Gd_{0.31}O_{1.845}$ (single crystal) and $Zr_{0.81}Y_{0.19}O_{1.905}$ (single crystal) by ac impedance spectroscopy, platinum electrodes were applied by the method given above, except the final sintering temperature used was 1000°C.

7.3. X-ray Diffraction.

The ceramic materials were examined by x-ray diffraction to ensure they were all single phase materials and to detect any reaction between the $La_{0.6}Sr_{0.4}Co_{0.2}Fe_{0.8}O_{3-\delta}$ and $Ce_{0.9}Gd_{0.1}O_{1.95}$ at elevated temperatures. The lattice parameters of all the samples and the solubility limits of cobalt and iron in $Ce_{0.9}Gd_{0.1}O_{1.95}$ were also calculated using x-ray diffractometry. A Philips PW1720 diffractometer, equipped with a graphite secondary monochromator, and using Cu-K_α radiation (λ=1.54178Å) was used for the measurements.

The lattice parameters of the solid-solutions were calculated as follows. Peak positions in the range of 2θ = 70 to 140° were determined by profile fitting and the positions were corrected by reference to a silicon internal standard. The true lattice parameter was determined by linear regression analysis of the lattice parameter versus $\cos^2\theta$, to obtain the lattice parameter at $\cos^2\theta = 0$.

7.4. Scanning Electron Microscopy.

The morphology of the $La_{0.6}Sr_{0.4}Co_{0.2}Fe_{0.8}O_{3-\delta}$ electrodes was examined using a Jeol JSM 5300 scanning electron microscope operating with a primary electron beam at 30keV. Electron microscopy was carried out in the department of mechanical engineering by Mr. J. Wells.

7.5. Atomic Force Microscopy.

The topography of the surfaces of the dense ceramic samples was investigated using a Quesant atomic force microscope (AFM). Surface roughness values can be calculated from the topographical information from the AFM. The particle size and distribution of the $La_{0.6}Sr_{0.4}Co_{0.2}Fe_{0.8}O_{3-\delta}$ electrodes were also examined using AFM.

The AFM consists of a sharp tipped probe (radius 10 to 50nm) attached to a piezoelectric material. In the instrument used in this work, the probe can be scanned across a sample surface over an area up to 40μm. The force between the sample surface and the tip of the AFM can be monitored as the probe is scanned

across the surface. The tip is never in contact with the surface, but a small distance is maintained by a feedback loop involving the piezoelectric material. The movement required to maintain this distance is recorded and thus the topography of the sample surface can be monitored. The AFM is, in principle, able to measure height variations of one atomic step while the lateral resolution is around 5nm.

7.6. AC Impedance Spectroscopy.

AC impedance spectroscopy was used to determine the ionic conductivity of a series of fluorite electrolyte materials. It was also used to examine the polarisation resistance of the $La_{0.6}Sr_{0.4}Co_{0.2}Fe_{0.8}O_{3-\delta}$ electrodes on a $Ce_{0.9}Gd_{0.1}O_{1.95}$ (SSC) electrolyte.

The majority of the experiments were carried out in an atmosphere of air, however, some experiments were carried out using flowing streams of oxygen, dry nitrogen (passed through a $CaSO_4$ desiccant) or wet nitrogen (passed through water). The gases used in the experiments are outlined in table 7.3.

Sample	Atmosphere
$Ce_{0.9}Gd_{0.1}O_{1.95}$	Air wet N_2 dry N_2
$Ce_{0.69}Gd_{0.31}O_{1.845}$ (single crystal)	Air N_2 O_2
$Zr_{0.85}Y_{0.15}O_{1.925}$	Air
$Zr_{0.81}Y_{0.19}O_{1.905}$ (single crystal)	wet N_2 dry N_2
$La_{0.6}Sr_{0.4}Co_{0.2}Fe_{0.8}O_{3-\delta}$	Air

Table 7.3. Atmospheres used for examining the electrical behaviour of samples using AC impedance spectroscopy.

AC impedance spectroscopy was carried out using two types of frequency response analyser (FRA). A Hewlett-Packard HP4192A FRA with a frequency range of 10Hz to 13MHz and an applied voltage of 50mV was used to examine the electrolyte materials and a Solartron 1260 phase gain analyser using a frequency range of 0.01Hz to 10MHz and an applied voltage of 20mV was used to examine the electrode behaviour. A temperature range of 200°C-900°C was used throughout the range of experiments.

7.6.1. Response of an Electrolyte Under an AC field.

If a small AC potential is applied to an electrolyte, a current will ensue, related to the impedance of the material through Ohms law, given by equation 7.3.

$$Z = \frac{V}{I} \qquad \text{eqn. (7.3)}$$

Z is the impedance, V is the applied voltage and I is the resultant current. It should be noted that the impedance is the time dependent transfer function between the applied voltage and the current, whereas the resistance is the steady state relationship between the voltage and current. Thus the impedance is a function of the frequency of the signal whereas the resistance is independent of the frequency.

The applied AC voltage can be given by equation 7.4 and the resultant current by equation 7.5.

$$V = V_0 \exp\{j\omega t\} \qquad \text{eqn. (7.4)}$$

$$I = I_0 \exp\{j(\omega t + \phi)\} \qquad \text{eqn. (7.5)}$$

where V_0 and I_0 are the amplitude of the voltage and subsequent current, respectively, ω is the angular frequency of the signal ($2\pi f$), t is the time and ϕ is the phase difference between the two sinusoidal wave functions. The phase difference arises from the natural dielectric response time of the material or due to other polarisation effects occurring at grain boundaries. Thus, the impedance can be expressed as,

$$Z = \frac{V_o \exp\{j\omega t\}}{I_o \exp\{j(\omega t + \phi)\}} \qquad \text{eqn. (7.6)}$$

This can simply be reduced to,

$$Z = \frac{V_o}{I_o} \exp\{-j\phi\} \qquad \text{eqn. (7.7)}$$

If the modulus of the impedance is expressed as,

$$|Z| = \frac{V_o}{I_o} \qquad \text{eqn. (7.8)}$$

then we obtain,

$$Z = |Z| \exp\{-j\phi\} \qquad \text{eqn. (7.9)}$$

This can also be expressed in Cartesian co-ordinates as,

$$Z = |Z| \cos\phi - j|Z| \sin\phi \qquad \text{eqn (7.10)}$$

The real impedance can thus be expressed as equation 7.11 and the imaginary impedance as equation 7.12.

$$Z' = |Z| \cos\phi \qquad \text{eqn (7.11)}$$

$$Z'' = |Z| \sin\phi \qquad \text{eqn (7.12)}$$

where Z' is the real impedance and Z'' is the imaginary impedance, such that equation 7.10 is now given by,

$$Z = Z' - jZ'' \qquad \text{eqn. (7.13)}$$

and the modulus of the impedance can be expressed as,

$$|Z|^2 = (Z')^2 + (Z'')^2 \qquad \text{eqn. (7.14)}$$

Because the complex impedance is frequency (and time) dependant, if various processes occurring within a ceramic electrolyte relax at different rates, it is possible to deconvolute them as a function of frequency.

If a single crystal of an electrolyte (i.e. a pure ionic conductor) is considered then the material behaves as a dielectric conductive material. That is the material has resistive component (arising from its conductivity) and a capacitive component (arising from its natural dielectric response).

The current through a dielectric conductive material is given from Maxwell's equations, as

$$I = \frac{V}{R} + C\frac{\partial V}{\partial t} \qquad \text{eqn. (7.15)}$$

where C, the capacitance is related to the relative permitivity of the material by,

$$C = \frac{\varepsilon_0 \varepsilon_r A}{\ell} \qquad \text{eqn. (7.16)}$$

ε_0 is the permitivity of free space, ε_r is the relative permitivity of the dielectric, A is the cross sectional area of the material and ℓ is the thickness of the material. If the voltage applied is a small sinusoidal perturbation, as given by equation 7.4, then the resulting current is given by,

$$I = \frac{V}{R} + j\omega CV \qquad \text{eqn. (7.17)}$$

which can be expressed as,

$$I = V\left(\frac{1}{R} + j\omega C\right) \qquad \text{eqn. (7.18)}$$

Now, given equation 7.3, the complex impedance can be expressed as,

$$Z = \frac{V}{I} = \frac{V}{V\left(\frac{1}{R} + j\omega C\right)} \qquad \text{eqn. (7.19)}$$

to give,

$$Z = \frac{1}{\left(\frac{1}{R} + j\omega C\right)} \qquad \text{eqn. (7.20)}$$

and thus,

$$Z = \frac{R}{(1 + j\omega CR)} \qquad \text{eqn. (7.21)}$$

or,

$$Z = R\left(\frac{1}{1 + j\omega CR}\right) \qquad \text{eqn. (7.22)}$$

If we define, $\tau = RC$, then equation 7.22 becomes 7.23,

$$Z = R\left(\frac{1}{1 + j\omega\tau}\right) \qquad \text{eqn. (7.23)}$$

Given equation 7.16 and $R = \frac{\ell}{\sigma A}$ it is clear that,

$$\tau = RC = \frac{\varepsilon_0 \varepsilon_r}{\sigma} \qquad \text{eqn. (7.24)}$$

which gives it the units of seconds. Thus τ is said to be the characteristic relaxation time for the response of the dielectric material. Note that τ, unlike the measured resistance and capacitance, is a geometry independent parameter. Given the relative permitivity of both ceria and zirconia is around 20, the characteristic relaxation time can be calculated from the conductivity. For example, if the conductivity is of the order of 10^{-3}S/cm, the characteristic relaxation time will be of the order of 10^{-5}seconds. If the complex impedance is plotted in the frequency domain the response will occur with a characteristic frequency of the order of 10^{5}Hz. If the temperature of the material was increased such that the conductivity increased (as is the case for ceria and zirconia) to say 10^{-1}S/cm, then the response will occur at around 10^{7}Hz, which is at the limit of the apparatus used. Thus with knowledge of the relative permitivity of a material, the upper limit to conductivity that can accurately be measured using AC impedance spectroscopy can be determined.

Equation 7.23 will produce a semi-circle with a centre at co-ordinates $(R/2, 0)$ and a diameter, R, when plotted on a Cartesian complex plane as a function of

frequency. This is mathematically equivalent to the impedance generated by a resistor and capacitor in parallel. Thus, electrolyte materials are often modelled using electrical equivalent resistor-capacitor (RC) circuits.

If a polycrystalline ceramic material is considered then the oxygen ions will have to travel across grain boundaries as well as through the grains themselves. The transport across grain boundaries produces a second response, also behaving as a parallel RC electrical network. The resistance associated with the grain boundaries can be considered as the resistance of the phase itself, or as a constriction resistance due to the proportion of oxygen ions which are unable to travel across the grain boundary. If all the oxygen ions cannot traverse the grain boundary, a space charge region will develop. Thus the capacitance associated with the grain boundary is not due to the relative permitivity of the grain boundary phase, but rather is associated with the polarisation occurring at the interface. Since the capacitance associated with a space charge region is higher than that due to the natural dielectric response of the material the relaxation time associated with the grain boundaries will be longer than for the bulk. Therefore, the grain boundary response is only seen at lower frequencies.

If the characteristic relaxation time associated with the grain boundary is significantly longer than the characteristic relaxation time associated with the intracrystal movement of oxygen ions, the two responses will be easy to separate in the frequency domain. In the electrolyte materials examined in this work, there is normally some two to three orders of magnitude difference in the characteristic relaxation times of the two processes, and so two semi-circlular responses are identified. Figure 7.1 shows the effect of the difference in characteristic relaxation time between two responses of equal magnitude.

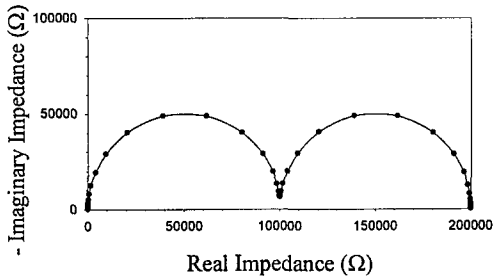


Figure 7.1 (a)

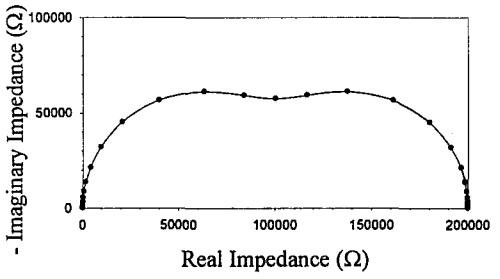


Figure 7.1 (b)

Figure 7.1. Generated AC impedance spectra given two responses of 100kΩ and (a) $\tau_1 = 10^{-7}$ secs, $\tau_2 = 10^{-4}$ secs and (b) $\tau_1 = 10^{-5}$ secs, $\tau_2 = 10^{-4}$ secs.

It is clear that where there are three orders of magnitude difference in the time constant, the semi-circles are easy to separate, but when the difference is as small as one order of magnitude, deconvolution becomes more difficult. However, a non-linear least squares fitting routine may employed to deconvolute the two responses with only a small degree of uncertainty.

In practise, perfect semi-circles, with the centre on the x-axis are seldom obtained. In general, some degree of depression below the axis occurs. This is normally attributed to the inhomogeneities within the material. Therefore a statistical distribution of the relaxation frequency can be added into equation 7.23, to give,

$$Z = R\left(\frac{1}{1+(j\omega\tau)^{1-\alpha}}\right) \qquad \text{eqn. (7.25)}$$

where α is the angle by which the semi-circle is depressed below the x-axis.

The results obtained using AC impedance spectroscopy for studying electrolytes are discussed in Chapter 9.

7.6.2. Response of an Electrode Under an AC field.

The behaviour of electrodes under an AC field tends to be very complex and hence considerably more difficult to interpret than electrolytic behaviour. This is because there are a number of contributing parameters to the polarisation resistance of the electrode, and hence RC electrical equivalence is seldom observed.

A variety of processes can occur at the electrode. These include charge transfer from the current collector to the electrode, charge transfer from the electrode to the electrolyte, the reduction of oxygen gaseous molecules and their subsequent incorporation into the electrode (or directly into the electrolyte at the triple phase boundary of the gas/electrode/electrolyte), diffusion of oxygen ions through the bulk of the electrode and diffusion of oxygen gas through the pores of the electrode. Because of the complexity of the behaviour and the fact that different types of electrode can have massively different responses, it is not appropriate to discuss the subject in detail here. A variety of mathematical equations describing

the behaviour of mixed conducting porous cathodes given certain rate determining steps have been put forward by Adler *et al* [2]. Other mathematical expressions may be appropriate given different morphologies or materials properties.

It is important to note at this stage, however, that electrode responses generally have a significantly larger characteristic relaxation time than electrolyte materials, thus enabling separation of the electrode response a whole, from the electrolyte.

The results obtained using AC impedance spectroscopy for studying electrodes are discussed in Chapter 8.

7.7. Diffusion Measurements.

The diffusion of both cations and oxygen ions has been studied. The instrument used to measure the penetration profile in both cases was an Atomika 6500 secondary ion mass spectrometer (SIMS). The technique employed to introduce the diffusing species differed however. In the following sections the introduction of a tracer isotope of oxygen will be described, then the method used to diffuse cations into electrolyte materials. A separate section is included describing the SIMS and the limitations of the instrument associated with the specific experiments described here.

7.7.1. $^{16}O/^{18}O$ Isotope Exchange.

The diffusion of oxygen ions in various fluorite materials was investigated by introducing a tracer isotope of oxygen to the system. The method of introducing the tracer isotope (in this case ^{18}O) was to anneal the sample in a large volume of gas with known enrichment of the ^{18}O isotope.

Prior to the annealing experiment the samples were all ground flat and polished with successively finer grades of diamond polish down to ¼ micron. This produced a consistent surface finish in order to compare the results from various experiments.

The samples were annealed in the apparatus shown schematically in figure 7.2. The samples were situated in a silica tube, which was heated by a "roll-on" furnace. The furnace set-up allows very fast heating and cooling rates of the sample (several hundred degrees Celsius per minute).

The apparatus was evacuated to $< 5 \times 10^{-7}$ mbar before research grade oxygen (99.996%) of natural isotopic abundance was introduced. The samples were then annealed at the required temperature and pressure for a duration of 4-10 times that of the exchange anneal. The furnace was then removed and the sample quenched to room temperature. This ensures that the sample is in chemical equilibrium with the oxygen gas that is used in the exchange anneal. If the sample is not in chemical equilibrium with the gas then the resulting difference in chemical potential between the oxygen in the gas and the solid will produce chemical diffusion effects and so the forward and reverse surface reactions given by equations 6.11 and 6.12, respectively will not have the same reaction rates. That is, the material will either lose oxygen or gain oxygen, and the overall chemical reaction will not be in the steady state.

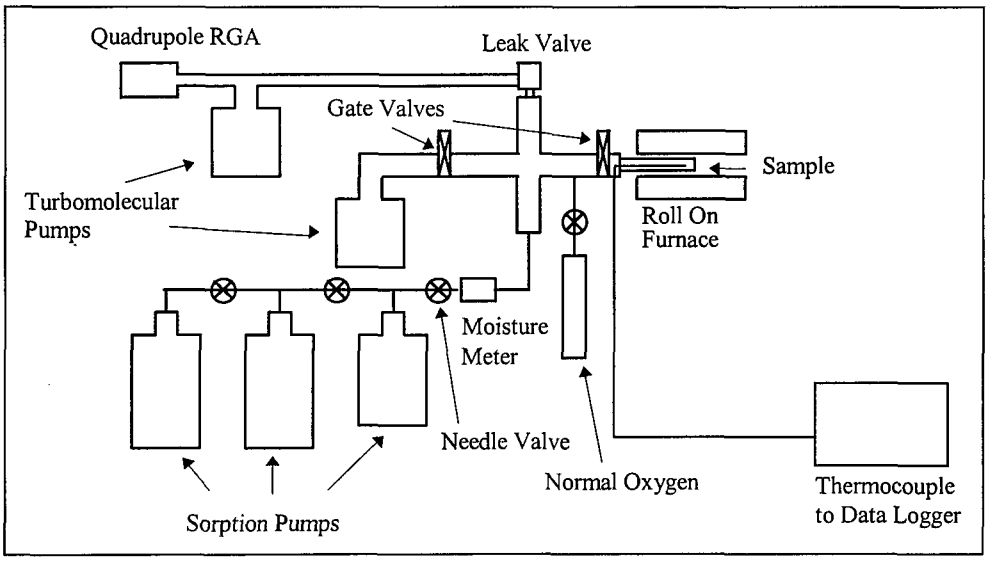


Figure 7.2. Schematic illustration of the $^{16}O/^{18}O$ isotope exchange apparatus.

Once the samples had cooled, the apparatus was again evacuated, and oxygen enriched in the ^{18}O isotope was introduced via molecular sieve sorption pumps. The sample was then rapidly heated by rolling the preheated furnace over the sample holder. A constant temperature was then maintained for a set time before the sample was quenched by removing the furnace.

Once the sample had cooled the labelled oxygen was cryogenically recovered using the molecular sieve sorption pumps. During the exchange anneals the isotopic composition of the labelled oxygen can be monitored by introducing a small quantity of the gas into a quadrupole residual gas analyser via a controlled leak valve. Alternatively, the composition of the gas can be determined in a separate experiment where a single crystal of silicon is oxidised in the isotopically enriched gas, and the composition of the oxide monitored using SIMS. The concentration of ^{18}O in the gas phase is required to be known accurately for use in determining the diffusion and surface exchange coefficient from the solution to the diffusion equation. It is also important that the concentration of ^{18}O in the gas phase does not change during the exchange anneal. Any change in concentration will result in deviation from the behaviour described by the solution to Fick's 2nd law given in equation 6.20. With the large volume of oxygen used in the exchange experiments, no significant change in gas composition was noted.

During the anneals the temperature was monitored to an accuracy of 1°C with a k-type thermocouple. The data from the thermocouple was logged with a data logger attached to a PC. From the thermocouple data the temperature and the time of the anneal could be calculated. However, during heating and cooling of the samples, the thermal inertia of the sample holder introduced an uncertainty in the exact duration of the anneal time. In order to minimise the uncertainty in the anneal time, a correction was made for the effect of the heating and cooling periods, given by De Souza [3] and based on the method described by Killoran [4]. The error induced by the heating and cooling is minimal when very long anneals are used but can be significant when short anneals at high temperatures are employed.

7.7.2. Cation Diffusion Couples.

In order to study the diffusion of various transition metals in the fluorite materials given above, so-called diffusion couples were produced. A variety of methods were utilised, outlined below.

The first was a thin layer of the transition metal oxide (TMO) applied to the fluorite substrate by pulsed laser deposition (PLD) [5]. This method was

employed for the low temperature diffusion experiments of manganese into polycrystalline $Zr_{0.85}Y_{0.15}O_{1.925}$.

The second method was the application of a dense sample of the TMO to the fluorite substrate. This method was used for the diffusion of manganese into single crystal $Zr_{0.81}Y_{0.19}O_{1.905}$. However, when this procedure was employed to study the diffusion of cobalt and iron into $Ce_{0.9}Gd_{0.1}O_{1.95}$, significant cracking of the $Ce_{0.9}Gd_{0.1}O_{1.95}$ pellet occurred. This was attributed to the large difference in thermal expansion of the two materials. Therefore a third method was employed. In this method transition metal nitrates were intimately mixed with powders of the same composition of the fluorite substrate in a 50:50 ratio by weight. The powder mixture was then heated to decompose the nitrates to form a TMO/MO_2 composite powder. This powder was then pressed on to the fluorite substrate before the diffusion anneal. This method was used for the study of diffusion of cobalt and iron into $Ce_{0.9}Gd_{0.1}O_{1.95}$ and the high temperature diffusion experiments of manganese into polycrystalline $Zr_{0.85}Y_{0.15}O_{1.925}$.

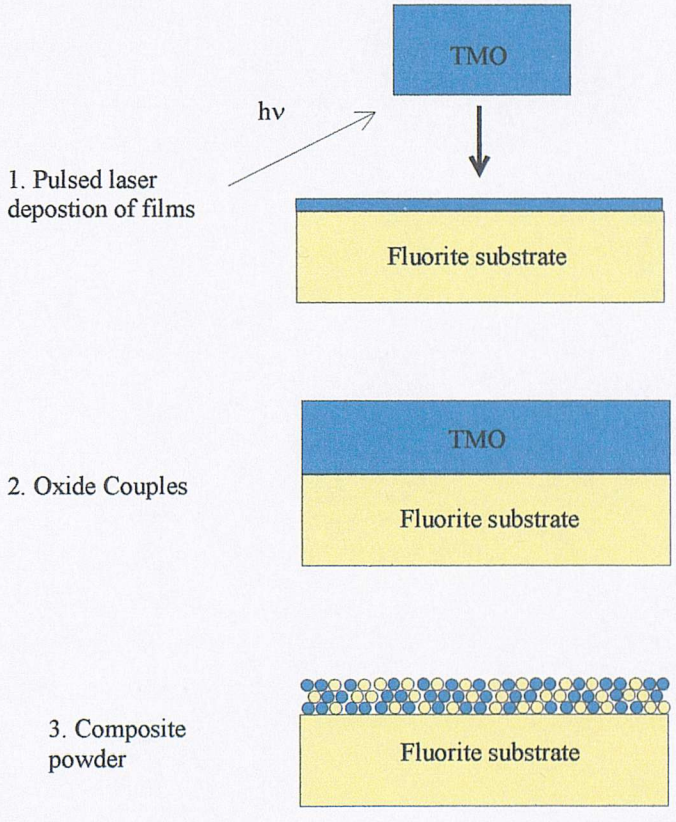


Figure 7.3 Schematic illustration of the diffusion systems used for the study of cation diffusion.

filtration system is a Wein filter [6] (not shown in figure 7.4). The beam is then focused with an electrostatic lens. The primary ion beam can be scanned over a small area (up to 2 x 2mm) of the sample. However, maintaining a fine focus of the ion beam over such a large scanned area can prove difficult.

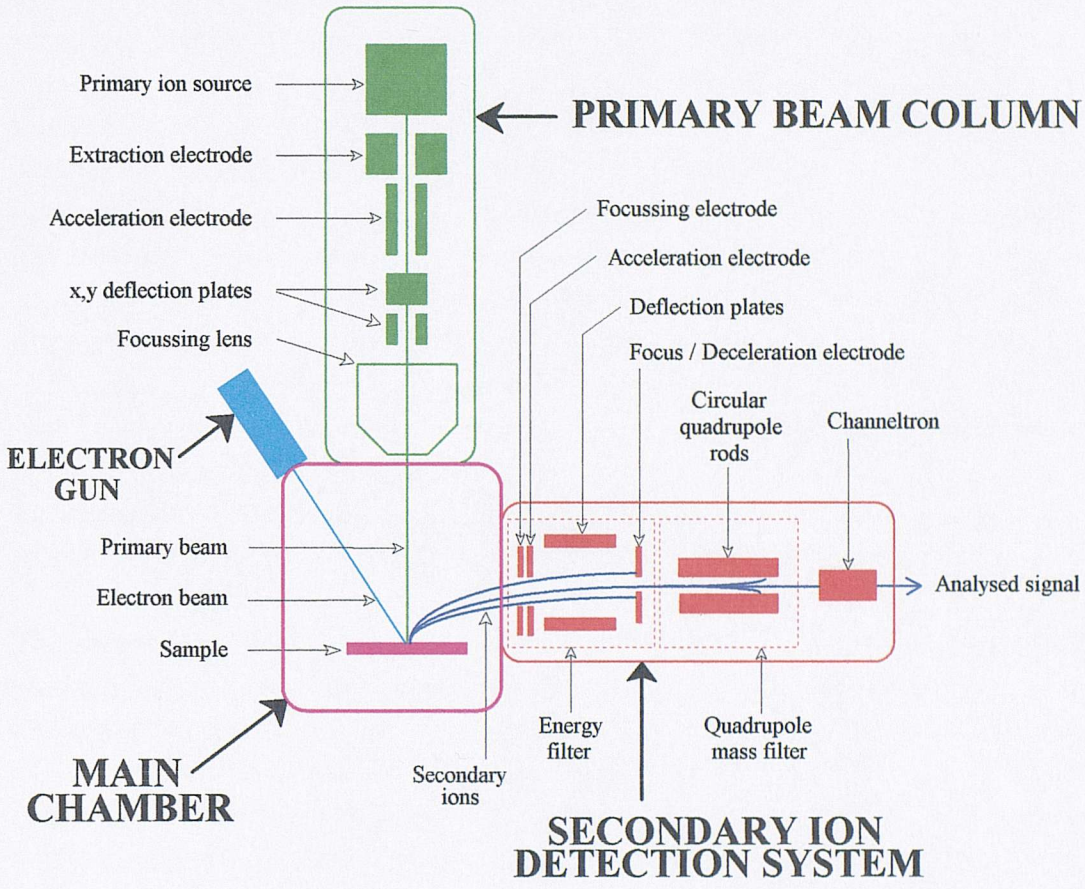


Figure 7.4. Schematic illustration of the Atomika 6500 Ion Microprobe (from [7]).

The sample under investigation is kept in the main chamber shown in figure 7.4. The main chamber is kept a pressure below 10^{-11} bar during analysis. This avoids adsorption of species onto the surface of the sample and also limits scattering of the ion and electron beams. The sample can be rotated through an angle of 0-90° from the horizontal plane shown in figure 7.4 to allow different angles of incidence of the primary ion beam. In this work, the sample was always kept at

normal incidence to the primary ion source. The electron beam is at a 45° angle to the primary ion beam and the sample.

Secondary ions emitted as a result of the collisions between the primary ion beam and ions at the surface and near surface the sample are focused and accelerated towards a mass spectrometer in the secondary ion detection system. The secondary ions are passed through an energy filter before being decelerated and passed through a quadrupole mass filter. A defined secondary ion energy window is required to allow optimum resolution in the quadrupole. The quadrupole mass filter is described in detail in [8] (pp419-442). In essence, the quadrupole only permits ions with a specific mass/charge ratio to pass through the system. The mass/charge ratio can be altered by changing the voltages applied to the rods of the quadrupole. In the Atomika 6500 used in this work, the mass/charge ratio able to pass through the quadrupole can be changed from 1 to ~250 a.m.u.. Once the secondary ions have been mass filtered, they are detected with a channeltron electron multiplier. A brief description of channeltron multipliers is given in ref. [8], p551. The channeltron is placed off axis to avoid interference from neutral species. The intensity of the sputtered secondary ions of any mass/charge ratio can then be analysed sequentially as a function of time.

The secondary ion optics can be controlled using an external computer system to produce the required mass resolution and intensity of the secondary ions. It is important for the analysis of ^{18}O profiles that the detection variables used for the ^{18}O isotope are identical to those used for the ^{16}O isotope to allow a direct comparison of the ion intensities. In the case of the cation study a quantitative study of the concentration of ions is not possible due to the different ion yields of the various cations.

7.8.2. Depth Profiling Mode of Analysis.

The depth profiling mode of analysis allows the measurement of depths upto ~10microns. In this mode the primary ion beam is rastered across a square region of the sample surface to produce a crater in the sample. The secondary ion intensities of the ions of interest are recorded sequentially as a function of time. The beam was rastered over an area of 300x300 microns in this work. The reason for this is because the ion beam intensity is not uniform over its diameter, but follows the approximate shape of a Gaussian distribution. Therefore, higher

sputter rates will result at the centre of the beam than at the edges. The area of analysis over which the secondary ions are measured can then be gated to avoid crater wall effects. The depth of the crater is then measured post-analysis using a Talystep (Rank-Taylor Hobson) surface profilometer. Assuming a constant sputter rate with depth, the time scale can easily be converted to a depth scale, thus the secondary ion intensities are effectively monitored as a function of depth. In the work presented here, the primary ion energy used was 10kV and the primary beam current varied between 20nA and 300nA, depending on the depth required. The electron beam used to charge neutralise the sample was accelerated at 1.6kV, with a current of 2.6A. The values chosen were determined empirically.

The profilometer has a 10% error associated with it. This error was further increased by the roughness seen at the bottom of the craters. This roughness was due to the original surface roughness and porosity of the sample. The roughness increased as a function of depth of the crater, therefore there is a maximum depth before the level of roughness becomes unacceptable.

A typical example of the raw data from the SIMS operated in the depth profile mode is shown in figure 7.5. From this data a diffusion coefficient can be calculated by fitting the data to the appropriate solution to the diffusion equation.

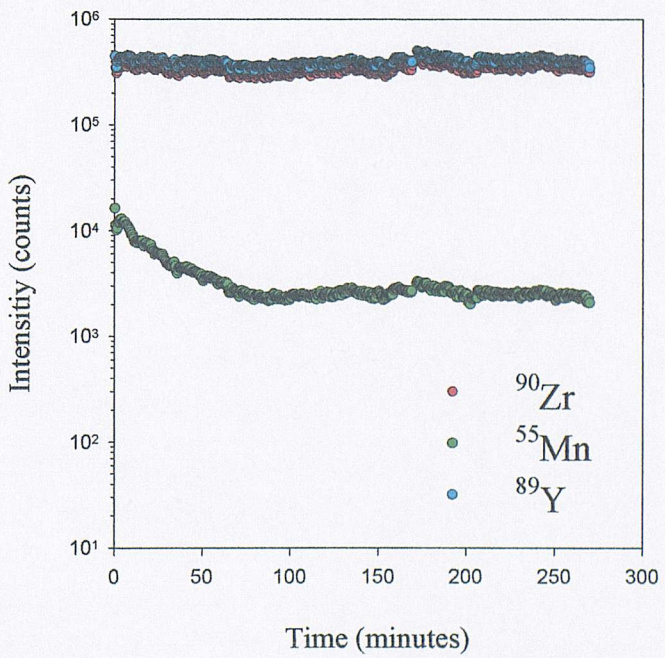


Figure 7.5. SIMS raw data for a depth profile of manganese into polycrystalline YSZ at 1250°C.

7.8.3. Line-scanning Mode of Analysis.

The line-scanning technique allows significantly longer depths to be monitored (up to ~1500microns). The line-scanning technique was developed for fast oxygen ion conductors by Chater *et al* [9]. The ^{18}O exchanged sample (or the manganese diffusion sample) is cut perpendicular to the diffusate surface (^{18}O or manganese). The cross-section is then mechanically polished. The sample is then placed in the SIMS with cross-section normal to the primary ion beam. An area is then rastered to clean the sample and then a highly focused beam is scanned laterally across the exposed surface. Again, the secondary ions of interest are recorded sequentially. In this case the length of the scan is controlled by the SIMS instrument and so no post-analysis is required to calculate the depth. There is an uncertainty in the lateral position of the ion beam which translates into an uncertainty in the penetration depth of around 10%. The line-scanning technique is shown schematically in figure 7.6.

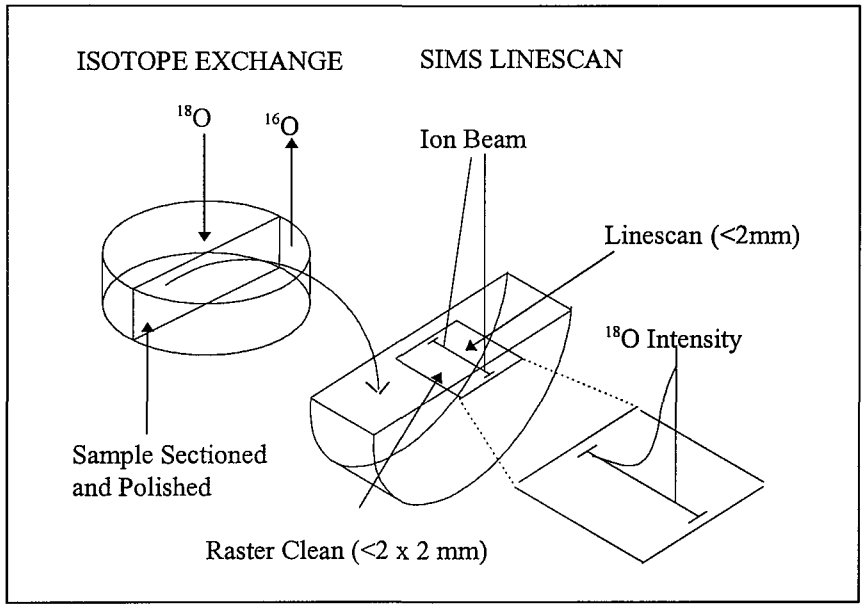


Figure 7.6. Schematic diagram summarising the SIMS/line-scan technique (redrawn from [9]).

The line-scanning mode also has minimum depth to which it can accurately monitor a diffusing species. This is due to width of primary ion beam. The beam was focused to a size of around 10-20 microns by maximising the energy (15kV) and reducing the beam current (0.5-5nA). However, a beam width of 10 microns

will have a large effect on the intensities measured if the depth is limited to say 50 microns. The effect of the beam diameter has been shown to significantly affect the shape of the diffusion profile, thus making determination of the diffusion length difficult, by a model developed by De Souza [3] for relatively short profiles. De Souza thus suggests the minimum line-scan length with a beam diameter of 10-20 microns is around 100 microns. A typical set of raw data from the line-scanning technique is shown in figure 7.7. From this an oxygen ^{18}O concentration profile, $C(x) = \frac{^{18}O}{^{16}O + ^{18}O}$ can be determined and fitted to the appropriate solution to the diffusion equation (equation 6.20).

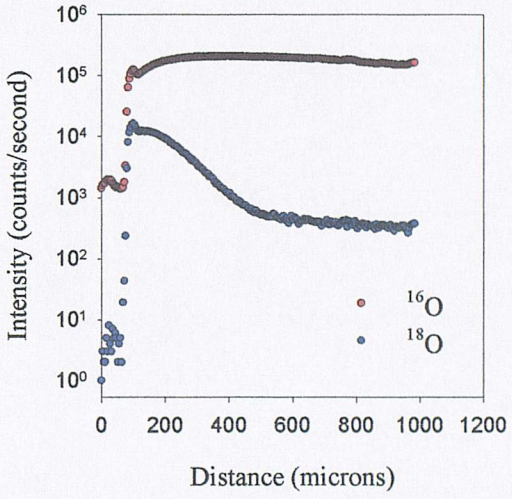


Figure 7.7. SIMS raw data for a line-scan for ^{18}O diffusion into single crystal CGO at 858°C.

7.8.4. Limitations of the SIMS Instrument.

There are some fundamental limitations to SIMS analyses given by the primary and secondary ion systems utilised. These can be divided into the lateral and depth resolution and the concentration detection limit. The detection limit of the SIMS is in the ppm range, and as a result more than adequate for the experiments undertaken here. The ultimate depth resolution of the instrument is governed by ion beam mixing of the target atoms caused by the collision cascade of the primary ion particle within the sample. The lateral resolution is governed by the primary ion beam dimensions, as mentioned above. The uncertainty in depth caused by ion beam mixing is of the order of nanometres for keV primary ion

beams. Since the penetration depths used in this work were seldom below 1 micron, ion beam mixing does produce a significant error. Descriptions of ion beam mixing phenomena can be found in, for example, [3,8]. A more significant depth error is introduced by roughening of the sample. As a result care was taken to ensure the samples were as flat and smooth as possible. Figure 7.8 shows an AFM image of the surface of a ceramic used for ^{18}O diffusion experiments and a single crystal of zirconia used for manganese diffusion. It is clear that the level of surface roughness is very small in both cases, although the polycrystalline material has a greater mean surface roughness.

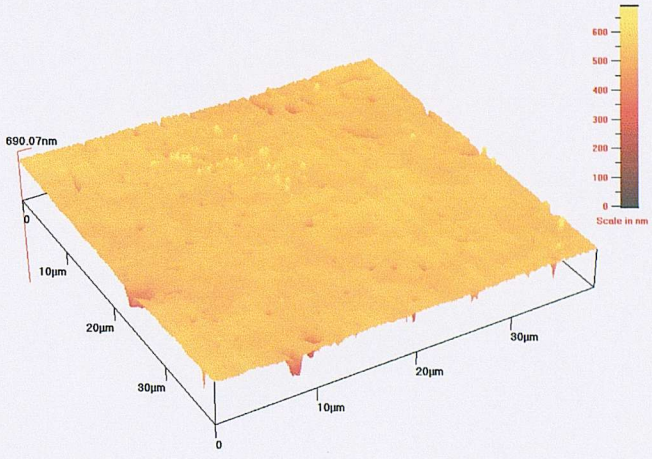


Figure 7.8 (a). Polycrystalline $Ce_{0.9}Gd_{0.1}O_{1.95}$.

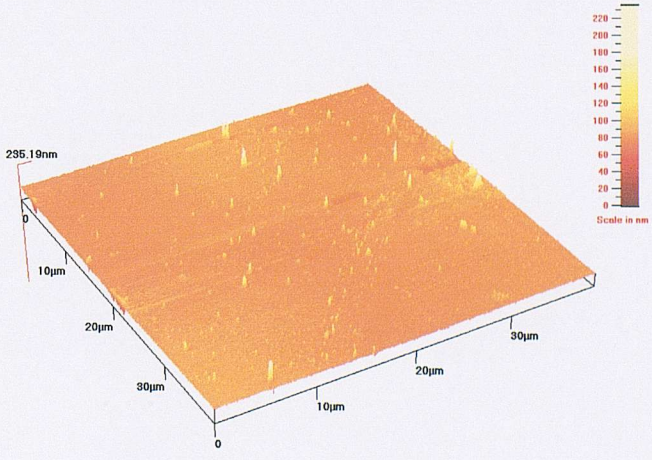


Figure 7.8 (b). Single crystal $Zr_{0.81}Y_{0.19}O_{1.905}$.

Figure 7.8. AFM images of the surface of CGO and YSZ.

In order to reduce the error due to the lateral resolution of the beam in the line-scanning mode, scans of over 250 microns were employed. However this introduces another limitation to the experiments.

The minimum time for a diffusion anneal is around 600 seconds due to uncertainties introduced to heating and cooling rates. The maximum length of an ^{18}O anneal is governed by limitations in time. It is not practical to use the exchange rig for more than one week for each anneal. Assuming the pre-anneal to equilibrate the sample is 10 times longer than the exchange anneal, then the exchange anneal is limited to around 15 hours, or 54000 seconds. The minimum depth we can measure is around 200 nanometres, governed by the topography of the sample, and the maximum depth is 1500 microns. However, a region between ~10 microns and 250 microns can also not be measured accurately. Therefore a range of oxygen diffusion coefficients that can be determined can be calculated from equation 6.20 and substituting the limits to depth and time given above. This is summarised in table 7.5, below, separating the two modes of analysis.

	Min D_T (cm^2/s) Anneal time 54000 secs	Max D_T (cm^2/s) Anneal time 600 secs
Depth profiling	5×10^{-16}	1×10^{-10}
Line-scanning	6×10^{-10}	3×10^{-6}

Table 7.5. Limitations to the oxygen tracer diffusion coefficient measurable using $^{16}O/^{18}O$ exchange/SIMS technique.

Similarly this can be adapted for the diffusion of cations, except the maximum diffusion anneal time is not limited to the same extent since a pre-anneal to equilibrate the sample is not necessary, nor is a UHV system required, therefore other furnaces in lower usage can be used. The longest anneal used in the study of cations was 400 hours. Table 7.6 shows the limitations of the cation solute diffusion coefficient measurable with these experimental limits.

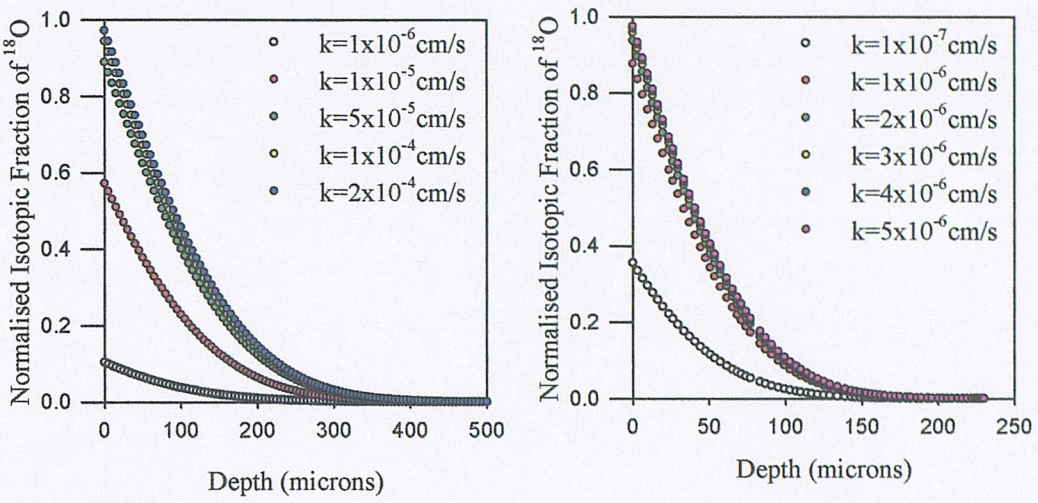
	Min D_{solute} (cm^2/s) Anneal time 2160000secs	Max D_{solute} (cm^2/s) Anneal time 600 secs
Depth profiling	1×10^{-17}	1×10^{-10}
Line-scanning	2×10^{-11}	3×10^{-6}

Table 7.6. Limitations to the diffusion coefficient measurable using $^{16}O/^{18}O$ exchange/SIMS technique.

It is clear from tables 7.5 and 7.6 that a wide range of diffusion coefficients can be measured. However, measuring diffusion coefficients above $3\times10^{-6}\,cm^2/s$ is difficult. There is also a small region around 10^{-10} cm^2/s which is difficult to measure accurately, as profiles will tend to lie in the transition depth where both depth profiling and line-scanning are at their upper and lower limits, respectively.

A further limitation is that regarding the surface exchange coefficient. It was shown in chapter 6 that as the ratio of k to D_T increases, the surface concentration will asymptotically approach the concentration of ^{18}O in the gas. This means at high $k:D_T$ ratios a large change in k will result in only a very small change in the surface concentration. The scatter which is evident in the ^{18}O signal (and thus the $C(x)=\frac{^{18}O}{^{16}O+^{18}O}$ values used in the solution to the diffusion equation) limit the accuracy to which k can be measured at high k/D_T ratios. The maximum value for the surface exchange coefficient for a given D_T can thus be estimated and the ultimate limit to k estimated from the Max D_T given in table 7.5.

Figure 7.9 shows the effect of changing k at $D_T=10^{-7}cm^2/s$ and $D_T=10^{-9}cm^2/s$ at $t=1000$ seconds and 20000 seconds, respectively. The profiles have generated from equation 6.20, using a program in MATLAB created by De Souza [3].



(a). $D_T = 10^{-7} cm^2 / s, t = 1000$ (b). $D_T = 10^{-9} cm^2 / s, t = 20000$

Figure 7.9. Effect of changing k on the shape of the diffusion profile at given values of D_T and anneal times.

Using the limitations of Max $D_{T,}$ and the minimum anneal time t = 600 diffusion profiles can be generated for given values of the surface exchange coefficient. These are shown in figure 7.10.

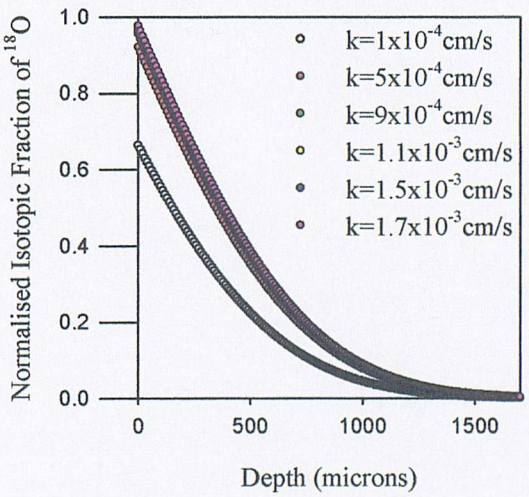


Figure 7.10. Effect of changing k on the shape of the diffusion profile at $D_T = 3 \times 10^{-6}, t = 600$.

It is evident from figures 7.9 and 7.10 that when the value of the surface exchange coefficient is more than three orders of magnitude greater than the tracer diffusion coefficient, it becomes almost impossible to determine the absolute value of k. An increase in k by a factor of 5 leads to less than a 1% change in the surface concentration. This is less than the scatter in the data given in figure 7.7. It is also evident therefore that the maximum value of the surface exchange coefficient that can be determined with any precision is $\sim 5 \times 10^{-4}$ cm/s. If the exchange rate is greater than this it can not be detected with any accuracy.

The small effect on the surface concentration by increasing the surface exchange coefficient above a certain value was also illustrated by the plot of $C_{surface}$ against h' in figure 6.10.

The tracer diffusion results using the $^{16}O/^{18}O$ isotope exchange method are presented in Chapter 10 and the surface exchange results are given in Chapter 11. The initial results of the cation diffusion study are given in Appendix A.

7.9. References.

[1] B. T. Melekh, V. M. Egorov, Yu. M. Baikov, N. F. Kartenko, Yu. N. Filin, M. E. Kompan, I. I. Novak, G. B. Venus and V. B. Kulik, Solid State Ionics, **Vol 97**, (1997) p465.

[2] S.B. Adler, J.A. Lane and B.C.H. Steele, J. Electrochem. Soc. **Vol 143** (1996) p3554.

[3] R.A. De Souza, Ph.D. Thesis, University of London (1996).

[4] D. R. Killoran, J. Electrochem. Soc., **Vol 109** (1962) p170.

[5] G.C.Tyrrell, T.H. York and I.W. Boyd, Appl. Surf. Sci. **Vol 86** (1995) p50.

[6] W. Wein, Verh. Deutsch. Phys. Chem, **Vol 16** (1897) p165.

[7] S.B. Patel, Ph.D. Thesis, University of London (1994).

[8] A. Benninghoven, F.G. Rüdenauer and H.W. Werner. In Secondary Ion Mass Spectrometry, John Wiley and Sons, Inc., New York (1987).

[9] R.J. Chater, S. Carter, J.A. Kilner and B.C.H. Steele, Solid State Ionics, **Vol 53-56** (1992) p859.

8. Electrode Behaviour of Perovskite Cathodes on $Ce_{0.9}Gd_{0.1}O_{1.95}$.

8.1. Introduction.

The material properties required for the successful operation of a cathode in electrochemical devices such as SOFC and COG were described in chapters 1 and 2. The electrochemical function of the cathode is to increase the rate at which oxygen from the gas phase is incorporated into the electrolyte, to provide an even current distribution across the area of the electrolyte, and to convert the electronic current in the connecting wires/current collecting material to the ionic current that passes through the electrolyte. The overall reaction at the cathode can be written grossly as:

$$\tfrac{1}{2}O_2\,(\text{gas}) + 2e^-\,(\text{electrode, current collector}) \rightarrow O^{2-}\,(\text{electrolyte}) \quad \text{eqn. (8.1)}$$

However, the processes that make up this overall reaction are not well understood. The matter appears to be complicated by the fact that different electrode materials operate in different ways and also by the wide range of hypotheses for the cathodic processes given in the literature. Several possible steps for the reduction of oxygen at a solid surface were given in chapter 6. The reduction process at a cathode is further complicated by the fact that three phases are present and in contact with each other. The point where the electrolyte, electrode and gas are all in contact with each other is known as the triple phase boundary.

The overall polarisation resistance of the cathode is due to the energy required for reaction 8.1 to occur. If an attempt is to be made to reduce this polarisation resistance, then the processes which provide the main energy barrier to the reaction must be determined. Steady state analysis methods do not provide information concerning the individual steps therefore methods such as current interruption [1,2], AC impedance spectroscopy [3,4,5,6] or state space modelling [7] are used.

In this chapter all of the myriad of possible reaction mechanisms and their respective equations governing the polarisation resistance are not given. However, a selection of the more plausible proposed mechanisms will be mentioned, then the results obtained for the mixed conducting perovskite

$La_{0.6}Sr_{0.4}Co_{0.2}Fe_{0.8}O_{3-\delta}$ on a $Ce_{0.9}Gd_{0.1}O_{1.95}$ electrolyte will be presented. Finally the data will be compared to a proposed model for the electrode reaction.

In general the nature of electrode reaction is expected to be different for slow oxygen ion diffusers and for fast oxygen ion diffusers. In the case of slow oxygen ion diffusers the reaction occurs primarily at the triple phase boundary. For fast oxygen ion conductors the reaction may occur over a larger volume of the electrode material. The overall transport of oxygen in both slow and fast ion conductors is illustrated schematically in figure 8.1.

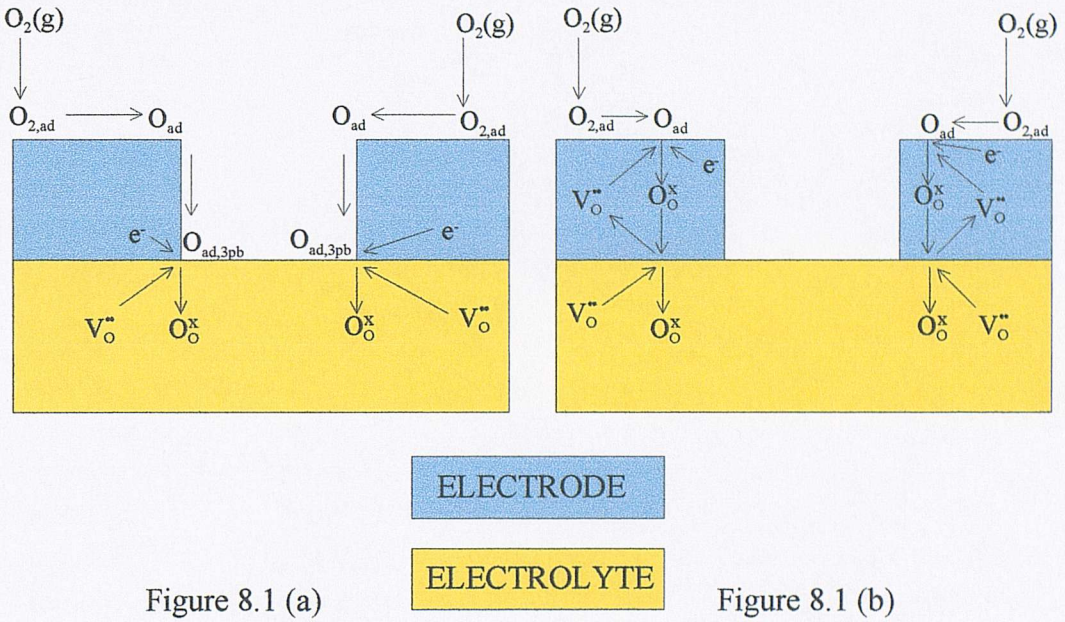


Figure 8.1 (a) Figure 8.1 (b)

Figure 8.1. Schematic illustration of the electrode process in (a) a slow oxygen ion conductor and (b) a fast oxygen ion conductor.

8.2. Slow Oxygen Ion Conductors.

For very slow oxygen ion conductors such as lanthanum manganite, and noble metals such as gold or platinum, it is widely considered that the reduction reaction occurs at or near the triple phase boundary [1,8]. If oxygen is only incorporated into the electrolyte at the triple phase boundary then oxygen gas must diffuse through the pores or be adsorbed onto the surface of the electrode

and diffuse along the surface to the triple phase point. The adsorbed oxygen can then be incorporated into the bulk of the electrolyte if an oxygen vacancy from the electrolyte and two electrons from the electrode are available. Therefore gas phase diffusion through the pores, surface diffusion of an adsorbed species, ionisation of the adsorbed species and incorporation of the oxygen into the electrolyte all contribute to the overall polarisation resistance. This process can be described by the following set of equations.

$$O_{2(pores,1)} \rightarrow O_{2(pores,2)} \qquad \text{eqn. (8.2)}$$

$$O_{2(pores,2)} + S_{ad} \rightarrow O_{2,ad} \qquad \text{eqn. (8.3)}$$

$$O_{2,ad} + S_{ad} \rightarrow 2O_{ad} \qquad \text{eqn. (8.4)}$$

$$O_{ad,1} \rightarrow O_{ad,2} \qquad \text{eqn. (8.5)}$$

$$O_{ad,2} + V^{\bullet\bullet}_{O,electrolyte} + 2e^{'} \rightarrow O^{\times}_{O} + S_{ad} \qquad \text{eqn. (8.6)}$$

Equation 8.2 represents the diffusion of oxygen through the pores from site 1 to site 2. Equation 8.3 shows the physisorption of oxygen gas at a site for adsorption, S_{ad}. Equation 8.4 shows the dissociation of the adsorbed molecule at another site for adsorption. Equation 8.5 then represents the diffusion of the adsorbed species along the surface of the electrode from site 1 to site 2 and equation 8.6 shows the charge transfer reaction as the adsorbed molecule is ionised and then transferred into the electrolyte, leaving behind an adsorption site.

Any of these steps may be rate limiting and the rate limiting step may change depending on the conditions to which the electrode is being subjected. For example, Badwal *et al* [5] suggest for a platinum electrode at high temperatures the electrode polarisation resistance is governed by surface diffusion of adsorbed oxygen along the platinum surface. Several other workers have reported that gas phase diffusion provides the limiting step [9,10]. The effect of gas phase diffusion is more significant at low oxygen partial pressures [6,11]. The dissociative adsorption of the oxygen molecule is also often cited as the rate limiting step for noble metal cathodes [3]. It is important to note that if several serial processes are occurring, all with different activation energies, then the relative importance of each process will change with temperature. It also likely that oxygen partial pressure and the degree of overpotential to which the cathode

is exposed will also change the importance of each process as both pO_2 and the overpotential will alter the oxygen stoichiometry of a perovskite cathode. It is therefore unlikely that any one step is rate limiting for all cases.

If the charge transfer process across the electrode/electrolyte interface is rate limiting (described by equation 8.6) then the polarisation resistance is determined by the Butler-Volmer relationship of current to voltage, given as equation 8.7 [12,13].

$$I = I_0\left(\exp\left\{\frac{\alpha_a nF\eta}{RT}\right\} - \exp\left\{\frac{-\alpha_c nF\eta}{RT}\right\}\right) \qquad \text{eqn. (8.7)}$$

where α_a and α_c are the anodic and cathodic transfer coefficients, respectively, n is the number of charges transferred in each reaction, I is the current density, I_0 is the exchange current density and the other symbols have their usual meanings. The magnitude of I_0 is dependent on the electrode and the electrolyte material. η is the overpotential of the cathode describing how far away from the equilibrium potential the system is and is defined as,

$$\eta = V - V_{rev} \qquad \text{eqn. (8.8)}$$

where V_{rev} is the equilibrium or reversible potential and V is the potential difference across the interfacial layer. The charge transfer resistance, R_{ct} can be determined by differentiating equation 8.7 with respect to η, where,

$$\frac{1}{R_{ct}} = \frac{\partial I}{\partial \eta} \qquad \text{eqn. (8.9)}$$

In the case where there is only a very small overpotential, such that $V \cong V_{rev}$ then combining equations 8.8 and 8.9, equation 8.10 is obtained.

$$R_{ct} = \left(\frac{RT}{nF}\right) \Big/ I_0 \qquad \text{eqn. (8.10)}$$

If the polarisation resistance of the electrode is governed by a gas phase mass transport process the concentration of adsorbed species able to take part in the charge transfer process will be less than the equilibrium value. Therefore a concentration gradient through the electrode will develop and create a driving

force for the flow of oxygen ions. In this case the current density will be proportional to the concentration gradient, such that,

$$I \alpha \theta_{eq} - \theta$$

where θ is the fraction of occupied adsorbed sites and θ_{eq} is the fraction of adsorbed sites under equilibrium conditions. There is thus a limiting current density, I_L where $\theta = 0$. (I_0 occurs when $\theta = \theta_{eq}$.) It can then be shown that the current density through the electrode for a mass transport limitation (i.e. concentration polarisation) can be expressed as [14,15],

$$I = I_L\left(\exp\left\{\frac{nF\eta}{RT}\right\} - 1\right) \qquad \text{eqn. (8.11)}$$

At small overpotentials, equation 8.11 can be linearised to give,

$$I = I_L \frac{nF\eta}{RT} \qquad \text{eqn. (8.12)}$$

It is clear then that at small overpotentials there is a linear dependence of current to the overpotential so that the cathode material shows Ohmic behaviour. The mass transfer resistance, R_{mt}, at small overpotentials can then be found by differentiating equation 8.12 with respect to η.

$$\frac{1}{R_{mt}} = \frac{\partial I}{\partial \eta} \qquad \text{eqn. (8.13)}$$

to give,

$$R_{mt} = \left(\frac{RT}{nF}\right) \Big/ I_L \qquad \text{eqn. (8.14)}$$

The limiting current density is proportional to $pO_2^{1/2}$ [14] and as such mass transfer polarisation at low overpotentials (or $I \rightarrow 0$) is also proportional to $pO_2^{1/2}$. The charge transfer resistance can be shown to be proportional to $pO_2^{1/4}$ [15]. Thus resistance measurements as a function of oxygen partial pressure are a useful tool in determining the rate determining step in a triple phase boundary mechanism.

8.3. Fast Oxygen Ion Conductors.

For slow oxygen ion conductors it is reasonable to neglect diffusion through the bulk of the electrode as a possible pathway for the transport of oxygen into the electrolyte. However, for fast oxygen ion conductors such as the lanthanum cobaltites, oxygen may be able to pass through the bulk of the electrode as well as along its surface, thus increasing the total current through the electrode and hence reducing the polarisation resistance. The reduction in the polarisation resistance has been seen experimentally by several workers [1,14,16].

The reaction mechanism for this bulk diffusion mechanism can be described in a similar method to that used to describe slow oxygen ion conductors [17]. Gas phase diffusion described by equation 8.2 is the same for this mechanism.

$$O_{2(g)} + S_{ad} \rightarrow 2O_{ad,electrode} \qquad \text{eqn. (8.15)}$$

$$O_{ad,electrode} + V^{\bullet\bullet}_{O,electrode} + 2e^{'} \rightarrow O^{\times}_{O,electrode} \qquad \text{eqn (8.16)}$$

$$O^{\times}_{O,electrode}(1) + V^{\bullet\bullet}_{O,electrode}(2) \rightarrow O^{\times}_{O,electrode}(2) + V^{\bullet\bullet}_{O,electrode}(1) \qquad \text{eqn. (8.17)}$$

$$O^{\times}_{O,electrode} + V^{\bullet\bullet}_{O,electrolyte} \rightarrow O^{\times}_{O,electrolyte} + V^{\bullet\bullet}_{O,electrode} \qquad \text{eqn. (8.18)}$$

Equation 8.15 describes the dissociative adsorption of oxygen molecules onto the electrode surface occurring at an unspecified adsorption site. The adsorbed oxygen is then incorporated into the bulk of the electrode (away from the triple phase boundary) as described by equation 8.16. Equation 8.17 summarises the diffusion of oxygen ions from one point in the electrode to another. Equation 8.18 describes the transfer of oxygen ions from the electrode into the electrolyte.

It should be noted that all materials exhibit some oxygen ion conductivity. Thus both processes are likely to occur to a greater or lesser extent in all materials. Therefore the three phase boundary mechanism for slow oxygen ion conductors can be considered to be one limiting case (and the bulk diffusion for fast oxygen ion conductors the other limiting case) of a given reaction, rather than a totally different process [14].

As with the slow oxygen ion conducting electrodes, it is possible there is one rate limiting step in the overall reaction. Any of the steps such as gas phase diffusion, dissociative adsorption, eqn. 8.15, incorporation of oxygen, eqn. 8.16, diffusion of oxygen ions, eqn. 8.17 or transfer of oxygen ions from the electrode into the electrolyte, eqn. 8.18 could be the rate determining step given certain conditions. Gas phase diffusion is described in the same way as for slow oxygen ion conductors and transfer of oxygen ions from the electrode into the electrolyte is similar to the charge transfer process given earlier, and thus follows a Butler-Volmer type response. It should be noted that equations 8.15 and 8.16 (dissociative adsorption and incorporation of oxygen) can be combined to give the surface exchange reaction described in chapter 6. There are therefore two possible limiting processes which have not yet been considered, surface exchange and diffusion through the bulk.

Given certain assumptions, if the rate limiting process is the diffusion of oxygen through the bulk of the mixed ionic electronic conducting electrode it can be shown that the steady state resistance of the electrode, R_{diff}, is given by [6,15,17],

$$R_{diff} = \left(\frac{RT}{4F^2}\right) \cdot \frac{\ell}{S} \cdot \frac{f_D}{C_i D_T} \qquad \text{eqn. (8.19)}$$

where ℓ is the thickness of the electrode, S is the area of the electrode/electrolyte interface, D_T and f_D are the tracer diffusion coefficient and correlation factor, respectively (see chapter 4), C_i is the concentration of oxygen sites in the electrode and the other symbols have their usual meanings. There are some assumptions required in creating the above expression, which are outlined below,

1. The electronic conductivity is much greater than the oxygen ion conductivity.
2. The diffusion of oxygen is driven by a chemical potential gradient between the electrode/gas interface and the electrode/electrolyte interface.
3. There are no interactions between the oxygen vacancies so their chemical potential is determined directly from their concentration.
4. The concentration of electrons throughout the thickness of the electrode is constant.
5. The thickness of the electrode is constant over the whole area of the electrode and the electrode/gas interfacial area is equal to the electrode/electrolyte interfacial area.

6. The overpotential is small enough so it does not affect the concentration of oxygen vacancies (and thus oxygen sites) in the mixed conductor and $D_V f_D\left[V_O^{\bullet\bullet}\right] = D_T C_i$.

The time dependent impedance response due to diffusion through a finite length electrode as been given by Siebert *et al* [17] and Lane [15]. The equation is shown in an adapted form to include tracer diffusion coefficients (as measurable from SIMS) rather than vacancy diffusion coefficients.

$$Z_{diff} = \left(\frac{RT}{4F^2}\right)\cdot\frac{\ell}{S}\cdot\frac{f_D}{C_i D_T}\cdot\frac{\tanh\left(\sqrt{\frac{j\omega\left[V_O^{\bullet\bullet}\right]f_D}{D_T C}\cdot\ell^2}\right)}{\sqrt{\frac{j\omega\left[V_O^{\bullet\bullet}\right]f_D}{D_T C_i}}} \qquad \text{eqn (8.20)}$$

This produces a characteristic shape known as a finite length diffusion Warburg impedance spectrum and has been seen experimentally in dense silver electrodes [18].

If the exchange of oxygen from the gas with the electrode is the rate limiting step then another expression can be derived. Equation 8.22 is based on that given by Adler *et al* [6] with a few specified alterations.

$$R_{ex} = \left(\frac{RT}{2F^2}\right)\cdot\frac{1}{kC_i S} \qquad \text{eqn. (8.21)}$$

where k is the surface exchange coefficient. This assumes the electrode/electrolyte area is equal to the electrode/gas area, that is, there is no porosity in the electrode. The equation also uses the expression $kC_i = r_O\left(\alpha_f + \alpha_b\right)$ (taken from [6]).

If the electrode has a small degree of porosity or surface roughness the surface area will be increased. Therefore a geometric factor must be included to reflect the fact that the active area for exchange is the gas/electrode interface over the whole volume of the electrode, rather than the electrode/electrolyte cross sectional area. This then produces equation 8.22,

$$R_{ex} = \left(\frac{RT}{2F^2}\right) \cdot \frac{1}{kC_i A_{g/el}} \qquad \text{eqn. (8.22)}$$

where $A_{g/el}$ is the total area of the gas/electrode interface.

As with the diffusion limitation, a time-dependent impedance can be given

$$Z_{ex} = \left(\frac{RT}{2F^2}\right) \cdot \frac{1}{kC_i A_{g/el}} \cdot \left(\frac{1}{1 + j\omega\tau_{ex}}\right) \qquad \text{eqn. (8.23)}$$

where τ_{ex} is the time constant for the surface exchange process. This process will thus exhibit the shape of a semi-circle. In this case, the resistance due to the exchange process is clearly strongly dependent on the microstructure. If a very fine particle size is used to provide a large active surface area, then the resistance will decrease substantially.

It is also apparent that although the terms "slow oxygen ion conductor" and "fast oxygen ion conductor" have been used to described the two limits to the electrode process, for the so-called "bulk diffusion mechanism" to significantly decrease the polarisation resistance, the surface exchange coefficient of the material must also be substantial.

It has been shown in chapter 6 and by several pieces of work by Kilner and De Souza (see for example [19,20]) that the surface exchange coefficient and tracer diffusion coefficient are related in the mixed conducting perovskite materials. It is therefore likely that given certain electrode microstructures, the resistance to diffusion will be of a similar magnitude to the resistance due to the surface exchange process. In the case of a porous material, the exchange process is taking place over the entire volume of the electrode and diffusion can then occur from the site of exchange to the electrode/electrolyte boundary. Using this theory, a continuum model has been developed by Adler *et al* [6]. This model is appropriate for calculating the AC response of a symmetrical cell consisting of two identical, porous, mixed conducting electrodes exposed to the same gas atmosphere. The model used here assumes the only contributions to the electrode polarisation resistance are the diffusion of oxygen ions in the mixed conductor and the exchange of oxygen gas at the mixed conductor/gas interface. As with the diffusion limited resistance, similar assumptions are required to reduce the number of variables in the equation. These are,

1. The electronic conductivity is much greater than the oxygen ion conductivity.
2. The diffusion of oxygen is driven by a chemical potential gradient between the electrode/gas interface and the electrode/electrolyte interface.
3. There are no interactions between the oxygen vacancies so their chemical potential is determined directly from their concentration.
4. The concentration of electrons throughout the thickness of the electrode is constant.
5. The thickness of the electrode is constant over the whole area of the electrode and there is a homogeneous particle size and distribution throughout the electrode.
6. The equations are linearised around the zero bias ($I \rightarrow 0$) solution.

Using these assumptions the total area specific polarisation resistance for this chemical reaction, R'_{chem}, is given by Adler *et al* [6] as,

$$R'_{chem} = \left(\frac{RT}{2F^2}\right).\sqrt{\frac{\tau_{el}}{(1-\varepsilon_{el})\left[V_O^{\bullet\bullet}\right]D_v a_{por} r_0(\alpha_f + \alpha_b)}} \qquad \text{eqn. (8.24)}$$

D_v is the vacancy diffusion coefficient, τ_{el} is the tortuosity of the electrode, ε_{el} is the porosity of the electrode, a_{por} is the specific surface area (i.e. per unit volume) of the electrode, r_0 is the exchange neutral flux density and α_f and α_b are constants specific to the mechanism of the exchange reaction. Using the expressions for the tracer diffusion coefficient and surface exchange coefficient, $D_V f_D\left[V_O^{\bullet\bullet}\right] = D_T C_i$ and $kC_i = r_O(\alpha_f + \alpha_b)$ and S as the cross sectional area of the sample, the chemical resistance to the reaction can be expressed as,

$$R_{chem} = \left(\frac{RT}{2F^2 S}\right).\sqrt{\frac{\tau_{el} f_D}{(1-\varepsilon_{el})D_T C_i^{\,2} a_{por} k}} \qquad \text{eqn. (8.25)}$$

The time dependant impedance can then be expressed as,

$$Z = R_{chem}\sqrt{\frac{1}{1-j\omega\tau_{chem}}} \qquad \text{eqn. (8.26)}$$

Where τ_{chem} is the relaxation time defined as,

$$\tau_{chem} = \frac{\left[V_O^{\bullet\bullet}\right](1-\varepsilon_{el})}{Aa_{por}kC_i} \qquad \text{eqn. (8.27)}$$

A is a thermodynamic factor, given in equation 4.41. This again gives a very characteristic shape of the impedance spectrum, known as a Gerischer impedance.

The shapes of the impedance spectra for the finite length diffusion limited process, the surface exchange limited process and the combined diffusion and exchange process are all shown on a normalised Nyquist plot of imaginary against real impedance, given as figure 8.2.

It is clear from figure 8.2. that each limiting situation has a different shaped impedance spectra and therefore a good insight into the dominant response can be gained solely from the shape of the spectra obtained. It should also be noted that a charge transfer limitation will produce a semi-circular response (with a relatively short time constant) and a gas phase diffusion limitation will also produce a semi-circular response but with a very large characteristic relaxation time.

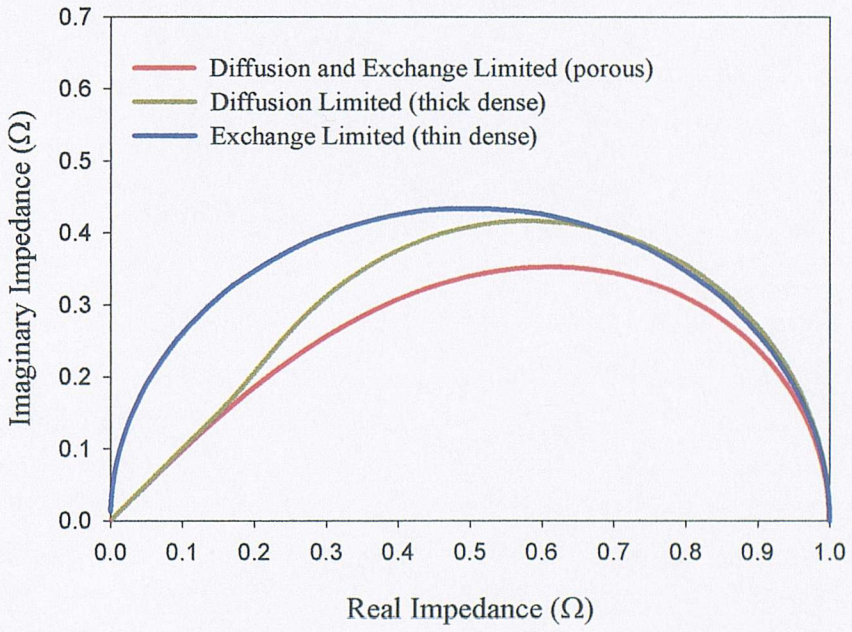


Figure 8.2. Impedance spectra for fast oxygen ion conducting cathodes where surface exchange and bulk diffusion are rate limiting.

8.4. Morphology of the $La_{0.6}Sr_{0.4}Co_{0.2}Fe_{0.8}O_{3-\delta}$ Electrode.

The $La_{0.6}Sr_{0.4}Co_{0.2}Fe_{0.8}O_{3-\delta}$ electrode was deposited on a $Ce_{0.9}Gd_{0.1}O_{1.95}$ electrolyte by painting on a slurry, burning off the organic material and then firing the electrode as described in chapter 7. Therefore the microstructure is not optimised to produce the lowest polarisation resistance possible. However, if the microstructure is known to allow estimates of the porosity, tortuosity and surface area of the electrode then the experimental results can be compared to those predicted by the equations presented in the previous sections.

Figure 8.3 shows a secondary electron image from SEM of the electrode on the electrolyte material. The electrode is approximately 12μm thick. The electrode shows a reasonable degree of porosity (20-30%) although some agglomeration of the particles appears evident. The contact between the electrode and the electrolyte appears good.

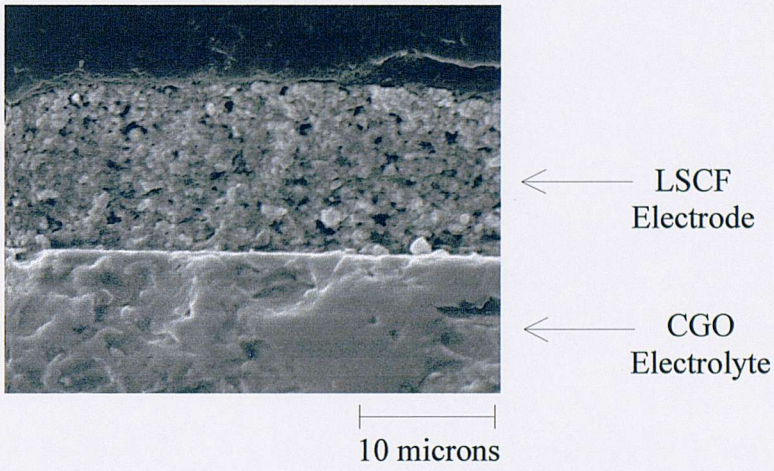


Figure 8.3. Scanning electron micrograph of the cross sectional view of a $La_{0.6}Sr_{0.4}Co_{0.2}Fe_{0.8}O_{3-\delta}$ electrode on a $Ce_{0.9}Gd_{0.1}O_{1.95}$ electrolyte.

Figure 8.4 shows an AFM image of the top view of the electrode. The particles are very fine giving a large surface area but it is clear that there is not a homogeneous distribution of the particles and agglomerations are visible. The specific surface area was investigated using BET. The specific surface area was found to be $1.33 m^2/g$. This can be converted to cm^2/cm^3 with knowledge of the lattice parameter, density and porosity of the electrode material.

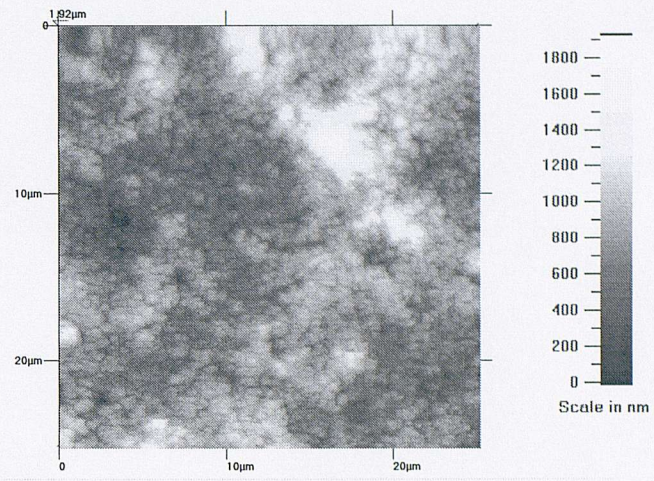


Figure 8.4. Atomic force micrograph of the top view of a $La_{0.6}Sr_{0.4}Co_{0.2}Fe_{0.8}O_{3-\delta}$ electrode on a $Ce_{0.9}Gd_{0.1}O_{1.95}$ electrolyte.

8.5. Polarisation Behaviour of the $La_{0.6}Sr_{0.4}Co_{0.2}Fe_{0.8}O_{3-\delta}$ Electrodes.

The electrode polarisation resistance for symmetrical $La_{0.6}Sr_{0.4}Co_{0.2}Fe_{0.8}O_{3-\delta}$ electrodes on a $Ce_{0.9}Gd_{0.1}O_{1.95}$ electrolyte was measured using AC impedance spectroscopy, applying a 20mV alternating signal with zero DC bias, as described in chapter 7. A frequency sweep from 0.01Hz to 10MHz was used and the measurements were made in air. Typical impedance spectra obtained are shown in figure 8.5.

For the high frequency data (the left hand side), the response is due to the grains and grain boundaries of the CGO electrolyte. The electrolyte response becomes distorted at high temperatures where the resistance is small and large frequencies are required to measure the signal. This is because the time constant of the electrolyte response is small at high temperatures. The reactance of an inductor is directly proportional to the frequency, therefore, at high frequencies and small impedances, internal inductive effects become more pronounced.

It is immediately clear that the electrode response is not semi-circular in shape. It thus appears to have some diffusion limitation, but it is not immediately evident whether it is a finite length diffusion limitation (equation 8.20) or a combined

diffusion and exchange limitation over the entire volume of the electrode (equations 8.26, 8.25 and 8.27).

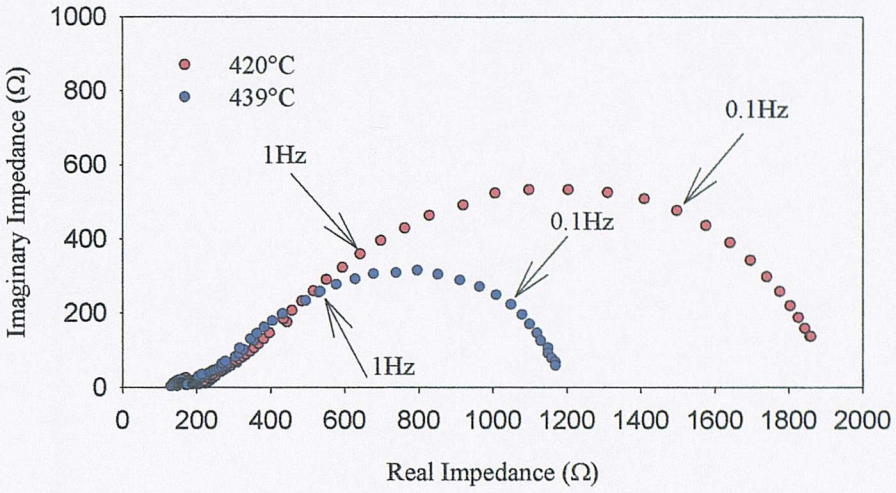


Figure 8.5. Impedance spectra for symmetrical $La_{0.6}Sr_{0.4}Co_{0.2}Fe_{0.8}O_{3-\delta}$ electrodes at 420°C and 439°C in air.

The resistance of the electrode can be determined from the high frequency and low frequency intercepts with the x-axis. At the lower temperatures the response had to be extrapolated to the x-axis at the low frequency end of the spectrum.

The area specific resistance (i.e. the measured resistance multiplied by the cross sectional area of the sample) can be plotted on a graph against the reciprocal of temperature in order to determine an activation energy for the electrode response. This is shown in figure 8.6.

The activation energy for the electrode polarisation resistance was calculated from a linear regression of the data and found to be 132±3kJ/mol. The activation energy of tracer diffusion and surface exchange in $La_{0.6}Sr_{0.4}Co_{0.2}Fe_{0.8}O_{3-\delta}$ is 186kJ/mol and 105kJ/mol, respectively [21]. Therefore the activation energy for the electrode polarisation resistance falls between the activation energy for these two processes. If the polarisation was dominated by diffusion (as given by equation 8.20) then the activation energy for electrode resistance would be expected to be the same as that measured in the tracer diffusion experiments. It therefore appears likely that a combination of diffusion and exchange controls the polarisation resistance of the electrode.

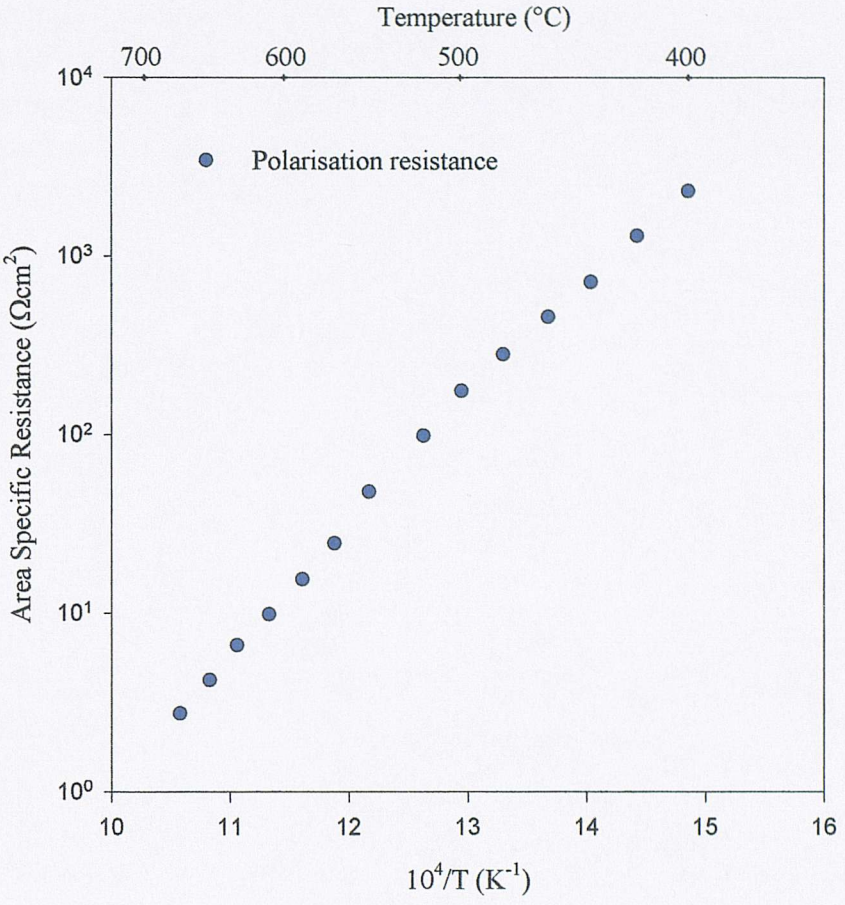


Figure 8.6. Area specific resistance of $La_{0.6}Sr_{0.4}Co_{0.2}Fe_{0.8}O_{3-\delta}$ electrodes in air as a function of temperature.

Thus, two scenarios are possible. The first is that diffusion and exchange takes place over the entire volume of the electrode as suggested by Adler *et al* [6] or the second is that exchange takes place on the surface furthest away from the electrolyte and then diffuses through the electrode. Thus the surface exchange limited resistance (equation 8.23) would be in series with the finite length diffusion resistance (equation 8.20) and the two terms can then simply be added.

8.6. Comparison of the Experimental Polarisation to the Models.

If the values of the tracer diffusion coefficient and the surface exchange coefficient taken from the data of Benson *et al* [21] are substituted into equations 8.26, 8.25 and 8.27, together with the value of a_{por}= 17000cm^2/cm^3 (from the

BET measurements), A, the thermodynamic factor taken from thermogravimetric analysis (TGA) of Benson *et al* [22], the porosity (30%) and the tortuosity (estimated at 1.5) then an impedance spectrum can be generated. A generated impedance spectrum for $La_{0.6}Sr_{0.4}Co_{0.2}Fe_{0.8}O_{3-\delta}$ at 420°C is shown together with the experimental data in figure 8.7.

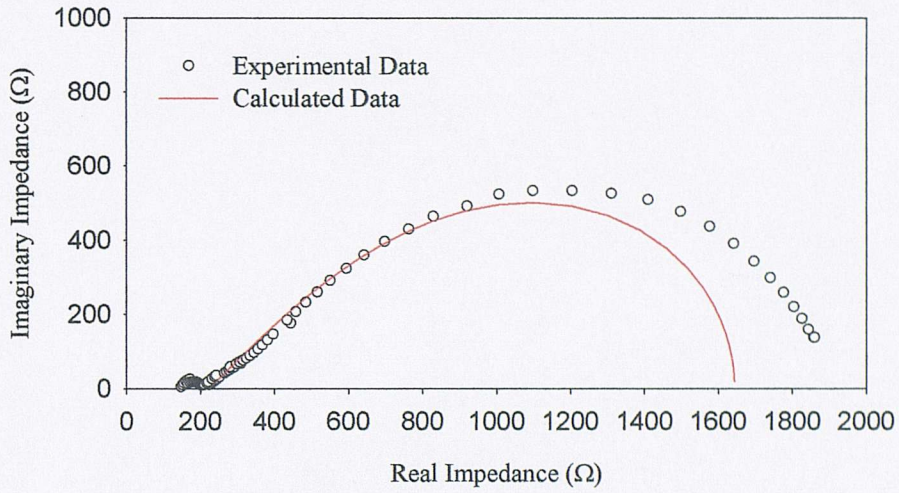


Figure 8.7. Impedance spectrum of $La_{0.6}Sr_{0.4}Co_{0.2}Fe_{0.8}O_{3-\delta}$ at 420°C together with a generated profile using equations 8.26, 8.25 and 8.27.

It is very important to note that the calculated data is not a fit to the experimental data using electrical equivalent circuits which is most commonly seen in the literature. This is a response calculated from entirely independent data obtained from tracer diffusion measurements and knowledge of the microstructure of the material from microscopy.

It is clear that the calculated polarisation resistance matches the shape of the experimentally determined polarisation resistance very well. The magnitude of the two values are also closely matched. There is a deviation from the theoretical impedance spectrum at the low frequency end of the spectrum. This can be attributed to several factors. The first is the heterogeneity shown in figure 8.4 will lead to an extension of the semi-circle with respect to the x-axis. Another possibility is that gas phase diffusion may be playing a part in the polarisation resistance. This will manifest itself as a semi-circular response at the low frequency end of the spectrum.

Figure 8.8 shows a comparison of the polarisation resistance calculated from the model with the experimentally obtained values. As can be seen the values are in good agreement over the entire temperature range.

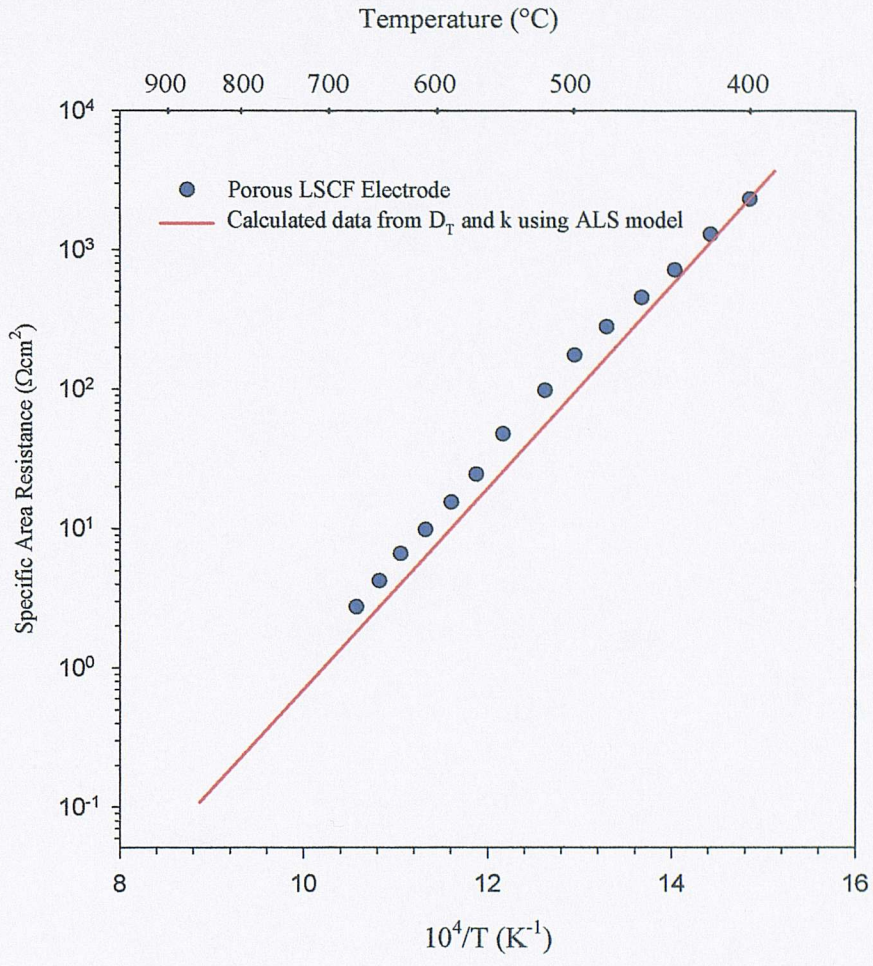


Figure 8.8. Comparison of experimental polarisation resistance for $La_{0.6}Sr_{0.4}Co_{0.2}Fe_{0.8}O_{3-\delta}$ with the resistance obtained from the ALS model.

Furthermore, the activation energy for the calculated resistance is 138kJ/mol which is very close to the experimentally observed value. It therefore appears that the model developed by Adler *et al* [6] known as the ALS model, is in good agreement with experimental results both qualitatively in terms of the shapes of the impedance spectra, and also quantitatively for the electrode morphology used here. It should be noted that with very different electrode morphologies, gas phase diffusion, for example, may play a more significant role and thus greater deviation from the ALS model may ensue.

If the exchange process takes place only at the external surface of the electrode away from the electrolyte and the oxygen diffuses then through the bulk of the electrode, the surface exchange limited resistance (equation 8.23) is added in series with the finite length diffusion resistance (equation 8.20) and the total resistance of the electrode is easily calculated by equation 8.28.

$$R_{Total} = R_{diff} + R_{ex} \qquad \text{eqn. (8.28)}$$

This total resistance can then be compared to the experimental resistance on an Arrhenius graph. This is shown in figure 8.9.

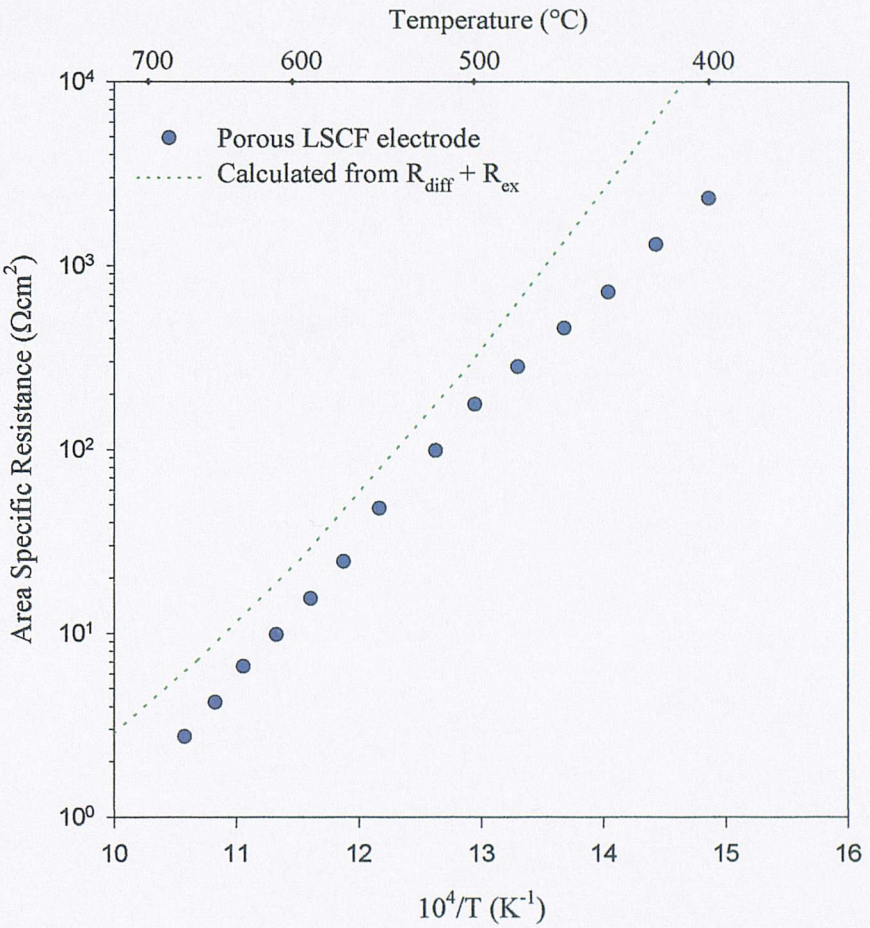


Figure 8.9. Comparison of experimentally obtained polarisation resistance for $La_{0.6}Sr_{0.4}Co_{0.2}Fe_{0.8}O_{3-\delta}$ with the resistance obtained from the sum of the finite length diffusion resistance and the surface exchange resistance.

There is a more noticeable deviation from the experimental behaviour using this model than for the ALS model, particularly at low temperatures. This is because of the high activation energy for diffusion, making oxygen transport at low temperatures very slow. It would therefore appear less likely for the exchange process to occur only at the furthest electrode/gas interface and to diffuse through the entire length of the electrode. This fact also implies that the entire length of the electrode is not being used to reduce oxygen gas but will act only as a current collector. This is particularly the case at low temperatures where the diffusion is slower in comparison to the rate of oxygen exchange.

It should also be noted that as the ALS model provides an accurate description of the electrode behaviour, then charge transfer across the electrode/electrolyte interface is not an important factor in the polarisation resistance. This therefore implies that the electrode response should be independent of the electrolyte material, assuming no reaction between the electrode and electrolyte occur and no impurities affect the electrode response.

Again, it is stressed that in this chapter the impedance spectra have not been fitted to an electrical equivalence circuit to obtain the "best fit". Instead the impedance spectra have been compared to data obtained from an entirely independent set of experiments using tracer diffusion measurements and microstructural knowledge of the electrode.

8.7. References.

[1] Y. Takeda, R. Kanno, M. Noda, Y. Tomida and O. Yamamoto, J. Electrochem. Soc., **Vol 134** (1987) p2656.

[2] K. Sasaki, J.-P. Wurth, R. Gschwend, M. Gödickemeier and L.J. Gaukler, J. Electrochem. Soc., **Vol 143** (1996) p530.

[3] J.E. Bauerle, J. Phys. Chem. Solids, **Vol 30** (1969) p2657.

[4] M. Mogensen, in Proc. of the 14th Risø International Symposium on Materials Science, edited by F.W. Poulsen, J.J. Bentzen, T. Jacobsen, E. Skou and M.J.L. Østergård, Risø National Laboratory, Roskilde, Denmark, (1993), p117.

[5] S.P.S. Badwal, H.J. de Bruin and A.D. Franklin, Solid State Ionics, **Vol 9/10** (1983) p973.

[6] S.B. Adler, J.A. Lane and B.C.H. Steele, J. Electrochem. Soc., **Vol 143** (1996) p3554.

[7] A. Mitterdorfer and L.J. Gaukler, in Proc. of the 5th Int. Symp. on Solid Oxide Fuel Cells, Eds.U. Stimming, S.C. Singhal, H. Tagawa and W. Lehnert, The Electrochemical Society, Pennington, NJ, **PV 97-18**, Aachen, (1997) p1177.

[8] J. Fouletier, P. Fabry and M. Kleitz, Electrochimica Acta, **Vol 40** (1995) p204.

[9] D. Braunshtein, D.S. Tannhauser and I. Reiss, J. Electrochem. Soc., **Vol 128** (1981) p82.

[10] T.H. Estell and S.N Flengas, J. Electrochem. Soc., **Vol 118** (1971) p2620.

[11] H. Deng, M. Zhou and B. Abeles, Solid State Ionics, **Vol 80** (1995) p213.

[12] J.O'M. Bockris, N. Bonciocat and F. Gutmann, in An Introduction to Electrochemical Science, Wykeham Publications Ltd., London (1974) p49.

[13] J.S. Newman, in Electrochemical Systems, 2nd Edition, Prentice Hall, Englewood Cliffs, NJ (1991) p188.

[14] M. Kleitz, T. Kloidt and L. Dessemond, in Proc. of the 14th Risø International Symposium on Materials Science, edited by F.W. Poulsen, J.J. Bentzen, T. Jacobsen, E. Skou and M.J.L. Østergård, Risø National Laboratory, Roskilde, Denmark, (1993), p89.

[15] J.A. Lane, Ph.D. Thesis, University of London (1996).

[16] E. Ivers-Tiffée, M. Schießl, H.J. Oel and W. Wersing, in Proc. of the 14th Risø International Symposium on Materials Science, edited by F.W. Poulsen, J.J. Bentzen, T. Jacobsen, E. Skou and M.J.L. Østergård, Risø National Laboratory, Roskilde, Denmark, (1993), p69.

[17] E. Siebert, A. Hammouche and M. Kleitz, Electrochimica Acta, **Vol 40** (1995) p1741.

[18] E. Schouler, Ph.D. Thesis, Grenoble (1979).

[19] J.A. Kilner, in Proc. of 2nd Int. Symp. on Ionic and Mixed Conducting Ceramics, Eds. T.A. Ramanarayanan, W.L. Worrel and H. Tuller, The Electrochem. Soc., (1994) p174.

[20] R.A. De Souza, Ph.D. Thesis, University of London (1996).

[21] S.J. Benson, R.J. Chater and J.A. Kilner, in Proc. of the 3rd Int. Symp. On Ionic and Mixed Conducting Ceramics, Eds. T.A. Ramanarayanan, W.L. Worrel, H.L. Tuller, M. Mogensen and A.C. Khandkar, The Electrochemical Society, Inc., Pennington, NJ, **PV 97-24**, Paris (1997).

[22] S.J. Benson, D. Waller, J.A. Lane and J.A. Kilner, presented at the 11th Int. Conf. On Solid State Ionics, Honolulu (1997).

9. Conductivity of $Ce_{1-x}Gd_xO_{2-\delta}$ and $Zr_{1-x}Y_xO_{2-\delta}$ Electrolytes.

9.1. Introduction.

In chapter 8 the polarisation resistance of a prospective cathode material was examined. For the successful operation of a SOFC or COG the electrolytic resistance must be kept to a minimum as well as the cathodic polarisation resistance. It is also important in an electrolyte material that the predominant charge carriers are oxygen ions and other charged species, such as electrons, electron-holes or protons, do not contribute significantly to the overall conductivity of the material (see chapters 1-4). The transport properties of stabilised zirconias and doped ceria materials have been the subject of intensive studies for many years due to their technological importance [1,2,3,4,5,6,7,8]. There are a phenomenal number of publications on the ionic conductivity of doped zirconia materials alone. In general, the results on the ionic conductivity of zirconia based materials are reasonably consistent, despite subtle variations in the dopant level and the presence of a number of impurities. The effect of impurities in the ceria based materials appears to create a larger difference in the conductivities observed [9].

Despite the consistency in the conductivity measurements obtained for zirconia, there appears to be different interpretations of the processes governing the temperature dependence of the conductivity. Kilner *et al* [10] have shown that the effect of the binding enthalpy of a defect associate, for example $\left\{Y'_{Zr}V_O^{\bullet\bullet}\right\}^{\bullet}$, can significantly affect the population of free vacancies in fluorites at low temperatures. This introduces a curvature in an Arrhenius graph of the logarithm of conductivity against the reciprocal of the temperature. However, despite the evidence of curvature in their work, Orliukas *et al* [4] state that the actual number of mobile, charge carrying oxygen vacancies remains constant, and equal to the number of extrinsic vacancies created by the dopant, over the entire temperature range of their investigation.

The electronic conductivity of stabilised zirconia materials [3] and doped ceria materials [8] have been found to be negligible in oxygen atmospheres. There are some inconsistencies in the literature regarding protonic conductivity in both yttria stabilised zirconia and gadolinia doped ceria. Wagner [11] showed that the

solubility of interstitial protons ($H_i^{\cdot}$) in YSZ was of the order of 10^{-4}, expressed as a mole fraction. Wagner also quoted a protonic diffusion coefficient of the order of 10^{-7}-10^{-6} cm^2/s at 900-1000°C. If the solubility of protons is that suggested by Wagner, then the protonic conductivity would be negligible compared to the oxygen ionic conductivity. More recently Aaberg *et al* [12] also suggested that protonic diffusion in zirconia is considerable, and moreover, suggested that, under anodic conditions, a larger number of protons may be injected into YSZ than predicted by the solubility measurements of Wagner. If the solubility of protons is considerable, an appreciable effect on the conductivity will be observed. The possibility of considerable proton solubility in gadolinia doped ceria has also been suggested in the work of Steele *et al* [13,14].

A discrepancy in the oxygen diffusivity obtained using tracer measurements and conductivity measurements has also been observed by Manning *et al* in high quality single crystals of yttria stabilised zirconia [15]. Small differences in the conductivity of both zirconia [4] and ceria [8] samples have also been seen when using DC or AC methods.

There is, therefore, a need to re-evaluate the oxygen transport properties of these materials. In the remainder of this chapter the oxygen ion conductivity, measured by AC impedance spectroscopy, of various doped zirconia and ceria materials will be presented and discussed. The oxygen ion diffusivity measured by tracer experiments using secondary ion mass spectroscopy will be presented in chapter 10, and a comparison between the results obtained by AC impedance and SIMS discussed. In chapter 11, results of the oxygen exchange process on the surface of these oxide materials will be given.

9.2. $Ce_{0.69}Gd_{0.31}O_{1.845}$ Single Crystal.

The work on the single crystal of CGO was carried out in conjunction with Mr. E. Ruiz-Trejo, at the Department of Materials, Imperial College.

Several segments of a CGO single crystal were cut on the same direction with no specific crystallographic orientation. These samples were polished down to ¼μm finish using a diamond spray. One sample was then selected for electrical conductivity measurements and the others used for tracer diffusivity experiments. Platinum electrodes were painted on both sides of the sample and sintered at

1000°C. The measurements were carried out in air, oxygen and nitrogen using an impedance analyser (Hewlett Packard 4192A). The range of temperature was 190-550°C, the voltage applied was 50 mV and the frequency range 10Hz - 13MHz. Three typical impedance spectra obtained for the single crystal in oxygen are shown in figure 9.1.

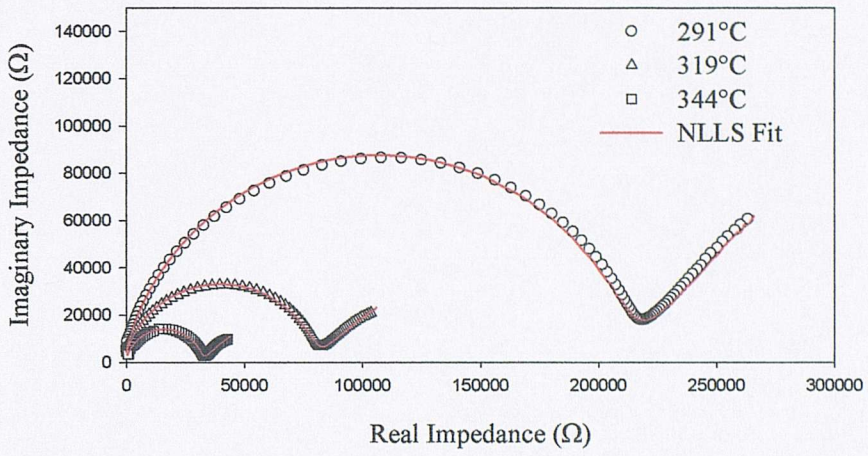


Figure 9.1. Impedance spectra obtained for single crystal CGO in oxygen.

The red line shows a non-linear least square (NLLS) regression assuming a resistor and capacitor electrical equivalent circuit with a statistical distribution in the time constant, as given by equation 7.25. As expected for a single crystal the impedance plot shows only one complete semicircle attributed to the bulk response plus a signal that can be attributed to the electrode response. This impedance shape was observed within the span of temperatures examined. The conductivity is thus obtained from the value of resistance given by the NLLS fit. A graph of the conductivity of the sample as function of temperature in three atmospheres, oxygen, air and nitrogen, is shown in figure 9.2.

As can be seen, all measurements lie on one line yielding the same conductivity values in this range of temperatures. It is therefore reasonable to assume this material is a pure oxygen ion conductor in this oxygen partial pressure range. An approximate value for the migration and association enthalpies for the sample in air have been calculated using equations 3.54 and 4.19. These are given as $\Delta H_m = 77 kJ / mol$ and $\Delta H_a = 37 kJ / mol$, respectively. This value of migration enthalpy is high for a doped ceria solid solution [16]. However, due to the small temperature range and the low data concentration, it is difficult to identify a separate term for the migration enthalpy and association enthalpy and

thus little confidence can be placed in these values. Therefore the activation energies for the conduction process were calculated using a simple linear regression analysis. The activation energies obtained were 109 ± 1 kJ/mol (nitrogen), 110 ± 1 kJ/mol (air) and 107 ± 1 kJ/mol (oxygen). These values are very similar to the sum of the migration enthalpy and association enthalpy, as expected.

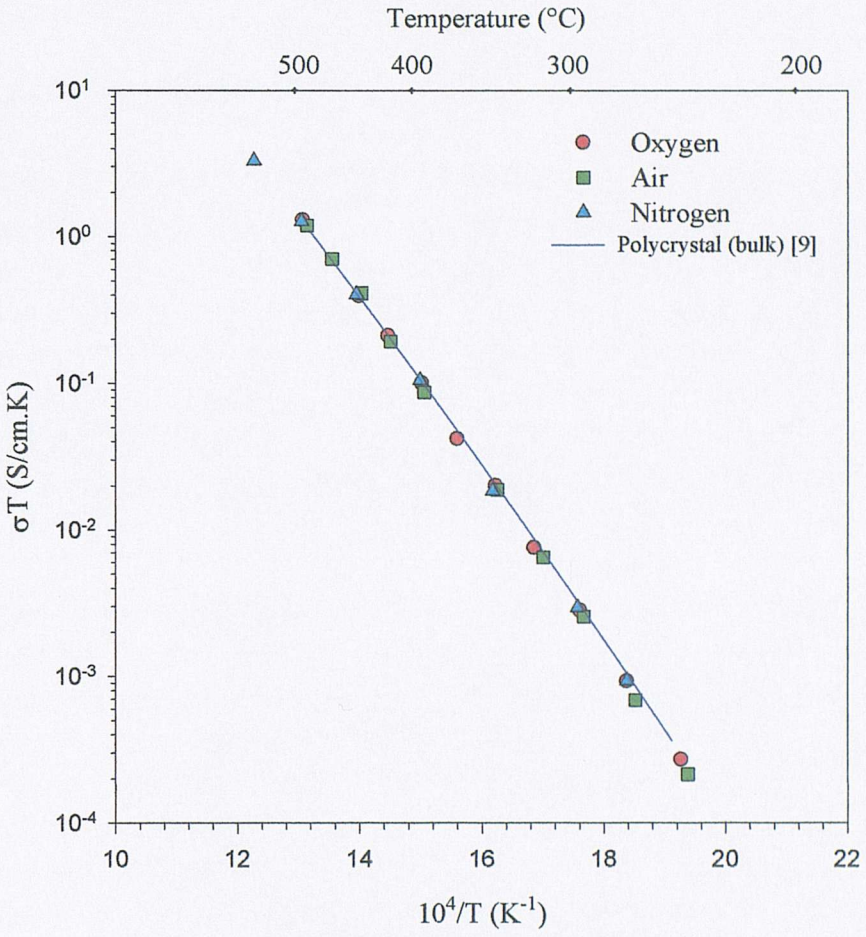


Figure 9.2. Arrhenius graph of conductivity of single crystal CGO in various atmospheres.

Figure 2 also contains the bulk conductivity of polycrystalline $Ce_{0.70}Gd_{0.30}O_{2-\delta}$ obtained by Ralph, in air, displayed as a continuous line [9]. The results are in excellent agreement with the single crystal data and display a similar activation energy. This shows that in AC impedance spectroscopy the bulk and grain boundary resistances can be accurately separated.

The activation energies obtained for the single crystal are higher than those generally reported for gadolinia doped ceria with a lower dopant concentration

[7,8]. This is consistent with the argument given in chapter 4 and by Kilner and Waters [10] that at high defect concentrations, a large number of vacancies can be trapped as defect associates. Thus a large association enthalpy contribution to the overall activation energy for conduction is expected at these high dopant concentrations.

9.3. $Ce_{0.9}Gd_{0.1}O_{1.95}$ Polycrystal.

Polycrystals of $Ce_{0.9}Gd_{0.1}O_{1.95}$ (powder supplied by SSC and prepared according to the details provided in Chapter 7) have been examined using AC impedance spectroscopy in air, dry N_2 and wet N_2. It has already been established that the material is a pure ionic conductor within this range of oxygen partial pressure. However, by exposing the sample to water vapour for a prolonged period of time it may be possible to introduce protons into the sample (as suggested by Kiratzis *et al* [14]) and thus affect the overall conductivity of the material. The sample examined in air had platinum electrodes painted on both sides of the sample, sintered at 1000°C.

A slightly more complicated procedure was required to perform the measurements in the wet and dry atmospheres. The platinum electrodes were painted on to the sample. The electrodes were sintered on in a mixture of 20% O_2 (research grade) and 80% oxygen free nitrogen (OFN), in a sealed glass tube at 1000°C for two hours. The glass tube was then evacuated ($\sim 10^{-10}$ atm, <1.5 v.p.m H_2O) and the samples annealed at 900°C for 48 hours to remove any water, and hence protonic carriers, from the sample. However during this process the ceria sample reduced considerably. Therefore, the sample was then annealed again in research grade O_2 at 900°C, to re-oxidise the sample. The partial pressure of water vapour was less than 2 v.p.m H_2O during the oxidation process. The electrical measurements were first carried out in a flowing atmosphere of dry, oxygen free nitrogen (OFN) which was passed through a desiccant (anhydrous calcium sulphate).

The OFN was then passed through water to produce a wet atmosphere. The sample was heated to 700°C and left overnight to equilibrate to the new atmosphere. Measurements were then carried out in the wet atmosphere over the entire temperature range.

Figure 9.3. shows typical low temperature impedance spectra for polycrystalline $Ce_{0.9}Gd_{0.1}O_{1.95}$ in wet and dry atmospheres. The high frequency semicircle is due to the bulk response and low frequency response is due to the grain boundaries. The shape and time constant (5×10^{-6} seconds) of the bulk response is essentially unaffected by the presence of water vapour. The small difference in response in the wet and dry atmospheres is most likely due to the difference in temperature of the two measurements.

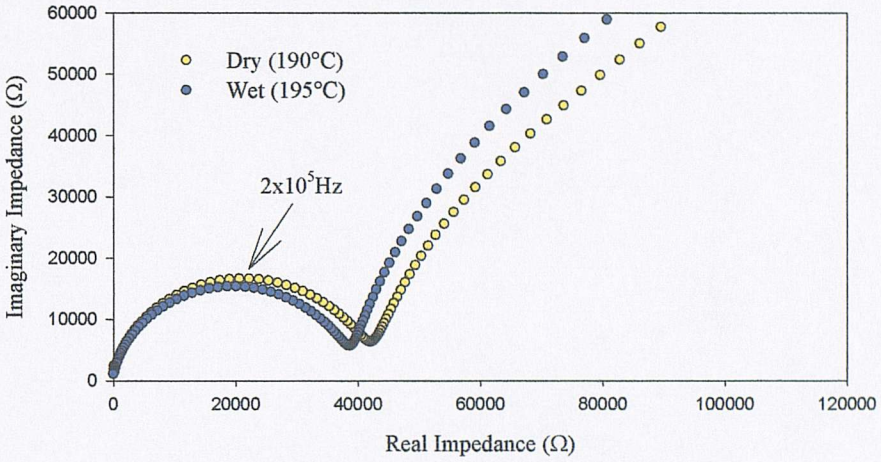


Figure 9.3. Impedance spectra obtained for polycrystalline $Ce_{0.9}Gd_{0.1}O_{1.95}$ in wet and dry nitrogen.

The grain boundary response is not complete at these low temperatures and hence the resistance calculated for the grain boundary is less accurate than that obtained for the bulk. Again, a NLLS regression was used to obtain the resistance and hence the conductivity of the material.

Figure 9.4. shows an Arrhenius graph of the bulk and grain boundary conductivity of the $Ce_{0.9}Gd_{0.1}O_{1.95}$ sample in the wet and dry atmosphere. It is clear that the bulk conductivity is totally unaffected by the presence of water vapour. This suggests that the proton solubility in $Ce_{0.9}Gd_{0.1}O_{1.95}$ is very low or the incorporation kinetics of protons at 700°C are too slow to allow a significant number of protons into solution. There is a slight difference in the grain boundary response in the wet and dry atmospheres. However, the data is more scattered for this response and so it is not possible to infer a meaningful discrepancy. It has been shown that severe reduction of ceria materials results in micro-cracking at the grain boundaries [17]. This may be the cause of both the scatter in the grain boundary response and also the small difference between the two atmospheres.

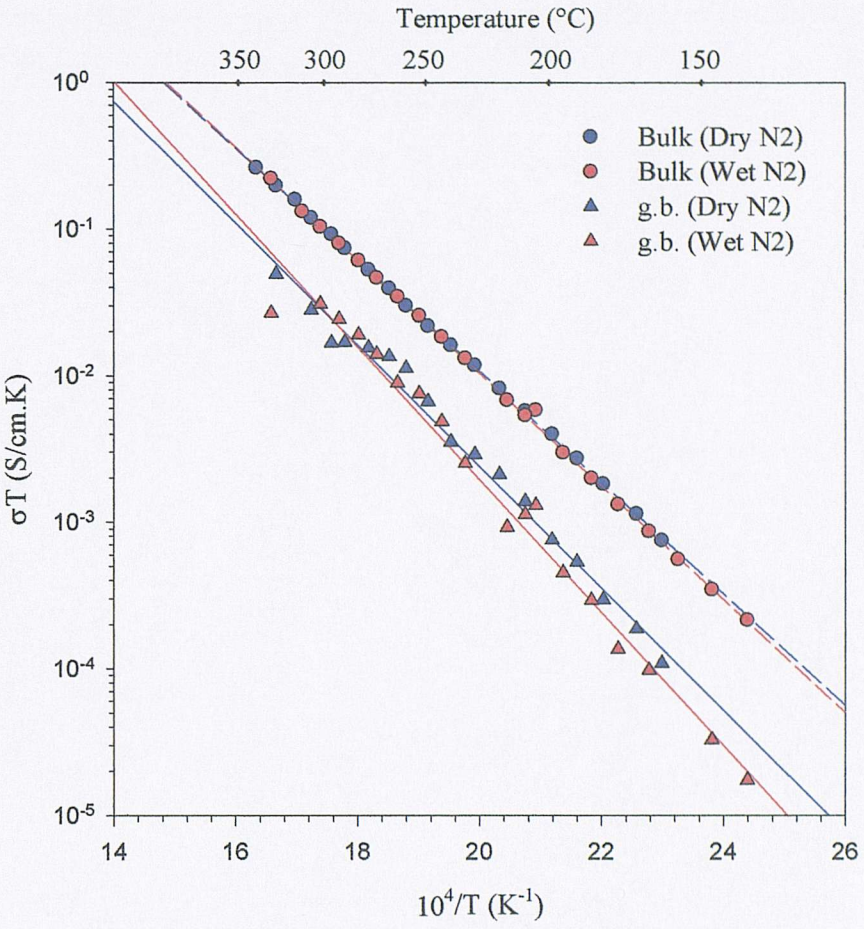


Figure 9.4. Arrhenius graph of the bulk and grain boundary conductivity of $Ce_{0.9}Gd_{0.1}O_{1.95}$ in a wet and dry atmosphere.

The activation energy for the bulk conductivity in dry N_2 is 73kJ/mol, the grain boundary is 80kJ/mol and the total conductivity is 74kJ/mol, over the temperature range examined. This is lower than the value obtained for the 30% doped single crystal sample. This could be due to the presence of higher order defect associates created by the higher level of doping in the single crystal producing a larger association enthalpy or even the formation of stoichiometric second phases leading to an increase in the migration enthalpy. Due to the narrow temperature range it was not possible to derive migration and association enthalpies.

Figure 9.5. shows the conductivity of $Ce_{0.9}Gd_{0.1}O_{1.95}$ in air. This data set spans a greater temperature range and so a migration enthalpy and association enthalpy could be estimated using the quadratic equation for the concentration of free

oxygen vacancies given by equation 3.54 and equation 4.19 describing the conductivity.

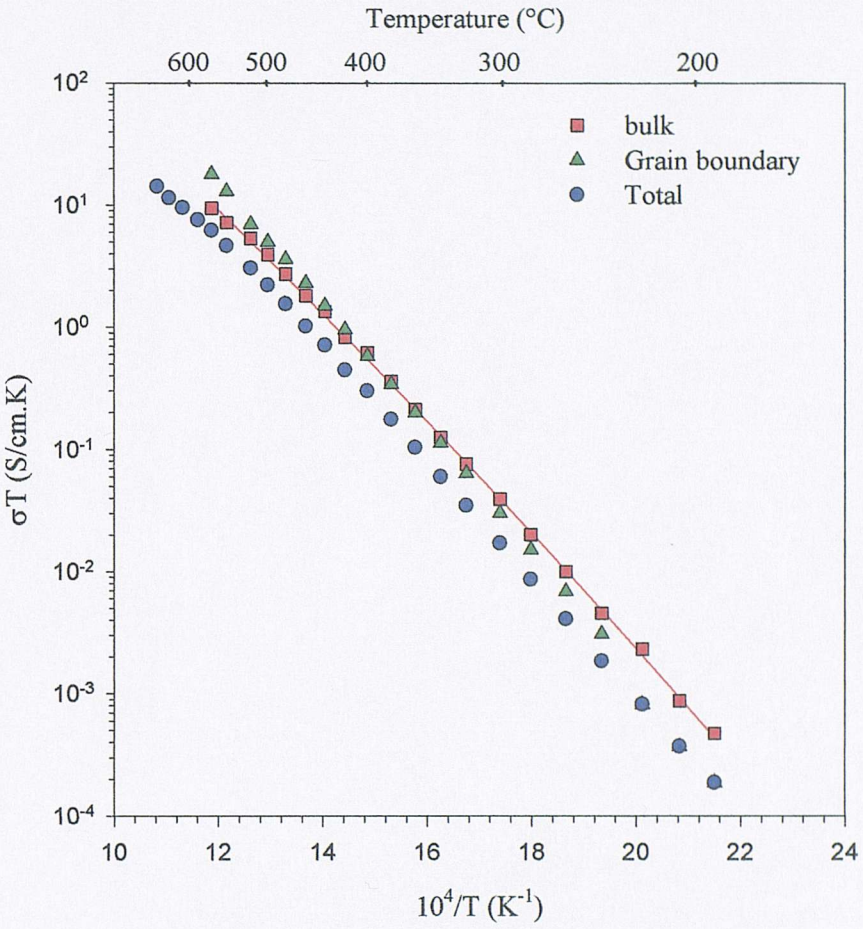


Figure 9.5. Conductivity of polycrystalline $Ce_{0.9}Gd_{0.1}O_{1.95}$ in air as a function of temperature.

Using equations 3.54 and 4.19, ΔH_m was calculated to be 61kJ/mol and ΔH_a was 25kJ/mol. Thus the total activation energy is given as 86kJ/mol. The activation energy for the grain boundary is 97kJ/mol, calculated from a linear regression of the data. The value of migration enthalpy is similar to 63kJ/mol predicted by atomistic computer simulations for indium doped ceria [16].

The total conductivity obtained in the wet and dry atmospheres is compared with the total conductivity obtained in air in figure 9.6. As can be seen, there is very little difference in the conductivity in any of these atmospheres. This suggests that the material is within the ionic domain and also the reduction caused in the sample by annealing in a vacuum is fully reversible.

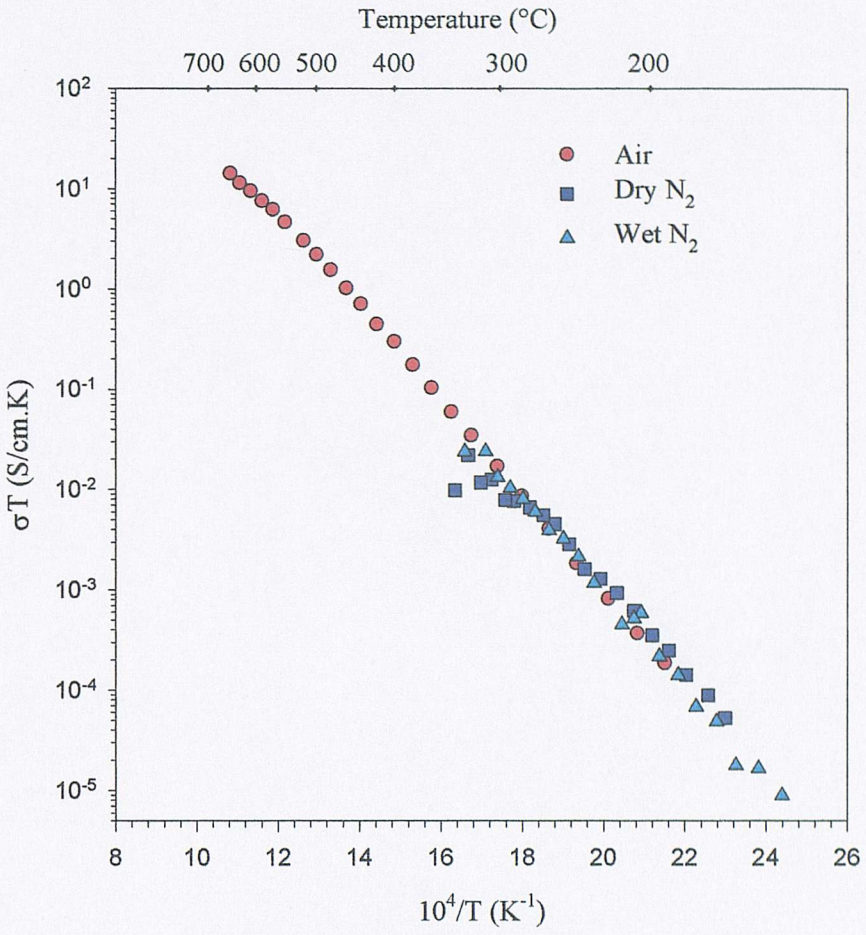


Figure 9.6. Comparison of the total conductivity of $Ce_{0.9}Gd_{0.1}O_{1.95}$ in a wet and dry nitrogen atmosphere and air.

9.4. $Zr_{0.85}Y_{0.15}O_{1.925}$ Polycrystal.

Polycrystalline samples of YSZ were examined using AC impedance spectroscopy in air, over a temperature range of 300-800°C. The resistance of the bulk and the grain boundaries were obtained from a NLLS fit of the semi-circles. However, at the higher temperatures the semi-circles became indistinct and so the high frequency intercept of the x-axis for the electrode response was used to calculate the total resistance of the grains plus the grain boundaries. The conductivities are plotted as a function of temperature in figure 9.7. Also shown in figure 9.7 is the data for single crystal YSZ obtained by Manning *et al* [15].

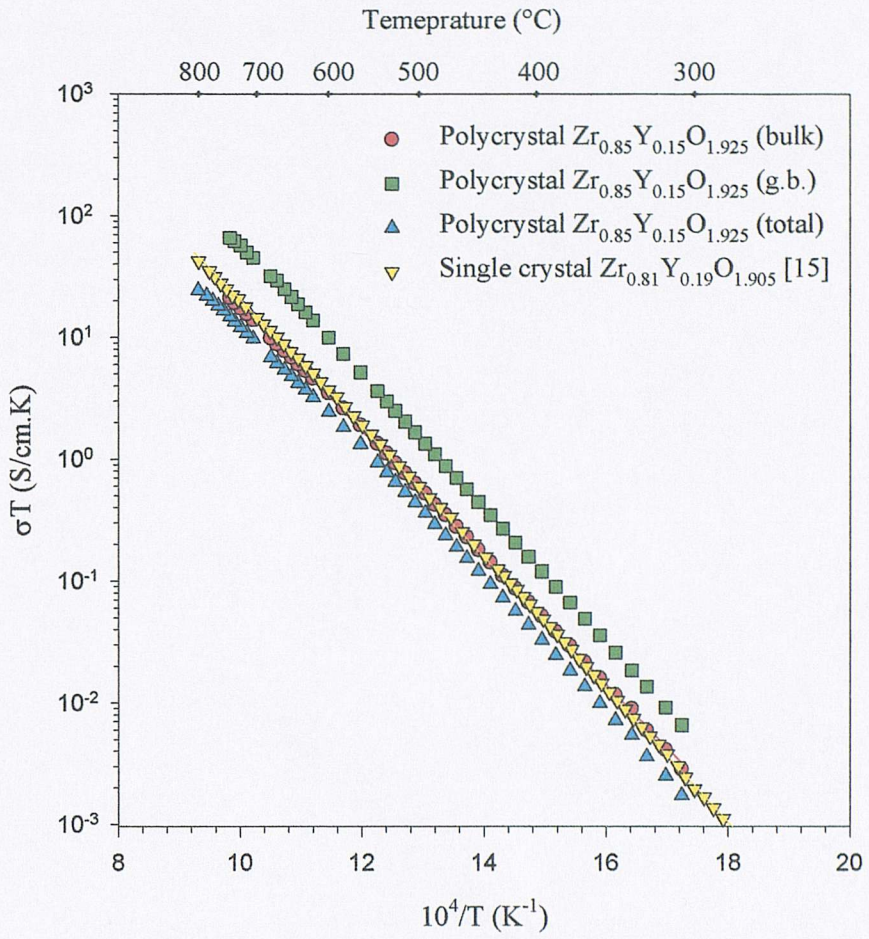


Figure 9.7. Conductivity of polycrystalline $Zr_{0.85}Y_{0.15}O_{1.925}$ and single crystal $Zr_{0.81}Y_{0.19}O_{1.905}$ as a function of temperature.

The polycrystalline sample has a very similar bulk conductivity to the single crystal material over the entire temperature range. However, the resistance of the grain boundaries makes the total conductivity of the polycrystalline material lower than the conductivity of the single crystal.

The migration enthalpy for the bulk of the polycrystalline sample was calculated to be 77kJ/mol and the association enthalpy 23kJ/mol using a regression analysis from equations 3.54 and 4.19. These values are similar to the values calculated by Manning *et al* [15] for the single crystal sample. They gave an association enthalpy of 25kJ/mol and a migration enthalpy of 81kJ/mol, calculated over a similar temperature range. The association enthalpy is also similar to that calculated for the polycrystalline sample of $Ce_{0.9}Gd_{0.1}O_{1.95}$. However, the migration enthalpy is higher for the zirconia based samples. The activation energy for the grain boundaries was found to be 105kJ/mol.

9.5. $Zr_{0.81}Y_{0.19}O_{1.905}$ Single Crystal.

A single crystal of $Zr_{0.81}Y_{0.19}O_{1.905}$ has been examined using AC impedance spectroscopy in wet and dry atmospheres of flowing nitrogen. The procedure used was the same as that described in section 9.3 for the ceria sample, except the sample did not need to be re-oxidised after annealing in the low water pressure vacuum and the sample was left at 900°C overnight in a wet atmosphere of flowing nitrogen. The measurements were made using both increasing and decreasing temperature cycles. Figure 9.8 shows the conductivity of the single crystal of YSZ as a function of temperature in the wet and dry atmospheres.

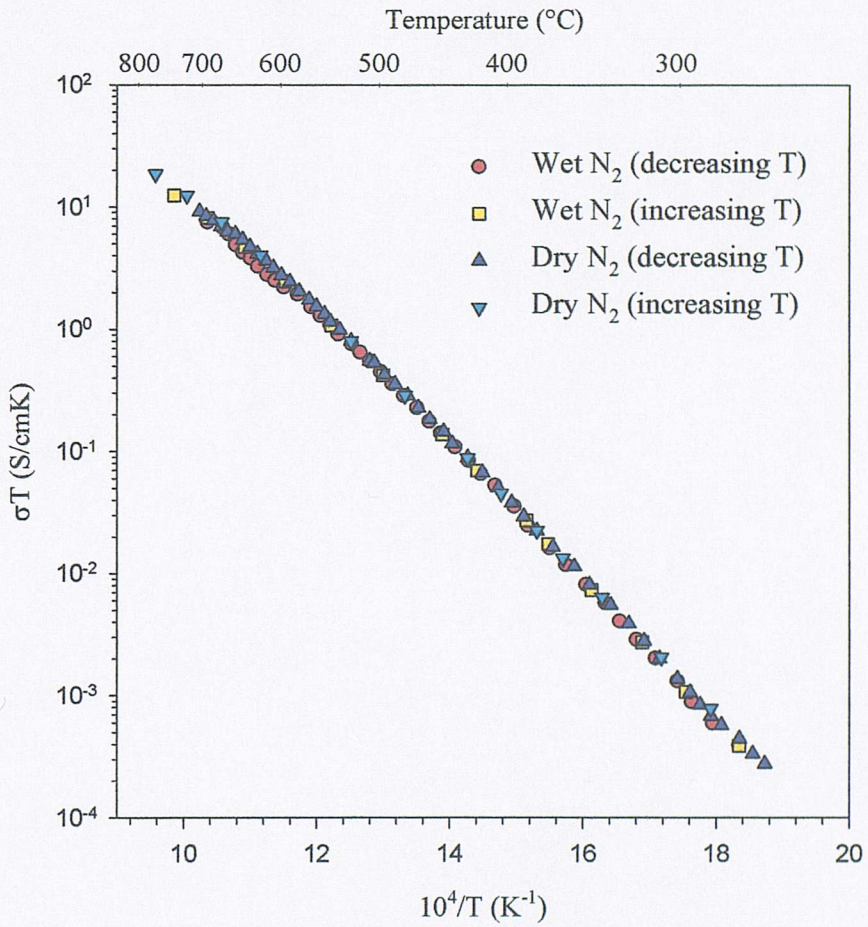


Figure 9.8 Conductivity of single crystal of YSZ as a function of temperature in the wet and dry atmospheres.

It is clear from figure 9.8 that there is no discernible difference in the conductivity of YSZ in wet or dry atmospheres. It is also evident that the results are repeatable using an increasing or decreasing temperature range (i.e. no

hysterisis is evident). This indicates either or both of the following: (i) the kinetics of proton incorporation are slow at 900°C; (ii) the thermodynamics of the process only permit a small solubility of protons. This result is in agreement with Wagner [11] who stated that the solubility of protons in YSZ is very small, and thus will not affect the conductivity. The results also agrees well with the data on the polycrystalline ceria sample where no protonic conductivity was evident.

The ionic conductivity of the YSZ single crystal in the wet and dry atmospheres is compared to the polycrystalline YSZ and single crystal data of Manning *et al* [15] in figure 9.9.

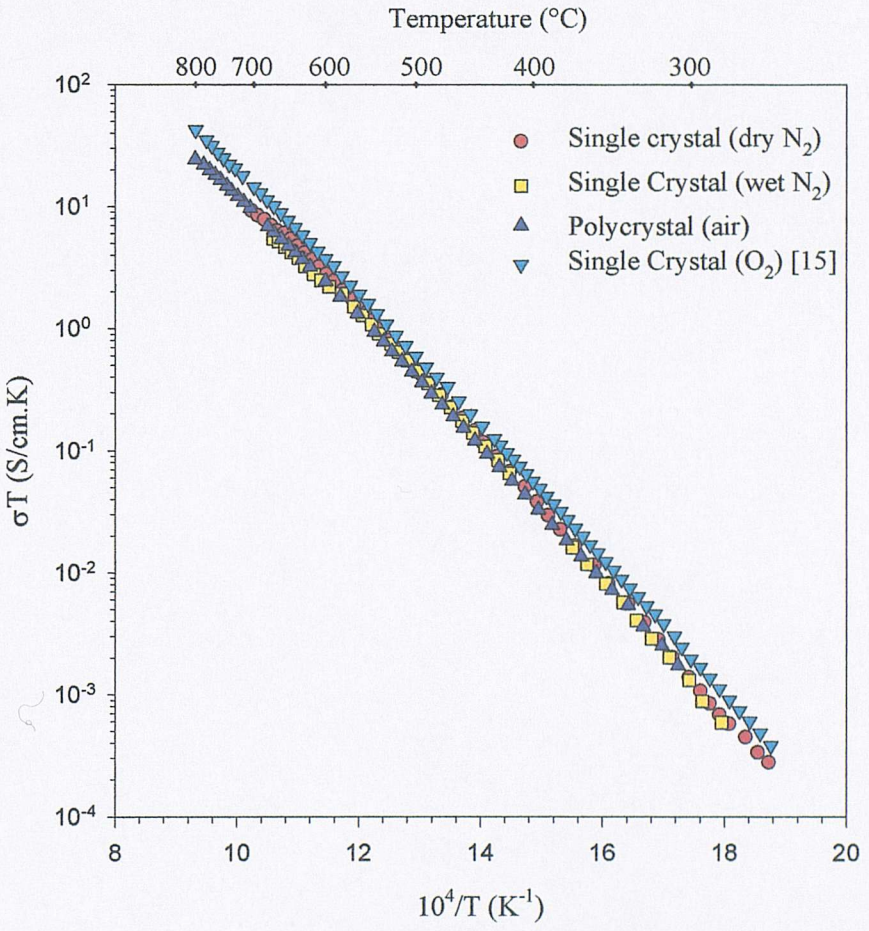


Figure 9.9. Comparison of polycrystalline and single crystal YSZ in different atmospheres.

It is clear that all the conductivity data for this level of doping in the YSZ system is very similar, irrespective of the atmospheres used or whether the sample is a polycrystal or single crystal. The possibility of systematic errors in the

instrumental set-up make it difficult to identify a unique reason for the small differences in conductivity.

9.6. Comparison of the Conductivity Data for the Fluorite Materials.

The conductivity data for the series of fluorite materials examined here is presented in figure 9.10. For the polycrystalline samples, the bulk conductivity is used.

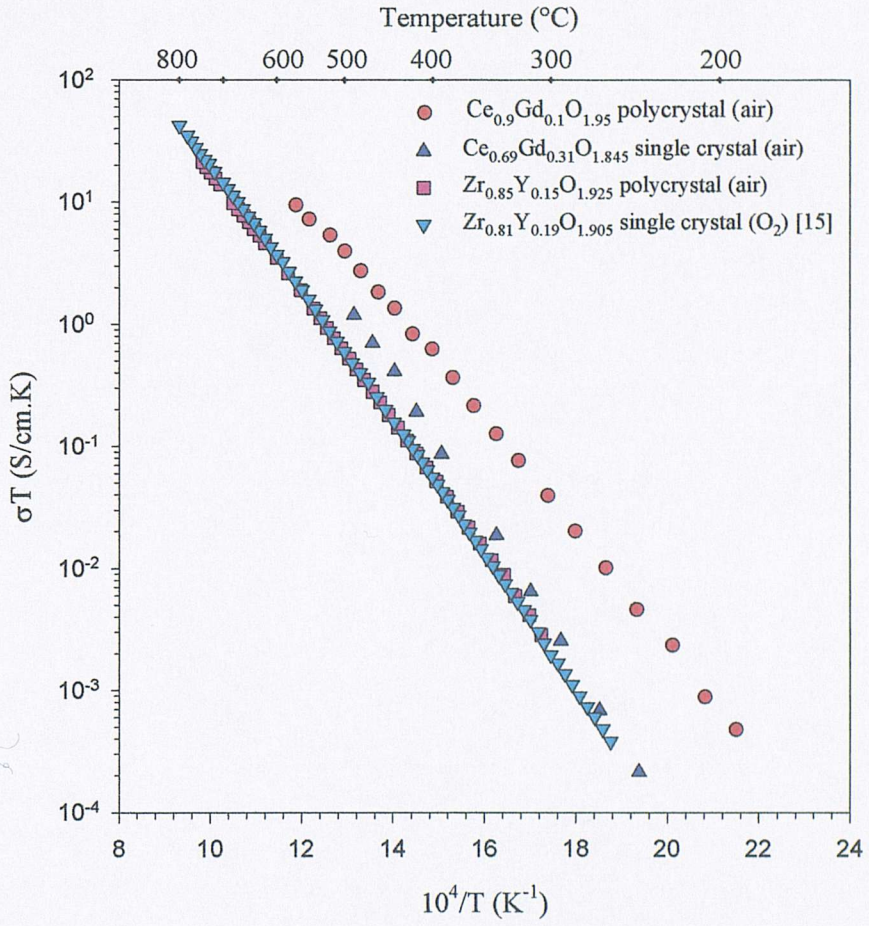


Figure 9.10. Comparison of the conductivity of YSZ and CGO materials obtained using AC impedance spectroscopy.

At the lower temperatures the $Ce_{0.9}Gd_{0.1}O_{1.95}$ sample has the highest conductivity. However, at higher temperatures (around 600°C) the single crystal of $Ce_{0.69}Gd_{0.31}O_{1.845}$ has a higher conductivity. At higher temperatures still (800-

900°C, by extrapolation), the YSZ samples have a high conductivity. This is due to the difference in activation energies for the materials.

The migration enthalpy, the association enthalpy and the overall activation energy for the conduction process for these materials are shown in table 9.1.

	Atmosphere	ΔH_m (kJ/mol)	ΔH_a (kJ/mol)	E_a (kJ/mol)
$Ce_{0.9}Gd_{0.1}O_{1.95}$	Air	61	25	86
$Ce_{0.69}Gd_{0.31}O_{1.845}$	Air	77	37	106
$Zr_{0.81}Y_{0.19}O_{1.905}$	O_2	81	25	107
$Zr_{0.85}Y_{0.15}O_{1.925}$	Air	77	23	99

Table 9.1 Activation energy for the conductivity of selected fluorites.

In all cases the association enthalpy contributes significantly to the activation energy for conduction at the lower temperatures. The association enthalpy of all the materials are similar with the exception of the single crystal of CGO. This material is very highly doped and the fact that the association enthalpy increases for this dopant concentration suggests that the binary associate model is not an accurate description of highly doped materials. The larger migration enthalpy also suggests that microdomains of ordered phases may exist in at this level of dopant concentration. Vacancy ordering has been seen in both YSZ [18] and ceria based fluorites [19,20].

The association enthalpy calculated for zirconia is similar to that found by Filal [21] for YSZ using AC impedance spectroscopy. The association enthalpy for $Ce_{0.9}Gd_{0.1}O_{1.95}$ (25kJ/mol) is somewhat higher than the value of 12kJ/mol found by Gerhardt-Anderson [22] for $Ce_{0.98}Gd_{0.02}O_{1.99}$. Butler *et al* [23] made calculations of the binding enthalpy of $\left\{Gd'_{Ce}V_O^{\bullet\bullet}\right\}^{\bullet}$ associates and found them to be 17kJ/mol. Interestingly, they also calculate the binding enthalpy for an oxygen vacancy associated with two gadolinium dopant cations and find it to be 25kJ/mol. This may suggest that for the $Ce_{0.9}Gd_{0.1}O_{1.95}$ composition, the simple binary associate model no longer holds. Recently, Grimes [24] recalculated the binding enthalpies for $Ce_{0.98}Gd_{0.02}O_{1.99}$ and found them to be 21kJ/mol for a simple binary associate, correcting for dopant concentration.

The migration enthalpy of the materials also matches previous experimental and calculated data. Filal found the migration enthalpy of YSZ to be 86kJ/mol [21]

while Ralph and Kilner obtained an activation energy of 73kJ/mol for $Ce_{0.9}Gd_{0.1}O_{1.95}$ [8], although they made no attempt to calculate a migration and association enthalpy. Ralph and Kilner also obtained a higher activation energy by increasing the dopant level in CGO.

At the higher temperatures, the activation energy approaches the calculated migration enthalpy [16] and so the association enthalpy plays a lesser role. Thus, at low temperatures there is near full association and at high temperatures (>1000K) the material is close to full dissociation.

9.7. References.

[1] P. Aberlard and J.F. Baumard, Phys. Rev. B, **Vol 26** (1982) p1005.

[2] A.E. Hughes and S.P.S. Badwal, Solid State Ionics **Vol 46** (1991) p265.

[3] M.J. Verkerk, A.J.A. Winnubst and A.J. Burggraaf, J. Mater. Sci. **Vol 17** (1982) p3113.

[4] A. Orliukas, P. Bohac, K. Sasaki and L.J. Gaukler, in Proc. of the 14th Risø International Symposium on Materials Science, edited by F.W. Poulsen, J.J. Bentzen, T. Jacobsen, E. Skou and M.J.L. Østergård, Risø National Laboratory, Roskilde, Denmark, (1993) p369.

[5] A. Orliukas, P. Bohac, K. Sasaki, M. Gödickemeier and L.J. Gaukler, in Proc. of the 14th Risø International Symposium on Materials Science, edited by F.W. Poulsen, J.J. Bentzen, T. Jacobsen, E. Skou and M.J.L. Østergård, Risø National Laboratory, Roskilde, Denmark, (1993), p363.

[6] W. Bakker, C. Milliken, J. Hartvigsen, S. Elangovan and A. Khandkar, in Proc. of the 5th International Symposium on SOFC, Eds. U. Stimming, S. Singhal, H. Tagawa and W. Lehnert, The Electrochemical Society, Inc., **PV 97-40**, Aachen, (1997) p254.

[7] J. M. Ralph and J. A. Kilner, in Proc. of the 2nd European SOFC Forum, Ed B. Thorstensen, Oslo, (1996) p773.

[8] J.M. Ralph and J.A. Kilner, in Proceedings of the 5th International Symposium on SOFC, Eds. U. Stimming, S. Singhal, H. Tagawa and W. Lehnert Electrochemical Society **PV 97-40**, Aachen, (1997) p1021.

[9] J.M. Ralph, Ph.D. Thesis, University of London (1998).

[10] J.A. Kilner and C.D. Waters, Solid State Ionics, **Vol 6**, (1982) p253.

[11] C. Wagner, Ber. Bunsenges. Physik. Chem. **Vol 72** (1968) p778.

[12] R.J. Aaberg, R. Tunold, S. Tjelle, and R. Ødegård, in Proc. of the 17th Risø International Symposium on Materials Science, Eds. F.W. Poulsen, N. Bonanos, S. Linderoth, M. Mogensen and B. Zachau-Christiansen, Denmark (1996) 511-516.

[13] M. Sahibzada, R.A. Rudkin, B.C.H. Steele, I.S. Metcalfe and J.A. Kilner, in Proceedings of the 5th International Symposium on SOFC, Eds. U. Stimming, S. Singhal, H. Tagawa and W. Lehnert Electrochemical Society **PV 97-40**, Aachen, (1997) p244.

[14] N. Kiratzis, B.C.H. Steele, J.M. Ralph, M. Sahibzada, A. Atkinson and J.A. Kilner, in Proc. of the 3rd Int. Symp. On Ionic and Mixed Conducting Ceramics, Eds. T.A. Ramanarayanan, W.L. Worrel, H.L. Tuller, M. Mogensen and A.C. Khandkar, The Electrochemical Society, Inc., Pennington, NJ, **PV 97-24**, Paris (1997).

[15] P.S. Manning, J.D. Sirman, R.A. de Souza and J.A. Kilner, Solid State Ionics, **Vol 100**, (1997) p1.

[16] A.K.A. Pride, S. Vyas, R. Grimes, J.A. Gardner and R. Wang, Phys. Rev. B **Vol 52** (1995) p13214.

[17] S.P.S. Badwal, F.T. Ciacchi and J. Drennan, to be published in the Proc. of the XIth Conference on Solid State Ionics, Honolulu (1997).

[18] I.R. Gibson and J.T.S. Irvine, J. Mat. Chem., **Vol 5** (1996) p895.

[19] D.J.M. Bevan and J. Kordis, J. Inorg. Nucl. Chem., **Vol 26** (1964) p1509.

[20] L.M. Atlas, J. Phys. Chem. Solids, **Vol 29** (1968) p91.

[21] M. Filal, C. Petot, M. Mokcha, C. Chateau and J.L. Carpentier, Solid State Ionics, **Vol 80** (1995) p27.

[22] R. Gerhardt-Anderson, and A.S. Nowick, Solid State Ionics, **Vol 5** (1981) p547.

[23] V. Butler, C.R.A. Catlow, B.E.F. Fender and J.H. Harding, Solid State Ionics, **Vol 8** (1983) p109.

[24] R. Grimes, to be published.

10. Oxygen Diffusion in Doped Cerium and Zirconium Oxides.

10.1. Introduction.

In Chapter 9 the oxygen ion conductivity of various single crystal and polycrystalline fluorite materials measured by AC impedance spectroscopy was discussed. In this chapter values of the tracer diffusivity of the same group of materials obtained by SIMS analysis (described in Chapter 7) are presented. The oxygen surface exchange data from these results are discussed in Chapter 11. The tracer diffusion results are compared to values obtained from the literature, in particular the SIMS work of Manning *et al* [1] and Solmon [2] on single crystals of YSZ, and to the conductivity measurements from Chapter 9 using the Nernst-Einstein relationship.

A selection of promising solid oxide electrolytes for use in electrically driven COGs and SOFCs have been selected for this diffusion study. $Ce_{0.9}Gd_{0.1}O_{1.95}$ is currently being extensively studied as an alternative to YSZ as an electrolyte. It is therefore important to accurately determine the oxygen ion transport properties of this material and compare them to YSZ. This was done using AC impedance spectroscopy in Chapter 9, which showed that that the bulk conductivity of CGO was significantly lower than YSZ, but the grain boundary contribution of CGO is large. By altering the composition of CGO, it is possible to improve its total conductivity [3]. In this chapter the oxygen tracer diffusivity of several compositions of CGO are studied and compared to polycrystalline and single crystal YSZ. The first data on single crystal CGO is also presented.

10.2. Oxygen Diffusion in Single Crystal $Ce_{0.69}Gd_{0.31}O_{1.845}$.

The work on the single crystal of CGO was carried out in conjunction with Mr. E. Ruiz-Trejo. The single crystal specimen obtained from Prof. Y. Baikov was sectioned into several plates, all with the same unspecified orientation. The samples were polished to a ¼μm finish before the ^{18}O isotope annealing process. All measurements were made using the line-scanning method. Table 10.1 shows the anneal temperatures and times in the diffusion experiments on the single

crystals. A typical set of raw line-scan data for the single crystal taken at 858°C is shown in figure 10.1.

$Ce_{0.69}Gd_{0.31}O_{1.845}$ Single crystal	
Temperature (°C)	Time (seconds)
568	28475
639	27852
711	537
811	618
858	571
950	547

Table 10.1. Anneal temperatures and times in the diffusion experiments on $Ce_{0.69}Gd_{0.31}O_{1.845}$.

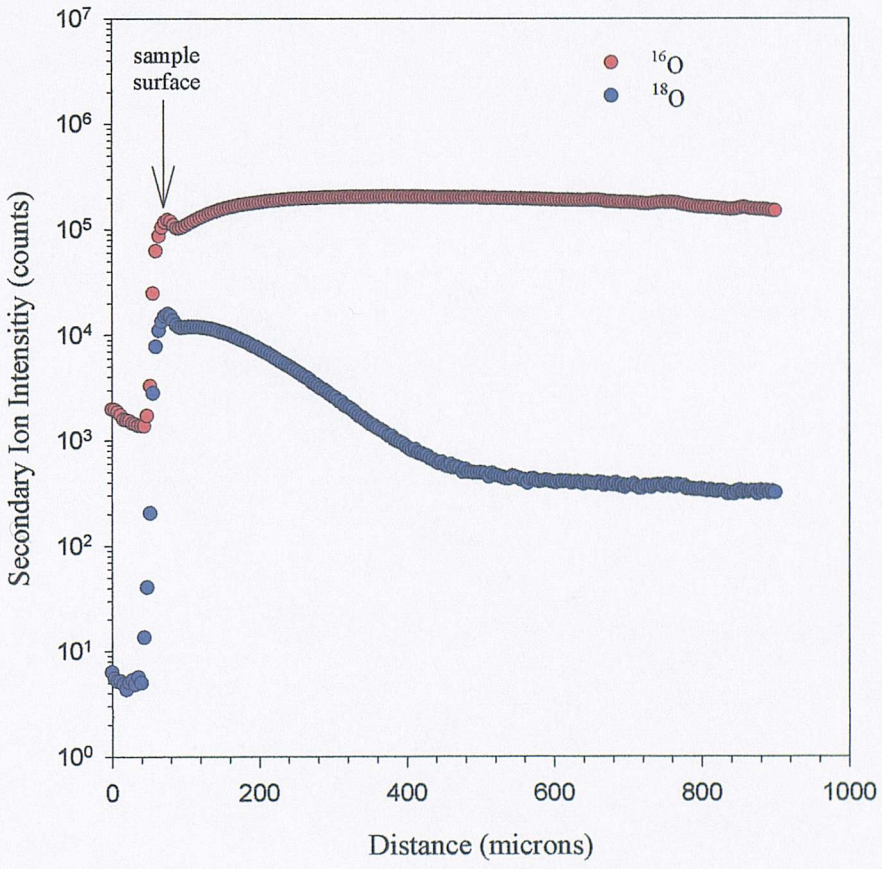


Figure 10.1. Raw line-scan data for oxygen diffusion in a $Ce_{0.69}Gd_{0.31}O_{1.845}$ single crystal annealed at 858°C for 571 seconds.

The primary ion beam was scanned across the exchanged surface and through the sample. Due to the finite width of the primary ion beam, a step function increase in the signal at the surface of the sample is not seen. Therefore, the surface of the sample is taken as the point where the secondary ion intensity for both the signals reaches its maximum. This introduces a small uncertainty into the depth measurement and also to the surface concentration of the sample. The point taken as the sample surface is shown in figure 10.1.

The ^{18}O isotopic fraction (normalised to the background concentration and the concentration of tracer isotope in the exchange gas) can then be calculated. Two typical, high temperature ^{18}O diffusion profiles are shown in figure 10.2. In both cases the surface concentration is high, making the SIMS analysis relatively straightforward.

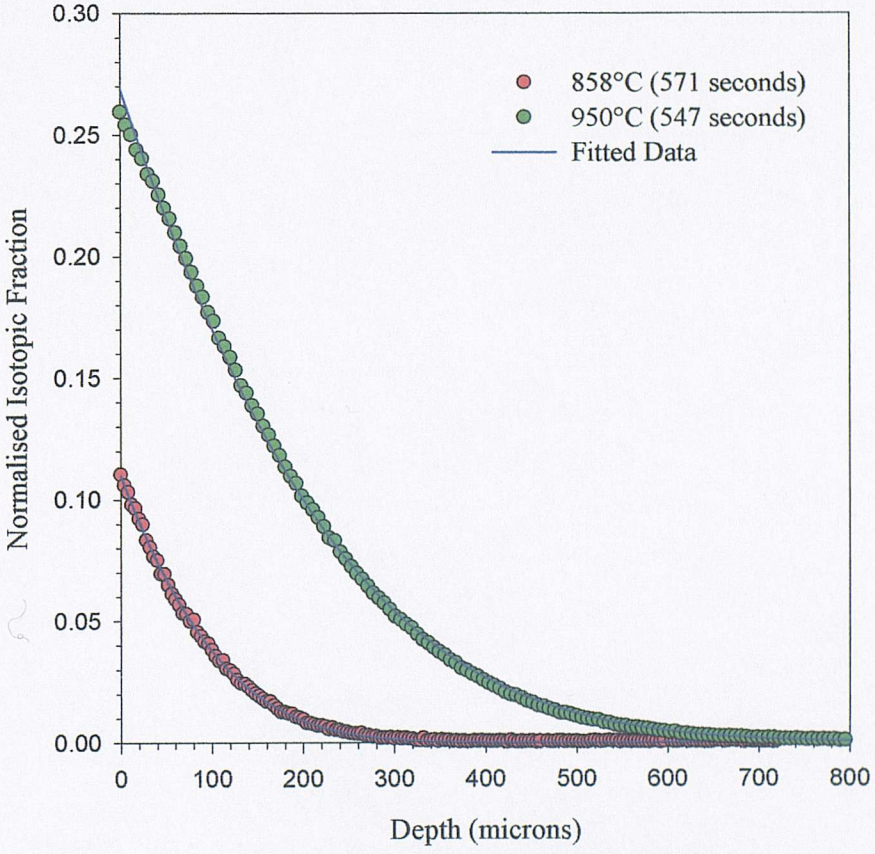


Figure 10.2 Typical high temperature ^{18}O diffusion profiles obtained for single crystal $Ce_{0.69}Gd_{0.31}O_{1.845}$.

The blue fitted data line in figure 10.2 is the result of a regression analysis based on the solution to Fick's 2nd law, described by equation 6.20. The profile at 858°C is described very accurately by equation 6.20. The profile at 950°C shows

a small deviation from the regression at the sample surface. This could be due to the uncertainty created by the interpretation of the position of sample surface. Alternatively, because of the high concentration of ^{18}O and the long diffusion profile, there could be a small depletion in the concentration of the gas during the anneal which would reduce the sample surface concentration slightly.

At the low anneal temperatures the concentration of ^{18}O was very much lower. This made the SIMS analysis significantly more difficult. In order to improve the statistics many line-scans (between 50 and 100) were done on each sample. The secondary ion intensities were then averaged and the isotopic fraction subsequently calculated. A typical low temperature ^{18}O diffusion profile for the $Ce_{0.69}Gd_{0.31}O_{1.845}$ single crystal is shown in figure 10.3. The profile still follows the solution to Fick's 2nd law (shown as the solid line), however it is clear that despite the care taken to improve the statistics the data exhibits more scatter and the fit is not as good.

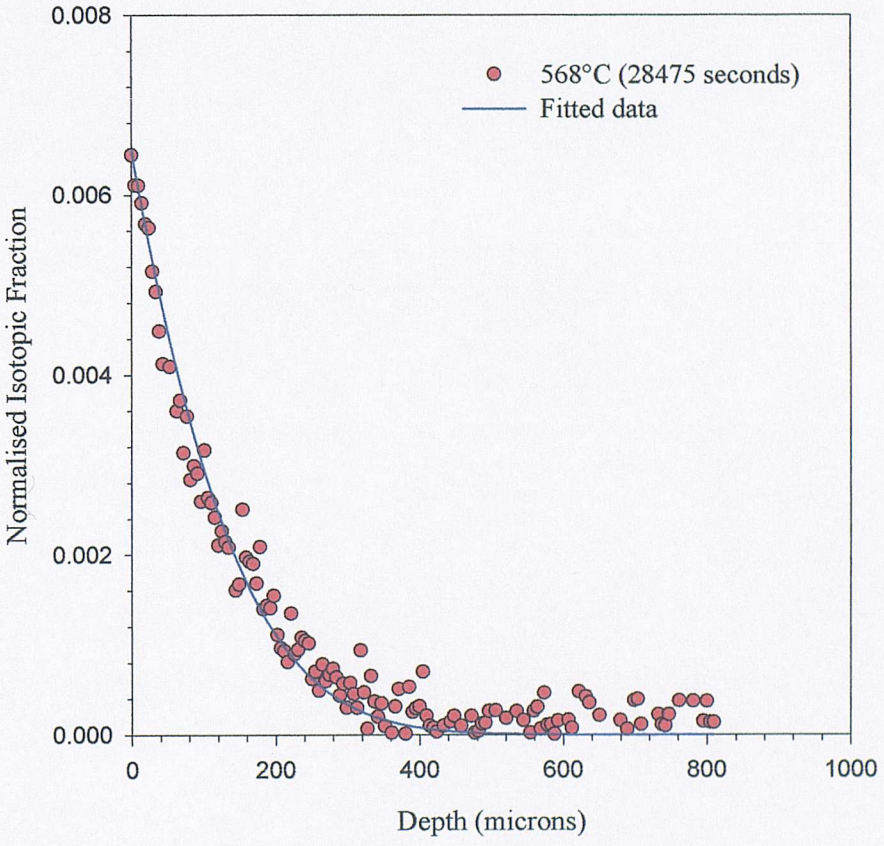


Figure 10.3 Typical low temperature (568°C) ^{18}O diffusion profile obtained for single crystal $Ce_{0.69}Gd_{0.31}O_{1.845}$.

The tracer diffusion coefficients obtained throughout the temperature range are given in table 10.2, together with the values for the surface exchange coefficient (obtained from the regression analysis). Figure 10.4 shows the tracer diffusivity as a function of reciprocal temperature. The surface exchange coefficients will be discussed in Chapter 11.

The line in figure 10.4 is a linear regression of the data. The tracer diffusivity can be defined from the linear regression by equation 10.1

$$D_T = 0.035^{+0.050}_{-0.021} \exp\left(\frac{-112 \pm 7 kJ/mol}{RT}\right) \qquad \text{eqn. (10.1)}$$

The uncertainties quoted are the standard uncertainties calculated from the linear regression of the data. The error in the pre-exponential term is very large due to the extrapolation of data taken in a relatively narrow temperature range to $T = \infty$. The uncertainty in the activation energy is considerably smaller and reflects the small deviation from a straight line in the results. A full analysis of the errors in each measurement is not practical due to the problems involved in the summation of errors from different sources. In all the following Arrhenius type equations, both in this chapter and Chapters 11 and 12, the standard uncertainties from the linear regression will be quoted.

$Ce_{0.69}Gd_{0.31}O_{1.845}$ Single crystal		
Temperature (°C)	D_T (cm^2/s)	k (cm/s)
568	3.0×10^{-9}	2.0×10^{-9}
639	1.7×10^{-8}	6.1×10^{-9}
711	6.0×10^{-8}	3.9×10^{-8}
811	1.2×10^{-7}	9.9×10^{-7}
858	2.2×10^{-7}	2.4×10^{-6}
950	5.7×10^{-7}	1.0×10^{-5}

Table 10.2. Values of the tracer diffusion coefficient and the surface exchange coefficient for single crystal $Ce_{0.69}Gd_{0.31}O_{1.845}$.

This is the first set of tracer diffusion measurements on a single crystal of CGO and so direct comparison with data from the literature is not possible. Tracer diffusion measurements performed on single crystals of $Zr_{0.81}Y_{0.19}O_{1.905}$ by Manning *et al* [1] and by Solmon [2] yield values of the activation energy of

96kJ/mol and 119kJ/mol, respectively. The AC impedance data on the single crystal of CGO in oxygen gave an activation energy for ionic conduction of 107kJ/mol. This value is in excellent agreement with the activation energy for tracer diffusion. A more detailed comparison of the two sets of results is given later in this chapter.

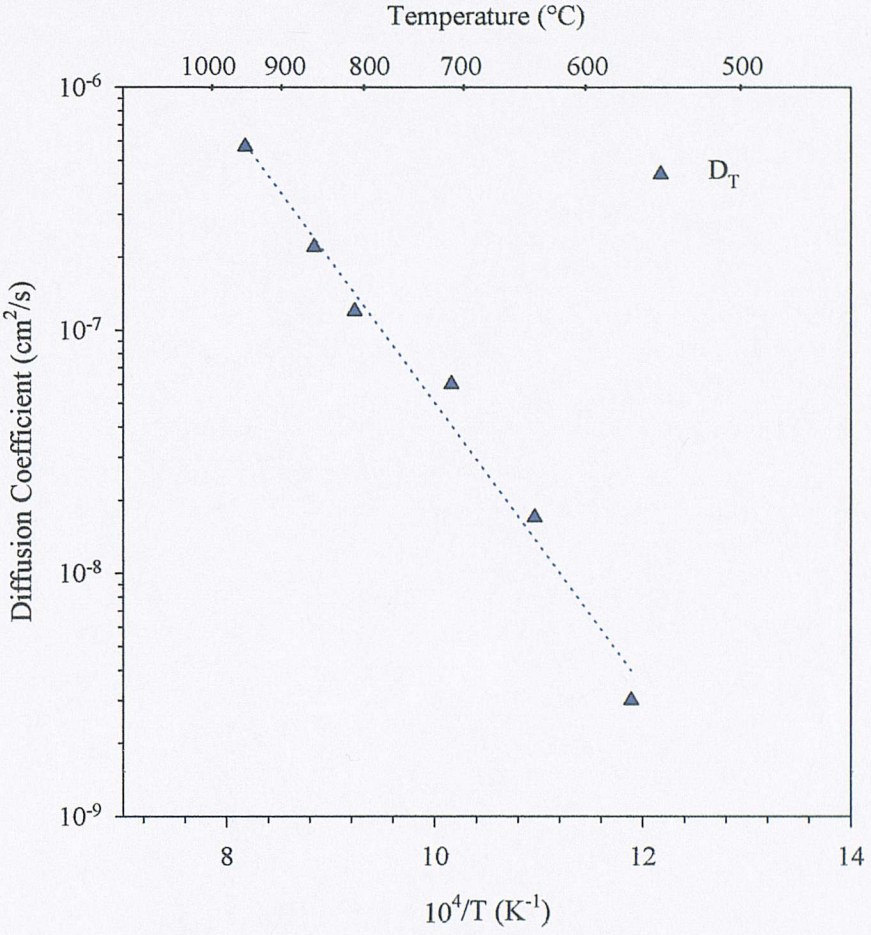


Figure 10.4. Tracer diffusivity of single crystal $Ce_{0.69}Gd_{0.31}O_{1.845}$ as a function of reciprocal temperature.

10.3. Oxygen Diffusion in Polycrystalline $Ce_{0.9}Gd_{0.1}O_{1.95}$.

Tracer diffusion measurements were made on polycrystals of $Ce_{0.9}Gd_{0.1}O_{1.95}$ polished to a ¼μm finish. The line-scanning method was used for all the temperatures, except the lowest temperature (486°C). The anneal temperatures and times used for the diffusion experiments on the $Ce_{0.9}Gd_{0.1}O_{1.95}$ samples are shown in table 10.3.

Two typical high temperature diffusion profiles are shown in figure 10.5. As with figures 10.2 and 10.3. the blue line is the result of a regression analysis based on equation 6.20.

$Ce_{0.9}Gd_{0.1}O_{1.95}$ Polycrystal	
Temperature (°C)	Time (seconds)
486	2730
560	38325
790	15157
889	10995
915	780
974	3565
1033	707

Table 10.3. Anneal temperatures and times in the diffusion experiments on $Ce_{0.9}Gd_{0.1}O_{1.95}$.

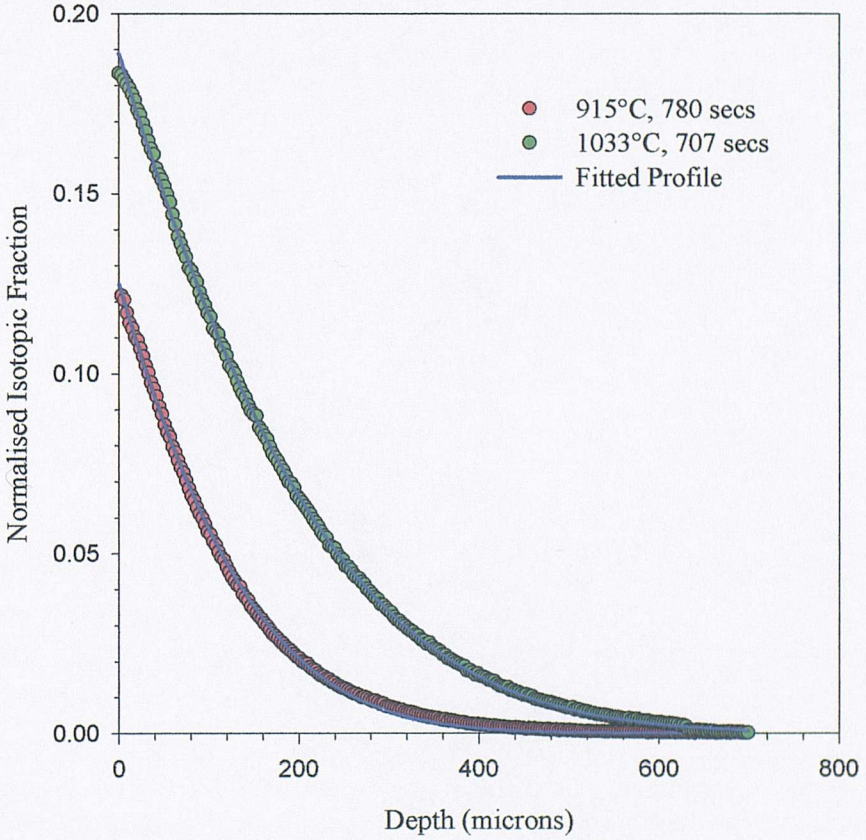


Figure 10.5. Typical high temperature ^{18}O diffusion profiles obtained for polycrystalline $Ce_{0.9}Gd_{0.1}O_{1.95}$.

The regression analysis accurately describes the diffusion profile and so diffusion and surface exchange coefficients can readily be obtained from the curves. These values are shown in table 10.4 an plotted in an Arrhenius form in figure 10.6. Again, the surface exchange data will be discussed in the following chapter. The dotted line in figure 10.4 is the result of a linear regression of the data and is defined by equation 10.2.

$$D_T = 0.0011^{+0.0027}_{-0.0008} \exp\left(\frac{-88 \pm 10 \text{kJ/mol}}{RT}\right) \qquad \text{eqn. (10.2)}$$

There is more scatter in this data set than for the single crystal and this is shown by the larger uncertainty in the activation energy calculated by the linear regression. The reason for the scatter in the data is likely due to small inhomogeneities in the sample as a result of the processing techniques employed in making the samples. Also, the diffusion profiles often traverse several grain boundaries in the polycrystalline material, and so the diffusion coefficients calculated also include a contribution from the grain boundaries.

$Ce_{0.9}Gd_{0.1}O_{1.95}$ Polycrystal		
Temperature (°C)	D_T (cm^2/s)	k (cm/s)
486	5.0×10^{-10}	3.0×10^{-10}
560	8.3×10^{-9}	5.8×10^{-10}
790	2.7×10^{-8}	2.7×10^{-9}
889	9.0×10^{-8}	3.4×10^{-8}
915	1.9×10^{-7}	1.8×10^{-6}
974	1.4×10^{-7}	8.3×10^{-7}
1033	5.2×10^{-7}	5.4×10^{-6}

Table 10.4. Values of the tracer diffusion coefficient and the surface exchange coefficient for polycrystalline $Ce_{0.9}Gd_{0.1}O_{1.95}$.

The value for the activation energy from the SIMS data is in very good agreement with the value of 89kJ/mol obtained for the total conductivity from AC impedance spectroscopy. The activation energy for the $Ce_{0.9}Gd_{0.1}O_{1.95}$ material is also lower than that for the $Ce_{0.69}Gd_{0.31}O_{1.845}$ single crystal, in agreement with data from AC impedance spectroscopy. Further comparisons will be made later in this chapter.

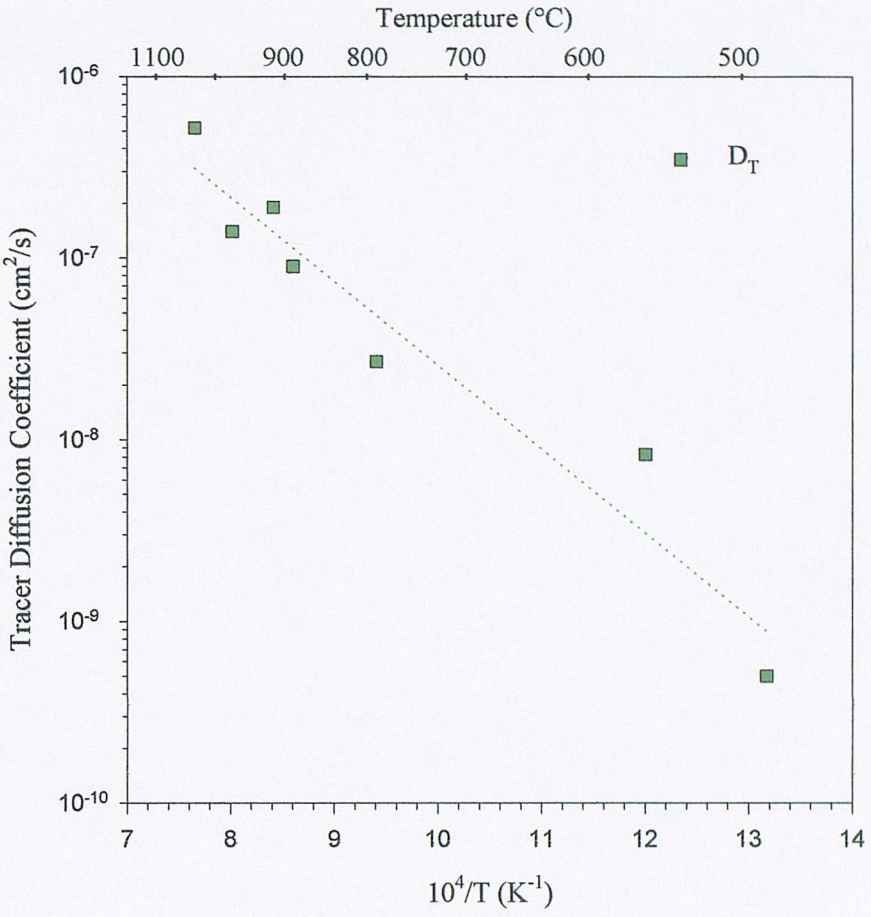


Figure 10.6. Tracer diffusivity of polycrystalline $Ce_{0.9}Gd_{0.1}O_{1.95}$ as a function of temperature.

10.4. Oxygen Diffusion in $Ce_{0.8}Gd_{0.2}O_{1.9}$ and $Ce_{0.8}Gd_{0.18}Pr_{0.02}O_{2-x}$ Polycrystals.

The tracer diffusion measurements made on polycrystals of $Ce_{0.8}Gd_{0.2}O_{1.9}$ and $Ce_{0.8}Gd_{0.18}Pr_{0.02}O_{2-x}$ were undertaken using the line-scanning method for all the temperatures examined. The anneal temperatures and times used for the diffusion experiments on the $Ce_{0.8}Gd_{0.2}O_{1.9}$ and $Ce_{0.8}Gd_{0.18}Pr_{0.02}O_{2-x}$ samples are shown in table 10.5.

$Ce_{0.8}Gd_{0.2}O_{1.9}$		$Ce_{0.8}Gd_{0.18}Pr_{0.02}O_{2-x}$	
Temperature (°C)	Time (seconds)	Temperature (°C)	Time (seconds)
508	33409	701	5901
605	39641	802	936
701	5901	899	824
941	941	941	767
		995	632

Table 10.5. Anneal temperatures and times used in the diffusion experiments on $Ce_{0.8}Gd_{0.2}O_{1.9}$ and $Ce_{0.8}Gd_{0.18}Pr_{0.02}O_{2-x}$.

Typical diffusion profiles obtained for the $Ce_{0.8}Gd_{0.18}Pr_{0.02}O_{2-x}$ sample are shown in figure 10.7. The diffusion profiles are in general accurately described by the linear regression analysis based on equation 6.20. However, the diffusion profile at 899°C does show some deviation from the theoretical profile. Due to the depth of the profile, it is unlikely to be affected by line-scan limitations caused by the width of the primary ion beam. It is possible that there may be gas phase depletion of the ^{18}O concentration although there is little evidence of this at the higher temperature (941°C) profile. The surface ^{18}O concentration and hence the surface exchange coefficient is higher than anticipated from the other results. It is possible that sectioning the sample to use the line-scanning method may have affected the surface of the sample and thus the apparent concentration of ^{18}O at the surface. The diffusion profile at 802°C also shows a deviation from the theoretical profile and furthermore there is more scatter in the measurement. The "humps" seen in the profile at ~240 microns and ~600 microns could be indicative of some porosity or another form of inhomogeneity in the sample. Diffusion measurements taken at lower temperatures did not produce an error function decay as expected from the solution to Fick's 2nd law. This could also be a result of porosity or inhomogeneities in the material. Figure 10.8 shows an optical micrograph of a $Ce_{0.8}Gd_{0.18}Pr_{0.02}O_{2-x}$ sample, with a thermal etch at 1400°C for 2 hours. It is evident from the micrograph that there is little porosity. However, the grain size is small (~0.5-2 microns) and appears to have a bi-modal distribution of grain sizes. This may account for some of the deviations seen in the diffusion profiles.

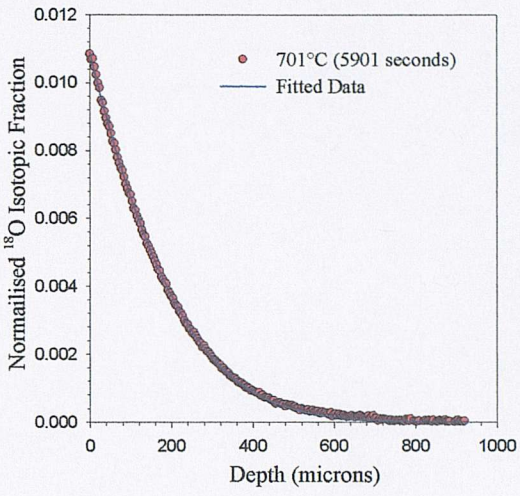


Figure 10.7. (a)

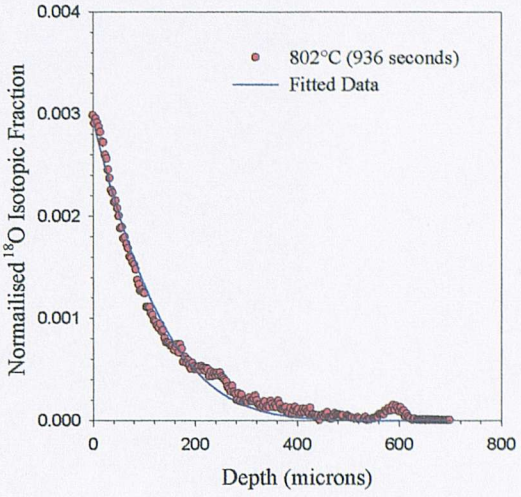


Figure 10.7. (b)

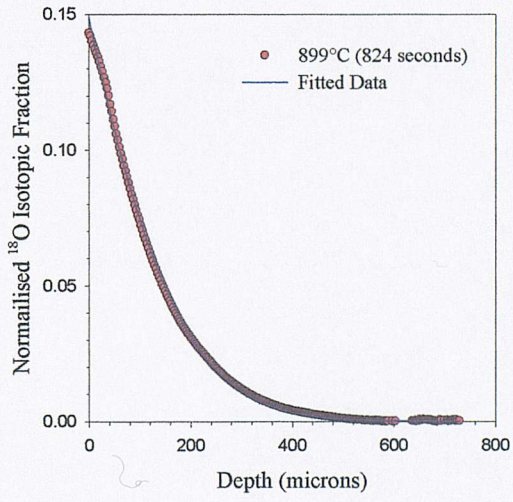


Figure 10.7. (c)

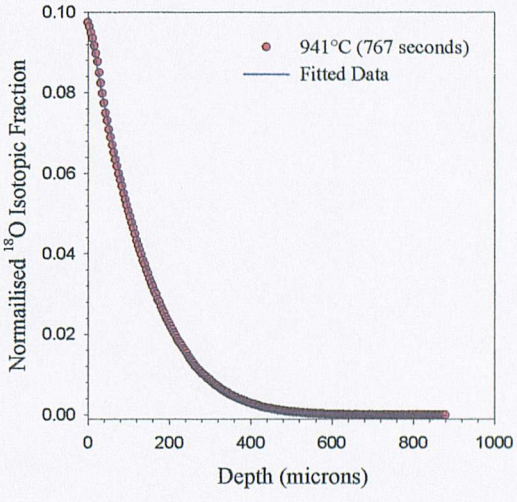


Figure 10.7. (d)

Figure 10.7. Typical diffusion profiles for polycrystalline $Ce_{0.8}Gd_{0.18}Pr_{0.02}O_{2-x}$.

The tracer diffusion and surface exchange coefficients obtained for the $Ce_{0.8}Gd_{0.18}Pr_{0.02}O_{2-x}$ sample are given in table 10.6.

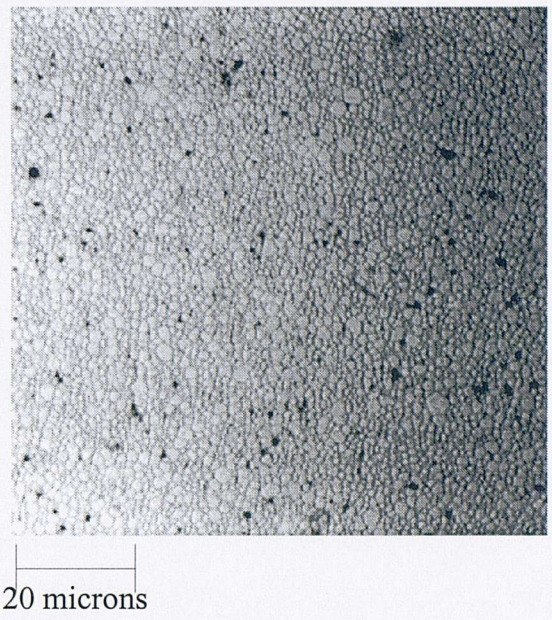


Figure 10.8. Optical micrograph of $Ce_{0.8}Gd_{0.18}Pr_{0.02}O_{2-x}$.

$Ce_{0.8}Gd_{0.18}Pr_{0.02}O_{2-x}$ Polycrystal		
Temperature (°C)	D_T (cm^2/s)	k (cm/s)
701	6.4×10^{-8}	3.2×10^{-8}
802	1.8×10^{-7}	3.7×10^{-8}
899	2.3×10^{-7}	2.5×10^{-6}
941	2.8×10^{-7}	1.8×10^{-6}
995	5.1×10^{-7}	9.5×10^{-6}

Table 10.6. Tracer diffusion and surface exchange coefficients obtained for polycrystalline $Ce_{0.8}Gd_{0.18}Pr_{0.02}O_{2-x}$.

Two diffusion profiles obtained for the polycrystalline $Ce_{0.8}Gd_{0.2}O_{1.9}$ sample are shown in figure 10.9, together with the diffusion profiles obtained for $Ce_{0.8}Gd_{0.18}Pr_{0.02}O_{2-x}$ at the same temperature. The $Ce_{0.8}Gd_{0.2}O_{1.9}$ and $Ce_{0.8}Gd_{0.18}Pr_{0.02}O_{2-x}$ diffusion profiles shown were exchange annealed at the same time, thus the anneal temperatures and times are the same for both materials. It is clear that the diffusion length is essentially unaffected by the presence of praseodymium at both temperatures, but the concentration of ^{18}O at the sample surface (and hence the surface exchange coefficient) is lower in the $Ce_{0.8}Gd_{0.2}O_{1.9}$ sample. Table 10.7 shows the tracer diffusion and surface exchange coefficients obtained for the $Ce_{0.8}Gd_{0.2}O_{1.9}$ sample.

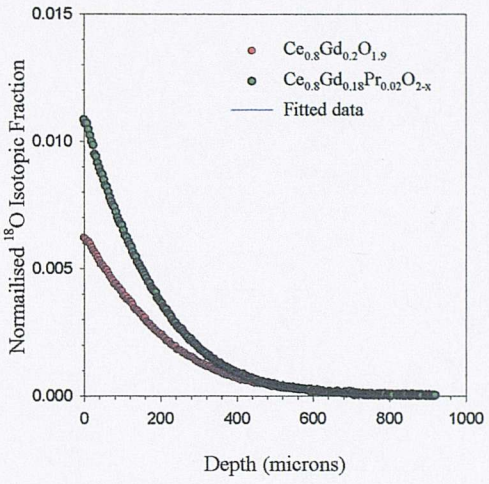


Figure 10.9. (a) 701°C, 5901secs

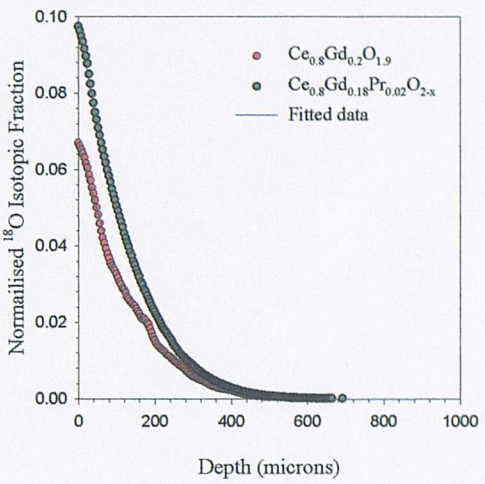


Figure 10.8. (b) 941°C, 767secs

Figure 10.9. Typical diffusion profiles $Ce_{0.8}Gd_{0.2}O_{1.9}$ compared with $Ce_{0.8}Gd_{0.18}Pr_{0.02}O_{2-x}$ at the same temperature and anneal times.

$Ce_{0.8}Gd_{0.2}O_{1.9}$Polycrystal		
Temperature (°C)	D_T (cm^2/s)	k (cm/s)
508	4.7×10^{-9}	3.2×10^{-10}
605	1.7×10^{-8}	1.4×10^{-9}
701	8.0×10^{-8}	2.5×10^{-6}
941	2.8×10^{-7}	1.8×10^{-6}

Table 10.7. Tracer diffusion and surface exchange coefficients obtained for polycrystalline $Ce_{0.8}Gd_{0.2}O_{1.9}$.

At 701°C the diffusion profile is very accurately described by the regression analysis based on equation 6.20. The profile at 941°C is also well described by the theoretical profile although there is some evidence of "humps" in the profile at around 200 microns. Again, this may be due to some porosity or another inhomogeneity in the material.

Figure 10.10 shows the diffusion data for the $Ce_{0.8}Gd_{0.18}Pr_{0.02}O_{2-x}$ and $Ce_{0.8}Gd_{0.2}O_{1.9}$ samples as a function of temperature. The dotted lines are the result of a linear regression analysis and are defined by equations 10.3 and 10.4 for the $Ce_{0.8}Gd_{0.18}Pr_{0.02}O_{2-x}$ and $Ce_{0.8}Gd_{0.2}O_{1.9}$ materials respectively.

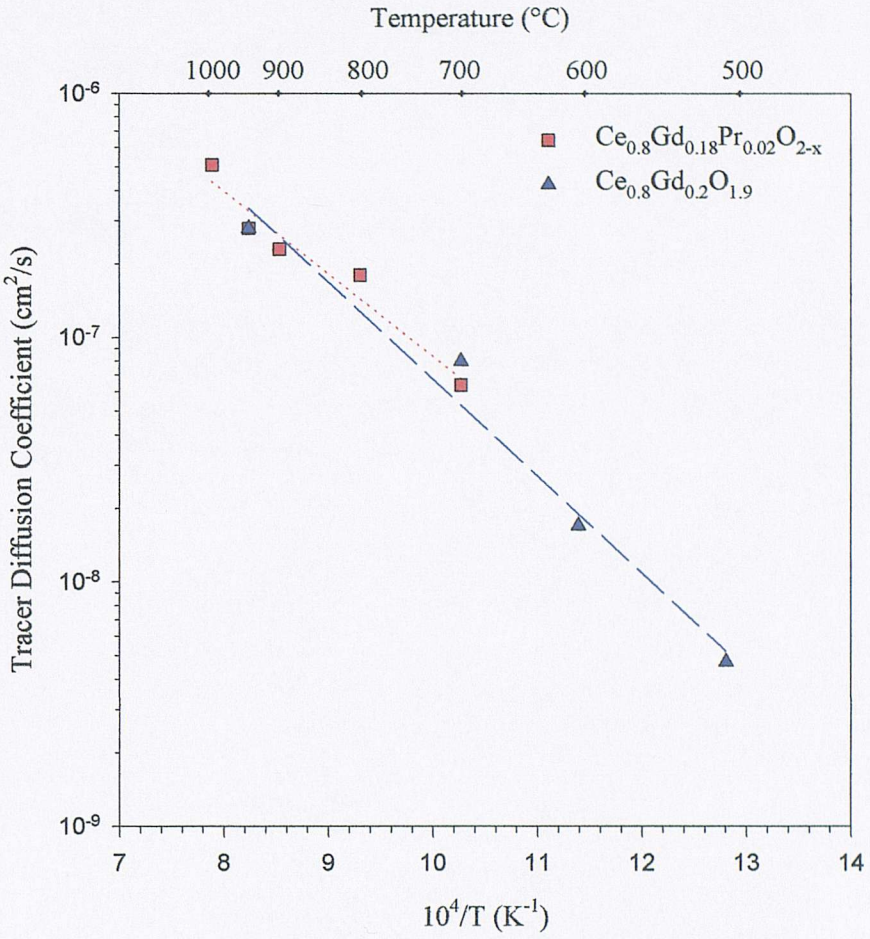


Figure 10.10. Tracer diffusion coefficient of $Ce_{0.8}Gd_{0.18}Pr_{0.02}O_{2-x}$ and $Ce_{0.8}Gd_{0.2}O_{1.9}$ as a function of temperature.

$$D_T = 0.0002^{+0.0003}_{-0.00001}\exp\left(\frac{-65\pm 9\text{kJ/mol}}{RT}\right) \qquad \text{eqn. (10.3)}$$

$$D_T = 0.0006^{+0.0013}_{-0.0004}\exp\left(\frac{-76\pm 8\text{kJ/mol}}{RT}\right) \qquad \text{eqn. (10.4)}$$

The activation energy for the praseodymium doped sample is the same, within the uncertainty limits given, as $Ce_{0.8}Gd_{0.2}O_{1.9}$. The magnitude of the tracer diffusivity is also essentially unaffected by the presence of praseodymium. Ralph measured the conductivity of $Ce_{0.8}Gd_{0.18}Pr_{0.02}O_{2-x}$ and $Ce_{0.8}Gd_{0.2}O_{1.9}$ using AC impedance spectroscopy and found the conductivity of the praseodymium doped sample slightly greater than $Ce_{0.8}Gd_{0.2}O_{1.9}$ [4]. This may suggest that there is a

small contribution to the conductivity from electronic carriers. However, the measurements of Ralph were carried out at lower temperatures, 200-500°C and so direct comparisons are difficult.

10.5. Oxygen Diffusion in Polycrystalline $Zr_{0.85}Y_{0.15}O_{1.925}$.

The work on polycrystalline $Zr_{0.85}Y_{0.15}O_{1.925}$ was completed in conjunction with Mr. P.S. Manning, Department of Materials, Imperial College. Line-scan measurements were used for all the temperatures examined. The anneal temperatures and times employed are given in table 10.8.

$Zr_{0.85}Y_{0.15}O_{1.925}$ Polycrystal	
Temperature (°C)	Time (seconds)
508	33409
605	39641
651	11099
698	3825
701	5901
805	990
898	626
941	767
1000	687
1097	545

Table 10.8. Anneal temperatures and times used in the diffusion experiments on $Zr_{0.85}Y_{0.15}O_{1.925}$.

Two typical diffusion profiles are shown in figure 10.11. The ^{18}O isotopic concentration at the surface of the sample annealed at 701°C is again small. Both the profiles are described well by the regression analysis based on equation 6.20. Table 10.9 shows the tracer diffusion and surface exchange coefficients obtained and figure 10.12 shows the tracer diffusivity as a function of temperature for the $Zr_{0.85}Y_{0.15}O_{1.925}$ polycrystalline material, together with the data of Manning *et al* [1] for single crystal zirconia with the composition $Zr_{0.81}Y_{0.19}O_{1.905}$.

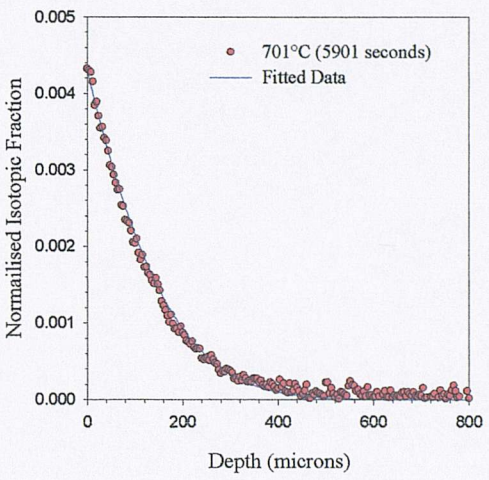


Figure 10.11. (a)

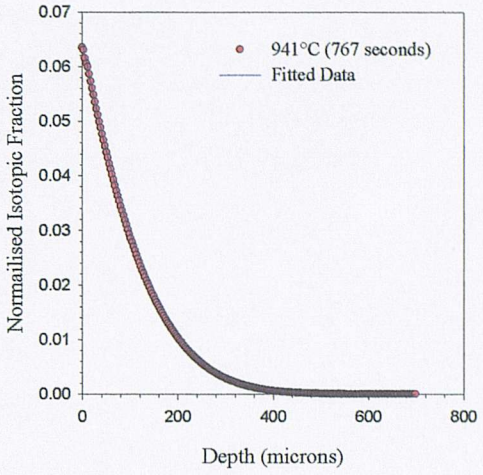


Figure 10.11. (b)

Figure 10.11. Typical ^{18}O diffusion profiles obtained for polycrystalline $Zr_{0.85}Y_{0.15}O_{1.925}$.

$Zr_{0.85}Y_{0.15}O_{1.925}$ Polycrystal		
Temperature (°C)	D_T (cm^2/s)	k (cm/s)
508	1.2×10^{-9}	1.0×10^{-9}
605	5.9×10^{-9}	1.2×10^{-9}
651	9.2×10^{-9}	3.2×10^{-9}
698	4.4×10^{-8}	7.8×10^{-9}
701	3.5×10^{-8}	9.4×10^{-9}
805	1.2×10^{-7}	7.5×10^{-8}
898	1.9×10^{-7}	1.1×10^{-6}
941	2.1×10^{-7}	1.0×10^{-6}
1000	2.7×10^{-7}	4.4×10^{-6}
1097	4.7×10^{-7}	4.1×10^{-6}

Table 10.9. Tracer diffusion and surface exchange coefficients obtained for polycrystalline $Zr_{0.85}Y_{0.15}O_{1.925}$.

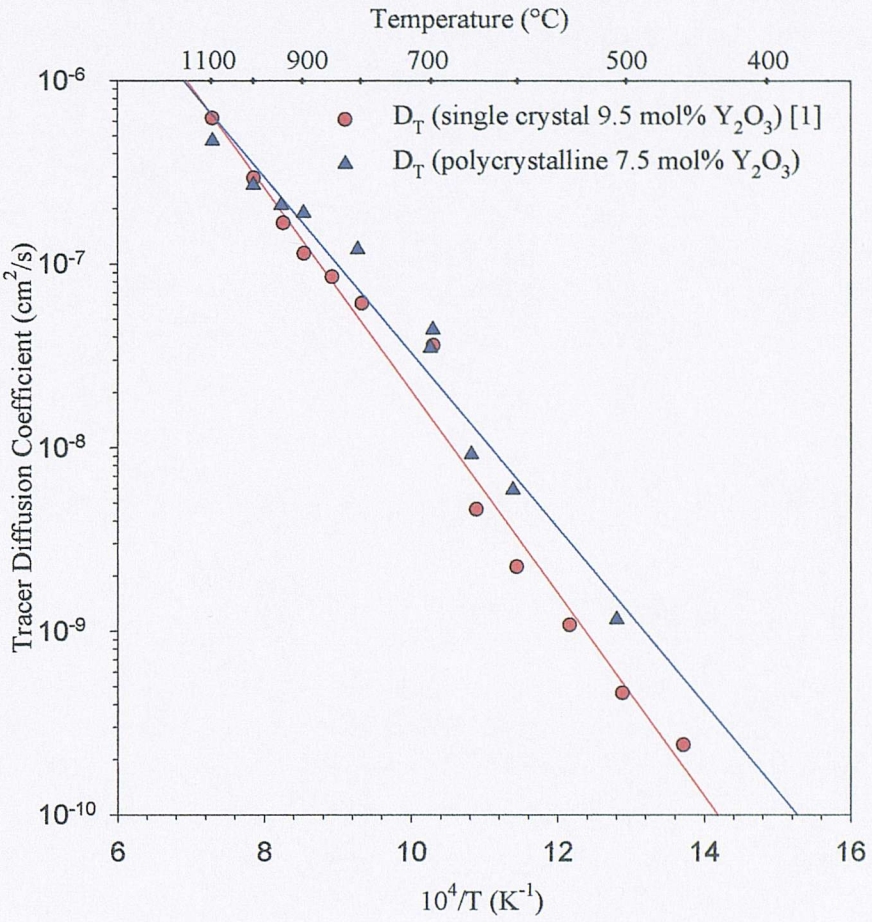


Figure 10.12. Tracer diffusivity of polycrystalline $Zr_{0.85}Y_{0.15}O_{1.925}$ and single crystal $Zr_{0.81}Y_{0.19}O_{1.905}$ as a function of reciprocal temperature.

The linear regression of the polycrystalline data can be described by equation 10.5.

$$D_T = 0.0020^{+0.0021}_{-0.0010} \exp\left(\frac{-91 \pm 6 kJ/mol}{RT}\right) \qquad \text{eqn. (10.5)}$$

This is similar to the results obtained for the single crystal material. The linear regression for the single crystal data of Manning *et al* [1] is described by equation 10.6.

$$D_T = 0.007^{+0.005}_{-0.003} \exp\left(\frac{-106 \pm 5 kJ/mol}{RT}\right) \qquad \text{eqn. (10.6)}$$

There is slightly more scatter evident in the polycrystalline data (as was seen with the CGO materials) and this is manifested in the degree of uncertainty in the activation energy for the two materials. The activation energy for the 7.5mol% Y_2O_3 doped zirconia polycrystal is a little smaller than the 9.5mol% Y_2O_3 doped single crystal zirconia. This is in general agreement with the data obtained for ionic conductivity from AC impedance spectroscopy (shown in chapter 9). The value obtained for the activation energy for 7.5mol% YSZ from the SIMS is slightly less than that obtained by AC impedance spectroscopy (100kJ/mol), however, the difference is within the limits of experimental error.

10.6. Comparison of Tracer Diffusivities Obtained for Different Materials.

The activation energies obtained for the five materials examined in this work are given in table 10.10 and the oxygen tracer diffusivities obtained for the materials are shown as a function of temperature in figure 10.13. In figure 10.13, the symbol (P) represents a polycrystalline sample and the symbol (S) a single crystal. It is important to note when comparing the values of activation energy and the actual magnitude of the oxygen tracer diffusivity that the polycrystalline material represents a total diffusivity (bulk + grain boundaries) whereas the data for the single crystal is only the result of a bulk response.

Material	Activation Energy (kJ/mol)
$Ce_{0.9}Gd_{0.1}O_{1.95}$	88 ± 10
$Ce_{0.8}Gd_{0.2}O_{1.9}$	76 ± 8
$Ce_{0.69}Gd_{0.31}O_{1.845}$	112 ± 7
$Ce_{0.8}Gd_{0.18}Pr_{0.02}O_{2-x}$	65 ± 9
$Zr_{0.85}Y_{0.15}O_{1.925}$	91 ± 6

Table 10.10. Activation energy for oxygen tracer diffusivity in various fluorite materials.

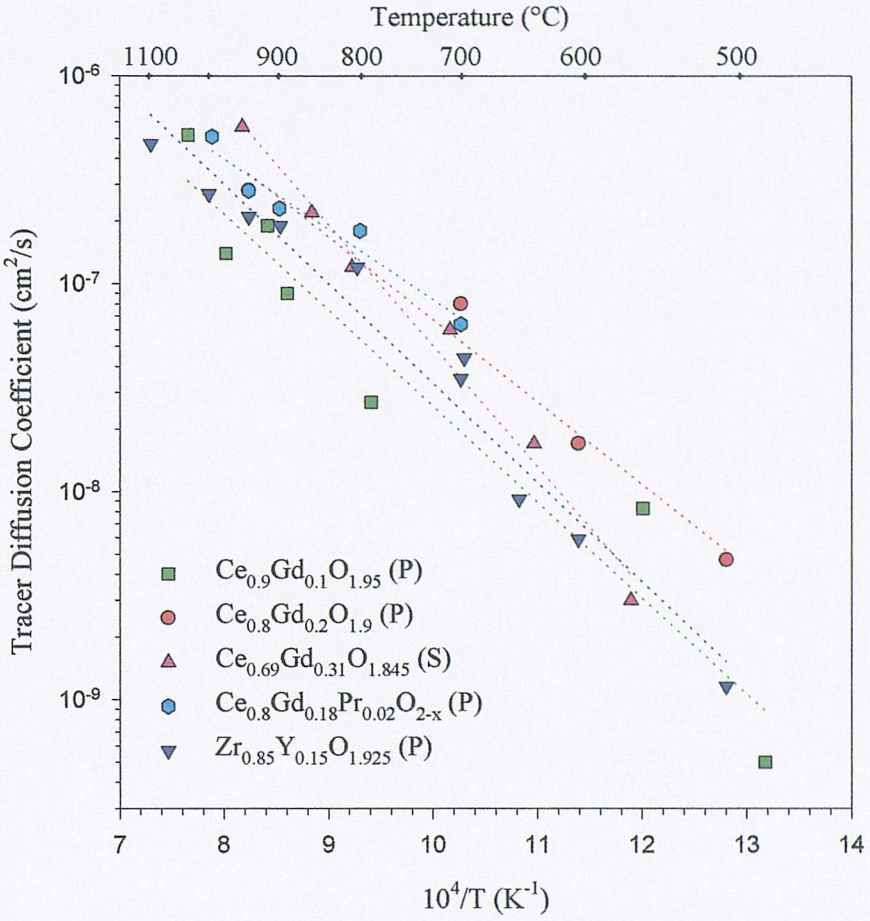


Figure 10.13. Oxygen tracer diffusivity in various fluorite materials as a function of reciprocal temperature.

The activation energies of the $Ce_{0.9}Gd_{0.1}O_{1.95}$, $Ce_{0.69}Gd_{0.31}O_{1.845}$ and $Zr_{0.85}Y_{0.15}O_{1.925}$ materials compares well with the data obtained from AC impedance spectroscopy given in Chapter 9. Of the CGO materials, the $Ce_{0.8}Gd_{0.2}O_{1.9}$ sample has the lowest activation energy then the $Ce_{0.9}Gd_{0.1}O_{1.95}$ sample and the $Ce_{0.69}Gd_{0.31}O_{1.845}$ single crystal has the highest activation energy. This trend is similar to that seen by Ralph and Kilner [3] where the activation energy for the total conductivity measured by AC impedance spectroscopy shows a decrease with increasing gadolinia content, followed by an increase above 11.5mol% Gd_2O_3.

The activation energy for the $Ce_{0.8}Gd_{0.18}Pr_{0.02}O_{2-x}$ sample is very low and is similar to the theoretical migration enthalpy for CeO_2 based materials. It is possible that because this material was examined in a high temperature regime (700-1000°C), the material is behaving as an unassociated dilute solution, despite

the large dopant concentration. If the binding enthalpy for defect associates is relatively low, then very few oxygen vacancies will be trapped in defect associates or clusters at such high temperatures.

Due to the difference in activation energies of the various materials, different compositions show the highest tracer diffusivity at different temperatures. At low temperatures (~500°C), the $Ce_{0.8}Gd_{0.2}O_{1.9}$ sample has the highest tracer diffusivity. The $Ce_{0.9}Gd_{0.1}O_{1.95}$, $Ce_{0.69}Gd_{0.31}O_{1.845}$ and $Zr_{0.85}Y_{0.15}O_{1.925}$ materials all have a similar tracer diffusivity at 500°C. At 1000°C to 1100°C the oxygen diffusivity of YSZ is similar to $Ce_{0.8}Gd_{0.2}O_{1.9}$ and $Ce_{0.8}Gd_{0.18}Pr_{0.02}O_{2-x}$. Due to the high activation energy of $Ce_{0.69}Gd_{0.31}O_{1.845}$, the oxygen diffusivity above 900°C is considerably larger than the other fluorite materials.

Based on this data, the best material, in terms of the oxygen ion mobility, for an electrochemical device operating in the low to intermediate temperature range is $Ce_{0.8}Gd_{0.2}O_{1.9}$. However, recently the oxygen ion conductivity of $Ce_{0.9}Gd_{0.1}O_{1.95}$ materials has been significantly improved by reducing the level of impurities in the material, thus reducing the grain boundary impedance [4].

10.7. Comparison of Tracer Diffusivities with Data from the Literature.

There is very little work on oxygen tracer diffusivities measured by SIMS on highly doped ceria systems. The work of Carter *et al* [5] on lanthanum doped ceria has a low dopant concentration, and thus the tracer diffusivity is small, while the yttria doped ceria data is very limited. Floyd used gas phase analysis to determine the oxygen tracer diffusivity in yttria doped ceria with a high dopant concentration [6]. The lack of SIMS data published reflects the difficulties in performing tracer experiments on ceria based materials due to the low oxygen surface exchange rate and the insulating nature of the samples, making ion beam induced charging a problem when measuring the oxygen ion intensities. Figure 10.14 shows the tracer diffusivity of $Ce_{0.9}Gd_{0.1}O_{1.95}$ and $Ce_{0.8}Gd_{0.2}O_{1.9}$ compared with the data of Carter *et al* [5] and Floyd [6].

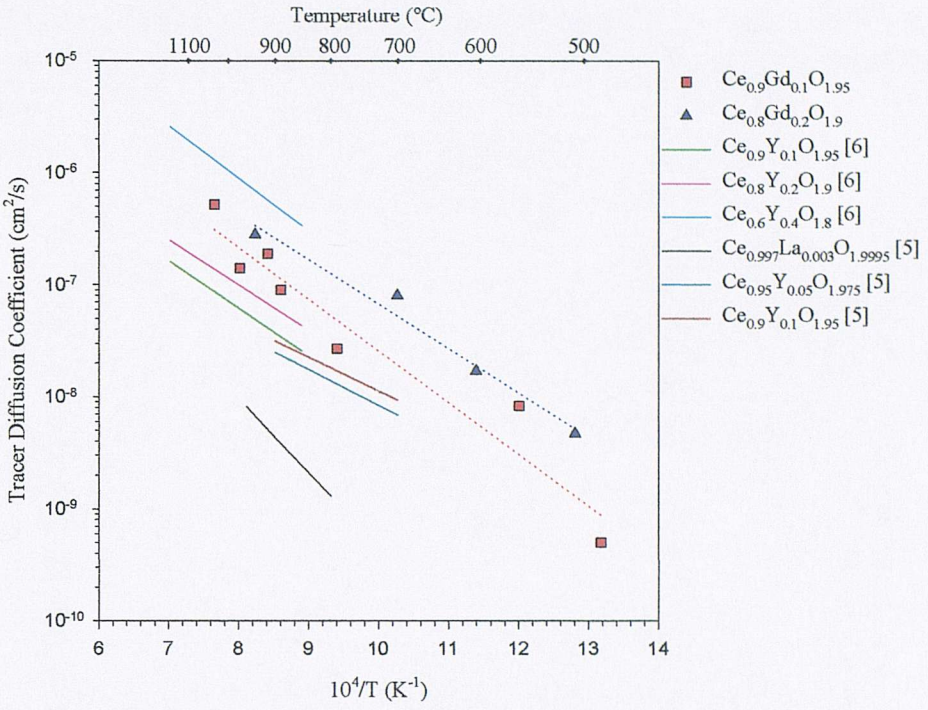


Figure 10.14. Comparison of the oxygen tracer diffusivity of CGO with other ceria based fluorites [5,6].

The data of Carter is very much lower than the other data due to the small concentration of dopant and hence a small concentration of vacancies. The data of Floyd is comparable with SIMS data on the CGO materials given here. Furthermore, both Floyd and Carter *et al* saw an increase in the tracer diffusivity with increasing yttria dopant concentration (and hence oxygen vacancy concentration). Floyd's data also shows a minima in the activation energy at the $Ce_{0.8}Y_{0.2}O_{1.9}$ concentration, as seen in this work with the gadolinia doped sample. Floyd's measurements show the $Ce_{0.9}Y_{0.1}O_{1.95}$ sample has an activation energy of 81kJ/mol, $Ce_{0.8}Y_{0.2}O_{1.9}$ an activation energy of 77kJ/mol and $Ce_{0.6}Y_{0.4}O_{1.8}$ an activation energy of 90kJ/mol. The activation energies from the data of Carter *et al* on $Ce_{0.9}Y_{0.1}O_{1.95}$ is slightly less. The activation energies for the $Ce_{0.9}Y_{0.1}O_{1.95}$ and $Ce_{0.8}Y_{0.2}O_{1.9}$ samples are very similar to that found in the gadolinia doped samples of the same composition. The higher doped material of Floyd has an activation energy less than that found in this work, although a single crystal was used here whereas Floyd used polycrystalline materials which may affect the results.

There is somewhat more oxygen tracer diffusion data on stabilised zirconia systems. The work of Simpson and Carter [7] is often cited as a reference point

for tracer diffusion experiments on fluorite materials. Figure 10.15 shows a comparison of the tracer diffusivity of $Zr_{0.85}Y_{0.15}O_{1.925}$ with other zirconia based fluorites.

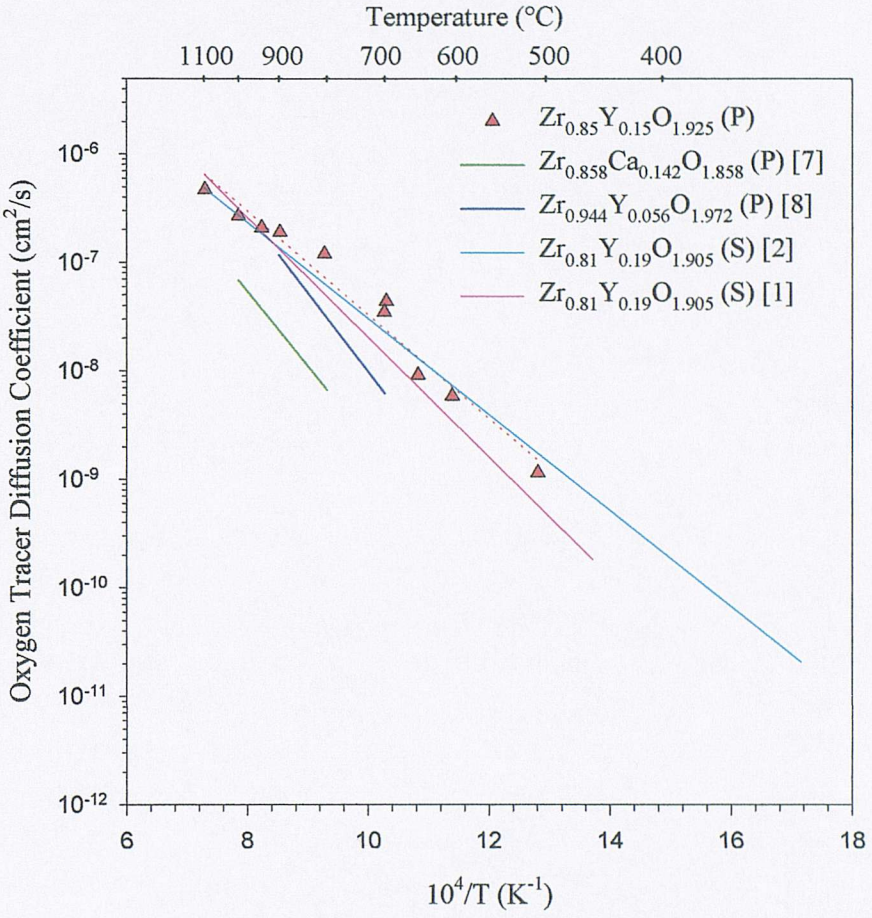


Figure 10.15. Comparison of the oxygen tracer diffusivity of YSZ with other zirconia based fluorites [1,2,7,8]

The tracer diffusivities of $Zr_{0.85}Y_{0.15}O_{1.925}$ polycrystalline samples are very similar to the values obtained for single crystals of YSZ with a similar composition by both Manning *et al* [1] and Solmon [2] in the same temperature range. The data of Simpson and Carter [7] and Kim *et al* [8] are slightly lower in the temperature range measured.

A similar trend in the activation energies for oxygen diffusion as seen for the ceria based fluorites can be seen in the zirconia materials. The calcia stabilised zirconia examined by Simpson and Carter [7] has a very high concentration of oxygen vacancies and so has a high activation energy. The data of Kim *et al* [8] on yttria stabilised zirconia with a low dopant (and thus low oxygen vacancy

concentration) also has a high activation energy, while the intermediate doped materials (i.e. this work and that of Manning *et al* [1] and Solmon [2]) have an activation energy between the values of Simpson and Carter [7] and Kim *et al* [8]. Thus a minima at around the same dopant level as seen for ceria solid solutions is observed for zirconia based fluorites. This phenomena provides some evidence that the oxygen diffusion processes in both these fluorite materials are controlled by similar mechanisms. It also suggests that in both cases there is a high binding energy for defect associates, or clusters, at high dopant levels.

10.8. Comparison of Tracer Diffusion with Ionic Conductivity from AC Impedance Spectroscopy.

There has been very little work published comparing oxygen ion conductivity with oxygen tracer diffusivity on the same samples of fluorite materials. Manning *et al* [1] produced a comprehensive study over a wide range of temperatures on high quality single crystals of $Zr_{0.81}Y_{0.19}O_{1.905}$. Their data was shown in figure 4.4, in Chapter 4. In their work, the tracer diffusivity was lower than the oxygen ion conductivity, giving a Haven ratio (as defined by, e.g., Murch [9]) of less than unity. This is as expected for a vacancy mechanism in a cubic lattice [9,10,11]. However, the Haven ratio obtained by Manning *et al* [1] deviates from the value of 0.653 predicted for a simple cubic system [9]. At high temperatures (above 700°C) they observed a Haven ratio of 0.48, while at low temperatures a Haven ratio of 0.33 was seen. They relate this change to a possible order/disorder transition in the oxygen vacancies observed in $Zr_{0.83}Y_{0.17}O_{1.915}$ at 650°C [12]. The possibility of electronic or protonic conduction affecting the results was discounted due to the low electronic transference number (10^{-4} [13]) and the conductivity results obtained in wet and dry atmospheres (see Chapter 9).

The reason for the lack of data comparing tracer diffusion measurements and ionic conductivity is small partly because performing tracer diffusion measurements is difficult but also due to errors associated with measuring the ionic conductivity and the fact that the most accurate data from tracer diffusion is obtained at high temperatures and the most accurate data from AC impedance spectroscopy is at significantly lower temperatures. There is clearly significant scatter in the tracer diffusion measurements, particularly in the polycrystalline

materials. There is also the possibility of systematic errors in both measurement techniques. In AC conductivity measurements where small samples were used, contact between the experimental AC impedance head and the sample can often produce problems. Thus the cross sectional area of the pellet which is used in calculations of the conductivity is not always equal to the active area of the conductive path, therefore producing a systematic error in the conductivity.

A further source of error is in determining the temperature of the experiments. Small differences in the temperature from both experiments can lead to large errors in determining the ratio between the two types of diffusion coefficient. However, because all three materials produced similar results, it is reasonable to assume that the Haven ratio calculated is a real value rather than one brought about by errors in the experiments. The following discussion assumes that the data presented in Chapter 9 and the previous sections in this Chapter are accurate and that the work of Manning *et al* [1] forms a reasonable basis for discussion.

Murch [9] predicted a change in the Haven ratio with an order/disorder transition. Murch also states that the value of 0.65 for the Haven ratio is only appropriate for unassociated dilute solutions. At the high level of dopant used in the work of Manning *et al* [1], this is unlikely to be the case, particularly at low temperatures where the concentration of $\left(Y'_{Zr}V_O^{\bullet\bullet}\right)^{\bullet}$ defect associates is expected to be high. If the material is not behaving as an unassociated dilute solution, the theoretical value of the Haven ratio will be incorrect. Furthermore, Weller and Schubert [14] suggested that the charged defect associates will reorientate in an electric field, thus contributing to the electrical conductivity but not to the tracer diffusivity. If there are more $\left(Y'_{Zr}V_O^{\bullet\bullet}\right)^{\bullet}$ defect associates present at lower temperatures then the Haven ratio will be smaller at lower temperatures, as seen by Manning *et al* [1].

It should be noted that the definition of the Haven ratio provided by Murch [9] is the ratio of the tracer diffusivity to the D.C. ionic conductivity, thus the possibility of re-orientation of dipoles due to an electric field is discounted, and the conductivity correlation factor can be regarded as unity. In the work of Manning *et al* [1] and the work undertaken here, an AC field is applied and thus dipole re-orientation cannot be discounted. Thus the ratio measured by Manning *et al* and in this work is not strictly speaking a Haven ratio, but this term is still applied here.

In this work, three materials have been examined using AC impedance spectroscopy and SIMS: single crystal $Ce_{0.69}Gd_{0.31}O_{1.845}$, polycrystalline $Ce_{0.9}Gd_{0.1}O_{1.95}$ and polycrystalline $Zr_{0.85}Y_{0.15}O_{1.925}$. Figure 10.16 shows a comparison of the tracer diffusion coefficient with diffusion obtained from the electrolyte response from AC impedance spectroscopy (hereafter named AC conductivity diffusion, or D_σ) for single crystal $Ce_{0.69}Gd_{0.31}O_{1.845}$. Figure 10.17 shows a comparison of the tracer diffusion coefficient with D_σ (electrolyte grains plus grain boundaries) for polycrystalline $Ce_{0.9}Gd_{0.1}O_{1.95}$ and figure 10.18 compares the tracer diffusion coefficient with D_σ (electrolyte grains plus grain boundaries) for polycrystalline $Zr_{0.85}Y_{0.15}O_{1.925}$. The AC conductivity diffusion coefficient is calculated from the oxygen ion conductivity using the Nernst-Einstein relationship, given as equation 10.7 [10],

$$D_\sigma = \frac{kT\sigma_i}{Nq^2} \qquad \text{eqn. (10.7)}$$

k is the Boltzmann constant, T is the absolute temperature, σ_i is the ionic conductivity, N is the concentration of oxygen sites per volume and q is the charge of the oxygen ion. It should be noted that the various correlation factors have been omitted from this equation, thus the ratio between D_T and D_σ is given by the Haven ratio.

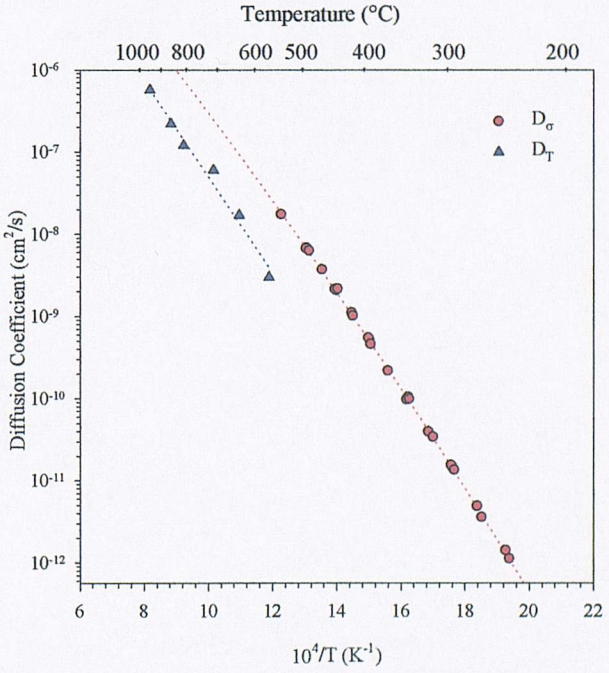


Figure 10.16. Comparison of the tracer diffusion coefficient with the AC conduction diffusion coefficient for single crystal $Ce_{0.69}Gd_{0.31}O_{1.845}$.

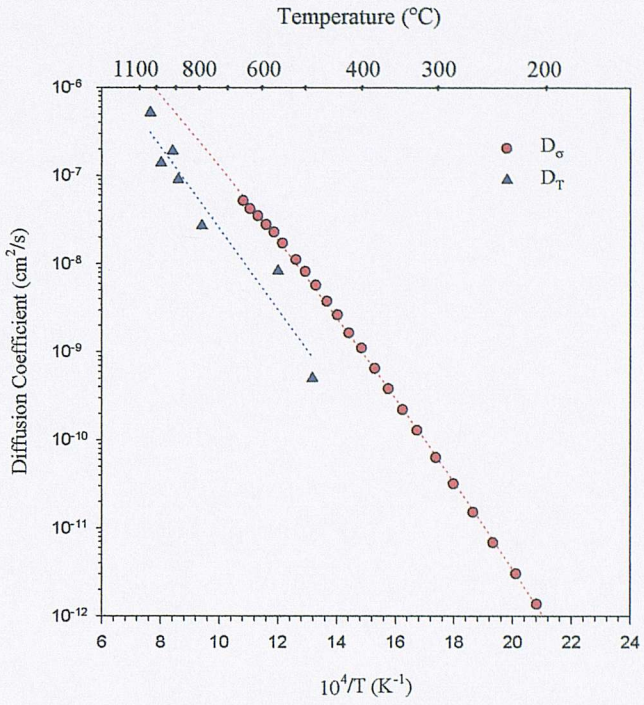


Figure 10.17. Comparison of the tracer diffusion coefficient with the AC conduction diffusion coefficient for polycrystalline $Ce_{0.9}Gd_{0.1}O_{1.95}$.

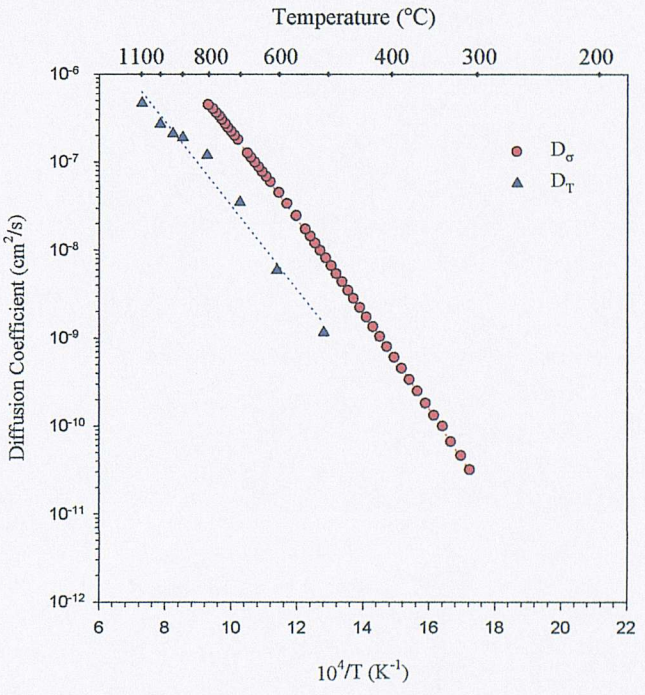


Figure 10.18. Comparison of the tracer diffusion coefficient with the AC conduction diffusion coefficient for polycrystalline $Zr_{0.85}Y_{0.15}O_{1.925}$.

In all cases, the tracer diffusion coefficient is less than the AC conductivity diffusion coefficient in the temperature range examined. As with the data of Manning *et al* [1], the ratio between the two measurements deviates from the predicted value 0.65. In figures 10.16 and 10.17 the conductivity data has been extrapolated to enable a comparison of the two diffusion measurements at the same temperatures. Calculation of the Haven ratio for all the materials is made difficult by the scatter in tracer diffusion data. The Haven ratio has been estimated at 600°C and 800°C from the ratio between the regression lines in figures 10.16 to 10.18. These values are shown in table 10.11.

Material	Haven ratio	
	600°C	800°C
$Ce_{0.69}Gd_{0.31}O_{1.845}$ (S)	0.14	0.17
$Ce_{0.9}Gd_{0.1}O_{1.95}$ (P)	0.16	0.20
$Zr_{0.85}Y_{0.15}O_{1.925}$ (P)	0.15	0.14

Table 10.11. Haven ratio for $Ce_{0.69}Gd_{0.31}O_{1.845}$ single crystals, $Ce_{0.9}Gd_{0.1}O_{1.95}$ and $Zr_{0.85}Y_{0.15}O_{1.925}$ polycrystals.

The Haven ratios calculated for the three materials are somewhat less than those reported by Manning *et al* [1] on single crystal $Zr_{0.81}Y_{0.19}O_{1.905}$. The two ceria based materials follow the same trend observed by Manning *et al* where the Haven ratio is larger at higher temperatures. This is due to the curvature in the AC conductivity diffusion caused by the association binding enthalpy. This suggests that the materials are behaving more like an unassociated dilute solution in the high temperature regime. However, the AC impedance data does not extend to a high enough temperature to determine if a Haven ratio of 0.65 is approached. The polycrystalline $Zr_{0.85}Y_{0.15}O_{1.925}$ data shown in figure 10.18 does not follow the same trend as the ceria materials or the data of Manning *et al*. The Haven ratio is of a similar value to the ceria based materials, however, the same increase with temperature is not observed. It is not immediately obvious why this should be the case.

There are several possible explanations why the Haven ratio in all three materials is significantly lower than predicted from computer simulations, however there is insufficient data, and too much scatter in the data to determine which, if any, of the most obvious explanations are correct. It is unlikely that the small Haven ratio is caused by electronic conductivity in any of these materials which are

known to have a very small electronic transference number [13,15]. Protonic contributions to the conductivity were also shown to be very unlikely in Chapter 9. Other possible explanations arise because in the tracer diffusion measurements mass transport is being monitored while in the ionic conductivity measurements charge transport is being monitored. This means that if species other than an O^{2-} are involved in either measurements (such as O^{-} or even neutral oxygen) the Haven ratio would not be 0.65. A more likely explanation is that the charge defect associates present in high concentrations at lower temperatures reorientate in an AC field contributing to the electrical conductivity but not to a long range diffusion process.

Ordering of the oxygen vacancies would also lead to a deviation from 0.65 in the Haven ratio. There have been reports of ordering in YSZ materials, with an order/disorder transition occurring at around 650°C [12]. Atlas [16,17] proposed a statistical model to account for partial ordering of anion vacancies in hypostoichiometric fluorite materials. In this work, the model was compared to the data of Bevan and Kordis [18] for non-stoichiometric ceria solid solutions and good agreement was found. Atlas later proposed a model for defect ordering in $UO_{2\pm x}$ [19]. Bevan [20] showed the formation of stoichiometric intermediate phases of $Ce_{32}O_{58}$, $Ce_{32}O_{56}$ and $Ce_{32}O_{55}$ in hypostoichiometric ceria solutions as a result of ordering of the anion and cation sub-lattices, although Bevan and Kordis [18] later suggest that the intermediate phases have the composition $Ce_{11}O_{20}$, Ce_9O_{16} and Ce_7O_{12}. These ordering effects are likely to occur in highly doped ceria materials which consequently have a large number of oxygen vacancies. This will therefore affect the diffusion and conduction behaviour of the materials such that dilute solution theory is not appropriate and deviations from the calculated Haven ratio are expected.

These comparisons are further complicated in the case of the polycrystalline materials. In the tracer diffusion measurements the long range diffusion is being measured when the line-scanning technique is employed. Therefore the tracer diffusion coefficient measured is an effective diffusion coefficient for the bulk plus some grain boundaries. In the AC impedance spectroscopy data the conductivity of the bulk and all the grain boundaries are being measured.

In the calculation of the Haven ratio for the materials given above the total conductivity was used to calculate D_σ not just the bulk response. The total conductivity has to be used because the D_T involves grain boundaries. However, the Nernst-Einstein equation (equation 10.7) is appropriate for lattice transport

and does take into account boundary phenomena such as grain boundaries. Certainly the concentration of oxygen sites per unit volume at grain boundaries is expected to be different than in the bulk. Therefore, a comparison of tracer diffusion measurements and ionic conductivity in polycrystalline materials requires greater understanding of the grain boundary contribution to the overall ionic transport. It should also be noted that if the depth profiling method of analysis is employed in the SIMS, the number of grain boundaries traversed is very small thus adding to the difficulties. The single crystal data of Manning *et al* [1] and the work done on the single crystal of CGO presented here is a better comparison of the two measurement techniques.

In future work, to avoid many of the problems regarding defect associates, it would be more appropriate to compare DC electrical conductivity measurements to tracer diffusion measurements as dipole reorientation effects are thus eliminated. The other advantages of using DC conductivity is that long range transport is monitored (as with tracer diffusion) and higher temperatures are possible with DC techniques than with AC impedance.

In order to obtain the most accurate values of the Haven ratio, measurements should therefore be performed using DC electrical conductivity and line-scanning SIMS analysis on single crystal materials over the same temperature range.

10.9. References.

[1] P.S. Manning, J.D. Sirman, R.A. De Souza and J.A. Kilner, Solid State Ionics, **Vol 100** (1997) p1.

[2] H. Solmon, Ph.D. Thesis, Université Paris, (1992).

[3] J.M. Ralph and J.A. Kilner, in Proc. Of the 2nd European SOFC Forum, Eds. B. Thorstensen, Oslo, Norway (1996) p773.

[4] J.M. Ralph, Ph.D. Thesis, University of London (1998).

[5] S. Carter, R.J. Chater, J. Kajda, K.M. Liddicott, J.A. Kilner and B.C.H. Steele, in Proc. of the 1st Int. Symp. On Ionic and Mixed Conductors, Eds. T.A. Ramanarayanan and H. Tuller, The Electrochem. Soc. Inc., Phoenix, Arizona (1991) p84.

[6] J.M. Floyd, Indian Journal of Technology, **Vol 11** (1973) p589.

[7] L.A. Simpson and R.E. Carter, J. Am. Ceram. Soc. **Vol 49** (1966) p139.

[8] B.-K. Kim, S.J. Park, H. Hamaguchi, J. Am. Ceram. Soc. **Vol 77** (1994) p2648.
[9] G.E. Murch, Solid State Ionics, **Vol 7** (1982) p177.
[10] P. Shewmon, in "Diffusion in Solids", 2nd Edition, The Minerals, Metals, and Materials Society (1989).
[11] Y.-M. Chiang, D. Birnie III and W.D. Kingery, in Physical Ceramics, John Wiley & Sons, Inc., New York (1997).
[12] I.R. Gibson and J.T.S. Irvine, J. Mat. Chem., **Vol 5** (1996) p895.
[13] W.D. Kingery, H.K. Bowen and D.R. Uhlmann, in Introduction to Ceramics, 2nd Edition, John Wiley and Sons, Inc., New York (1976) p853.
[14] M. Weller and H. Schubert, J. Am. Ceram. Soc., **Vol 69** (1986) p573.
[15] J.M. Ralph and J.A. Kilner, in Proceedings of the 5th International Symposium on SOFC, Eds. U. Stimming, S. Singhal, H. Tagawa and W. Lehnert Electrochemical Society **PV 97-40**, Aachen, (1997) p1021.
[16] L.M. Atlas, J. Phys. Chem. Solids, **Vol 29** (1968) p91.
[17] L.M. Atlas, J. Phys. Chem. Solids, **Vol 29** (1968) p1915.
[18] D.J.M. Bevan and J. Kordis, J. Inorg. Nucl. Chem., **Vol 26** (1964) p1509.
[19] L.M. Atlas, J. Phys. Chem. Solids, **Vol 29** (1968) p1349.
[20] D.J.M. Bevan, J. Inorg. Nucl. Chem., **Vol 1** (1955) p49.

11. Oxygen Exchange on the Surface of Fluorites.

11.1. Introduction.

Oxygen surface exchange and the surface exchange coefficient were discussed in detail in Chapter 6 for a variety of different oxide materials. Various models were presented together with data for different materials obtained by workers using both SIMS and gas phase analysis. In this chapter the values of the oxygen surface exchange coefficient for single crystal $Ce_{0.69}Gd_{0.31}O_{1.845}$ and polycrystalline samples of $Ce_{0.9}Gd_{0.1}O_{1.95}$, $Ce_{0.8}Gd_{0.2}O_{1.9}$, $Ce_{0.8}Gd_{0.18}Pr_{0.02}O_{2-x}$, and $Zr_{0.85}Y_{0.15}O_{1.925}$ are presented and discussed. The values for the surface exchange coefficient of the above materials were given in Chapter 10, tables 10.2, 10.4, 10.6, 10.7 and 10.9. The data for these materials together with some of the data given in Chapter 6 is used to develop a possible model for the mechanism of surface exchange.

11.2. Surface Exchange Coefficients of Polycrystalline $Ce_{0.9}Gd_{0.1}O_{1.95}$.

A graph of the surface exchange coefficient as a function of reciprocal temperature for $Ce_{0.9}Gd_{0.1}O_{1.95}$ is given in figure 11.1, together with the values of the tracer diffusion coefficient at these temperatures.

For this material there are two temperature regimes with different activation energies for the surface exchange coefficient. The dotted blue line is the result of a linear regression on the low temperature data and the dashed blue line is the result of a linear regression on high temperature data. At high temperatures (>750°C) the activation energy is high $\left(\Delta H_{EX} = 330\text{kJ/mol}\right)$ while at lower temperatures, the activation energy is low $\left(\Delta H_{EX} = 50\text{kJ/mol}\right)$. The high temperature regression of the data is defined by equation 11.1.

$$k = 1.4 \times 10^{8}{}^{+1.7 \times 10^{16}}_{-1.4 \times 10^{8}} \exp\left(\frac{-330 \pm 190\text{kJ/mol}}{RT}\right) \qquad \text{eqn. (11.1)}$$

As with the tracer diffusion data the error in the pre-exponential constant is very large and not a meaningful value due to the extrapolation of data over a small temperature range to $T = \infty$.

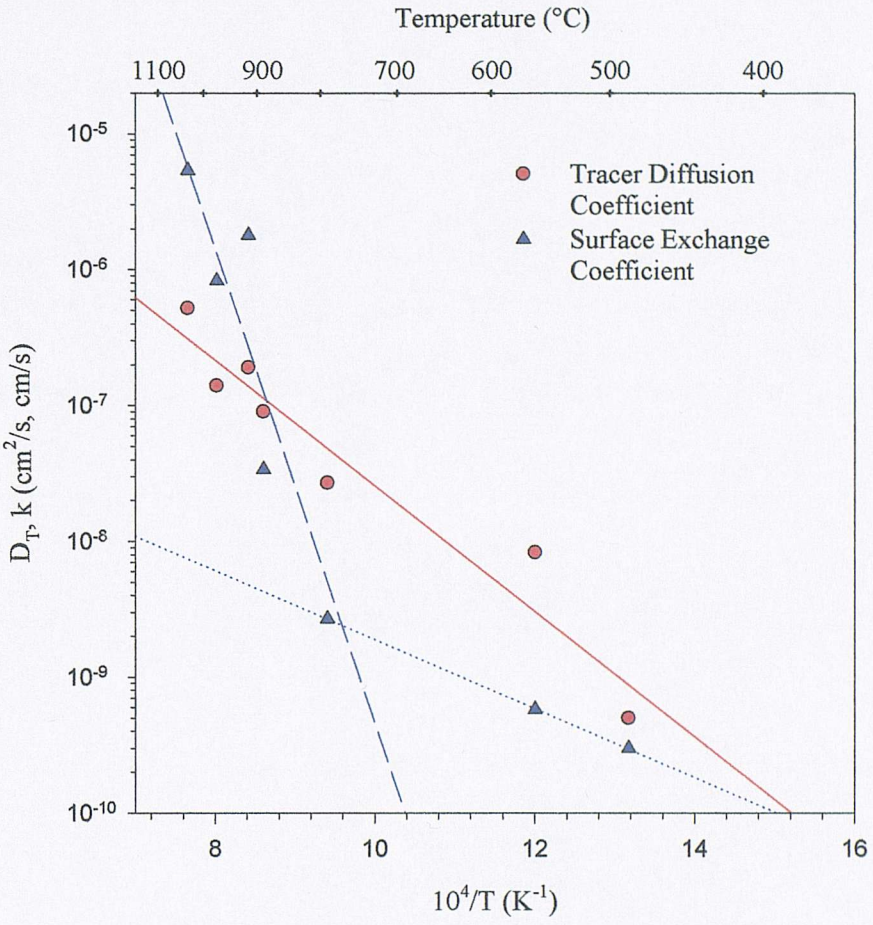


Figure 11.1. Oxygen surface exchange coefficient of polycrystalline $Ce_{0.9}Gd_{0.1}O_{1.95}$ as a function of reciprocal temperature.

The error in the activation energy in the high temperature regime is also very large due to the scatter in the data. However, despite this large error it is still clear that there are two distinct temperature regimes. If the activation energy was constant at 330kJ/mol throughout the entire temperature range then there would be no evidence of a diffusion profile at the low temperatures due to the extremely slow surface kinetics that would exist.

This data was the first the first reported observation of a change in the activation energy for the surface exchange coefficient of fluorite materials, and was published in the proceedings of the 17th Risø Symposium in 1996 [1]. The same

result was also observed by Manning *et al* [2] on single crystal $Zr_{0.81}Y_{0.19}O_{1.905}$ and compared to this data for polycrystalline $Ce_{0.9}Gd_{0.1}O_{1.95}$. For $Zr_{0.81}Y_{0.19}O_{1.905}$ the activation energy changed from 210kJ/mol above ~650°C to 70kJ/mol below ~650°C.

In this paper the two sets of data were compared using an "h plane" plot, a plot of log k against log D_T, first employed by Kilner [3] to compare a range of perovskite and fluorite materials. The two sets of data show a remarkable correlation. This plot is shown in figure 11.2. This strong correlation implies that YSZ and CGO have the same mechanisms for surface exchange and diffusion. Since the YSZ is a single crystal and the CGO was polycrystalline, the correlation also implies that the change in the activation energy of the oxygen surface exchange coefficient is not due to a grain boundary mechanism.

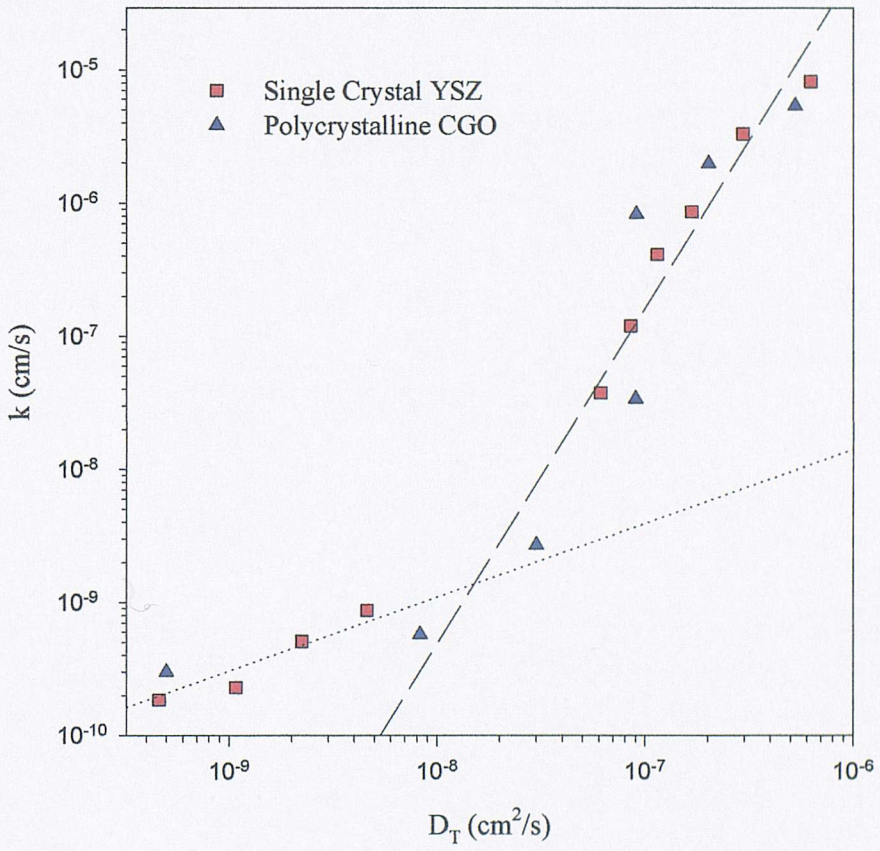


Figure 11.2. "h-plane" plot of k and D_T values obtained for single crystal $Zr_{0.81}Y_{0.19}O_{1.905}$ and polycrystalline $Ce_{0.9}Gd_{0.1}O_{1.95}$.

The slope of the relationship changes from 0.6 below ~700°C to 2.5 above ~700°C. This is quite different to a review of results on fluorites by Kilner [3] where only one slope with a gradient of approximately unity was obtained. However, much of the data used in this review was obtained on samples suspended by either a platinum mesh or wire. It is believed that the platinum will catalyse the surface exchange reaction, thus the true surface exchange coefficient of the materials are not been measured. The effect of surface modifications to the oxygen surface exchange coefficient will be discussed later in this chapter.

11.3. Surface Exchange Coefficients of Single Crystal CGO.

A graph of the surface exchange coefficient as a function of reciprocal temperature for $Ce_{0.69}Gd_{0.31}O_{1.845}$ is given in figures 11.3, together with the values of the tracer diffusion coefficient at these temperatures.

For this material two temperature regimes where the activation energy for the surface exchange coefficient is different are again seen. The dotted and dashed blue lines are the result of linear regression analyses on the low and high temperature data, respectively. At high temperatures (>700°C) the activation energy is again high $\left(\Delta H_{EX} = 230\text{kJ / mol}\right)$ while at lower temperatures, the activation energy is low $\left(\Delta H_{EX} = 100\text{kJ / mol}\right)$. The high temperature regression of the data is defined by equation 11.2.

$$k = 1.3 \times 10^{5}\ ^{+1.3\times10^{6}}_{-1.1\times10^{5}} \exp\left(\frac{-230 \pm 22\text{kJ / mol}}{RT}\right) \qquad \text{eqn. (11.2)}$$

Again, the error in the pre-exponential constant is not a meaningful indication of the quality of the data. For this data the uncertainty in the activation energy is considerably smaller. This is probably due to the fact that the material is a single crystal and thus the diffusion profiles obtained do not have any problems associated with the grain boundaries. Furthermore, the polycrystalline materials are more likely to have impurities due to the preparation method. These will segregate to the surface of the material and thus may play a role in the oxygen surface exchange. The effect of impurities on the surface of the materials will be discussed later in this chapter.

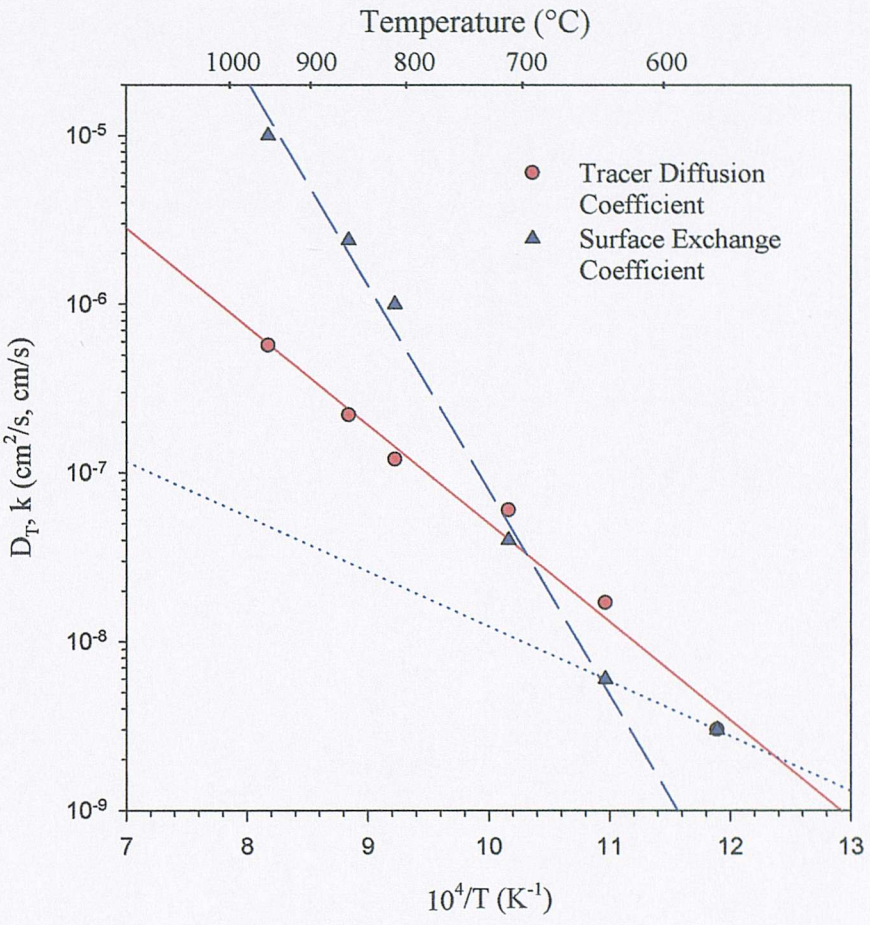


Figure 11.3. Oxygen surface exchange coefficient of single crystal $Ce_{0.69}Gd_{0.31}O_{1.845}$ as a function of reciprocal temperature.

The value of the activation energy for the oxygen surface exchange coefficient is lower than that obtained for the polycrystalline sample of $Ce_{0.9}Gd_{0.1}O_{1.95}$ but very similar to that obtained from the single crystal YSZ data of Manning *et al* [2]. However, it should be noted that the large uncertainty in the activation energy of k for $Ce_{0.9}Gd_{0.1}O_{1.95}$ overlaps the data obtained for the single crystal CGO and YSZ. This similarity also indicates the CGO and YSZ have the same limiting steps for oxygen surface exchange.

11.4. Surface Exchange Coefficients of Polycrystalline $Ce_{0.8}Gd_{0.2}O_{1.9}$.

The surface exchange coefficient plotted as a function of reciprocal temperature for polycrystalline $Ce_{0.8}Gd_{0.2}O_{1.9}$ is given in figure 11.4, together with the values of the tracer diffusion coefficient at these temperatures.

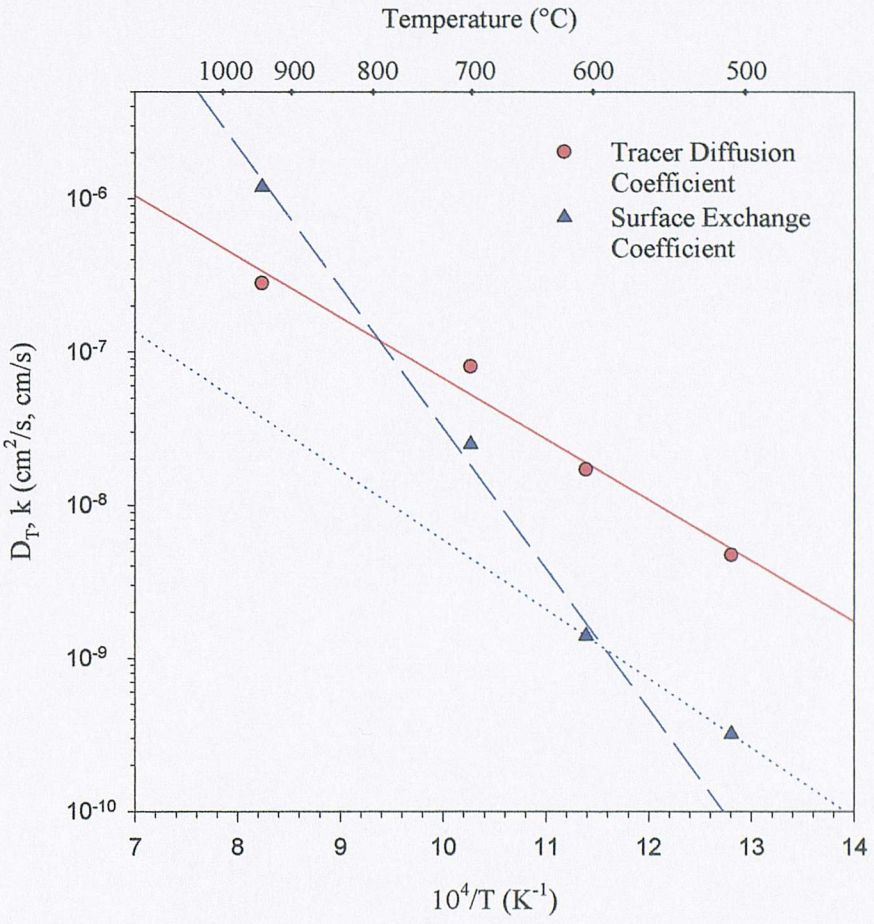


Figure 11.4. Oxygen surface exchange coefficient of polycrystalline $Ce_{0.8}Gd_{0.2}O_{1.9}$ as a function of reciprocal temperature.

From this data alone it not possible to determine if there are two temperature regimes where the activation energy for k is different. However, if this material behaves as the other fluorite materials a change in slope would be seen at around 600-700°C. Therefore, the slope for the highest three temperatures and the lowest two temperatures have been calculated. These are $\Delta H_{EX} = 190 kJ / mol$ for the high temperatures and $\Delta H_{EX} = 90 kJ / mol$ for the low temperatures. Despite the fact that the lack of data means these results have little meaning, they are remarkably similar to the values obtained for the other three fluorite

materials. However, these activation energies will not be used in the following discussion and comparison of the data.

11.5. Surface Exchange Coefficients of Polycrystalline $Ce_{0.8}Gd_{0.18}Pr_{0.02}O_{2-x}$.

The data for the surface exchange coefficient and tracer diffusion coefficient of $Ce_{0.8}Gd_{0.18}Pr_{0.02}O_{2-x}$ plotted as a function of reciprocal temperature is shown in figure 11.5. Again, there is evidence of a change in the activation energy for the oxygen surface exchange at around 750°C. The temperature range of this data makes determination of the activation energy in the low temperature regime impossible. The result of the high temperature linear regression is defined by equation 11.3.

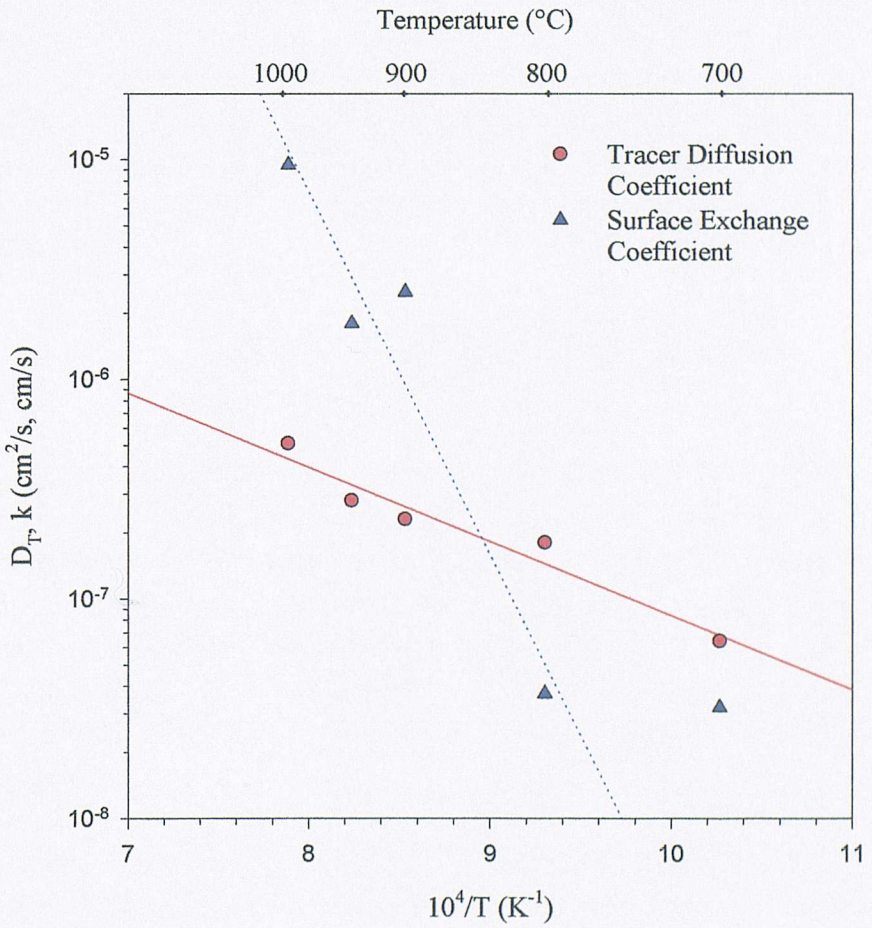


Figure 11.5. Oxygen surface exchange coefficient of polycrystalline $Ce_{0.8}Gd_{0.18}Pr_{0.02}O_{2-x}$ as a function of reciprocal temperature.

$$k = 1.2 \times 10^{8}{}^{+8.4 \times 10^{10}}_{-1.2 \times 10^{8}} \exp\left(\frac{-320 \pm 65\text{kJ / mol}}{RT}\right) \qquad \text{eqn. (11.3)}$$

Again there is a significant error in the activation energy due to the scatter in the data, but this value is very similar to that obtained for $Ce_{0.9}Gd_{0.1}O_{1.95}$ in the high temperature regime.

11.6. Surface Exchange Coefficients of Polycrystalline $Zr_{0.85}Y_{0.15}O_{1.925}$.

Figure 11.6 shows a graph of k and D_T as a function of reciprocal temperature for polycrystalline $Zr_{0.85}Y_{0.15}O_{1.925}$. Again the data is more scattered than the single crystal data suggesting that obtaining a low impurity concentration (and other surface flaws) is more difficult in polycrystalline materials than in single crystals; or that the grain boundaries themselves are affecting the results. Two temperature regimes are again observed. The activation energy in the high temperature regime is 190kJ/mol and in the low temperature regime is 65kJ/mol. The result of the linear regression on the high temperature data is described by equation 11.4.

$$k = 1.9 \times 10^{3}{}^{+5.9 \times 10^{3}}_{-1.4 \times 10^{3}} \exp\left(\frac{-190 \pm 16\text{kJ / mol}}{RT}\right) \qquad \text{eqn. (11.4)}$$

This value for the activation energy is slightly lower than the 230kJ/mol obtained by Manning *et al* [2] for single crystal YSZ and is somewhat lower than the values obtained for the ceria based samples. However, the scatter in the data, particularly at the very high temperatures makes a comparison difficult. For example, if the highest temperature data point at 1097°C which deviates significantly from the regression line is excluded from the regression, the value for the activation energy becomes $210 \pm 13\text{kJ / mol}$ which is close to the value of Manning *et al.*

The fact that the removal of one data point can make such a marked difference to the value of activation energy calculated makes comparison and interpretation of these data sets difficult. Ideally, there should be a similar data density to that obtained from the AC impedance spectroscopy measurements. However, due to

the complexity and time required to make each tracer measurement, it was not possible to obtain such a high data density for all the materials examined.

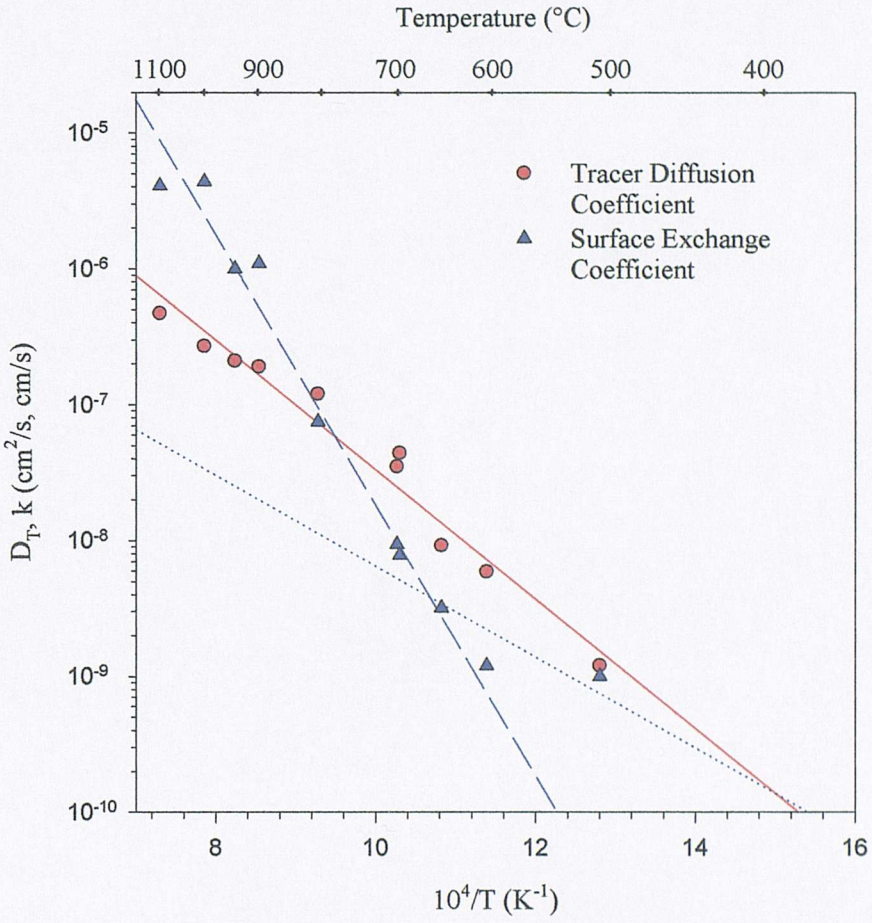


Figure 11.6. Oxygen surface exchange coefficient of polycrystalline $Zr_{0.85}Y_{0.15}O_{1.925}$ as a function of reciprocal temperature.

11.7. Comparison of the Surface Exchange Coefficients of CGO and YSZ.

The activation energy obtained for the fluorite materials examined in this study are shown in table 11.1, together with the values of Manning *et al* for single crystal YSZ.

Material	ΔH_{EX} (kJ/mol)	
	Low Temperature	High Temperature
$Ce_{0.9}Gd_{0.1}O_{1.95}$	50	330 ± 190
$Ce_{0.69}Gd_{0.31}O_{1.845}$	100	230 ± 22
$Ce_{0.8}Gd_{0.18}Pr_{0.02}O_{2-x}$		320 ± 65
$Zr_{0.85}Y_{0.15}O_{1.925}$	65	190 ± 16
$Zr_{0.81}Y_{0.19}O_{1.905}$ [2]	70	212 ± 10

Table 11.1. Activation energy for oxygen surface exchange on various fluorite materials.

The errors for the low temperature values of activation energy are not quoted because the errors calculated are the result of the standard uncertainty in the linear regression analysis on the data and not actual errors associated with the measurements themselves. This means that the value of the uncertainty is dependent on the number of data points used in the linear regression as well as the scatter in the data. For example, if only two data points are used (as was the case for $Ce_{0.8}Gd_{0.2}O_{1.9}$) the standard uncertainty would be zero. In all cases very few data points were used in calculating the low temperature value of activation energy, and so the errors assigned would be unrealistically small. For example in the case of $Ce_{0.9}Gd_{0.1}O_{1.9}$, the uncertainty associated with the low temperature data is only 500J / mol, i.e. 1%.

The scatter in the polycrystalline data is in general greater than in the single crystal data. This may be an effect of the grain boundaries but is more likely to be a reflection of the surface finish of the materials. The AFM images of typical polycrystalline and single crystal samples was shown in figure 7.8. This figure shows that surface roughness of the single crystal samples is much less than the polycrystalline samples as a result of the preparation and polishing methods used. The porosity in the polycrystalline also adds to the surface roughness and thus reduces the quality of finish.

In general the high temperature activation energy for the surface exchange coefficient is lower for the YSZ materials than for the CGO materials. It is interesting to note that the electronic band gap of ceria is 5.5eV ($\equiv 530$kJ / mol) and the band gap of zirconia is 5eV ($\equiv 480$kJ / mol). These values are approximately twice the values obtained for the activation energy of surface exchange in YSZ and CGO, respectively. This suggests that in the high

temperature regime, the availability of free electrons able to take part in the charge transfer step of the surface exchange reaction is the rate limiting step for the reaction.

The same correlation between the materials in the low temperature regime is not evident. The activation energy for the YSZ materials lie in between the values for the CGO materials. However, two interesting features can be observed from these values. The first is that there appears to be a trend in the activation energy with dopant concentration. As the dopant level is increased, the activation energy for k increases. The lowest activation energy obtained is for $Ce_{0.9}Gd_{0.1}O_{1.95}$ (10% acceptor), then $Zr_{0.85}Y_{0.15}O_{1.925}$ (15%), then $Zr_{0.81}Y_{0.19}O_{1.905}$ (19%) and the highest is for $Ce_{0.69}Gd_{0.31}O_{1.845}$ (31%). As the dopant concentration increases, the concentration of oxygen vacancies increases. This may indicate that the supply of oxygen vacancies is the rate limiting step in this temperature regime.

The second interesting feature in this low temperature data is the correlation between the activation energy for oxygen surface exchange and for oxygen tracer diffusion. Table 11.2 shows the activation energy for k together with that for D_T on the same materials, presented in Chapter 10.

Material	Low Temp ΔH_{EX} (kJ/mol)	ΔH_{Diff} (kJ/mol)
$Ce_{0.9}Gd_{0.1}O_{1.95}$	50	88 ± 10
$Ce_{0.69}Gd_{0.31}O_{1.845}$	100	112 ± 17
$Zr_{0.85}Y_{0.15}O_{1.925}$	65	91 ± 6
$Zr_{0.81}Y_{0.19}O_{1.905}$ [2]	70	96 ± 5

Table 11.2. Comparison of the activation energy of k and D_T for various YSZ and CGO materials.

The activation energy for k in the low temperature regime follows the same trend as the activation energy for D_T. The values are almost identical for the single crystal CGO and for the other materials the values of ΔH_{EX} are approximately $\frac{2}{3}\Delta H_{Diff}$. This correlation in the activation energy for the two processes (exchange and diffusion) also suggests that in the low temperature regime the supply of oxygen vacancies is the rate determining step for oxygen exchange. This would suggest both that surface oxygen vacancies play an important role in the exchange process and that at low temperatures it is in the incorporation step which is rate limiting.

The transition seen in the activation energy for the surface exchange coefficient is similar to many extrinsic/intrinsic transitions seen in, for example, semi-conductor analysis. This may suggest that in the low temperature regime the exchange behaviour is affected by impurities. If the supply of electrons is the limiting step, then this suggestion is reasonable as small concentrations of impurities may form donor levels that would affect the electronic structure but not the oxygen diffusion properties of the material. Furthermore, because impurities (and dopant materials) are known to segregate to the surface in these materials [4], it is very likely the surface electronic structure will be different than in the bulk. Thus electrons may be able to take part in oxygen surface exchange but would not be readily transported in the bulk of the material, thus keeping $t_{ion} = 1$. Figure 11.7 shows the logarithm of the surface exchange coefficient plotted against the logarithm of the tracer diffusion coefficient on a so-called h-plane.

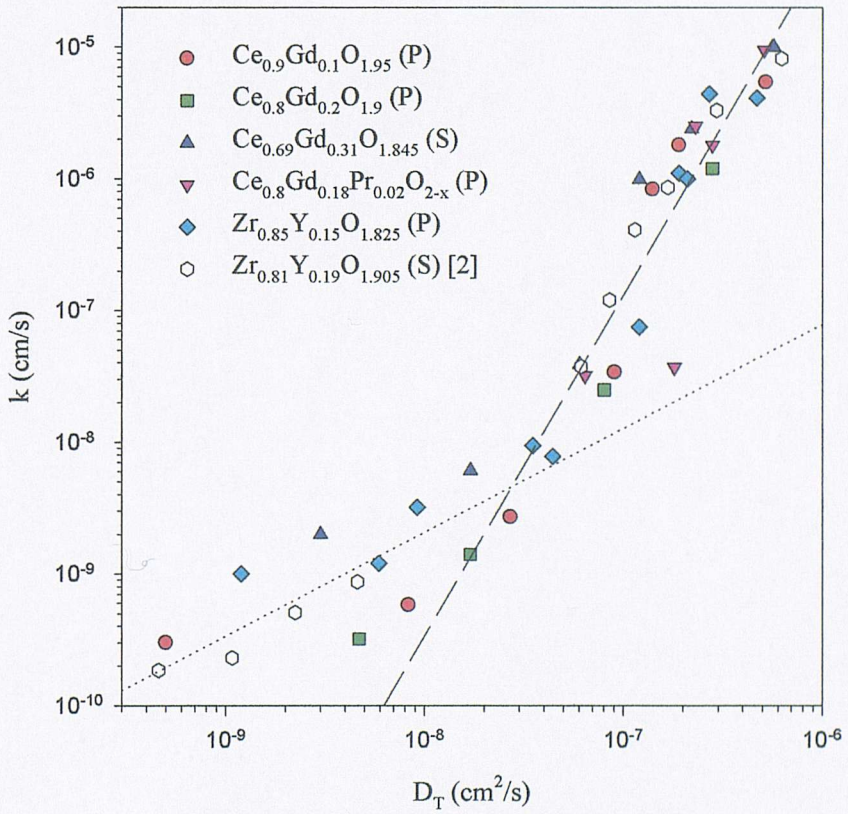


Figure 11.7. "h-plane" plot of k and D_T values obtained for YSZ and CGO materials.

There are clearly two slopes evident on this h-plane projection. This is a result of the change in the activation energy of k at around 700°C. The slope in the high temperature region is 2.6 and the slope in the low temperature region is 0.8. This plot follows the same trend, shown in figure 11.2, that was presented in the work of Manning *et al* [2] for two of these materials. Again there is a very good correlation of the results for all the materials, particularly in the high temperature regime where the ^{18}O surface concentrations are high, and thus the SIMS analysis is made easier. A strong correlation was also noted in the perovskite materials by Kilner [3] although no change in slope was seen, and the gradient was found to be somewhat lower at approximately 0.5.

It is also interesting to compare the values of surface exchange coefficient as a function of reciprocal temperature for the materials investigated. Figure 11.8 shows a graph of the surface exchange coefficient for the CGO materials and figure 11.9 shows a graph of k for the YSZ materials.

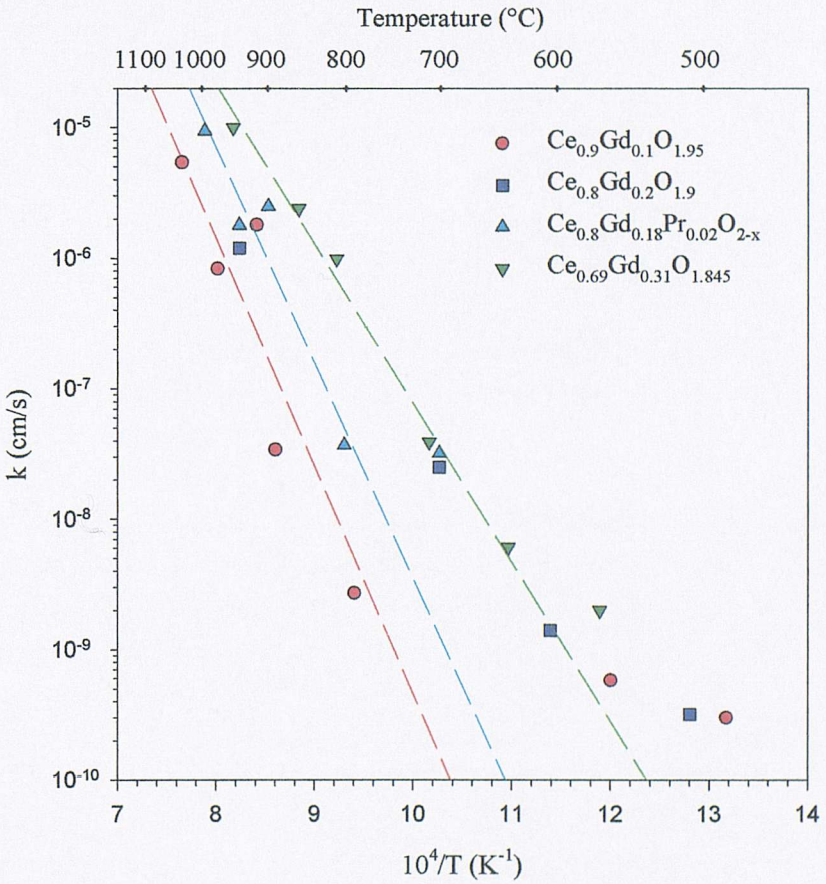


Figure 11.8. Graph of the surface exchange coefficient of various CGO materials as a function of reciprocal temperature.

The dashed lines on figure 11.8 are the results of the linear regression analyses carried out on the high temperature data. For the CGO materials there is a general increase in the value of the surface exchange coefficient with dopant concentration over the entire temperature range examined. This would indicate that oxygen vacancies are important in the oxygen exchange process even at high temperatures where the availability of electrons appears to be the rate determining step. This implies that the concentration of oxygen vacancies is involved in the pre-exponential constant k_O as is the case for diffusion where $\left[V_O^{\bullet\bullet}\right]$ appears in the pre-exponent term. This is also in agreement with the atomistic expression given by Kilner *et al* for k_O [5], given in Chapter 6 (equation 6.24).

It is also interesting to note that the addition of praseodymium to CGO appears to increase the surface exchange coefficient. This was illustrated in figure 10.9 where the ^{18}O surface concentration of $Ce_{0.8}Gd_{0.2}O_{1.9}$ was almost doubled at 701 and 941°C by the presence of 2% praseodymium (substituted for gadolinium). The surface exchange coefficient was 30% higher for the Pr doped material at 701°C and 50% higher at 941°C. Praseodymium will change its valence state more readily than either gadolinium or cerium, thus electronic carriers are more likely to occur in a praseodymium doped sample. The AC impedance data of Ralph [6] showed that the addition of praseodymium increased the conductivity of CGO. No difference in the diffusion coefficient was seen between $Ce_{0.8}Gd_{0.2}O_{1.9}$ and $Ce_{0.8}Gd_{0.18}Pr_{0.02}O_{2-x}$ suggesting that the increased conductivity seen with addition of praseodymium may be due to electronic carriers. Therefore, if the supply of electrons is the rate limiting step for surface exchange at high temperatures, the presence of praseodymium would be expected to increase the surface exchange coefficient, especially if praseodymium were to segregate to the surface.

The high temperature data for the two YSZ materials are very similar and the transition temperature where the activation energy changes also match. However, the values of the activation energy in the low temperature regime are higher for the polycrystalline sample than for the single crystal material. This could indicate that a substantial proportion of the exchange takes place at the grain boundaries or, that if the low temperature regime is dominated by impurities, then there is a higher impurity concentration in the polycrystalline material. The second suggestion is believed to be more likely since if the grain boundaries did enhance the rate of surface exchange then the effect would be seen over the entire

temperature range, the same effect would be noticeable in the CGO materials and substantially different activation energies would be expected.

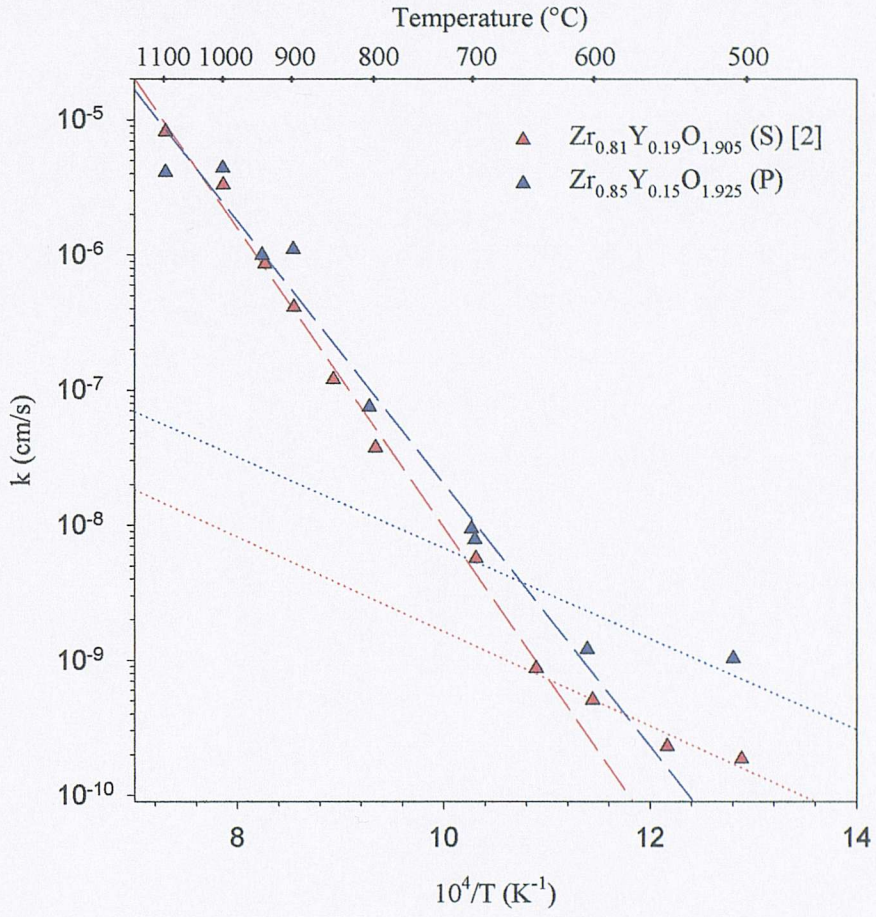


Figure 11.9. Graph of the surface exchange coefficient of polycrystalline and single crystal YSZ materials as a function of reciprocal temperature.

11.8. Comparison of Surface Exchange Data with Data from the Literature.

There has been very little data published on the surface exchange coefficient of fluorite materials, particularly at the low temperatures. This is a reflection of the difficulty in performing tracer experiments on these materials. The slow surface kinetics at low temperatures results in very low ^{18}O surface concentrations that can only be detected with sensitive surface analysis tools such as SIMS. The problem is further complicated by the low electronic conductivity of these

materials making charge compensation difficult. The data set presented earlier in this chapter represents the most comprehensive work on the oxygen surface exchange coefficient of fluorites to data. The only other data on fluorite materials spanning this temperature range is the work on YSZ by Manning *et al* [2].

There have been several sets of data published on a variety of fluorites at high temperatures (i.e. 700-1200°C). These include the work of Ando *et al* [7] on thoria, Simpson and Carter [8] on calcia stabilised zirconia (CSZ) and Kim *et al* [9] on 2.8mol% yttria stabilised zirconia (3YTZ). This data is plotted together with the high temperature data of some of the materials given above on figure 11.10.

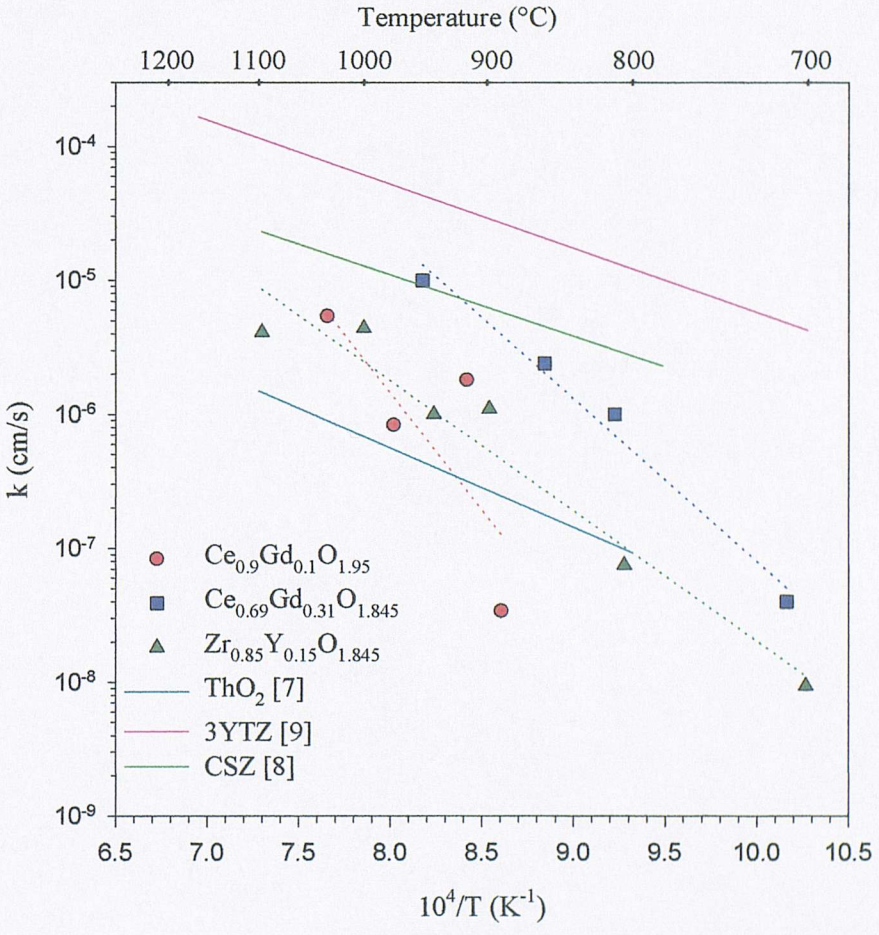


Figure 11.10. Arrhenius Graph of the surface exchange coefficient of various fluorites [7,8,9].

It is clear that surface exchange coefficients measured by Kim *et al* [9] and Simpson and Carter [8] are considerably larger than the values measured in this study. The activation energy obtained by these workers is smaller than obtained here (88kJ/mol for CSZ and 91kJ/mol for 3YTZ). The study of thoria by Ando *et al* [7] also has a low activation energy (116kJ/mol) but is substantially lower than the doped zirconias. This is because the thoria is not doped and so has very few oxygen vacancies.

It is believed that the method used by Kim *et al* [9] and Simpson and Carter [8] to determine the surface exchange coefficient is the reason why the values are so high and why the activation energies are low. In their studies the sample was suspended by a platinum wire or mesh while the tracer isotope was introduced. It is therefore likely that the platinum has catalysed the surface exchange reaction thus increasing the magnitude of the surface exchange reaction. The effect of platinum in contact with a sample surface is shown by figure 11.11. In this figure two diffusion profiles are shown. The dashed line is an ^{18}O diffusion profile obtained for a polished, bare sample of $Ce_{0.9}Gd_{0.1}O_{1.95}$ at 486°C. The solid line is an ^{18}O diffusion profile at 493°C obtained for a sample of $Ce_{0.9}Gd_{0.1}O_{1.95}$ which had a fine dispersion of platinum particles deposited on the surface. The surface of the CGO was not completely covered so the resultant exchange behaviour was not merely the result of the surface exchange rate of platinum, but shows the catalytic effect platinum particles have on CGO. As can be seen, the ^{18}O surface concentration has been increased by a factor of six by the platinum. It is therefore believed that tracer diffusion and exchange measurements made on samples in contact with platinum are not measuring the true value of the oxygen exchange coefficient but in fact are determining a measure of the catalytic activity of platinum on the given material.

The difference in activation energy is also believed to be due to the presence of platinum. In the high temperature regime the supply of electrons is the rate limiting step of the reaction. Therefore, the activation energy is half the electronic band gap (i.e. 250-300kJ/mol). However, if the material has a partial covering of platinum particles, electrons can be readily supplied by the platinum. Platinum has a very large electronic conductivity and so it is very unlikely that the supply of electrons will still be rate limiting. Thus, as at low temperatures for bare fluorite surfaces, the supply of oxygen vacancies may become rate limiting even at these high temperatures.

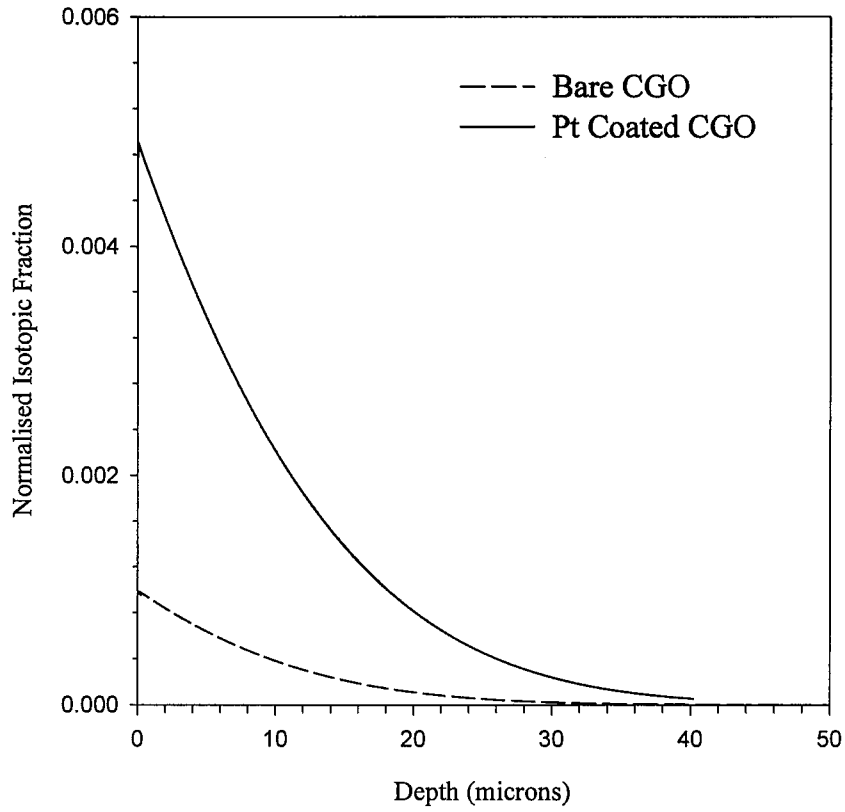


Figure 11.11. Effect on the ^{18}O surface concentration by coating CGO with platinum particles. (Bare CGO annealed at 486°C for 2730 seconds, Pt coated CGO annealed at 493°C for 2892 seconds).

The activation energies calculated for CSZ (88kJ/mol) and 3YTZ (91kJ/mol) at high temperatures are more similar to those found in the low temperature regime by Manning *et al* [2] on single crystal YSZ (70kJ/mol) and in this study on polycrystalline YSZ (65kJ/mol). The activation energy for the tracer diffusion coefficient of CSZ is 118kJ/mol and for 3YTZ is 125kJ/mol. Thus, $\Delta H_{EX} \approx \frac{2}{3} \Delta H_{Diff}$ for these two materials. This is also a similar relation to the activation energy calculated for tracer diffusion at low temperatures in this study.

The data of Kim *et al* [9] and Simpson and Carter [8] appears to add confidence to the many of the hypotheses given above. First, that at low temperatures, the oxygen exchange rate of bare fluorite surfaces is substantially affected by the presence of surface impurities. Secondly, at high temperatures, the oxygen exchange rate of bare fluorite surfaces is limited by the supply of electrons and

thirdly, at low temperatures the oxygen surface exchange rate is limited by the supply of oxygen vacancies.

It is interesting to note the effect that particles of the potential electrode material, LSCF, has on the ^{18}O surface concentration. Figure 11.12 shows a comparison of CGO coated with LSCF particles with the CGO coated with platinum. The samples were annealed at the same temperature and time.

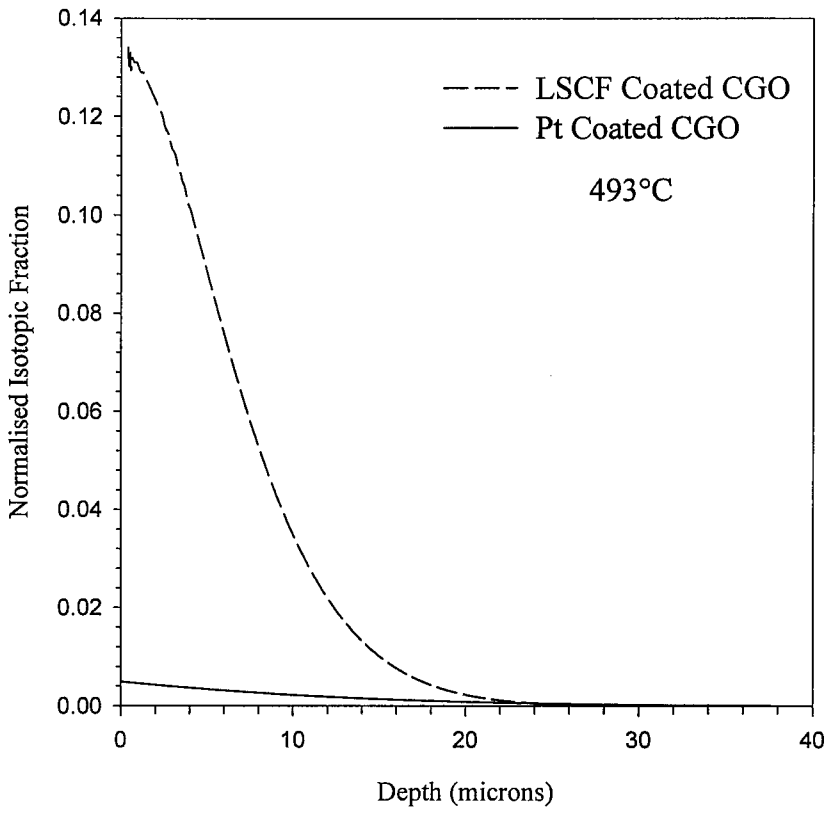


Figure 11.12. Comparison of the ^{18}O surface concentration of CGO covered with LSCF particles and platinum particles.

It is immediately obvious that the LSCF has a much more marked effect on the surface concentration than the platinum. This suggests that LSCF catalyses the oxygen exchange reaction better than platinum and this may be, in part, the reason why LSCF is a better electrode than platinum on CGO. However, the percentage of surface coverage of the two coatings has not be compared and so the extent of the increase may be misleading.

11.9. Atomistic Mechanism of Oxygen Surface Exchange.

Using the data and information given above and the information provided in Chapter 6 the following mechanism for surface exchange for fluorite materials is proposed. It is emphasised that this hypothesis is not intended to be a unique description of the surface exchange mechanism, nor that it is appropriate for all materials in all environments.

11.9.1. Suggested Mechanism for Surface Exchange on Fluorites at High Temperatures.

The gas phase analysis on fine powdered YSZ at 900°C given in figure 6.16 showed no formation of the $^{34}O_2$ cross molecule. This means that molecular exchange occurs. In the high temperature regime of these fluorite materials the activation energy for surface exchange suggests that the rate determining step is the supply of electrons. It is therefore believed that oxygen molecules are readily adsorbed onto the surface of the fluorite. Two oxygen ions from the surface of the crystal can combine to form an oxygen molecule, leaving four electrons to fully ionise the adsorbed molecule. As soon as electrons are provided the adsorbed molecule can be incorporated into the bulk. Figure 11.13 shows a possible schematic representation of this procedure. Figure 11.13 (a) shows the adsorption of an oxygen molecule (equation 11.5). Figure 11.13 (b) shows the rotation of an oxygen ion to an equivalent site, effectively forming a surface oxygen vacancy. It is possible to envisage the new oxygen site as a surface interstitial. This is essentially surface anti-Frenkel disorder (equation 11.6). Figure 11.13 (c) shows the combination of the oxygen surface interstitial and a second oxygen surface ion to form an oxygen molecule leaving four electrons and another oxygen vacancy (equation 11.7). This step which is a high electron transfer process is believed to rate determining. The electrons are likely to be loosely bound to the surface oxygen vacancies. The surface mobility of the electrons is higher than the bulk mobility thus the electrons will move to the adsorbed oxygen molecule where they will combine to form a charged adsorbed species which will then dissociate to form two oxygen adatoms (figure 11.13 (d)). These oxygen adatoms can then move into the bulk of the lattice via the oxygen vacancies, shown by figure 11.13 (e). Thus molecular exchange occurs.

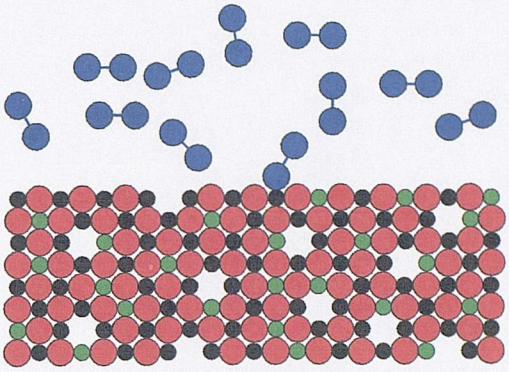


Figure 11.13 (a)

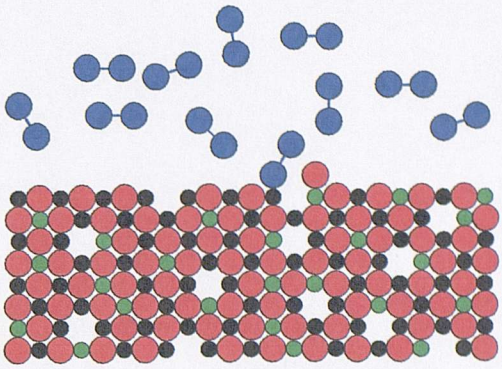


Figure 11.13 (b)

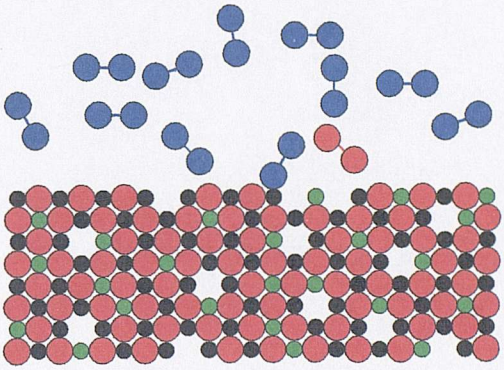


Figure 11.13 (c)

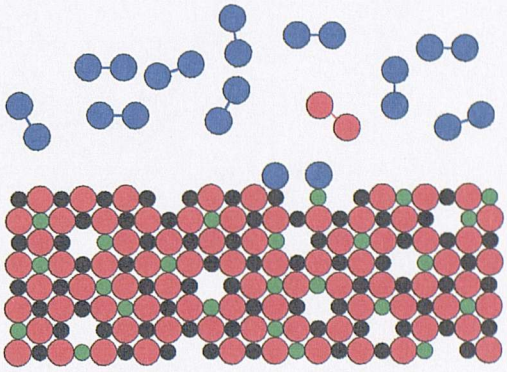


Figure 11.13 (d)

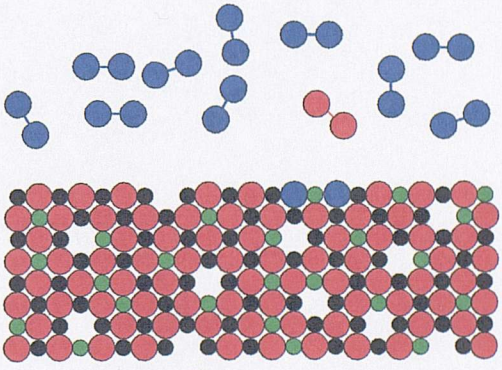


Figure 11.13 (e)

Figure 11.13. Schematic illustration of the proposed mechanism for oxygen exchange on fluorite surfaces at high temperatures.

$$O_{2,gas} \rightarrow O_{2,ad} \qquad \text{eqn. (11.5)}$$

$$^{s}O_{O}^{x} \rightarrow {}^{s}O_{i}^{''} + {}^{s}V_{O}^{\bullet\bullet} \qquad \text{eqn. (11.6)}$$

$$^{s}O_{O}^{x} + {}^{s}O_{i}^{''} \rightarrow O_{2,gas} + {}^{s}V_{O}^{\bullet\bullet} + 4e' \; * \qquad \text{eqn. (11.7)}$$

$$O_{2,ad} + 4e' \rightarrow 2O_{ad}^{''} \qquad \text{eqn. (11.8)}$$

$$2O_{ad}^{''} + 2{}^{s}V_{O}^{\bullet\bullet} \rightarrow 2{}^{s}O_{O}^{x} \qquad \text{eqn. (11.9)}$$

* This equation is believed to represent the rate limiting step of the oxygen exchange reaction. (The superscript "s" represents a surface site.)

The above set of equations shows the complete exchange reaction, not just the forward reaction. Thus the total number of moieties on the reactant sides equals the number on the product side. No specific site for adsorption has been given although clearly surface oxygen vacancies are involved in the exchange mechanism.

In order to help verify that the supply of electrons is the rate determining step at high temperatures, exchange measurements should be made at a constant (high) temperature as a function of oxygen partial pressure. The fluorite materials are in the ionic domain down to low pO_2 and so a variation of several orders of magnitude from $pO_2 = 1$ to $pO_2 = 1 \times 10^{-3}$ atmospheres could be achieved without changing the oxygen stoichiometry. However, the concentration of electrons will vary with $pO_2^{-1/4}$. (See Chapter 3, equation 3.41 and figure 3.8.) Thus, if the surface exchange coefficient is proportional to the concentration of electrons then $k \propto pO_2^{-1/4}$.

11.9.2. Suggested Mechanism for Surface Exchange on Fluorites at Low Temperatures.

The gas phase analysis on fine powdered YSZ at 450°C given in figure 6.16 shows the substantial formation of the $^{34}O_2$ cross molecule. This means that atomic exchange occurs. The relationship between the activation energy for

surface exchange and for tracer diffusion in these materials indicates that the supply of oxygen vacancies is rate determining.

It is thus believed that after oxygen gas molecules are adsorbed on the fluorite surface they must find surface oxygen vacancies at which to sit. The adsorption of the oxygen molecule is represented by equation 11.10 and figure 11.14 (a).

$$O_{2,gas} \rightarrow O_{2,ad} \qquad \text{eqn. (11.10)}$$

A surface vacancy will then diffuse to the oxygen molecule. The diffusion of a surface vacancy is shown in figure 11.14 (b). It is believed that the diffusion of the surface vacancy to the adsorbed molecule is the rate limiting step. At these low temperatures where the mobility of electrons and oxygen vacancies are low, it is believed that electrons (probably provided by surface impurities) will be trapped at surface vacancies making the oxygen vacancy a neutral moiety. This is represented by equation 11.11.

$$V_O^{\bullet\bullet} + 2e' \rightarrow V_O^{\times} \qquad \text{eqn. (11.11)}$$

The oxygen molecule will then sit in the vacant site. This is represented by equation 11.12 and figure 11.14 (c).

$$O_{2,gas} + {}^{s}V_O^{\times} \rightarrow \left({}^{s}O_O^{\times} - O\right)_{ad} \qquad \text{eqn. (11.12)}$$

The term $\left({}^{s}O_O^{\times} - O\right)_{ad}$ in equation 11.12 represents an adsorbed oxygen molecule sitting in an oxygen vacancy and is shown by the cyan coloured molecule in figure 11.14 (c).

The molecule is then dissociated leaving a neutral adsorbed oxygen and a normal, filled oxygen surface site. This process is represented by equation 11.13.

$$\left({}^{s}O_O^{\times} - O\right)_{ad} \rightarrow O_O^{\times} + O_{ad} \qquad \text{eqn. (11.13)}$$

Equation 11.13 is represented by the breaking of the molecular bond in figure 11.14 (d).

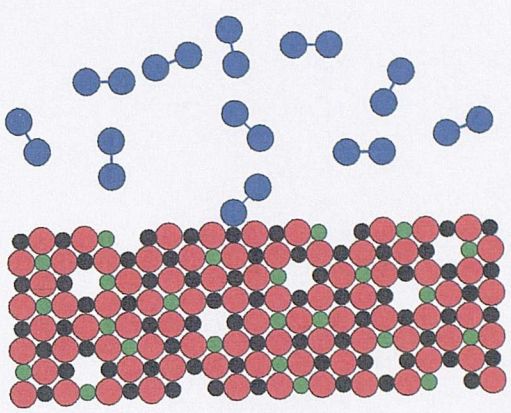


Figure 11.14 (a)

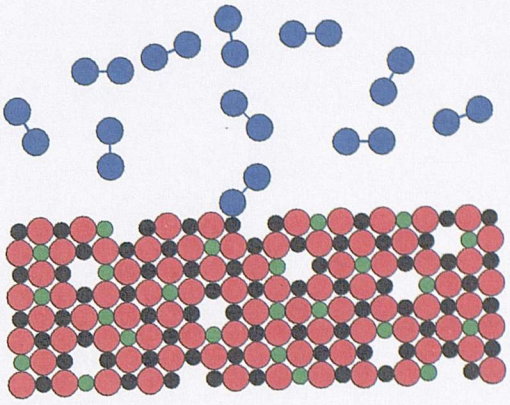


Figure 11.14 (b)

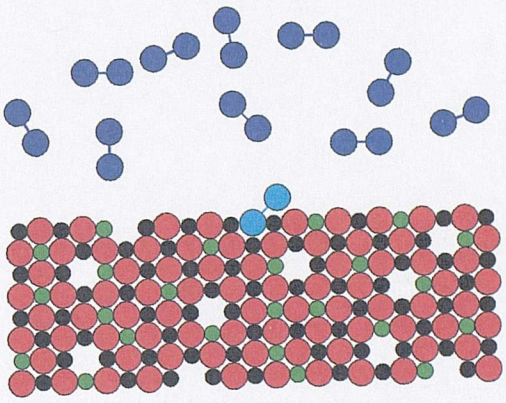


Figure 11.14 (c)

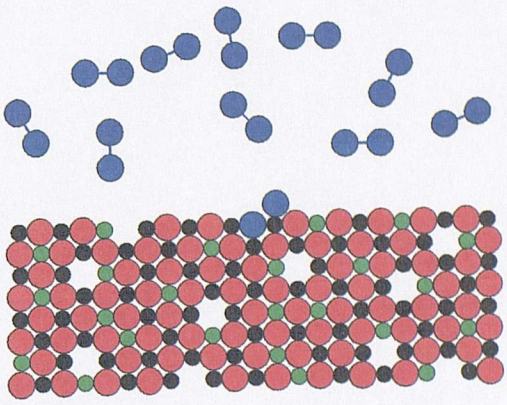


Figure 11.14 (d)

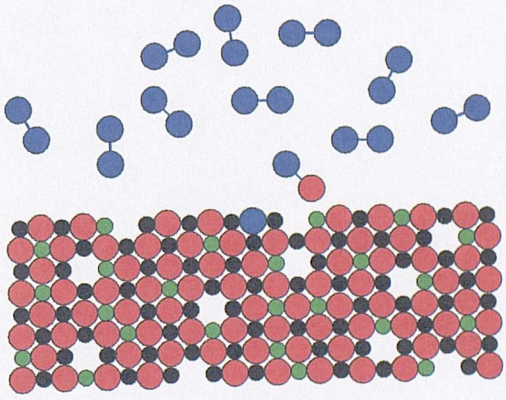


Figure 11.14 (e)

Figure 11.14. Schematic illustration of the proposed mechanism for oxygen exchange on fluorite surfaces at low temperatures.

The adsorbed oxygen can then readily combine with a surface oxygen ion to leave a surface oxygen vacancy and two strongly bound electrons, making the vacancy a neutral moiety. This is represented by equation 11.14 and by figure 11.14 (e).

$$O_{ad} + O_O^{\times} \rightarrow O_{2,gas} + V_O^{\times} \qquad \text{eqn.(11.14)}$$

Thus cross molecules are formed and the reaction is limited by the diffusion of surface oxygen vacancies.

It is important to emphasis that the schematic illustrations given in figures 11.13 and 11.14, and those presented earlier in Chapter 6, represent a static image of the oxygen exchange process. It is recognised that the surface exchange process is dynamic and the actual rate of collisions of gaseous oxygen molecules with the oxide surface is far greater than the number of exchanges. Furthermore, surface vacancies and adsorbed oxygen species are expected to be very mobile such that when a vacancy is formed at one location, it does necessarily remain there for an adsorbed oxygen ion to move into. However, visualisation of a dynamic surface is very difficult and figures 11.13 and 11.14 offer a more recognisable image of the exchange process. The figures also only show one adsorbed oxygen molecule to enable a clearer representation of the exchange process, although it noted that an adsorbed layer of oxygen will cover most of the surface at low temperatures.

Boukamp *et al* [10] have offered an alternative explanation to the formation of ^{34}O or ^{32}O molecules based on the dynamics of the process. They suggest that the relative rates of the dissociation of an adsorbed oxygen $\left(O_{2,ad} \rightarrow 2O_{ad}\right)$ and the incorporation of the adsorbed oxygen into the bulk $\left(O_{ad} \rightarrow O_O^{\times}\right)$ determine which molecular species is formed. If the adsorbed oxygen dissociates rapidly and is able then to move across the oxide surface for a substantial time before being incorporated into the bulk then ^{34}O cross molecules are likely to be formed. However, if the dissociation of oxygen is difficult, but once dissociated are rapidly incorporated into the bulk, then ^{32}O molecules are likely to be created. This does not contradict the processes described above but is merely an alternative method of explaining the results.

11.10. References.

[1] J.D. Sirman and J.A. Kilner, in Proceedings of the 17th Risø International Symposium on Materials Science, Eds. F.W. Poulsen, N. Bonanos, S. Linderoth, M. Mogensen and B. Zachau-Christiansen, Denmark (1996) p417.

[2] P.S. Manning, J.D. Sirman and J.A. Kilner, Solid State Ionics, **Vol 93** (1997) p125.

[3] J.A. Kilner, in Proc. of the 2nd Int. Symp. On Ionic and Mixed Conducting Ceramics, Eds. T.A. Ramanarayanan, W.L. Worrel and H.L. Tuller, The Electrochemical Society, Inc., Pennington, NJ, **PV 94-12**, (1994) p174.

[4] A.E. Hughes, J. Am. Ceram. Soc. **Vol 78** (1995) p369.

[5] J.A. Kilner, R. A. de Souza and I.C. Fullarton, Solid State Ionics, **Vol 86-88** (1996) p703.

[6] J.M. Ralph, Ph.D. Thesis, University of London (1998).

[7] K. Ando, Y. Oishi, and Y. Hidaka, J. Chem. Phys., **Vol 65** (1976) p2751.

[8] L. A. Simpson, and R. E. Carter., J. Am. Ceram. Soc., **Vol 49** (1966) p139.

[9] B. K. Kim, S. J. Park, and H. Hamaguchi., J. Am. Ceram. Soc., **Vol 76** (1993) p2119.

[10] B.A. Boukamp, B.A. van Hassel, I.C. Vinke, K.J. de Vries and A.J. Burggraaf, Electrochim. Acta, **Vol 38** (1993) p1817.

12. Conclusions and Future Work.

The oxygen diffusion and surface exchange coefficients of materials with the fluorite crystal structure have been made using $^{16}O/^{18}O$ isotope exchange followed by SIMS. The ionic conductivity of a selection of fluorite materials and the electrode polarisation resistance of LSCF have been determined using AC impedance spectroscopy. The data from the two measurement techniques have also been compared. In this chapter, the results contained in Chapters 8 to 11 are reviewed and suggestions for future work are made.

In Chapter 8 the polarisation resistance of symmetrical LSCF electrodes on a CGO electrolyte was measured using AC impedance spectroscopy. The microstructure of the electrodes was examined using optical and atomic force microscopy. These results were then compared to results calculated from oxygen tracer diffusion and exchange coefficients for LSCF from SIMS using a model for the electrode reaction. The model states that for mixed ionic electronic conductors with fast oxygen ion diffusion, the electrode resistance is determined by a combined diffusion and exchange reaction occurring over a large volume of the electrode. This is different to materials with poor oxygen ion conductivity, such as lanthanum strontium manganite, where the reaction occurs primarily at the gas/electrode/electrolyte triple phase boundary. The experimental and calculated results were very similar, suggesting that the model provides an accurate description of the electrode behaviour.

The conductivity data in Chapter 9 was used to determine the migration enthalpy of oxygen vacancies and the binding enthalpy of defect associates in highly doped fluorite materials. It was also used to allow a comparison of the tracer diffusion data presented in Chapter 10. The binding enthalpy provided a major contribution to the overall activation energy in all these highly doped materials. The binding enthalpy of $Ce_{0.69}Gd_{0.31}O_{1.845}$ was considerably larger than for $Ce_{0.9}Gd_{0.1}O_{1.95}$, suggesting that at high dopant concentrations the binary associate model is not an accurate description of the defect structure of these materials. To allow a better determination of the migration and binding enthalpy, a larger temperature range should be used. Thus measurements on bars of materials rather than pellets should be employed to increase the resistance of the sample.

Tracer diffusion coefficients of single crystal $Ce_{0.69}Gd_{0.31}O_{1.845}$ and polycrystalline $Ce_{0.9}Gd_{0.1}O_{1.95}$, $Ce_{0.8}Gd_{0.2}O_{1.9}$, $Ce_{0.8}Gd_{0.18}Pr_{0.02}O_{2-x}$ and $Zr_{0.85}Y_{0.15}O_{1.925}$ were

presented in Chapter 10. This represents the most comprehensive set of diffusion results on the fluorite materials to date. The activation energy for tracer diffusion was similar to that found for conductivity in the same materials, given in Chapter 9. Again, the highly doped $Ce_{0.69}Gd_{0.31}O_{1.845}$ sample showed the highest activation energy. This is believed to be due to the presence of complex defect associates or microdomains of ordered seconds phases at such a high defect concentration. Similar trends in the activation energy were seen in the zirconia based materials. The tracer diffusion coefficients were compared with the AC conductivity diffusion coefficients for single crystal $Ce_{0.69}Gd_{0.31}O_{1.845}$ and polycrystalline $Ce_{0.9}Gd_{0.1}O_{1.95}$ and $Zr_{0.85}Y_{0.15}O_{1.925}$. In all cases, the AC conductivity diffusion coefficient was significantly higher than the tracer diffusion coefficient. Computer simulations predict a Haven ratio of 0.65 for simple cubic systems with a vacancy diffusion mechanism. However, the Haven ratio was calculated to be between 0.14 and 0.20, with no obvious variation with composition. Several explanations were postulated to account for the low value of the Haven ratio. The first was that the charged defect associates reorientate in an AC field, thus contributing to the AC conductivity but not to the long range diffusion process. The second was the presence of ordered phases in the crystal lattice which will affect the Haven ratio. Finally, the presence of grain boundaries in the polycrystalline materials was shown to add another uncertainty in the calculation of the Haven ratio.

In order to produce the most accurate values of the Haven ratio, experiments in future should be carried out using DC electrical conductivity measurements on single crystal materials, over the same temperature range as the tracer diffusion measurements. This removes the possibility of the reorientation of charged dipoles and the complication in interpretation of the results introduced by the presence of grain boundaries. Materials with a low dopant concentration should also be examined in order to determine the effect of defect associates on the Haven ratio.

In Chapter 11, the oxygen surface exchange coefficient of various CGO and YSZ materials was presented. A strong correlation between the surface exchange coefficient and the tracer diffusion coefficient for all the materials was seen. This indicates that the mechanism for both surface exchange and oxygen diffusion is the same for all these fluorite materials. There are two temperature regimes with different activation energies for the surface exchange coefficient evident for all compositions. At high temperatures the activation energy is approximately half the electronic band gap, while at low temperatures there is a strong correlation

between the activation energy for surface exchange and for tracer diffusion. Therefore, it was suggested that the supply of electrons is the rate limiting step for surface exchange at high temperatures and the supply of oxygen vacancies is the rate limiting step at low temperatures.

Further exchange measurements on these and other materials of similar composition should be carried in order to verify the correlation between the surface exchange coefficient and tracer diffusion coefficient. In particular, measurements around 600-800°C where the transition in the activation energy of the surface exchange coefficient occurs should be undertaken. There is still insufficient data to draw any categorical conclusions as to the reason for this change. The dependence of oxygen partial pressure on the surface exchange coefficient should also be measured to verify the hypothesis of the rate limiting step in the two temperature regimes. By reducing the pO_2, the concentration of electrons increases while the concentration of oxygen vacancies remains constant. Thus, if the supply of oxygen vacancies is rate limiting then changing the pO_2 should not affect the surface exchange coefficient, whereas if the supply of electrons is rate limiting then reducing the pO_2 should increase the surface exchange coefficient.

List of Publications.

Enhancement of the Surface Exchange Coefficient of Gadolinia Doped Ceria.
J.D. Sirman and J.A. Kilner, in Proc. of the 17th Risø International Symposium on Materials Science, Eds. F.W. Poulsen, N. Bonanos, S. Linderoth, M. Mogensen and B. Zachau-Christiansen, Denmark (1996) p471.

Surface Exchange Properties of $Ce_{0.9}Gd_{0.1}O_{2-x}$ Coated with $La_{1-x}Sr_xFe_{1-y}Co_yO_{3-\delta}$.
J.D. Sirman and J.A. Kilner, J. Electrochem. Soc. **Vol 143** (1996) L229.

Oxygen Self-Diffusion and Surface Exchange Studies of Oxide Electrolytes Having the Fluorite Structure.
P.S. Manning, J.D. Sirman and J.A. Kilner, Solid State Ionics **Vol 93** (1997) p125.

Manganese Diffusion into Single Crystal and Polycrystalline Yttria Stabilised Zirconia.
D. Waller, J.D. Sirman and J.A. Kilner, in Proc. of the 5th International Symposium on SOFC, Eds. U. Stimming, S. Singhal, H. Tagawa and W. Lehnert, The Electrochemical Society, Inc., **PV 97-40**, Aachen, (1997) p1140.

Cation Diffusion into a CGO Electrolyte.
J.D. Sirman, D. Waller and J.A. Kilner, in Proc. of the 5th International Symposium on SOFC, Eds. U. Stimming, S. Singhal, H. Tagawa and W. Lehnert, The Electrochemical Society, Inc., **PV 97-40**, Aachen, (1997) p1140.

The Kinetics of Oxygen Transport in 9.5 mol% Single Crystal Yttria Stabilised Zirconia.
P.S. Manning, J.D. Sirman and J.A. Kilner, Solid State Ionics **Vol 100** (1997) p1.

Comparison of Dense and Porous Perovskite Cathodes for Solid Oxide Fuel Cells and Ceramic Oxygen Generators.
J.D. Sirman, J.A. Lane and J.A. Kilner, in Proc. of the 3rd Int. Symp. On Ionic and Mixed Conducting Ceramics, Eds. T.A. Ramanarayanan, W.L. Worrel, H.L. Tuller, M. Mogensen and A.C. Khandkar, The Electrochemical Society, Inc., Pennington, NJ, **PV 97-24**, Paris (1997).

Oxygen Exchange and Diffusion in Materials with the Fluorite Structure.
J.A. Kilner, J.D. Sirman and P.S. Manning, in Proc. of the 3rd Int. Symp. On Ionic and Mixed Conducting Ceramics, Eds. T.A. Ramanarayanan, W.L. Worrel, H.L. Tuller, M. Mogensen and A.C. Khandkar, The Electrochemical Society, Inc., Pennington, NJ, **PV 97-24**, Paris (1997).

Oxygen Ion Diffusivity, Surface Exchange and Ionic Conductivity in Single Crystal Gadolinia Doped Ceria.
E. Ruiz-Trejo, J.D. Sirman, Y.M. Baikov and J.A. Kilner, in Proc. of the 11th Conference on Solid State Ionics, Honolulu (1997).

A Raman Microscopic Study of Manganese Transport in Yttria Stabilised Zirconia (YSZ).
D. Waller, S. Webb, J.D. Sirman and J.A. Kilner, in Proc. of the 11th Conference on Solid State Ionics, Honolulu (1997).

Appendix A. Cation Diffusion in YSZ and CGO.

A.1. Introduction.

The work on cation diffusion was completed in conjunction with Dr. D. Waller, Department of Materials, Imperial College. The diffusion anneals used were described in Chapter 7.

The long term stability of SOFCs and COGs is dependent on the interaction between the electrodes and the electrolyte. Thus it is important to determine the solubility and diffusivity of the electrode cations in the electrolyte. This appendix is not supposed to provide an in depth study of cation diffusion, but simply presents some of the initial diffusion data obtained using SIMS for manganese, lanthanum and strontium diffusion in single and polycrystal YSZ and the diffusion of cobalt and iron in polycrystalline CGO.

The solution to the diffusion equation used was different depending on the type of oxide couple used and the resultant shape of the diffusion profile. For the short diffusion lengths the solution to the diffusion equation used is given by equation A.1 [1].

$$C(x,t) = \frac{C_O}{2}\,\mathrm{erfc}\left[\frac{x}{2\sqrt{Dt}}\right] \qquad \text{eqn. (A.1)}$$

This solution is appropriate for a semi-infinite source of initial concentration C_O, in contact with a semi-infinite volume of zero initial concentration. For longer diffusion lengths it was often more appropriate to use the solution for a finite, thin film source containing an initial amount of solute M (mol/cm^2) as significant depletion of the source was apparent. This solution is given by equation A.2 [1].

$$C(x,t) = \frac{M}{2\sqrt{\pi Dt}}\exp\left[-\frac{x^2}{4Dt}\right] \qquad \text{eqn. (A.2)}$$

However, even though visual inspection of the diffusion profile showed one solution to fit much better than the other, the magnitude of the diffusion

coefficient calculated from a non-linear least squares regression was very similar irrespective of whichever solution was used.

In the following discussion the term "diffusion coefficient" is used to describe all the values of D calculated from equations A.1 or A.2. This term is an apparent diffusion coefficient and no attempt has been made to separate grain boundary terms or the fact that many of the transition metal oxides exist in a different oxidation or spin state (depending on their concentration in the fluorite) which will affect their ionic radii and thus the diffusivity.

A.2. Manganese Diffusion in Single Crystal YSZ.

A list of the diffusion temperatures and times used for manganese diffusion into single crystal YSZ was given in table 7.4. A typical diffusion profile is shown in figure A.1.

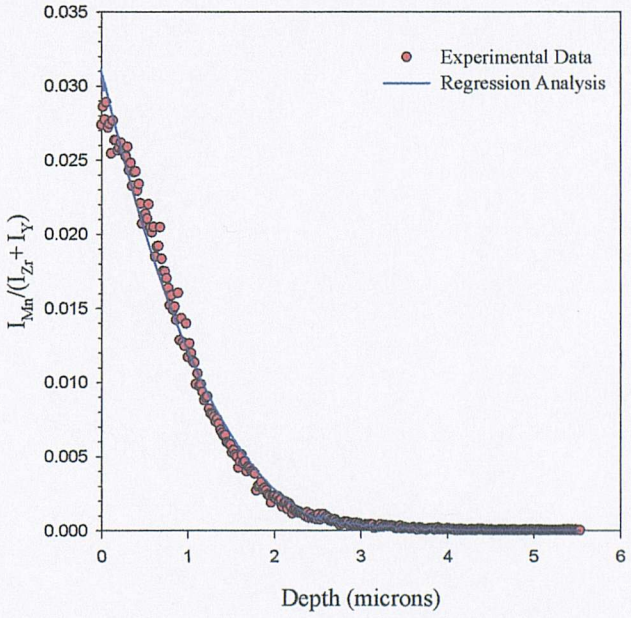


Figure A.1. Diffusion profile of manganese into single crystal YSZ at 1300°C.

I_x represents the secondary ion intensity of cation x. For this material the solution to the diffusion equation for a semi-infinite source provided a more accurate description of the diffusion profile than the finite, thin film source. The values of diffusion coefficient calculated from the regression analyses are given in table

A.1 and are plotted as a function of reciprocal temperature in figure A.2. Also shown on this graph is the data point obtained by Lau and Singhal [2] for manganese diffusion into single crystal YSZ at 1400°C, and the results of zirconium and yttrium tracer diffusion in single crystal YSZ obtained by Solmon [3].

Temperature (°C)	D (cm^2/s)
1250	7.8×10^{-16}
1250	4.8×10^{-16}
1300	4.9×10^{-15}
1350	7.7×10^{-15}
1400	2.6×10^{-14}

Table A.1. Values of the diffusion coefficient of Mn in single crystal YSZ from a Mn_2O_3 source.

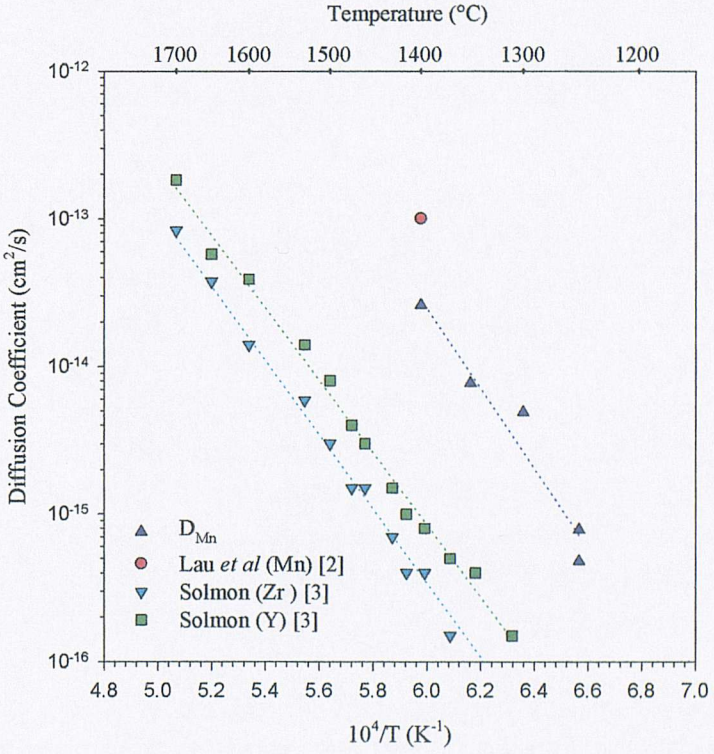


Figure A.2. Arrhenius graph of the diffusion coefficient of manganese into single crystal YSZ from a Mn_2O_3 source.

The linear regression of the data is described by equation A.3.

$$D = 4.7 \times 10^{2} \begin{matrix} +1.1 \times 10^{5} \\ 4.7 \times 10^{2} \end{matrix} \exp\left(-\frac{520 \pm 70 \text{kJ / mol}}{RT}\right) \qquad \text{eqn. (A.3)}$$

There is very little data in the literature available with which to compare these values. The only data on manganese diffusion in single crystal YSZ was that of Lau and Singhal [2]. Their value, obtained using electron probe micro analysis, is considerably higher than the values obtained in this study. The activation energy is similar to that obtained by Solmon [3] for zirconium and yttrium self-diffusion in YSZ (460kJ/mol) and the data of Kilo *et al* [4] for zirconium diffusion in calcia stabilised zirconia (~440kJ/mol), although the absolute magnitude is somewhat higher for the manganese diffusion. The similarity of the diffusion behaviour of manganese, yttrium and zirconium may not be surprising considering the ionic radii are not too dissimilar. In 8-fold co-ordination Mn^{2+} has a radii of 0.96Å, Y^{3+} a radii of 1.02Å and Zr^{4+} a radii of 0.84Å [5].

A.3. Manganese Diffusion in Polycrystalline YSZ.

A list of the diffusion temperatures and times used for manganese diffusion into single crystal YSZ was given in table 7.4. Both Mn_2O_3 and LSM sources were used. The diffusion profiles had a different shape depending on the temperature (and thus the diffusion length) of the anneals. At low temperatures (1100-1300°C) the solution assuming a semi-infinite source most accurately described the profile while at high temperatures (above 1400°C) the finite, thin film source described the diffusion profile better. This is not surprising considering the typical diffusion lengths. At temperatures below 1300°C the diffusion length was generally of the order of 0.5μm whereas at high temperatures the diffusion length was more typically 100-400μm. Therefore, significant depletion of the source is expected at high temperatures but not at the lower temperatures.

Two typical diffusion profiles for manganese diffusion from an Mn_2O_3 source into polycrystalline YSZ are shown in figures A.3 and A.4. In figure A.5 and A.6 typical diffusion profiles for manganese and lanthanum diffusion into polycrystalline YSZ are shown. Figure A.3 shows a diffusion profile at 1100°C together with the result of the regression analysis using equation A.1. Figure A.4

shows a diffusion profile at 1400°C and figures A.5 and A.6 at 1500°C, together with the result of the regression analysis using equation A.2.

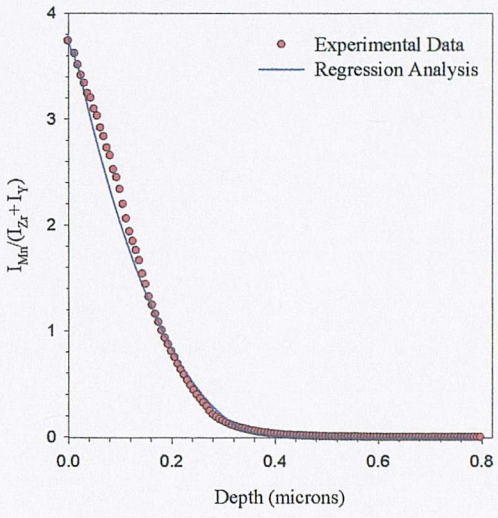


Figure A.3. Diffusion profile of manganese into YSZ at 1100°C from a Mn_2O_3 source.

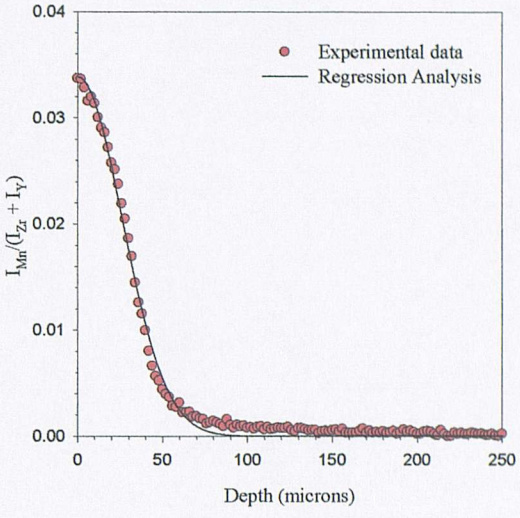


Figure A.4. Diffusion profile of manganese into YSZ at 1400°C from a Mn_2O_3 source.

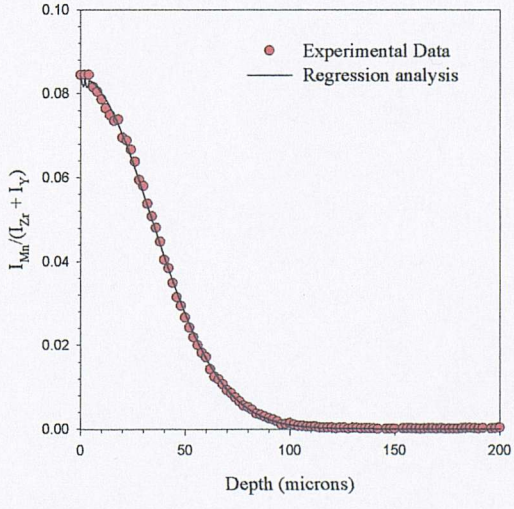


Figure A.5. Diffusion profile of manganese into YSZ from a LSM source at 1500°C.

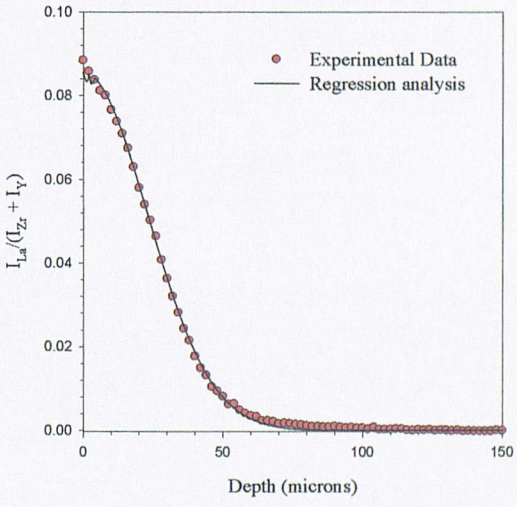


Figure A.6. Diffusion profile of lanthanum into YSZ from a LSM source at 1500°C

Table A.2 gives the values of the diffusion coefficient for manganese in YSZ from a Mn_2O_3 source and table A.3 gives the values of the diffusion coefficient for manganese, lanthanum and strontium in YSZ from a LSM source.

Depth profile analysis		Line-scanning analysis	
Temperature (°C)	D_{Mn} (cm^2/s)	Temperature (°C)	D_{Mn} (cm^2/s)
1100	4.7×10^{-16}	1400	5.3×10^{-12}
1100	4.7×10^{-16}	1400	6.4×10^{-12}
1100	6.8×10^{-16}	1420	2.5×10^{-11}
1150	3.7×10^{-15}	1420	2.2×10^{-11}
1200	3.4×10^{-14}	1500	1.1×10^{-9}
1250	2.8×10^{-13}	1500	1.0×10^{-9}
1250	2.5×10^{-13}	1500	1.1×10^{-9}
1250	4.3×10^{-13}		
1300	6.8×10^{-13}		

Table A.2. Values of the diffusion coefficient of
Mn into polycrystalline YSZ from a Mn_2O_3 source.

Temperature (°C)	D_{Mn} (cm^2/s)	D_{La} (cm^2/s)	D_{Sr} (cm^2/s)
1400	1.9×10^{-12}	1.3×10^{-12}	2.8×10^{-12}
1420	4.5×10^{-12}	2.2×10^{-12}	8.4×10^{-12}
1500	2.0×10^{-11}	9.7×10^{-12}	1.1×10^{-11}

Table A.3. Values of the diffusion coefficient of manganese,
lanthanum and strontium in polycrystalline YSZ from a LSM source.

Figure A.7 shows these diffusion coefficients as a function of reciprocal temperature. The data points of Lau and Singhal [2] and Waller *et al* [6] (using Raman spectroscopy) for manganese diffusion in polycrystalline YSZ from a Mn_2O_3 source at 1400°C are also shown for comparison.

The regression analysis of the diffusion data are described by equations A.4, A.5, A.6 and A.7 for manganese diffusion into YSZ from a Mn_2O_3 source and manganese, lanthanum and strontium diffusion in YSZ from a LSM source, respectively.

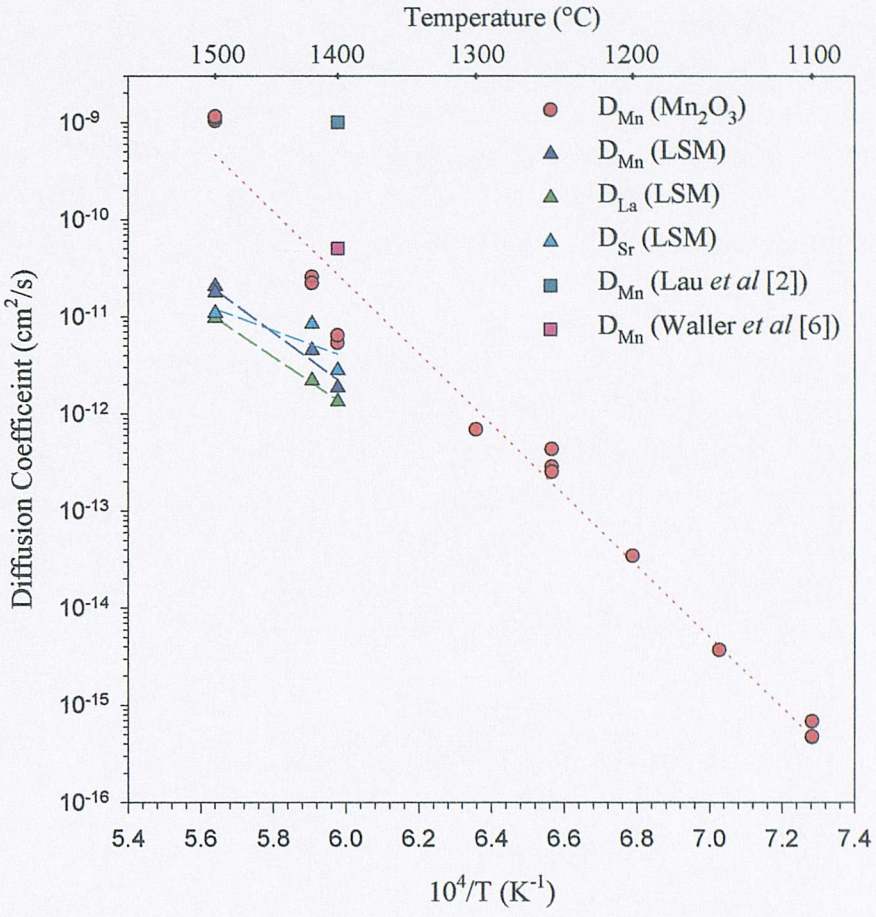


Figure A.7. Comparison of the diffusion coefficient of manganese, lanthanum and strontium into polycrystalline YSZ from a Mn_2O_3 and LSM source.

$$Mn_2O_3 \text{ source } D_{Mn} = 1.7 \times 10^{11}{}^{+1.2 \times 10^{12}}_{1.5 \times 10^{11}} \exp\left(-\frac{700 \pm 28 \text{kJ / mol}}{RT}\right) \qquad \text{eqn. (A.4)}$$

$$\text{LSM source} \quad D_{Mn} = 5.9 \times 10^{4}{}^{+1.6 \times 10^{6}}_{5.7 \times 10^{4}} \exp\left(-\frac{530 \pm 48 \text{kJ / mol}}{RT}\right) \qquad \text{eqn. (A.5)}$$

$$\text{LSM source} \quad D_{La} = 1.7 \times 10^{4}{}^{+6.4 \times 10^{4}}_{1.4 \times 10^{4}} \exp\left(-\frac{480 \pm 22 \text{kJ / mol}}{RT}\right) \qquad \text{eqn. (A.6)}$$

$$\text{LSM source} \quad D_{Sr} = 7.9 \times 10^{-4}{}^{+1.8 \times 10^{3}}_{7.9 \times 10^{-8}} \exp\left(-\frac{265 \pm 208 \text{kJ / mol}}{RT}\right) \qquad \text{eqn. (A.7)}$$

The diffusion coefficient of Lau and Singhal [2] is somewhat higher than the data in this work but the data of Waller *et al* [6] matches very closely. The activation energy for diffusion from the Mn_2O_3 source is higher than the activation energy from the LSM source. Oishi *et al* found the activation energy of zirconium and yttrium to be around 400kJ/mol [7] and Dimos and Kohlstedt [8] obtained a value of 560kJ/mol. This is lower than activation energy for diffusion from the Mn_2O_3 source but similar to the LSM source.

Figure A.8 shows a comparison of the single crystal data with the polycrystalline data from the Mn_2O_3 source. It is immediately clear that the polycrystalline samples exhibit a far greater rate of manganese diffusion than the single crystals. This strongly suggests that in polycrystalline YSZ the predominant path for manganese transport is down the grain boundaries. Using Raman spectroscopy, Waller *et al* [6] also demonstrated that the grain boundaries were the predominant path for manganese diffusion in polycrystalline YSZ.

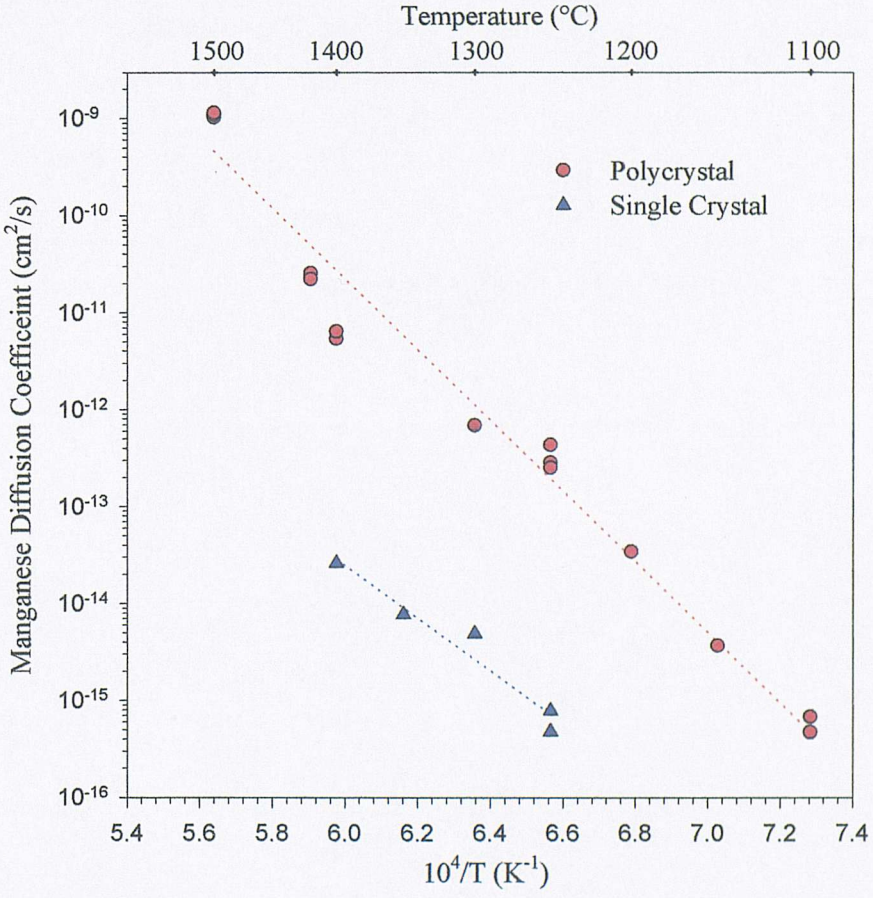


Figure A.8. Comparison of the diffusion coefficients of manganese in single crystal and polycrystalline YSZ from a Mn_2O_3 source.

A.4. Cobalt and Iron Diffusion in Polycrystalline CGO.

There has been no work published in the literature on cobalt and iron (constituents of the LSCF electrodes used in intermediate temperature SOFC and COG) into CGO. The following data are the results of initial experiments on the solubility and diffusion of iron and cobalt in CGO. The data set is limited but should provide a basis for future work on this system.

The solubility of cobalt and iron was determined by preparing solid solutions of cobalt/CGO and iron/CGO of known composition. X-ray powder diffraction patterns of the solid solutions were taken on a Phillips 1710 diffractometer in the region of $2\theta = 80 - 140^{\circ}$. Figure A.9 shows the diffraction peak for the (533) plane for iron/CGO solid solutions of various composition. Both the K-α_1 and the K-α_2 peaks are evident. Also shown is the peak corresponding to the silicon standard. There is clearly a shift in the peak position to higher angles with increasing iron content. This shows that the lattice parameter is decreasing in size as iron is added. There is almost no difference between the peak positions at 6.9% iron and 10% iron indicating there is little difference in the lattice parameter between these two compositions. The true lattice parameter of the solid solutions was calculated at $\cos^2\theta = 0$ by linear regression of the lattice parameter versus $\cos^2\theta$. The lattice parameter of iron/CGO is plotted as a function of iron concentration in figure A.10 (a) and the lattice parameter of cobalt/CGO as a function cobalt concentration in figure A.10 (b).

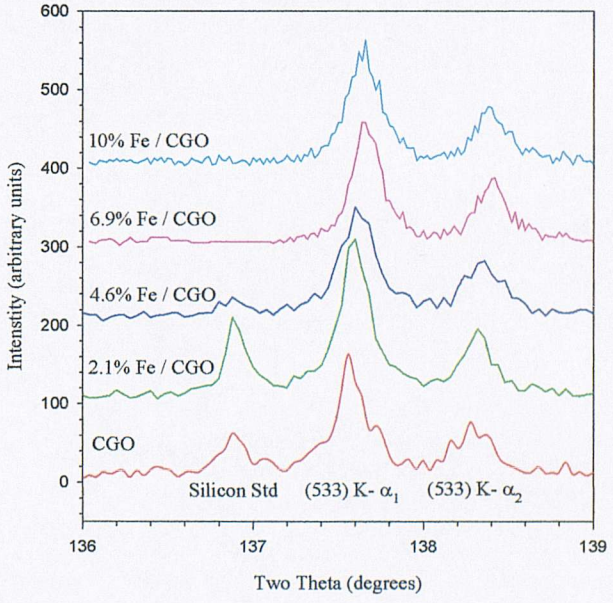


Figure A.9. X-ray diffraction patterns of iron/CGO solid solutions.

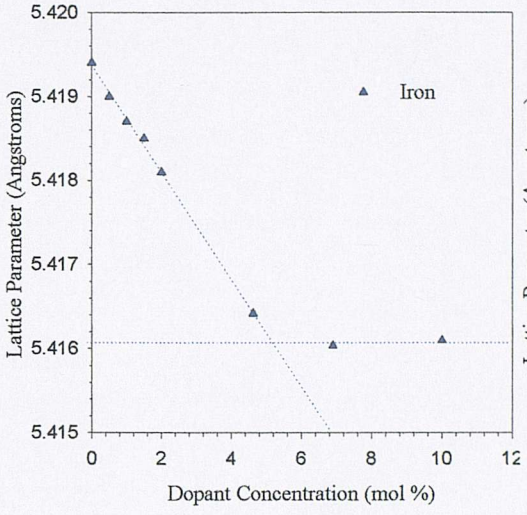


Figure A.10 (a). Fe/CGO

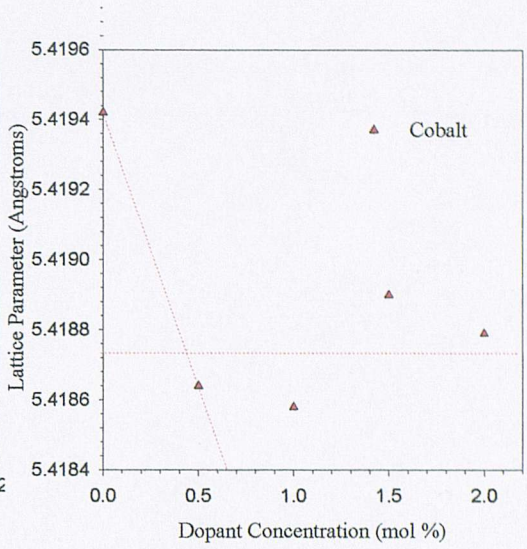


Figure A.10 (b). Co/GCO

Figure A.10. Lattice parameter of iron/CGO and cobalt/CGO as a function of dopant concentration.

In figure A.10 (a) there is a linear decrease in the lattice parameter of the solid solution with increasing iron content upto 4.7mol%, thus obeying Vegard's law. At 6.9mol% iron there is a deviation from the linear decrease in lattice parameter. Therefore, the solubility limit of iron in CGO has been reached. The lattice parameter at 10mol% iron also shows no further decrease. By extrapolation, the iron content in the 6.9mol% sample is 5.2mol%. Thus the solubility limit of iron in CGO is around 5mol%. For the cobalt/CGO solid solutions shown in figure A.10 (b) no decrease in the lattice parameter is seen above 0.5mol% cobalt. Thus the solubility limit of cobalt in CGO is less than 0.5mol%.

The solubility of iron in CGO is comparable to that of manganese in YSZ, but the solubility of cobalt is very low. This is good for the long term operation of SOFC but makes SIMS analysis of the diffusion of cobalt in CGO difficult due to the low concentrations seen.

The values of the diffusion coefficients of iron and cobalt in CGO are given in table A.4 and plotted as a function of reciprocal temperature in figure A.11. In figure A.11, the diffusion coefficients of manganese in polycrystalline YSZ from a Mn_2O_3 source are also shown.

Temperature (°C)	D_{Fe} (cm^2/s)	D_{Co} (cm^2/s)
1250	8.7×10^{-15}	8.0×10^{-15}
1250	4.2×10^{-15}	
1300		1.6×10^{-14}
1325		1.4×10^{-13}
1350	2.4×10^{-13}	7.9×10^{-13}
1350		1.4×10^{-13}
1375		4.0×10^{-13}
1425	1.4×10^{-12}	1.7×10^{-12}
1425	2.0×10^{-13}	2.2×10^{-13}
1450	7.4×10^{-12}	1.5×10^{-11}

Table A.4. Values of the diffusion coefficient of Co and Fe in polycrystalline CGO.

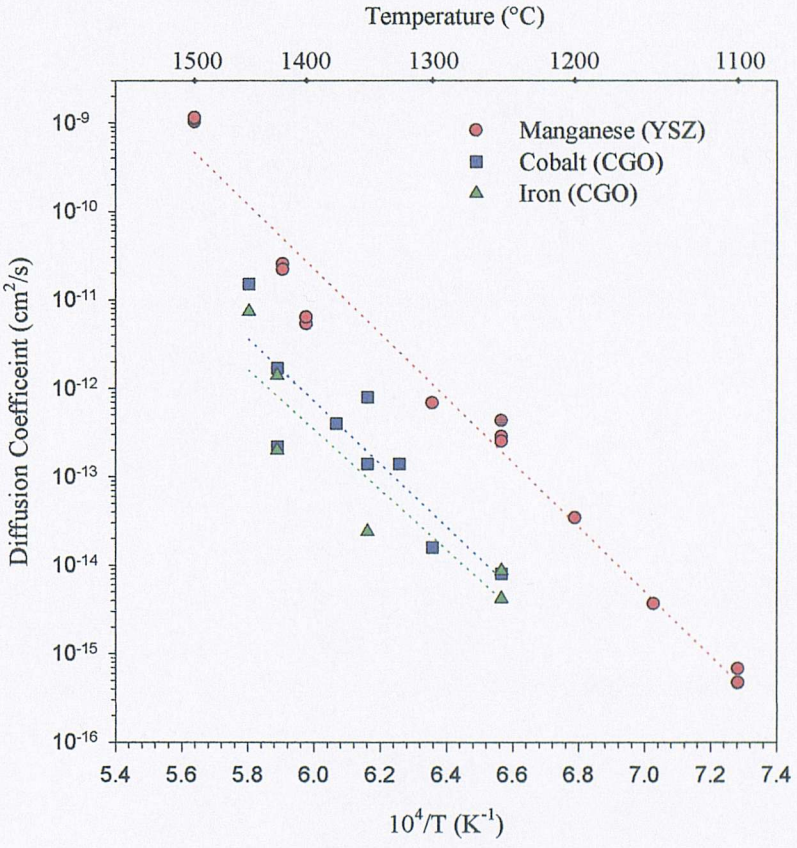


Figure A.11. Arrhenius graph of the diffusion coefficient of iron and cobalt into polycrystalline CGO.

The linear regression of the diffusion data for iron and cobalt are described by equations A.8 and A.9, respectively.

$$D_{Fe} = 8.3 \times 10^{7}{}^{+3.3 \times 10^{12}}_{8.3 \times 10^{7}} \exp\left(-\frac{650 \pm 140 kJ/mol}{RT}\right) \qquad \text{eqn. (A.8)}$$

$$D_{Co} = 1.5 \times 10^{9}{}^{+4.3 \times 10^{13}}_{1.5 \times 10^{9}} \exp\left(-\frac{680 \pm 140 kJ/mol}{RT}\right) \qquad \text{eqn. (A.9)}$$

The values for diffusion of iron and cobalt in CGO are very similar and they have similar activation energies. Within the uncertainty limits, the activation energies calculated for iron and cobalt diffusion in CGO are the same as that calculated for manganese in YSZ in a similar temperature regime. The magnitude of the diffusion coefficients of iron and cobalt are between one and two orders of magnitude lower than manganese diffusion in polycrystalline YSZ at these temperatures.

It would thus appear that in general the LSCF/CGO electrode/electrolyte couple shows better compatibility than the LSM/YSZ couple. The solubility of iron and particularly cobalt in CGO is less than manganese in YSZ. The diffusion rate of iron and cobalt into CGO is slower than manganese into YSZ and X-ray diffractometry showed no evidence of either strontium or lanthanum cerate phases forming when LSCF and CGO powders were heated to 1200°C [9] or 1400°C [10].

A.5. References.

[1] Y.-M. Chiang, D. Birnie III and W.D. Kingery, in Physical Ceramics, John Wiley & Sons, Inc., New York (1997).

[2] S. K. Lau and S.C. Singhal, in Proc. Corrosion 85, Boston, (1985) paper 345.

[3] H. Solmon, Ph.D. Thesis, L'Université Paris. (1992).

[4] M. Kilo, G. Borchardt, S. Weber, S. Scherrer and K. Tinschert, in Solute Point-Defect Interactions, Loccum (1997) p1.

[5] R.D. Shannon, Acta. Cryst., **Vol A38** (1976) p751.

[6] D. Waller, S. Webb, J.D. Sirman and J.A. Kilner, presented at the 11th Int. Conf. On Solid State Ionics, Honolulu (1997).
[7] Y. Oishi, K. Ando and Y. Sakka, in Advances in Ceramics, **Vol 7**, Eds. M.F. Yan and A.H. Heuer, The American Ceramic Society (1989) p208.
[8] D. Dimos and D.L. Kohlstedt, J. Am. Ceram. Soc., **Vol 70** (1987) p531.
[9] J.A. Lane, Ph.D. Thesis, University of London (1996).
[10] J.D. Sirman, D. Waller and J.A. Kilner, in Proc. of the 5th International Symposium on SOFC, Eds. U. Stimming, S. Singhal, H. Tagawa and W. Lehnert, The Electrochemical Society, Inc., **PV 97-40**, Aachen, (1997) p1159.